Generation of pure hydrogen from wet waste biomass via gasification in supercritical water and sequential reforming of the hydrocarbons

Zur Erlangung des akademischen Grades eines

DOKTORS DER INGENIEURWISSENSCHAFTEN

von der KIT-Fakultät für Chemieingenieurwesen und Verfahrenstechnik des

Karlsruher Instituts für Technologie (KIT)

genehmigte

DISSERTATION

von

M. Sc. Athanasios Angelos Vadarlis

aus

Volos (Thessalien), Griechenland

Tag der mündlichen Prüfung: 07.05.2026

Erstgutachter: Prof. Dr. -Ing. Jörg Sauer

Zweitgutachterin: Prof. Dr. Angeliki A. Lemonidou

Declaration

I, Athanasios Angelos Vadarlis, declare that this thesis represents my own work and that I have written it independently by myself, without the use of other documents or sources beyond those stated in the references.

Acknowledgements

In this section, I would like to acknowledge all the individuals and organizations who contributed to and supported this doctoral work.

I would like to thank, first and foremost, my wife, Eleni Kortesi, for encouraging me to move from Greece to Germany and pursue this doctoral thesis. Before coming to Germany, she also left her life behind and trusted that our future here would be the best one for us. It was a difficult decision, with many hurdles and challenges along the way. Nevertheless, she has always been there for me, making every step of the journey easier, more enjoyable, and truly worth living by her side.

My parents, Marios Vadarlis and Antzela Monika Feritsean, have dedicated most of their lives to offer me the best possible education, unwavering financial and emotional support, and a life enriched with knowledge, wisdom, acceptance, and diverse cultural influences that have shaped my personality and allowed me to grow into the European citizen I aspire to be. Their support and influence played a decisive role in my decision to pursue my doctoral thesis at the Karlsruhe Institute of Technology. For all of this—and so much more—I could not be more grateful to them. My younger brother, Angelos Vadarlis, has always been a source of support, consistently helping me and being there to talk, allowing me to share my thoughts and emotions with him. While older siblings are usually expected to guide the younger ones, he has undoubtedly influenced my life with his kind and courageous character, honesty, and profound wisdom.

My best friends and relatives have always offered a helping hand, with every encounter with them during my PhD journey feeling like a much-needed breath of fresh air and a tremendous source of encouragement.

I would like to express my sincere gratitude to my PhD supervisor, Prof. Dr.-Ing. Jörg Sauer, who welcomed me into his research group, even during the challenging times of the pandemic. Despite his demanding schedule, he always found time to support my work and contribute with his insightful ideas and extensive experience in chemical engineering. Our discussions were consistently fruitful and meaningful, deepening my understanding and enriching my knowledge at every step. His broad, holistic approach significantly shaped the direction of my doctoral thesis, making it both diverse and impactful. Moreover, Prof. Sauer made it possible for me to gain valuable exposure to

the academic world of chemical engineering, enabling me to attend and participate in numerous international conferences and seminars.

I am also deeply grateful to Dr. Nikolaos Boukis, who welcomed me into his research team and gave me the opportunity to work closely with him and learn by his side. As one of the leading researchers in the field of supercritical water gasification, I truly valued every moment he dedicated to teaching me about this complex process. From the very beginning of my doctoral journey, Dr. Boukis served as a mentor—offering guidance not only on my research and academic development, but also on personal growth and navigating life as a Greek researcher in Germany, a path he once walked himself. Thanks to his support and example, I became not only a better researcher and engineer, but also a better person. For all of this, I am truly grateful to him.

Prof. Dr. Angeliki A. Lemonidou was the first person to believe in me and support me in taking the next step by helping me find a position at the Karlsruhe Institute of Technology. As a professor, she had a profound impact on me during my bachelor's and master's studies—not only through her teaching, but also through the dedication she showed to each of her students. She has been an exemplary educator to countless chemical engineering students at the Aristotle University of Thessaloniki. Later on, she continued to advise me in my research, and her insightful and wise approach to scientific questions helped me overcome the major challenges I faced during my doctoral work. The time I spent learning from her, especially in areas such as chemical reaction engineering and catalysis, was truly invaluable.

I would like to thank Dr. Sofia Angeli for giving me the opportunity to collaborate with her from the very beginning of my doctoral work. Our collaboration was instrumental in advancing my dissertation and in gaining a deep understanding of the phenomena governing the process we developed in the laboratory.

I would also like to thank my close colleagues at the Institute of Catalysis Research and Technology (IKFT). In particular, I am grateful to Julian Dutzi, who was the colleague closest to me and supported me not only in the lab, but also through countless discussions on the various questions and challenges that arose during our time at IKFT. His passion, friendly character, quick decision-making, and sharp intellect had a strong impact on me. I was fortunate to work with him on several projects beyond our respective doctoral theses. Together, we explored new ideas with enthusiasm, enjoyed a strong spirit of teamwork, and made a meaningful contribution to the field by

publishing numerous scientific articles. Likewise, I would like to thank Dr. Dominik Neukum, who readily offered his help and teamwork whenever I needed it. With his strong background in catalysis and chemistry, his contributions to my doctoral thesis were invaluable and played a key role in enabling our work to be published in high-impact journals. I will never forget the dedication and readiness of Elena Hauer and Karl Weiss, who supported me with laboratory and analytical tasks, as well as with building the laboratory layout and resolving technical issues, respectively. Both were always there for me—willing to assist not only in every aspect of my work, but also to offer support in my personal life. They never missed a chance to celebrate our shared achievements in Dr. Boukis's team, making the journey all the more rewarding.

I would also like to thank my colleagues for their valuable support throughout my doctoral work. Stefan Henecka provided essential help in designing the laboratory layout and resolving technical issues. Holger Kahrau was responsible for building all the electrical equipment used in our setup and continuously supported its operation during our research. I am also especially grateful to Roland Fritz, whose assistance with every IT-related matter was always precise, timely, and reliable. For their unwavering support in handling all administrative matters efficiently, I would like to sincerely thank Michaela Schmidt, Kerstin Barnack, Monika Zimmer, and Martin Bergermann.

I would also like to thank the rest of the IKFT members who were there for me and contributed to making my daily life at the institute both enjoyable and safe. Their support and camaraderie created a welcoming and productive environment. These individuals are the driving force behind the outstanding and impactful research that IKFT consistently delivers in the fields of catalysis, renewable fuels, and chemical process development for a sustainable future.

I would also like to thank all the members of the HEPTA program, and especially my fellow PhD students. Together, we shared many insightful discussions about our research topics, as well as the challenges we faced throughout our PhD journeys. The mutual support, understanding, and collaboration within this group made a meaningful difference at every step along the way.

Last but not least, I would like to thank the Helmholtz Association for funding my position at KIT and supporting my research within the framework of the project *HEPTA* (Helmholtz European Partnership for Technological Advancement). I am also grateful

to all those who made this program a reality, enabling 12 PhD students from Greece and Germany to work collaboratively on diverse research topics related to climate and the environment.

«Σαν τη λογιάσεις μια δουλειά, όρτσα και μη φοβάσαι, αμόλα τη τη νιότη σου και μην την εφοβάσαι.» — Ν. Καζαντζάκης, *Βίος και Πολιτεία του Αλέξη Ζορμπά*.

"Once you set your mind on a task, charge ahead and fear nothing, pour your youth into it and never hold back." — N. Kazantzakis, *Zorba the Greek*.

Preamble

This thesis is publication-based, with most of the results and associated text already published in peer-reviewed journals. Several sections of the thesis are identical to those in the published articles, while other sections have been modified to create a cohesive style for this thesis. These modifications include writing style, citation format, and minor adjustments to figures and tables.

Chapter 1 provides a detailed introduction, incorporating the first two sections of a publication completed as part of this doctoral dissertation, titled *Catalytic Biomass Gasification in Supercritical Water and Product Gas Upgrading* (DOI: 10.1002/cben.202300007).

Chapters 2 (*Direct steam reforming of the product gas from ethanol gasification with supercritical water*, DOI: 10.1016/j.ijhydene.2023.08.108) and 3 (*Supercritical water gasification and subsequent steam reforming of the product gas under elevated temperature and pressure*, DOI: 10.1016/j.ijhydene.2025.02.197) present the experimental work conducted for this thesis, with each chapter based on a separate publication. As such, most of the text is identical to that in the respective publications. Figures in these chapters have been formatted to ensure a consistent layout throughout the thesis.

The final chapter, titled *Supercritical Water Gasification of Ethanol as Biomass Model Compound in Tandem with Steam Reforming: Kinetic Modeling of the Reforming Step and Techno-Economic Analysis of the Integrated Concept* (DOI: 10.1021/acs.iecr.4c01486) is based on the latest publication written within the framework of this doctoral research. It focuses on computational work, simulations, as well as techno-economic and theoretical analyses aimed at enhancing the understanding of the newly developed chemical process. A part of this publication, specifically the development of the kinetic model, is not included in this thesis, as it was created by another researcher, Dr.-Ing. Bruno Lacerda de Oliveira Campos.

At the beginning of each chapter, on the same page as the title, the corresponding publication is cited, along with the contributions of each author.

Abstract

Hydrogen is increasingly recognized as essential in the shift to renewable and sustainable raw materials, especially for decarbonizing energy and industrial sectors. Currently, hydrogen production largely relies on fossil fuels, underscoring the need to shift towards renewable sources like biomass. The gasification of biomass with supercritical water (SCWG) is particularly promising for converting organic biomass into hydrogen, utilizing feedstocks from diverse origins with a high water content. This thesis presents the development and laboratory-scale testing of a novel process for maximizing hydrogen yield from the SCWG of waste biomass model compounds. The designed process integrates SCWG with the subsequent steam reforming of hydrocarbons across four reactors in series: the SCWG reactor, a pre-reformer, a main steam methane reformer (SMR), and a water-gas shift (WGS) reactor. In the SCWG reactor, actual wet waste biomass or model compounds such as ethanol are gasified in supercritical water. For the purposes of this thesis, ethanol has been used, since its use provides a constant operation with high gasification efficiencies, similar product gas compositions with several waste biomass resources and without the need of additional gas cleaning units and technical constraints, e.g., clogging. The pre-reformer then uses a heterogeneous Ni-based catalyst to reform the heavier hydrocarbons than methane, produced during SCWG. The SMR completes methane reforming at elevated temperatures, while the WGS reactor promotes additional hydrogen production by converting residual CO into CO_2 and H_2.

In the first part of the experimental study, the first two reactors, i.e., the SCWG and the pre-reformer were tested. Ethanol was fed into the SCWG reactor, and various temperatures, pressures, and gas hourly space velocities (GHSV) were tested in the pre-reformer. The remarkable findings of this study include achieving complete conversion of hydrocarbons at relatively moderate reforming temperatures and that the excess steam from the SCWG reactor minimized coke formation on the catalyst but caused Ni crystallite sintering, resulting in minor activity loss after a long-term experiment.

The main steam methane reformer (SMR) was then integrated to the system, downstream of the pre-reformer and tested under different conditions, with two Ni-based catalysts, a NiO(14wt.%)/$CaAl_{12}O_9$ and a NiO(18wt.%)/$CaK_2Al_{22}O_{34}$ catalyst.

Both showed minor coke deposition due to excess steam, though Ni sintering occurred at high temperatures. The NiO(18wt.%)/$CaK_2Al_{22}O_{34}$ catalyst showed higher activity due to its higher Ni loading. Although carbon formation was minimized, the high S/C ratio, together with the high temperatures applied and the rather weak support interactions accelerated the sintering of the active metal. The concentration of ethanol in the feed to the system and its effect on the final product gas was also tested here. Increasing the ethanol concentration in the SCWG feed from 5 to 20 wt.% lowered the steam-to-carbon (S/C) ratio, causing a rise in CH_4 and other carbonaceous species, which shifted SMR and WGS reactions equilibria, significantly reducing CH_4 conversion and H_2 yield. However, despite the lower S/C ratio, coke formation remained minor, indicating the stability of this multi-step process in processing organics at high concentrations.

Following the successful lab-scale demonstration, the process was theoretically scaled up using a process simulation software, and a techno-economic analysis evaluated its profitability and competitiveness in hydrogen production. Results showed a remarkable profitability improvement by increasing the concentration of ethanol in the feed from 8 wt.% to 20 wt.% ethanol. A concentration of 15 wt.% is recommended, balancing technical challenges like poor gasification efficiency, coking and catalyst poisoning in downstream catalytic reactors. Scaling up to 50 t h^{-1} drastically reduced the costs of the produced hydrogen. When using waste biomass, which is the ultimate objective for this developed process, like sewage sludge, feedstock availability becomes crucial. For instance, a 50 t h^{-1} plant processing sewage sludge at a 15 wt.% concentration would require disposal capacity on the scale of a city like Hamburg, Germany.

A sensitivity analysis showed that the ethanol price had the most profound impact on the hydrogen price. Thus, a more detailed investigation of the influence of the feedstock price on the price of the produced hydrogen was carried out. Applying negative feedstock prices, i.e., considering a revenue from processing sewage sludge, significantly lowered the produced hydrogen price to 0–1.8 \$ kg_{H2}^{-1}, making it competitive with natural gas steam reforming. Although real waste biomass processing needs additional equipment, reduced feedstock costs could offset these expenses, as indicated by the sensitivity analysis.

This thesis encompasses the development of a novel chemical process, followed by detailed laboratory experiments to prove its feasibility and offer insights into the activity

and stability of heterogeneous Ni-based catalysts within a distinctive steam reforming reaction system, with the absence of similar systems in the literature. Finally, it addresses the process scale-up, including the design of all essential units, from reactors to heat exchangers, and concludes with an exergy and techno-economic analysis. This work thus covers a broad scope of research in chemical and process engineering.

Zusammenfassung

Wasserstoff wird zunehmend als entscheidend für den Übergang zu erneuerbaren und nachhaltigen Rohstoffen anerkannt, insbesondere zur Dekarbonisierung der Energie- und Industriesektoren. Derzeit basiert die Wasserstoffproduktion größtenteils auf fossilen Brennstoffen, was die Notwendigkeit eines Wechsels zu erneuerbaren Quellen wie Biomasse verdeutlicht. Die Vergasung von Biomasse mit überkritischem Wasser (SCWG) ist vielversprechend zur Umwandlung organischer Biomasse in Wasserstoff, indem sie Rohstoffe mit hohem Wassergehalt aus verschiedenen Quellen nutzt. Diese Arbeit präsentiert die Entwicklung und laborgestützte Prüfung eines neuartigen Prozesses zur Maximierung der Wasserstoffausbeute aus der SCWG von Abfallbiomasse-Modelsubstanzen. Das entworfene Verfahren integriert die SCWG mit der anschließenden Dampfreformierung von Kohlenwasserstoffen über vier Reaktoren in Serie: den SCWG-Reaktor, einen Pre-reformer, einen Haupt-Dampfmethanreformer (SMR) und einen Wasser-Gas-Shift (WGS)-Reaktor. Im SCWG-Reaktor werden Modellverbindungen wie Ethanol in überkritischem Wasser vergast. Der Vorreformer nutzt anschließend einen heterogenen Ni-basierten Katalysator zur Reformierung sowohl der schwereren Kohlenwasserstoffe als auch Methan, die während der SCWG entstehen. Der SMR vervollständigt die Methanreformierung bei hohen Temperaturen, während der WGS-Reaktor durch Umwandlung von Rest-CO in CO_2 und H_2 die H_2-Ausbeute erhöht.

Im ersten Teil der experimentellen Studie wurden die ersten beiden Reaktoren, d. h. der SCWG-Reaktor und der „Pre-reformer“, getestet. Ethanol wurde in den SCWG-Reaktor eingespeist, und im Pre-reformer wurden verschiedene Temperaturen, Drücke und Verweilzeiten getestet. Bemerkenswerte Ergebnisse dieser Studie waren die vollständige Umwandlung der höheren Kohlenwasserstoffe bei relativ moderaten Reformertemperaturen und die Tatsache, dass der überschüssige Dampf aus dem SCWG-Reaktor die Koksbildung auf dem Katalysator minimierte, jedoch zu einer leichten Sinterschädigung von Ni-Kristalliten führte, was nach einem Langzeitversuch einen geringfügigen Aktivitätsverlust verursachte.

Der Haupt-Dampfmethanreformer (SMR) wurde dann dem System nach dem Vorreformer hinzugefügt und unter verschiedenen Bedingungen mit zwei Ni-basierten Katalysatoren, einem NiO(14wt.%)/$CaAl_{12}O_9$ und einem NiO(18wt.%)/$CaK_2Al_{22}O_{34}$-

Katalysator, getestet. Beide zeigten nur geringe Koksablagerungen aufgrund des überschüssigen Dampfes, obwohl Ni-Sinterung bei hohen Temperaturen auftrat. Der NiO(18wt.%)/$CaK_2Al_{22}O_{34}$-Katalysator zeigte aufgrund seiner höheren Ni-Beladung eine höhere Aktivität. Obwohl die Kohlenstoffbildung minimiert wurde, beschleunigten das hohe Dampf-Kohlenstoff-Verhältnis, die hohen Temperaturen und die eher schwachen Wechselwirkungen mit dem Träger das Sintern des aktiven Metalls. Auch die Ethanolkonzentration im Feed und deren Einfluss auf das Endproduktgas wurden untersucht. Die Erhöhung der Ethanolkonzentration im SCWG-Feed von 5 auf 20 Gew.% senkte das Dampf-Kohlenstoff-Verhältnis und führte zu einem Anstieg von CH_4 und anderen kohlenstoffhaltigen Spezies, was die Gleichgewichte der SMR- und WGS-Reaktionen verschob und die Methanumwandlung sowie die Wasserstoffausbeute erheblich verringerte. Trotz des niedrigeren Dampf-Kohlenstoff-Verhältnisses blieb die Koksbildung jedoch gering, was eine Stabilität bei der Verarbeitung von Ethanol in hohen Konzentrationen anzeigt.

Nach der erfolgreichen Demonstration im Labormaßstab wurde der Prozess mit Hilfe eines Modells skaliert und durch eine techno-ökonomische Analyse bewertet. Die Ergebnisse zeigten eine deutliche Verbesserung der Rentabilität durch Erhöhung der Ethanolkonzentration im Feed von 8 auf 20 Gew.%. Eine Konzentration von 15 Gew.% wird empfohlen, da höhere Konzentrationen zu technischen Herausforderungen wie geringere Vergasungsumsatz, Koksbildung und Katalysatorvergiftung in nachgeschalteten katalytischen Reaktoren führt. Die Skalierung auf 50 t h^{-1} senkte die Kosten des produzierten Wasserstoffs drastisch. Bei der Verwendung von Abfallbiomasse wie Klärschlamm wird die Verfügbarkeit der Rohstoffe entscheidend. Zum Beispiel, eine 50 t h^{-1} Anlage, die Klärschlamm mit einer Konzentration von 15 Gew.% verarbeitet, würde eine Abfallentsorgungskapazität auf der Größenordnung einer Stadt wie Hamburg erfordern.

Eine Sensitivitätsanalyse zeigte, dass der Ethanolpreis den stärksten Einfluss auf den Wasserstoffpreis hatte. Daher wurde eine detaillierte Untersuchung des Einflusses des Rohstoffpreises auf den produzierten Wasserstoffpreis durchgeführt. Die Anwendung negativer Rohstoffpreise, wenn z.B. die Verarbeitung von Materialien wie Klärschlamm berücksichtigt wird, senkte den Preis des produzierten Wasserstoffs erheblich auf 0 - 1.8 \$ kg_{H2}^{-1} und machte ihn wettbewerbsfähig mit der Dampfreformierung von Erdgas. Obwohl die Verarbeitung von realer Abfallbiomasse zusätzliche

Prozesseinheiten erfordert, könnten niedrigere Rohstoffkosten diese zusätzlichen Kosten kompensieren, wie aus der Sensitivitätsanalyse hervorgeht.

Diese Arbeit umfasst die Entwicklung eines neuartigen chemischen Prozesses, gefolgt von detaillierten Laborexperimenten zum Nachweis der Machbarkeit und Einblicke in die Aktivität und Stabilität von heterogenen Ni-basierten Katalysatoren in einem neuartigen Dampfreformierungs-Reaktionssystem, das in der Literatur nicht zu finden ist. Abschließend wird der Prozess auf industriellen Maßstab ausgelegt, einschließlich der Konstruktion aller wesentlichen Einheiten, von Reaktoren bis zu Wärmetauschern, und mit einer Exergie- und techno-ökonomischen Analyse abgeschlossen. Diese Arbeit deckt damit ein breites Spektrum der Forschung in der chemischen und verfahrenstechnischen Ingenieurwissenschaften ab.

Table of Contents

Chapter 1. Introduction to the supercritical water gasification of biomass and the subsequent upgrading of the product gas for increased hydrogen production

The content of this chapter is sourced from the following publications:

Vadarlis A. A.; Angeli S. D.; Lemonidou A. A.; Boukis N.; Sauer J. Catalytic Biomass Gasification in Supercritical Water and Product Gas Upgrading. *ChemBioEng Reviews*. **2023**, *10* (4), 370–398. DOI: 10.1002/cben.202300007.

Declaration of contributions:

Athanasios A. Vadarlis conceptualized the work, performed the literature review, organized and analyzed the data, evaluated the results, and wrote the manuscript.

Sofia Angeli conceptualized the work, supported the data analysis, evaluated the results, contributed to the discussion, and reviewed the manuscript.

Angeliki Lemonidou conceptualized the work, evaluated the results, contributed to the discussion, and reviewed the manuscript.

Nikolaos Boukis supervised the work, contributed to the discussion, and reviewed the manuscript.

Jörg Sauer supervised the work, contributed to the discussion, and reviewed the manuscript.

1.1 The role of biomass supercritical water gasification as a technology for sustainable hydrogen production

Climate change is considered one of the greatest threats to the future life of humans and other living organisms [1]. Rising global temperature drastically affects climate change and its levels have increased rapidly due to human activities specifically related to energy and industrial sectors. Until now, most of the energy and the products needed in daily human lives come from fossil sources, which have generated enough carbon dioxide to significantly affect this rise in global temperature. On December 2015 in Paris, the World Climate Summit set the goal to reduce the emission of greenhouse gases and especially of CO_2 to net-zero by 2050 and to 50% by 2030 [1–3]. To achieve this, the decarbonisation of the energy sector and of the chemical industry is necessary. A promising step towards this goal is an energy transition based on various technologies for the production and use of hydrogen [4,5]. The importance of hydrogen is high, as in addition to its crucial role as raw material and intermediate product for the production of many important chemicals, such as ammonia and synthetic fuels, in a powerful energy carrier with combustion free of harmful carbon oxides [1].

Until today, hydrogen production is based mostly on the utilization of fossil fuels [1]. Instead, renewable energy resources must be utilised, one of them being biomass. Biomass originates from many resources mostly agricultural, municipal and animal [6]. Depending on its origin the composition may be different with the most important categories being the oil-based and lignocellulosic biomass. Its model compounds of the latter are the monomers that result from the breakdown of macromolecules that make up the biomass resources, e.g., glucose that originates from cellulose. A technology that utilises biomass for hydrogen production is the gasification with water under supercritical conditions (SCWG). Using supercritical water for biomass gasification is particularly effective for processing waste biomass with high water content, as it eliminates the need for feed pre-drying[7].

This technology developed in the 1970s, has gained a lot of scientific interest since then[8]. Under supercritical conditions, i.e., T > 374 °C and p > 221 bar, the density of water, its viscosity, ion dissociation constant and dielectric constant decrease dramatically in

comparison with its values under near critical conditions. This leads to a drastic decrease of its inorganic solubility and a drastic increase of its solubility in non-polar substances [8]. Under non-critical conditions, the non-polar compounds would remain un-dissolved and could result to char and tar formation. In addition, the low viscosity enhances the diffusivity of the reactants, leading in turn to higher reaction rates [9]. In the presence of supercritical water, biomass long chain molecules undergo hydrolysis and are converted into their respective monomers [8]. The main chemical reactions that govern the process of SCWG can be divided into three main categories. The first category contains the reactions of the biomass monomers and/or their pseudo-components with supercritical water to form hydrogen and carbon oxides [10]:

$$C_xH_yO_z + (2x - z)H_2O \rightarrow xCO_2 + \left(2x - z + \frac{y}{2}\right)H_2 \quad (1.1)$$

$$C_xH_yO_z + (x - z)H_2O \rightarrow xCO + \left(x - z + \frac{y}{2}\right)H_2 \quad (1.2)$$

The second category contains the reactions that involve the gas products from the steam reforming reactions, the methanation reaction of CO (Eq. 1.3) and the WGS, which stands for water-gas shift (Eq. 1.4):

$$CO + 3H_2 \leftrightarrow CH_4 + H_2O \qquad \Delta H^0 = -206\ kJ\ mol^{-1} \quad (1.3)$$

$$CO + H_2O \leftrightarrow CO_2 + H_2 \qquad \Delta H^0 = -41.2\ kJ\ mol^{-1} \quad (1.4)$$

Methane can also be formed by other reactions, such as by decarboxylation of acetic acid or by decarbonylation of acetaldehyde [11]. The third category is related to all the reactions that lead to tars formation, e.g., dehydration and condensation reactions [12,13] and to coke formation, i.e., coke from intermediates decomposition (Eq. 1.5), CO reduction (Eq. 1.6), Boudouard (Eq. 1.7) and CH_4 decomposition (Eq. 1.8) [8,14]:

$$C_xH_yO_z \rightarrow Coke \quad (1.5)$$

$$CO + H_2 \leftrightarrow C + H_2O \qquad \Delta H^0 = -131\ kJ\ mol^{-1} \quad (1.6)$$

$$2CO \leftrightarrow C + CO_2 \qquad \Delta H^0 = -172\ kJ\ mol^{-1} \quad (1.7)$$

$$CH_4 \leftrightarrow C + 2H_2 \qquad \Delta H^0 = 75\ kJ\ mol^{-1} \quad (1.8)$$

The SCWG of biomass is thus a valuable process for utilizing waste biomass with high water content and generating a product gas that consists of H_2, CH_4, CO_2, CO and other hydrocarbons, mainly C_2-C_3. It can be used as a fuel gas or a gas for downstream upgrading processes.

1.2 Development of the biomass supercritical water gasification technology

The SCWG of biomass is a process continuously developed since the late seventies[15]. Model et al.'s work was among the first on hydrothermal gasification [16]. Their experiments on glucose and cellulose, with or without Ni oxide catalyst in batch reactors had showed insignificant gas yields when working below the critical point of water. Above its critical point, water could facilitate the gasification, resulting in significant gas yields.

Later on, Elliot and his group contributed significantly to the early development of the catalytic hydrothermal gasification of biomass [17,18]. They designed and patented Ni-based catalysts with various metal promoters, facing the problems related with the loss of activity, i.e., crystallite sintering and support breakdown [16,19]. Elliot et al. were also among the first who worked with continuous-flow gasification of biomass and addressed the problems that are associated with its utilization, like reactor plugging[20–23].

Antal's group began investigating the SCWG of glucose and wet biomass feedstocks in 1990. Their early experiments were performed without any catalyst [11,24], achieving a carbon gasification efficiency higher than 85% but with a composition of the product gas well below the equilibrium values. They later used activated carbon and charcoal, generating complete gasification of 22 wt.% glucose and a hydrogen-rich gas, at 600 °C and 345 bar [25,26]. However, they reported deactivation of their catalysts after several hours of time on stream, plugging due to char formation and corrosion of the nickel alloy reactors.

Vogel et al. contributed significantly on the field of hydrothermal processing of biomass. Apart from investigating the performances of Ni-based catalysts supported on α-alumina, they experimented on Raney-Ni catalysts and on Ru/C as well [17,27–30]. The work of Vogel et al. on process development for the catalytic hydrothermal gasification [31,32], on salt

separation [27–29] and on the parameters that affect mostly coke and tar formation[30], is also remarkable.

Initial work at Karlsruhe Institute of Technology (KIT, formerly called Forschungszentrum Karlsruhe) focused on the SCWG of various feedstocks in batch and continuous tubular reactors [33–35]. Their key findings highlighted the significant increase in the H_2 yield by employing potassium-containing alkali salts, such as KOH and K_2CO_3. They later constructed a pilot-plant, called VERENA (German acronym for “Experimental facility for the exploitation of agricultural matter”), with a maximum feed flow rate of 100 kg h^{-1} and maximum operating temperature and pressure of 700 °C and 350 bar, respectively [36]. Tested organics were methanol [37], ethanol [38], crude and purified glycerol [39], pyroligneous acid [36], sewage sludge[40], corn silage [37], and digestated sludge [41]. Their concentration lied in the range 9 – 25 wt.%. They achieved gasification yields in the range 90 – 98%. However, their initial setup faced tube plugging, due to salt precipitation, and the operation could last for 3.5 hours. Two modifications were employed to overcome the salt precipitation. First, a specific reactor with a salt removal part on the bottom was designed to collect the separated solids, which is possible due to the reactor’s down-flow design [36,39]. The second configuration includes preheating the reactor feed below its supercritical point before entering the reactor to avoid any solids deposition upstream of the reactor and subsequent mixing with supercritical water at the top of the reactor for further heating to reach the desired operating temperature inside the reactor [36,38]. The two modifications could increase the continuous operation of the plant to 10 hours.

Laboratory-scale research on biomass SCWG at KIT has been ongoing for over two decades and remains active today. The research focuses on process development [42,43], testing different types of biomass [44,45], and deepening the understanding of how process parameters [46] and various homogeneous catalysts [33,34,47,48] affect H_2 yield and carbon gasification efficiency.

Matsumura’s group has made significant contributions to SCWG research. Their work on the supercritical water gasification of biomass has included studies on the reaction mechanisms of cellulose, xylan, and lignin mixtures [49], as well as the effects of carbon nanotubes and various catalysts, such as ruthenium supported on carbon nanotubes, on gasification efficiency, product gas composition, and the reactions occurring within the

system [50–52]. They had also addressed the problem of pre-treating biomasses that are very dry or absorb water quickly and thus, are not effectively converted into slurries to be fed to the gasification reactor. For the latter part of their work, they developed a process for the pre-treatment of the feedstock to the SCWG reactor [15], where a continuous reactor at 150 – 200 °C was fed with a mixture of water and pulverized cabbage for a residence time of 30 min, resulting in a product slurry that could be further fed into the SCWG reactor and offer higher gasification rates than the pulverized cabbage. The optimal temperature for this process was found to be 150 °C, since higher temperatures resulted in lower gasification rates.

Despite decades of development, SCWG technology still faces technical challenges that limit its commercial viability, prompting ongoing efforts to overcome these obstacles. Notable issues include reactor corrosion, clogging from salt and coke deposits in the reactor and piping[11,15], and low gasification efficiencies and hydrogen yields at relatively high organic concentrations in the feed [10,11,15]. Peterson et al. [11] suggest that for SCWG to be economically feasible, the organic content in the feed should be between 15-20 wt.%.

1.3 Literature review of recent research on the catalytic SCWG of biomass with emphasis on hydrogen production

The SCWG of organic substances involves reactions such as water gas shift and methanation, which have high activation energies and therefore need a catalyst [10,13,53–56]. Apart from that, it has been shown that catalysts can enhance carbon gasification efficiency and facilitate the approach to equilibrium gas yield [55,57]. Ni-based catalysts for example favour the cleavage of C-C bonds instead of favouring dehydration and condensation reactions, inhibiting therefore tars formation [56]. Figure 1.1 illustrates the classification of metal catalysts that can be used for the SCWG of biomass.

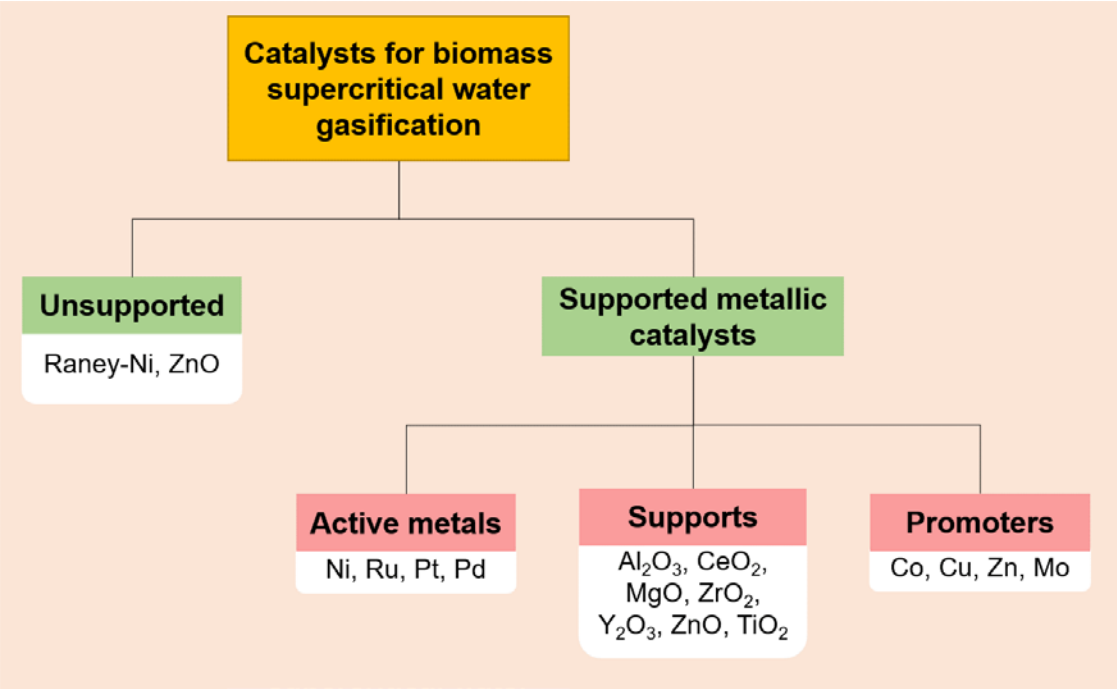

Figure 1.1 Classification of the metallic catalysts used in SCWG of biomass.

Apart from the heterogeneous catalysts, homogeneous ones based on alkali metals, e.g., KOH, $KHCO_3$, K_2CO_3, $Ca(OH)_2$, have been shown to promote hydrogen and carbon dioxide production [8,10,53]. Their main disadvantage is that they are difficult to recover from the output of the system and therefore a new batch of catalyst is required for each new feed. In addition, the inner surface of the reactor can act as a catalyst for the SCWG of organic solutions [58].

This chapter focuses on recent development in catalysts for the supercritical water gasification of biomass and its model compounds. Two main criteria, the carbon gasification efficiency or CGE, and the yield of the produced gases are used for evaluating the performance of the catalysts. The CGE is defined as the degree of conversion of carbon, which is contained in the organic feed, towards the product gases that contain it, i.e., CH_4, other hydrocarbons, CO and CO_2:

$$CGE\ (\%) = \frac{n_{C,prod.gas}}{n_{C,feed}} \tag{1.9}$$

The best case for the SCWG is to attain complete gasification of the organic feed. In this case, all the carbon that is present in the organic feed can be found in the product gases. However, this is an unrealistic scenario and, especially when real biomass is used as

feedstock, the CGE is a matter of optimization. In most of cases, a relatively high CGE is found when not only H_2, CO_2 and CO, are produced but also CH_4 and other hydrocarbons. In addition to CGE, the yield of H_2, CH_4 and total gas products are used in the discussion to compare the activities of the studied catalysts:

$$Y_i\left(\frac{mol}{kg}\right) = \frac{n_i}{m_{feed}}, \qquad i = H_2 \; or \; CH_4 \tag{1.10}$$

If the yields of all produced gases are added together, the total gas yield can be calculated as:

$$Y_{total}\left(\frac{mol}{kg}\right) = \frac{n_{H_2}+n_{CH_4}+n_{CO}+n_{CO_2}+n_{C_{2+}}}{m_{feed}} \tag{1.11}$$

Focus has been given on the catalysts that consist of a transition metal as the catalytically active phase and one or more metal oxides as the support. The catalysts are classified based on the supports, as their role is important both in the gasification and in reforming. At the end of this chapter a summary table, the Tab. 1.1, of the catalysts discussed in the main text is provided. This table contains the catalysts from the most representative sources. In this table, a new evaluation criterion is introduced expressing the quantity of hydrogen produced bound in methane and other hydrocarbons versus the total quantity of hydrogen in the products including the diatomic hydrogen:

$$R_{Hydrogen\,bound} = R_{Hb} = \frac{n_{Hydrogen\,in\,hydrocarbons}}{n_{Hydrogen\,in\,hydrocarbons} + 2n_{H_2}} \tag{1.12}$$

This parameter in combination with CGE indicates if the gas produced needs to be upgraded with a subsequent reforming process towards additional H_2 production.

1.3.1 Catalysts based on Al_2O_3

Azadi et al. [59] tested Ni-based catalysts with a variety of different supports for SCWG of a 2 wt.% glucose-water solution in a batch reactor. Among the catalysts tested, Ni/α-Al_2O_3 had the best performance and is reported in Tab. 1.1. They reported the reasons that make α-Al_2O_3 an ideal support for SCWG of glucose. The first reason is the high reducibility of Ni^{2+} cations on its surface. Secondly, α-Al_2O_3 has high stability under SCW conditions. In contrast, the γ-Al_2O_3 support loses its stability when it is exposed to SCW and undergoes phase transition to boehmite. This transition leads to obstruction of Ni

active sites. Furthermore, among all alumina phases, α-alumina has the least acidic sites, which, as they mention, promote polymerization reactions and thus, lead to tars formation, and also promote dehydration and consecutively hydrogenation reactions, leading to alkanes formation. Also, α-Al_2O_3 has remarkably high mechanical strength and low solubility in SCW.

Louw et al. [57] compared a Ni/Al_2O_3-SiO_2 catalyst with a homogeneous K_2CO_3 for the SCWG of primary paper waste sludge, or PWS. The results shown in Tab. 1.1, indicated that the heterogeneous Ni catalyst could approach the equilibrium, in contrast to the homogeneous one. The latter catalyst had very high H_2 yield but half the total gas yield that the Ni catalyst produced, i.e., 18.50 mol kg_{PWS}^{-1} and 40.62 mol kg_{PWS}^{-1} respectively. The K_2CO_3 catalyst promoted the WGS reaction, while Ni/Al_2O_3-SiO_2 promoted steam reforming and hydrogenations. However, in the study of Okolie et al. [60], where the catalytic SCWG of soybean straw was investigated, the Ni/Al_2O_3-SiO_2 had the worst performance in terms of H_2 yield and selectivity (3.5 mol kg^{-1} and 48% respectively). The best two catalysts were Ni/ZrO_2 and Ni/Al_2O_3 reaching H_2 yields of 8.1 mol kg^{-1} and 7 mol kg^{-1}, respectively, and are given in Tab. 1.1. The total gas yield of the Ni/Al_2O_3 was 24.1 mol kg^{-1}, whereas the respective yield of the Ni/ZrO_2 was 17.4 mol kg^{-1}. The H_2 selectivity of the Ni/ZrO_2 was double that of the Ni/Al_2O_3.

Table 1.1 Catalysts for SCWG of organic feedstock and their activity in terms of carbon gasification efficiency (CGE) and H_2 gas yield. The ratio R_{Hb} is also given to show how much of the produced hydrogen is bound to the hydrocarbons.

Catalyst	Feed	Temperature Pressure	HSV[a] (h^{-1})	Reaction time[a] (h)	CGE (%)	H_2 yield (mol kg_{feed}^{-1})	R_{Hb} (%)	Ref.
I)	Catalysts supported on Al_2O_3 and Raney-Ni catalysts							
Ni(4wt.%)-Mo(21wt.%)/Al_2O_3	C. vulgaris (7.3wt.%)	600 °C, 240 bar	-	0.033	62	-	73.33	55
Pt(0.63wt.%)-Pd(0.68wt.%)/Al_2O_3					65.8		83.02	
Co(5wt.%)-Mo(20wt.%)/Al_2O_3					64		87.24	
Ni(65wt.%)/Al_2O_3-SiO_2	Primary paper water sludge (10wt.%)	450 °C, 292 bar	-	2	85.9	6	84.01	57

Raney-Ni (50wt.% solid catalyst – 50 wt.% water)	Sugarcane bagasse (9wt.%)	400 °C, 250 bar	-	1.25	53.1	1.3	94.12	13
Ru-Ni(10wt.%)/ γ-Al_2O_3 (Ru/Ni molar ratio = 0.1)	Glucose (5wt.%)	600 °C, 240 bar 750 °C, 240 bar	6 6	-	99.2 99.6	25.5 53.9	34.25 5.38	12
Ni(5wt.%)/ α-Al_2O_3	Glucose (2wt.%)	380 °C, 230 bar	-	1	67	24.3	27.46	59
Ni(20wt.%)-Cu(5wt.%)/ γ-Al_2O_3 Ni(20wt.%)-Co(5wt.%)/ γ-Al_2O_3 Ni(20wt.%)-Sn(5wt.%)/ γ-Al_2O_3	Glucose (9wt.%)	400 °C, -	-	0.33	32.13 21.02 21.02	10.9 8.5 3.95	23.78 19.05 33.61	61
Ni(10wt.%)-Co(6wt.%)/Al_2O_3	Cellulose (1.6 wt.%)	350 °C, 165 – 180 bar	-	0.33	55.08	59	10.06	62
Ru(5wt.%)/ α-Al_2O_3	Glucose (5wt.%) Cellulose (5wt.%)	550 °C, 360 bar	-	0.166	96.2 96.4	10 8.5	62.70 63.68	63
Ru(5wt.%)/ γ-Al_2O_3 Ru(5wt.%)-Zn(1.5wt.%)/ γ-Al_2O_3	Bagasse (1.25 wt.%)	400 °C, -	-	0.25	45 30	14 15.6	3.85 2.88	64
Ni(12wt.%)/ α-Al_2O_3 Raney-Ni(68.2wt.%)	C. vulgaris (5wt.%)	385 °C, 260 bar	-	1.5	87 88	2.5 2.5	94.74 95.22	65
Raney-Ni(93.57wt.%) - Mo(0.31wt.%)	Sewage sludge (8.9wt.%)	450 °C, 214 – 286 bar	-	0.42	90.1	18.13	55.39	66
Ni(20wt.%)-Ce/Al_2O_3 (Ce/Ni molar ratio = 0.36,)	Lignin (20wt%)	650 °C, 260 bar	-	0.83	-	2.15	55.42	67
II)	Catalysts supported on CeO_2 or CeO_2-Al_2O_3							
Ni(10wt.%)/ CeO_2-Al_2O_3	Glucose (10wt.%)	400 °C, 235 bar	-	0.33	76.6	1	33.33	68
Ni(20wt.%)/ CeO_2 -γ-Al_2O_3 (Ce: 5wt.%)	Glucose (9.09wt.%)	400 °C, 245 bar	-	0.33	58.05	12.7	31.35	69

Ni(10wt.%)/ CeO_2-Al_2O_3	Glucose (12.5wt.%)	400 °C, -	-	0.5	10	0.85	39.29	70
Ni(20wt.%)/ CeO_2-Al_2O_3 (Ce=8.46wt.%)	Glucose (9.09wt.%)	400 °C, 245 bar	-	0.33	33.03	12.99	23.54	71
Ru(1wt.%)/CeO_2	HTL downs. Water (no pure water added)	600 °C, 460-520 bar	-	1	83.26	1.05	77.66	72
III)	Catalysts supported on MgO or MgO-Al_2O_3							
$Mg_{0.8}Ni_{0.2}O$	Oil palm frond (3wt.%)	400 °C, 250 bar	-	0.5	-	-	53.95	73
Ni(5wt.%)/MgO	Glucose (2wt.%)	380 °C, 230 bar	-	1	72	26.9	31.55	59
Ni (2.6wt.%)-Co(5.2wt.%)/ Mg-Al	Lignin (20wt.%)	650 °C, 260 bar	-	0.83	-	2.36	58.06	74
Ni(26.3wt.%) /$MgAl_2O_4$-Al_2O_3	Glucose (5wt%)	400 °C, 221 bar	-	0.33	70	11.8	57.55	75
Ni(28.6wt.%)/ $Mg_{0.6}$–$Al_{1.9}$	Glucose (9wt.%)	400 °C, 225-250 bar	-	0.33	70	11.77	56.68	76
SG[b] -Ni/ MgO-Al_2O_3 SC[b] -Ni/ MgO-Al_2O_3	Glycerol (20wt.%)	500 °C, 230 bar	-	0.33	68.3 55.3	6.52 9.77	74.47 57.14	77
Ni(10wt.%)/MgO	Glucose (12.5wt.%)	400 °C, -	-	0.5	-	0.8	39.39	70
Ru(1wt.%)/MgO	HTL[c] downs. water	600 °C, 460-520 bar	-	1	71.46	0.79	78.24	72
IV)	Catalysts supported on ZrO_2 or MgO-ZrO_2							
Ni(10wt.%)/ZrO_2 Ni(10wt.%)-Ce(1wt.%)/ ZrO_2	Soybean straw/water (1:10)	500 °C, 230-250 bar	-	0.75	21.5 33.5	8.10 10.90	46.71 47.09	60
Ni(15wt.%)/ZrO_2 Ni(15wt.%)-Co(5wt.%) /ZrO_2	Polyethylene glycol (2 g L^{-1})	390 °C, 240 bar	0.05	-	48.50 59	37.30 50	15.42 13.79	78
Ni/ZrO_2 (Ni/Zr molar ratio = 0.4:0.6)	Glycerol (20wt%)	500 °C, 230 bar	-	0.5	93.8	4.78	53.19	79
Ni(20wt.%)/ MgO-ZrO_2	Glycerol (5wt.%)	800 °C, 245 bar 700 °C, 245 bar	3600	-	95 -	70.58 58.64	17.72 20.59	80
Ni(15wt.%)/ZrO_2	Glycerol (3wt.%)	425 °C, 252 bar	0.83	-	97	12.92	59.52	81

V)	Catalysts based on yttrium-containing supports							
$Ni(5wt.\%)/Y_2O_3$ $Ni(5wt.\%)/YSZ$	Glucose (2wt.%)	380 °C, 230 bar	-	1	59 51	26.5 11.5	35.85 30.35	59
$Ni(19.5wt.\%)/Zr_{0.8}Y_{0.2}O_{2-\delta}$ $Ni(17.26wt.\%)/Zr_{0.4}Ce_{0.4}Y_{0.2}O_{2-\delta}$	Glucose (10wt.%)	500 °C, 230-240 bar	-	0.5	66 76	22 17	23.08 42.18	82
VI)	Catalysts supported on ZnO or CaO							
Ni(5wt.%)-Zn(5wt.%)/CaO	Empty palm fruit bunches (3.75wt.%)	380 °C, -	-	0.5	-	135 mol L^{-1}	2.58	83
Ni(1wt.%)/ZnO	Glucose (10wt.%)	400 °C, 241– 256 bar	-	0.33	21	0.2	29.41	84
VII)	Catalysts supported on TiO_2							
$Ni(10wt.\%)/TiO_2$ $Ni(10wt.\%)-Ce/TiO_2$ (Ce/Ni= 0.1)	Lignin (20wt.%)	650 °C, 260 bar	-	0.83	-	1.83 1.94	- -	67
$Ni(5wt.\%)/TiO_2$	Glucose (2wt.%)	380 °C, 230 bar	-	0.25	59	16.7	29.54	59
$Ni(15wt.\%)/TiO_2$	Glycerol (3wt.%)	425 °C, 252 bar	0.83	-	95-100	15.96	50	81
$Ni(1wt.\%)/TiO_2$	Glucose (10wt.%)	400 °C, 241-256 bar	-	0.33	19.5	2.5	28.57	84
$Ru(2wt.\%)/TiO_2$	C. vulgaris (7.3 wt.%)	600 °C, 240 bar	-	0.033	65	10	68.45	55
$Ru(1wt.\%)/TiO_2$	HTL downstream water[c] (no pure water added)	600 °C, 460-520 bar	-	1	88.7	0.91	77.19	72
$Zn(20wt.\%)/TiO_2$ $Ni(20wt.\%)/TiO_2$	Furfural 10wt.%	400 °C, -	-	0.33	12 10	17.38 4.5	31.36 51.05	85

[a] If the catalyst was used in a batch gasification process, then the reaction time is given. Otherwise, the GHSV, is given in h^{-1}; [b] SC stands for the synthesis of the catalyst with supercritical water and SG for the corresponding sol-gel technique; [c] HTL stands for Hydrothermal liquefaction of microalgae.

Kang et al. [74] prepared Ni-Co/Mg-Al catalysts for SCWG of lignin. Two different methods for catalyst preparation were tested, the coprecipitation and the impregnation. The catalyst that performed the best was prepared by coprecipitation and it is given in Tab. 1.1. They

reported the positive effect of Ni-based catalyst promoted with Co on hydrogen production and on CH_4 conversion via the steam reforming reaction at relatively high temperature [53,75]. Cobalt may act as carbon formation inhibitor and this was ascribed to the interaction with the Ni sites in Ni-Co alloys [86]. Li et al. [61] also reported that Co acts as an efficient promoter enhancing hydrogen selectivity for Ni-based catalysts. The beneficial effect of cobalt was confirmed in the study of Sun et al. [62] who reported 1.44 times increased H_2 yield of a Ni/Al_2O_3 catalyst for hydrothermal gasification of cellulose by adding 6 wt.% Co as a promoter (Tab. 1.1), despite the slightly lower specific surface area of the Co promoted catalyst. As the loading of Co increased, NiO and Co_3O_4 started to transform into $NiCo_2O_4$, increasing the interaction between Ni and Co and therefore preventing carbon deposition on Ni. Kang et al. [74] also found that for the $Ni-Co/MgO-Al_2O_3$ catalyst, the method of coprecipitation increased the amount of strong acidic sites, when compared to the method of impregnation [75,76]. Strong acidic sites benefit the lignin decomposition and the accessibility of hydrogen atoms [74,87]. Kang et al. [87] tested Ce-promoted Ni-based catalysts supported on Al_2O_3 at SCWG of lignin and cellulose feedstocks. They also tested un-promoted Ni/Al_2O_3 catalysts. The highest gas yield, both from lignin and from cellulose, was reported for $Ni-Ce/Al_2O_3$. The $Ni-Ce/Al_2O_3$ resulted in similar H_2 gas yields from both lignin and cellulose, of 2.15 and 1.90 mol kg^{-1}, respectively. In Tab. 1.1, $Ni-Ce/Al_2O_3$ catalyst and its performance on the gasification of lignin (20 wt.%) is given. Ce-promoted catalysts presented higher metal dispersion and better coke resistance. As demonstrated in earlier studies [67,68], Ce-promotion facilitates Ni dispersion and the weakening of interaction between Ni and Al_2O_3, thus helping its reducibility and the attenuation of carbon formation. Okolie et al. [60] came up with this argument as well, when they used Ce for the promotion of Ni/Al_2O_3 and Ni/ZrO_2 catalysts for SCWG of soybean straw. In addition, they proposed that Ce promoted steam reforming reactions and the oxidation of carbon deposits.

As Li et al. [76] reported, small amounts of Mg in Mg-Al supports, could enhance the hydrothermal stability under SCWG due to the formation of $MgAl_2O_4$ and hinder the formation of graphite carbon. However, Mg forms MgO, which retards the reduction of nickel oxides to nickel nanoparticles [76]. In one of their recent studies [75], they tested a $Ni/MgAl_2O_4-Al_2O_3$ catalyst prepared by co-precipitation in SCWG of different feedstocks. The catalyst promoted H_2 production and reached extremely high gasification efficiencies

of hydrogen and carbon, 160% (including the hydrogen coming from water in the feed) and 70% respectively, as reported in Tab. 1.1, with a 5 wt.% glucose feed solution.

A Ni/MgO-Al_2O_3 catalyst and a Ni/Al_2O_3 catalyst, prepared by supercritical water synthesis or SCWS, were used for SCWG of glycerol [77]. Their performances were compared with that of other catalysts that were synthesized by SCWS, including Ni/ZrO_2, Ni/CeO_2-ZrO_2, Ni/activated carbon or AC and Ni/carbon nano tubes, or CNT. The first two outperformed all the other tested catalysts in terms of CGE and H_2 yield. Their high H_2, CH_4 and CO_2 yields were attributed to their promotional effect on the reactions of WGS, methanation and of decomposition of organic molecules. It was reported that the Mg promotion led to the formation of the highly dispersed $MgAl_2O_4$ spinel, which enhanced the stability of the Ni/Al_2O_3 pore structure.

Ru-based catalysts supported on Al_2O_3 have been proved effective in SCWG of organic feedstock. Onwudili and Williams [63] performed gasification of glucose, xylan, cellulose and sawdust in supercritical water using a Ru/α-Al_2O_3 catalyst, given in Tab. 1.1. Implementation of Ru/α-Al_2O_3 increased the yield of gaseous products drastically, compared to the non-catalytic gasification. NaOH and CaO addition was proved beneficial by increasing the CH_4 and H_2 yields while decreasing the yield of produced CO_2, since they act as carbon capture agents, producing sodium carbonate and calcium carbonate respectively. The Ru/α-Al_2O_3 resulted in a CGE of 96% for glucose SCWG. Zhang et al. [12] used a RuNi/γ-Al_2O_3 for the SCWG of glucose as well, reported in Tab. 1.1. The addition of this catalyst reduced tar yield effectively. The Ni-Ru/Al_2O_3 bimetallic catalyst was also considered very effective in the SCWG of phenol and especially in catalysing the reforming of phenol to H_2, the CO methanation and the WGS reaction [88].

Promoting a Ru/γ-Al_2O_3 catalyst with Zn, for biomass SCWG can increase the total gas yield as well as the H_2 and CO yields. Barati et al. [64] investigated the SCWG gasification of bagasse. The carbon gasification yield and hydrogen production increased significantly with the use of a Ru-Zn/γ-Al_2O_3 catalyst (Tab. 1.1). The promotion with Zn also affected the total gas yield. More specifically, increasing the Zn concentration, increased the total gas yield and the H_2 yield, while it decreased the CH_4 yield. They attributed this trend to the blocking effect of Zn on the adsorption of H_2 and CO on the catalyst surface, leading therefore to inhibition of the methanation reaction.

Raney-nickel catalysts have been proved effective in the heterogeneous SCWG process since decades now [54,65,89] but they continue to attract research interest. Three different Raney-nickel catalysts were employed by Jin et al. [90] for the SCWG of grounded peanut shell particles at 400 °C, 220 – 240 bar and for 20 min of reaction time. It was found that they enhance the CGE, two or even three times the value it had without catalyst. The highest CGE was obtained with the Raney-nickel catalyst which contained ~90 wt.% Ni and was promoted with 1 wt.% Mo. While the one promoted with such a low Mo loading provided the highest CGE, the one that resulted in the highest H_2 yield was the one promoted with 15 wt.% Fe. Chen et al. [66] tested also Raney-nickel catalysts promoted with Mo (0.34 and 0.31 wt.%) and Fe (7.86 wt.%) for the SCWG of sewage sludge and their results are reported in Tab. 1.1. They found that both the highest CGE and the highest H_2 selectivity was achieved with the Raney-nickel catalysts with 0.31 wt.% Mo. This catalyst exhibited higher catalytic activity because of its larger specific surface area and larger pore volume. Their experiments were conducted under low temperature (350 – 450 °C), hence the methanation and the WGS could be promoted, especially when the catalyst loading was increased from 0.2 to 1.4 $g_{catalyst}\, g_{sludge}^{-1}$. They reported that the increase in catalyst loading increased the CGE and the total gas yield but it decreased slightly the H_2 selectivity.

Sheikhdavoodi et al. [13] studied the SCWG of sugarcane bagasse on a Raney-nickel catalyst and they came up with approximately similar CO_2 and CH_4 yields that were very high in comparison with the H_2 yield, given in Tab. 1.1. They argued that Raney-nickel facilitates the C-C bond cleavage and that it is a very efficient catalyst in CO hydrogenation/methanation. Its CGE however, was only 53.1% and this was attributed to the increased amount of sulphur in bagasse. Their results regarding hydrogen production, were comparable with the ones by Azadi et al. [56] who showed that the H_2 selectivity from the SCWG of different biomass resources on a Raney-nickel catalyst was lower from the corresponding values on a Ni/Al_2O_3 or a Ni/hydrotalcite. In their study however, Raney-nickel demonstrated the highest CGE.

Tiong et al. [65] examined the SCWG of two different microalgae species on a $Ni/\alpha\text{-}Al_2O_3$ and a Raney-nickel catalyst in a batch reactor at 385 °C, 260 bar for short and long reaction times, i.e., 15 min and 90 min respectively. Regardless of the feed, the Raney-

nickel catalyst showed higher CGE and higher H_2 and CH_4 yields than the Ni/α-Al_2O_3. The Raney-nickel catalyst contained traces of Na, which possibly enhances hydrogen production. The substantial difference in the activity of the two catalysts could be ascribed to the different surface areas, with the Raney-nickel having a larger surface area than the Ni/α-Al_2O_3.

Alumina can be considered as the most common support for metal oxide catalysts, in the forms of α-Al_2O_3 and γ-Al_2O_3. Many researchers prefer α-Al_2O_3 due to its overall better performance under supercritical water. Both Ni and Ru are commonly used as active metals on Al_2O_3. The effect of the active metal promoters on the catalytic performance has been widely studied on this support with the more efficient ones being Ru, Mo and Co. Promoters of the Al_2O_3 support are also investigated. According to the literature data coprecipitation and the SCWS methods are considered the most effective.

1.3.2 Catalysts based on CeO_2

Ceria, well known for its redox behaviour, has also been used as support in SCWG. Lu et al. [68] conducted SCWG of glucose utilizing Ni catalysts with different supports in order to compare their performances, reported in Tab. 1.1. Based on hydrogen yield, they ended up in the following descending order: CeO_2-Al_2O_3 > La_2O_3-Al_2O_3 > MgO-Al_2O_3 > Al_2O_3 > ZrO_2-Al_2O_3. The descending order, based on H_2 selectivity was: CeO_2-Al_2O_3 > La_2O_3-Al_2O_3 > ZrO_2-Al_2O_3 > Al_2O_3 > MgO-Al_2O_3. Regarding the carbon formation, they observed that graphitic coke was formed on Ni catalysts supported on mixed La-Al, Zr-Al and Mg-Al oxides, amorphous carbon on the other hand, was formed on alumina. No significant carbon formation was observed on Ni supported on mixed Ce-Al. They argued that the redox properties of ceria and its high oxygen storage capacity and mobility played a significant role in the prevention of carbon formation.

Lu et al. [69] also demonstrated the superiority of a Ni/CeO_2-γ-Al_2O_3 over a Ni/γ-Al_2O_3 catalyst for the gasification of glucose under supercritical water conditions. The results are given in Tab. 1.1. The performance superiority was based on the higher H_2 yield and selectivity and the better resistance to coke deposition. However, the surfaces of the used catalysts were covered with carbon and agglomeration of the Ni particles was also apparent. Nevertheless, the carbon formed on Ni/γ-Al_2O_3 was of graphitic structure,

whereas on the Ni/CeO_2-γ-Al_2O_3, was of filamentous type. In another study, addition of CeO_2 on Al_2O_3 support was found to suppress the formation of carbon filaments on a Ni catalyst [70]. In addition, the effect of Ce loading on the H_2 yield and on its selectivity [71] was explored, with the maximum H_2 yield attained for CeO_2 loading of 8.46 wt.% out of a range 1.22 to 10.83 wt.%.

In another study [72], which dealt with SCWG of the downstream water from microalgae hydrothermal liquefaction, a Ru(1wt.%)/CeO_2 catalyst was used and its H_2 and CH_4 yields were the highest among all the other Ru-based catalysts. However, it did not have the highest CGE.

In most of the studies, Ceria was used as a support in mixture with Al_2O_3 for Ni-based catalysts. It is therefore considered that the ability of ceria to prevent carbon formation was combined with the ability of alumina to provide supports of high surface area and high mechanical and thermal stability as well.

1.3.3 Catalysts based on MgO

Ding et al. [70] reported that, as shown in Tab. 1.1, a Ni/MgO catalyst, increases the H_2 yield of glucose SCWG by 62%, compared to the non-catalytic process and other Ni-based catalysts, a Ni/Al_2O_3 and a Ni/CeO_2/Al_2O_3. Yin et al. [91] reported similar results for maximum H_2 yield with a Ni/MgO catalyst, among other heterogeneous catalysts. Apart from H_2 yield, the CGE was also the highest for the Ni/MgO. However, similar CH_4 composition among all the tested Ni-based catalysts was reported indicating that Ni/MgO catalysts promote effectively the WGS reaction.

Mastuli et al. [73] synthesized Ni-Mg solid solutions as catalysts for SCWG of oil palm leaves. They reported an increase in H_2 and CO_2 concentration in the product gas with increasing Ni content. This behavior was related to the WGS reaction that was promoted by the Ni catalyst and to the un-promoted methanation reaction. $Mg_{0.8}Ni_{0.2}O$ exhibited the highest number of basic sites that react with H_2O, producing H_2 and the results from its activity are given in Tab. 1.1. It also had the largest surface area and the smallest crystallite size. They tested later the doped $Mg_{0.95}Ni_{0.05}O$ catalyst with a Ni-based one supported on MgO (Ni/MgO) [92]. They found that the supported Ni/MgO catalyst generated lower H_2 and higher CO composition than the MgO with a dopant of 5 wt.% Ni. They ascribed this to the higher

dispersion of the active metal and the specific surface area of the doped catalyst than that of the supported catalyst.

Liu et al. [80] demonstrated that the promotion of ZrO_2 with MgO increases H_2 yield in SCWG of glycerol (Tab. 1.1). They argued that the promotion with MgO leads to the formation of alkaline centres on the catalyst surface, which adsorb acidic intermediates. The alkaline centres of the MgO support act mainly as catalytic sites for the decomposition and generation of intermediate reactive compounds forming light gas products [93]. A drawback of this is that they can form char-like carbonaceous species and also form $Mg(OH)_2$, which has lower catalytic activity [94].

1.3.4 Catalysts based on ZrO_2

Okolie et al. [60] prepared a Ni/ZrO_2 with superior H_2 yield against all other catalysts, that were Ni-based as well, but on different supports: Al_2O_3, Al_2O_3-SiO_2, activated carbon, SiO_2 and carbon nano-tubes. The main reasons for this were ascribed to the high Ni dispersion on ZrO_2 support, strong metal-support interaction, minimised coke formation and the ability of the catalyst to participate in reactions between intermediate products and reactants.

In a study where SCWG of a model polyethylene glycol wastewater was carried out [78], different active metals all supported on ZrO_2: Ni(15wt.%)/ZrO_2, Co(15wt.%)/ZrO_2, W(15wt.%)/ZrO_2, Ni(15wt.%)-Co(5wt.%)/ZrO_2 and Ni(15wt.%)-W(5wt.%)/ZrO_2, were tested for their performance in terms of gas product yields, gasification and H_2 efficiencies. The study revealed the crucial role of ZrO_2, inhibiting the methanation and providing 2.7 times higher H_2 yield than the non-catalytic case. Among the various metals used, the activity of Ni was higher than that of Co and W (Tab. 1.1). Zhu et al. [79] and Liu et al. [80] attributed this to the ability of this catalyst to promote the WGS reaction.

Zhu et al. [79] tested different compositions of Ni/ZrO_2 for the SCWG of glycerol. The catalyst with the highest activity in their study, was the Ni/ZrO_2 with a molar ratio of Ni^{2+}/Zr^{4+} = 0.4:0.6. This catalyst, compared to the SCWG without a heterogeneous catalyst, reached approximately double H_2 and CO_2 yields and the smallest CO yield. Liu et al. [80] tested also Ni/ZrO_2 catalysts with varying Ni loading from 5 wt.% up to 20 wt.% for glycerol SCWG.

From their results, it could be concluded that the highest H_2 yield was attained with the highest Ni loading catalyst. Similarly with the above researchers, Li et al. [81] prepared a Ni(15wt.%)/ZrO_2 catalyst, which performed stably in the SCWG of glycerol under 80 h time-on-stream (TOS). The presence of the catalyst was beneficial as a 3-fold, 5-fold and a 150-fold increase in H_2, CO_2 and CH_4 yields respectively were observed, compared with the same non-catalytic experiments. The CGE of the catalyst was approximately 97%. It was reported that the phase and pore structure of Ni/ZrO_2 were altered during exposure under the SCWG conditions for this long TOS, a process called catalyst in-situ activation.

Another factor found to strongly affect the structure of the Ni/ZrO_2 catalyst and therefore its activity is the calcination temperature [95]. Kou et al. [95] performed SCWG of a diesel solution in an autoclave at 500 °C, 235 - 245 bar and for 30 min reaction time. They used Ni/ZrO_2 catalysts with different calcination temperatures and found that low calcination temperatures in range 500 °C – 600 °C led to Ni crystallites with sizes similar to that of the support pores, which were around 20 nm. Thus, the Ni particles blocked the pores of the support, totally prohibiting the diffusion of the reactants. High calcination temperatures (800 °C), on the other hand, led to microporous or nonporous structures upon which the Ni particles formed agglomerates. Medium calcination temperatures of 650 °C up to 750 °C provided catalysts with wide pore distributions. The highest carbon gasification efficiency was achieved in the presence of the catalyst with a calcination temperature of 700 °C. This catalyst had a Ni loading of 17.9 wt.% while the loading of the other catalysts ranged from 17.3 to 17.5 wt.%.

Zirconia is a highly promising support for Ni-based catalysts. It interacts strongly with Ni and thus prevents its sintering and coke formation. It also provides high dispersion to the active metal.

1.3.5 Catalysts based on oxides that contain yttrium (Y)

As previously reported in section 1.3.1, Azadi et al. [59] also tested Ni-based catalysts supported on two yttrium-containing supports, Y_2O_3 and YSZ, short for yttria stabilized zirconia, for the SCWG of glucose. They observed that the Ni/Y_2O_3 catalyst resulted in a moderate CGE and in a high hydrogen gasification efficiency (Tab. 1.1). This catalyst generated H_2 with a yield among the highest found in this study. Ni/YSZ did not perform

as good as Ni/Y_2O_3. In comparison with other catalysts, Ni/Y_2O_3 was the third most active catalyst in terms of H_2 yield and selectivity, after Ni/CNTs and Ni/MgO. Ni/YSZ surpassed Ni/CeO_2, Ni/AC and Ni/ZrO_2. YSZ was found to be the only stable catalyst support after 1 h of exposure at SCW, without any structural alterations.

Another team of researchers employed a $Ni/Zr_{0.8}Y_{0.2}O_{2-\delta}$ catalyst with varying Ni content for the gasification of glucose with supercritical water [82]. The maximum hydrogen yield and selectivity were reported for the $Ni_{0.5}/Zr_{0.8}Y_{0.2}O_{2-\delta}$ and are demonstrated in Tab. 1.1, which was ten times the yield without catalyst. The very low concentration of CO indicated that the catalyst effectively promoted the WGS reaction and the hydrogenation of CO as well. Addition of CeO_2 to the support to enhance the gasification efficiency, did not have any positive effect. Compared with the activity of the $Ni_{0.5}/Zr_{0.8}Y_{0.2}O_{2-\delta}$ catalyst, the $Ni_{0.5}/Zr_{0.4}Ce_{0.4}Y_{0.2}O_{2-\delta}$ decreased the H_2 yield and selectivity, whereas it increased the CH_4 yield. It was therefore argued that CeO_2 addition promoted further the methanation reaction.

Yttrium was also used as promoter of Ni(25wt.%)/activated carbon for the SCWG of valine [96], where it showed high activity in reforming light hydrocarbons such as C_2H_6 and C_3H_8 and in the WGS reaction.

Three different types of Y-containing support for Ni-based catalysts for the SCWG of glucose were found in the literature, the Y_2O_3, the YSZ and the Ce-promoted YSZ. It was found that all catalysts gasify efficiently glucose and promote methanation, but the higher CGE and CH_4 yield were obtained with the Ni-based catalyst supported on YSZ promoted with Ce.

1.3.6 Catalysts based on ZnO

Sinağ et al. [97] used ZnO and SnO_2 as active catalytic components for the gasification of cellulose at different reaction temperatures. The ZnO formed mostly H_2 and CO_2 at low temperatures, i.e., 300 °C and subcritical pressure, i.e., 80 bar, while the SnO_2 generated also considerable amount of CO, indicating that only the ZnO catalyzes effectively the WGS reaction. At higher temperatures, they reported the increase in the content of hydrocarbons, attributed mainly to the catalytic effect of the autoclave wall. The utilization

of ZnO for sulfur removal upstream of catalytic beds in continuous microalgae SCWG processes, kept the catalyst active for 55 h of operation, under 400 °C and 280 - 290 bar [29,98].

Yin et al. [91] tested a Ni/ZnO catalyst in glucose SCWG (Tab. 1.1). It was shown that Ni/ZnO could multiply the H_2 gas yield observed at non-catalytic gasification approximately five times. Its carbon gasification efficiency was the second highest after that of Ni/MgO. However, Ni/ZnO generated the lowest volume percentage of H_2 compared with the other tested catalysts in this study: Ni/MgO, Ni/Al_2O_3 and Ni/TiO_2, while its CO and CO_2 concentrations were the highest.

Sivasangar et al. [83] used ZnO (5 wt.% Zn) as a catalytic dopant into Ni(5wt.%)/CaO, resulting in the highest H_2 yield (Tab. 1.1) among other tested Ni(5wt.%)/CaO catalysts, which were doped with other elements. It was mentioned in this study that the catalyst doped with ZnO consisted of metallic Ni, ZnO and Ni_8Zn_2O supported on CaO. The latter structure was highly effective in the WGS reaction, the steam reforming reactions and the cleavage of C-C bonds, as the researchers stated. They also observed an enhancement of the methanation reaction with longer reaction time.

Integrating ZnO as a dopant of the active metal, mostly nickel, is an approach that has been proven beneficial for the generation of hydrogen from the SCWG of organic compounds. Zinc is known for its promotion of the WGS reaction. However, the utilization of zinc oxide as a support for Ni proved to be less efficient than other oxides in terms of H_2 yield and CGE.

1.3.7 Catalysts supported on TiO_2

In the study of Azadi et al. [59], the Ni-based catalyst supported on TiO_2, demonstrated moderate CGE of 60% and high H_2 yield of ~16 mol kg^{-1}, for the SCWG of glucose (Tab. 1.1). The yields of CO and CH_4 were in the range of 0.3 – 0.6 mol kg^{-1} and 1.8 – 3.5 mol kg^{-1} respectively. The range of CO_2 yields were comparable with that of H_2. At higher concentration of glucose (10 wt.% solution), it was shown elsewhere [84] that the CGE and the H_2 yield of a Ni/TiO_2 were reduced significantly. Kang et al. [67] demonstrated the better activity of a Ni/TiO_2 against other Ni-based catalysts with different supports, e.g., MgO

and ZrO_2. The addition of Ce (Ce/Ni molar ratio of 0.1) slightly enhanced the H_2 yield and decreased the CGE. The improvement in H_2 yield was attributed to the increased Ni dispersion. Another team compared catalysts on TiO_2 support but with different active metals (Ni, Zn, Cu and Co) [85]. They found that the Ni-based catalyst performed better in terms of stability under SCWG conditions for 20 min of reaction time, whereas the Zn-based catalyst had the highest H_2 yield. Li et al. [81] prepared Ni-based catalysts (15 wt.% Ni) supported on TiO_2, ZrO_2 and Ta_2O_5. They evaluated them in a continuous SCWG process of glycerol. It was found that while the Ni/TiO_2 catalyst gasified the glucose very effectively, its activity gradually decreased with TOS. From their analysis of the morphology of the used catalysts, it turned out that the Ni particles in the Ni/TiO_2 had formed aggregates and $NiTiO_3$. They also reported the formation of a superficial layer of deactivating graphite. Tab. 1.1 demonstrates these results.

Chakinala et al. [55] used a Ru(2wt.%)/TiO_2 catalyst in the gasification of microalgae in supercritical water and compared their results with a non-catalytic experiment under similar conditions. The Ru/TiO_2 catalyst reached complete gasification of algae at 700 °C. In the SCWG of downstream water from hydrothermal liquefaction from Shan et al. [72], Ru(1wt.%)/TiO_2 had a higher CGE than all the other Ru-based catalysts supported on other metal oxides: CeO_2, ZrO_2, Al_2O_3, MgO.

Titania is an efficient support for Ni- and Ru-based catalysts which showed high gasification efficiencies and satisfying CH_4 and H_2 yields. The Ru-based catalysts performed better than the Ni-based ones, in terms of CGE and CH_4 yield, even with more complex biomass resources.

From Table 1.1, it can be concluded, that the best performing catalysts in terms of high CGE and high H_2 yield, i.e., low R_{Hb}, were a Ru-Ni(10wt.%)/γ-Al_2O_3 with a Ru/Ni molar ratio of 0.1 and a Ni(20wt.%)/MgO-ZrO_2. These two catalysts were highly efficient in gasifying dilute feedstock of biomass model compounds. They likely promote the reactions of SMR and WGS in the gas phase resulting in high H_2 yield of around 54 mol kg_{feed}^{-1} for the Ru-Ni/γ-Al_2O_3 and 71 mol kg_{feed}^{-1} for the Ni/MgO-ZrO_2 and consequently in low R_{Hb} ratios. The main characteristic of the SCWG operating conditions under which these catalysts were evaluated, were temperatures in the range 700 – 800 °C and pressure 240 – 245 bar. This is indicative of the harsh conditions in terms of temperature

needed during gasification with supercritical water to achieve high H_2 production. It should be stressed though, that the feeds used were model compounds highly diluted in water and not real residual biomass.

On the other hand, catalysts tested under lower temperatures, i.e., 400 – 600 ˚C and medium to high pressures, i.e., 250 - 500 bar, were efficient in attaining CEs over 50% and very high R_{Hb} ratio in the range 60 – 99 %, which means that a high percentage of hydrogen was bound in the light hydrocarbons formed. In these cases, Ru as active metal or the Raney-Ni or the Ni(15wt.%)/ZrO_2 proved to be very active catalysts. More specifically, Ru on α-Al_2O_3 or TiO_2 or CeO_2, with low concentrations in the range 1 – 5 wt.%, achieved CEs in the range 83 – 96 % and R_{Hb} 63 – 77.6 % for dilute feedstock of cellulose and glucose but also for actual feedstock such as the downstream water from a hydrothermal liquefaction HTL process. The same trend was observed for the two other catalysts, Raney-Ni and Ni(15wt.%)/ZrO_2, which were subjected to low temperatures (385 °C and 425 °C) and medium pressures (260 and 252 bar), respectively. In particular, the Raney-Ni yielded a very high R_{Hb} ratio of 95%, with a dilute feed of 5 wt.% Chlorella vulgaris.

Overall, the presence of catalysts in SCWG is highly beneficial for the carbon gasification efficiency under mild conditions and in most of the cases the R_{Hb} ratio achieved is greater than 30%, i.e., a significant amount of the produced hydrogen is bound in the form of H-C bonds in the produced hydrocarbons, mostly in methane. Therefore, a downstream process that will convert the hydrocarbons into H_2 and carbon oxides should be implemented.

1.4 Upgrading of the SCWG product gas for increased H_2 production

In order to maximize pure hydrogen gas in the product from SCWG of waste biomass, a downstream upgrading process is necessary, which will transform the bound hydrogen into molecular H_2. Boukis and Stoll [36] reported that to result with pure hydrogen in the product stream, a reforming step of the produced hydrocarbons is required. Azadi and Farnood [99] mentioned a sequence of two steps including steam reforming and WGS following the catalytic SCWG of organic feed.

Steam methane reforming, commonly known as SMR, is the most common technology used for the production of hydrogen [100]. A methane source, e.g., natural gas or biogas, is utilised and reacts with steam at ratios of steam/CH_4 = 2.5 – 3 under temperature ranging from 700 to 1000 °C and a pressure range 3 – 30 bar [100–102]. The main reaction of this process, which is the reverse reaction of Eq. 1.3, involving as co-reactants methane and steam is highly endothermic [103]. A side reaction, is the WGS reaction (Eq. 1.4). If the feed consists also of hydrocarbons higher than methane, their steam reforming reactions and their decomposition should be also taken into consideration:

$$C_nH_m + H_2O \rightarrow nCO + \left(\frac{m}{2} + n\right) H_2 \tag{1.13}$$

$$C_nH_m \rightarrow nC + \frac{m}{2} H_2 \tag{1.14}$$

The aforementioned side reactions that generate coke, i.e., CO reduction (Eq. 1.6), Boudouard (Eq. 1.7) and the decomposition of methane (Eq. 1.8) also take place during SMR. A conventional SMR process operates in the presence of a nickel catalyst and produces syngas with a H_2/CO ratio of around three.

A simplified process flow diagram of SCWG coupled with SMR is illustrated in Figure 1.2. Biomass is gasified with supercritical water in the first reactor. The product gas must be purified from poisonous compounds like H_2S, HCl and COS, which contaminate the catalysts and inhibit steam reforming. Catalysts and adsorbents for this purpose are metal oxides of ZnO, CuO, Cr_2O_3, Al_2O_3 [104,105]. After the cleaning step, a pre-reformer converts all the hydrocarbons higher than methane to H_2, CO, CO_2 and CH_4 [105]. The methane steam reformer is located downstream of the pre-reformer and converts the reactants into syngas. The syngas is then converted via the WGS reaction to H_2 and CO_2. The last step of the process scheme is the purification of H_2 which is usually carried out in a pressure-swing adsorption unit [106]. These two processes, if combined, provide an alternative technology for syngas and especially for hydrogen production based on renewable resources.

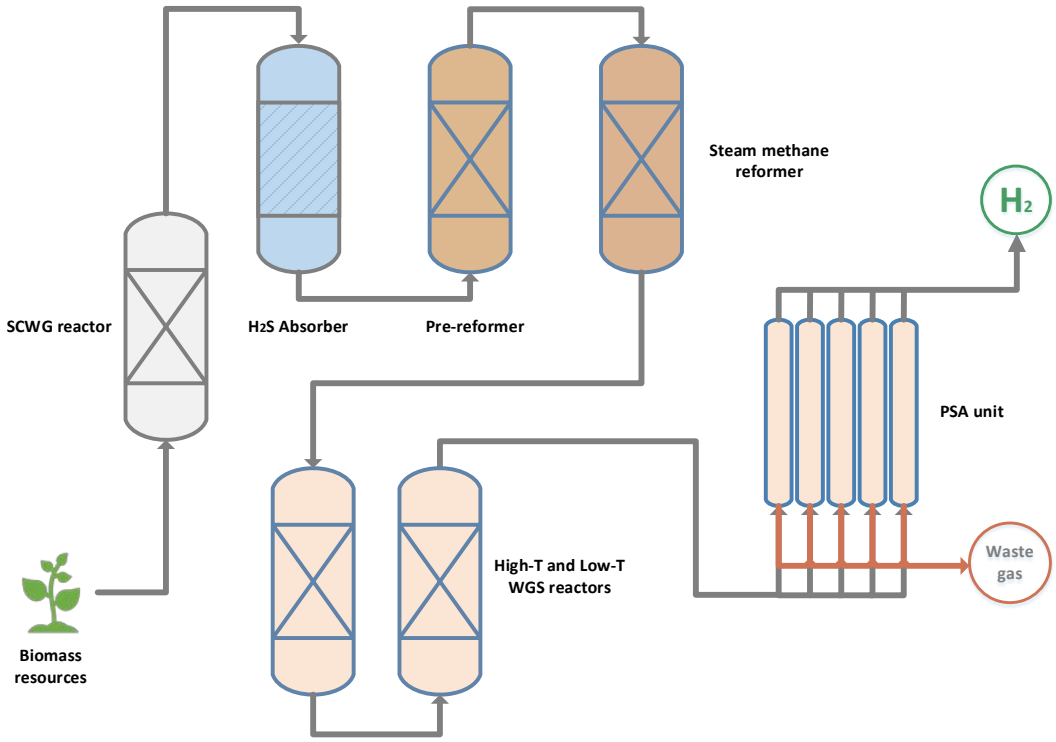

Figure 1.2 Simplified process diagram of supercritical water gasification and sequential reforming of the generated hydrocarbons.

1.5 Description of the conceptualized process and development of the laboratory scale set-up HydRA

This thesis focused on developing and investigating a process for the supercritical water gasification (SCWG) of biomass, followed by the steam reforming of the resulting product gas. To achieve this, a process concept was devised that includes all the necessary reactors and the required heat exchangers to transfer heat from the hot reactor products to the cold inlet streams. Figure 1.3 depicts the conceptualized process. As it will be mentioned later, ethanol (EtOH) was used as a biomass model compound. Initially, an EtOH/water solution, at 20 °C and 1 bar, with an EtOH concentration ranging from 5 wt.% up to 20 wt.% is fed via a pump to the gasification reactor, where SCWG of EtOH occurs at a pressure of 250–280 bar and a temperature of 600 °C. The product from SCWG is then depressurized and directed to a pre-reformer, where the steam reforming of the higher hydrocarbons takes place at pressures ranging from 1 to 40 bar and temperatures between 450 and 700 °C. This reactor utilizes a commercially available Ni-based catalyst. The resulting product gas, now free of higher hydrocarbons and containing only methane

as a hydrocarbon, is transferred to a third reactor, which operates at higher temperatures (700–800 °C) and at the same pressures as the pre-reformer. This third reactor, known as the steam methane reformer (SMR), also contains a Ni-based catalyst. The reformed gas exiting this reactor (S8) is free of hydrocarbons but contains carbon monoxide. It can be cooled down at temperatures in the range 190–250 °C, which are required in the fourth reactor, by transferring heat first to the inlet stream of the SMR reactor (S6) in the heat exchanger HE-03 and subsequently by preheating the feed to the SCWG reactor (S2) in the heat exchanger HE-02. In the fourth reactor, the carbon monoxide reacts with part of the remaining steam via the water-gas shift (WGS) reaction, using a catalyst such as CuO/ZnO [107]. This reaction occurs at significantly lower temperatures than the steam methane reformer but under the same pressure. The WGS product can be cooled down in a third heat exchanger (HE-01) by also providing heat to the inlet stream of EtOH/water solution. The product can only contain H_2 and CO_2 in the gas phase, while the remaining water can be separated from the dry gas after condensation.

This process has been submitted for patent at the German Trademark and Patent Office [108]. At the same time, a laboratory plant was constructed to investigate and validate the patented concept. The lab plant, named *HydRA* (Hydrogen from Reforming of Accessible organic matter), is shown in Figure 1.4.

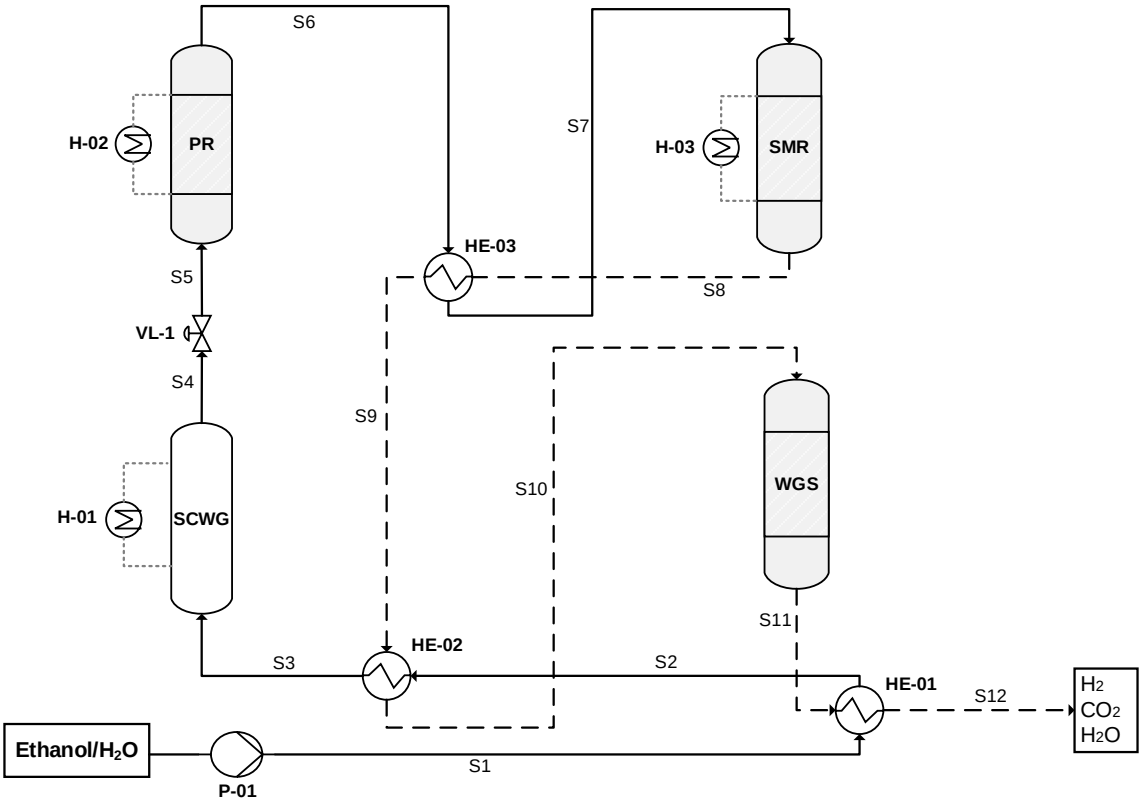

Figure 1.3 Process flow diagram of the conceptualized process. The required heat for the reactors carrying out endothermic processes are depicted with H-01, H-02, and H-03.

Figure 1.4 The HydRA laboratory layout.

1.6 Objectives of the thesis

The key purpose of this thesis was to investigate a newly designed process to improve H_2 yield from the supercritical water gasification of organic compounds. The process involved four reactors: the first for SCWG of simple biomass model compounds, followed by three fixed-bed catalytic reactors in series. Since the continuous operation and connection of these reactors had not been studied before, the approach was simplified. First, the operation of the first two reactors was examined, followed by the operation of the three reactors. This step-by-step method helped to understand how different operating parameters affected each reactor and the overall process. For instance, changing the ethanol concentration in the first reactor's feed significantly altered the gas composition, requiring adjustments in the steam reforming reactors to increase H_2 yield. Special attention was given to how the gasification product gas and the operating conditions in the steam reforming reactors impacted the catalysts' activity, stability, and structure.

After successfully demonstrating the lab setup's operation and its ability to significantly increase H_2 production by reforming all the hydrocarbons produced during gasification, the process was scaled up to an industrial level using the simulation software Aspen Hysys, followed by a techno-economic analysis.

The work was divided in three chapters:

- The first chapter (Chapter 2) focused on studying the operation of the first two reactors: the SCWG reactor and the subsequent pre-reformer. After characterizing the product gas from the SCWG reactor, operating conditions in the pre-reformer were varied to evaluate their impact on hydrocarbon conversion, H_2 yield, and catalyst behavior. A key aim was to identify the conditions under which complete conversion of hydrocarbons larger than methane could occur, aligning with the industrial role of pre-reformers in removing hydrocarbons before the main steam methane reformer. Given the unique feedstock composition, with a high S/C ratio and a mixture of hydrocarbons, hydrogen, and carbon oxides—unreported in literature thus far—the study also aimed to understand its effect on catalyst activity and stability, including potential carbon deposition, sintering, and other changes in catalyst performance.
- The second chapter (Chapter 3 in the main thesis) incorporated the third reactor, i.e., the main steam methane reformer. Unlike the pre-reformer, the SMR was designed with different materials to withstand higher temperatures under elevated pressures.

The focus was on achieving complete methane conversion and examining how operating conditions—temperature, pressure, and gas hourly space velocity (GHSV)—affected it. Another part of this experimental work involved varying the ethanol concentration in the feed to the SCWG reactor to study its impact on the product gas, the reactions, and the overall H_2 yield and hydrocarbon conversion in the final gas. Two different Ni-based catalysts were tested and compared to determine which was better suited for this specific steam reforming system and why.

- The final chapter (Chapter 4) focuses on scaling up the conceptualized process and integrating additional technologies to reduce atmospheric carbon dioxide emissions, such as oxyfuel combustion. An economic analysis was conducted to assess how variations in the concentration of organic matter in the feed and plant capacity impact the cost of produced hydrogen. Identifying an optimal concentration of organics in the feed is essential, as this variable significantly influences the technical feasibility of the process. Similarly, determining feasible plant capacity ranges is crucial for waste biomass-based chemical processes due to the variable availability of different biomass feedstocks. A sensitivity analysis was performed to identify the key cost drivers in hydrogen production. Additionally, the impact of feedstock prices on hydrogen production was examined, alongside a comparison of hydrogen production costs from other technologies, including conventional SMR, SMR with carbon capture, and electrolysis. This analysis aims to identify the conditions under which an industrially upscaled version of the developed process could compete with conventional technologies for renewable hydrogen production.

Chapter 2. Supercritical water gasification and pre-reforming of the product gas

The content of this chapter is sourced from the following publication:

Vadarlis A. A.; Neukum D.; Lemonidou A. A.; Boukis N.; Sauer J. Direct steam reforming of the product gas from ethanol gasification with supercritical water. *Int J Hydrogen Energy*. **2024**, *49*, 992–1008. DOI: 10.1016/j.ijhydene.2023.08.108.

Declaration of contributions:

Athanasios A. Vadarlis conceptualized the work, performed the experiments, processed and analysed the data, evaluated the results, and wrote the manuscript.

Dominik Neukum supported the experimental procedure, the data analysis, evaluated the results, contributed to the discussion, and reviewed the manuscript.

Angeliki Lemonidou conceptualized the work, evaluated the results, contributed to the discussion, and reviewed the manuscript.

Nikolaos Boukis conceptualized the work, supervised the work, contributed to the discussion, and reviewed the manuscript.

Jörg Sauer supervised the work, contributed to the discussion, and reviewed the manuscript.

Summary of Chapter 2

A continuous process for producing hydrogen from the gasification of ethanol with supercritical water (SCWG) is investigated, which involves a fixed bed steam methane reforming (SMR) reactor downstream of the SCWG reactor. Increasing temperature and decreasing space velocity in the SMR reactor resulted in increased hydrogen concentration and methane conversion. The catalyst activity was more affected at low than high pressures, presumably due to the kinetics of the SMR reaction. The significant increase in total hydrogen yield based on ethanol in the feed showed the importance of installing the reformer after gasification. The excessive steam from the SCWG reactor helped to prevent carbon formation, but it might have resulted in the sintering of the active metal. A long-time experiment proved the stability of the catalyst up to 49 h of time on stream (TOS) with a minor decrease in methane conversion from 84% to 78%.

2.1 Introduction

As mentioned in the first chapter, the SCWG of biomass generates a product gas that consists of H_2, CH_4, CO_2, CO and other hydrocarbons (mainly C_2-C_3) [15,72]. Part of hydrogen produced is bound in the hydrocarbons formed. To maximize pure hydrogen gas, a downstream upgrading process is necessary (SMR), which will transform the bound hydrogen into molecular H_2 [109]. Several authors have stated the importance of implementing a secondary reactor for the steam reforming of the hydrocarbons into further hydrogen production [15,99,109].

Most of the studies dealing with the upgrading of the product produced by gasification of biomass focussed on experimentally exploring the subsequent steam reforming of tar produced by biomass gasification [110–115]. However, the gasification in all studies was under atmospheric pressure. Gramms et al. [116] investigated the steam reforming of biomass pyrolysis vapors with a Ni-based zeolite catalyst. Sun et al. [117] used a Ni-based volcanic rock catalyst for steam and dry reforming of a gas mixture produced from gasification of pine nutshell.

There has been considerable work in literature regarding the simulation of processes that combine the SCWG of biomass resources with steam methane reforming. Rahbari et al. [118] carried out a simulation and techno-economic analysis of the integration of a steam reformer into a microalgae SCWG process with heat provided by solar energy. Ruya et al. [119] simulated and studied the exergy loss for the SCWG of empty fruit branch and palm oil mill with an integrated steam methane reformer. Zhang et al. [120] considered a sorption enhanced gasification of biomass utilizing the captured CO_2 for dry methane reforming. Recently, Hantoko et al. [121] designed a process that combined glycerol SCWG and a SMR reactor, which operated at the same pressure with the SCWG reactor (250 bar). From their simulation, they found that the implementation of a steam reformer resulted in increased H_2 yield and syngas production.

The scope of this work is to explore experimentally the potential of the combined process of biomass SCWG and steam reforming of the product gas and optimise the operation with a target to maximise hydrogen yield. This process combines the SCWG of aqueous ethanol solutions (as model compound for biomass) with a subsequent downstream steam reforming fixed bed reactor for the conversion of methane and any traces of heavier

hydrocarbons produced in the SCWG reactor, like a pre-reformer. The gasification product is directly fed to the second reactor, which utilizes all the water left from SCWG to steam reform the dry product gas. This excess steam may differentiate the operation from that of conventional SMR processes. For instance, carbon formation is expected to be minimized, as the excess amount of steam leads to high steam-to-carbon (S/C) ratios compared to the typical range. This, in turn, allows for lower temperatures to achieve complete methane reforming. Thus, the current study incorporated also lower reforming temperatures, as low as 450 °C, which is close to the lowest value of 400 °C found in the literature [100,122–125]. This work aims to investigate how the primary operating parameters, including temperature, pressure, and residence time in the SMR reactor, affect the performance of this reactor, in terms of product composition and specifically methane conversion and hydrogen yield. Furthermore, the heterogeneous catalyst used in the process is characterized to identify any morphological and structural changes that may occur during the reaction.

2.2 Materials and Methods

2.2.1 Experimental setup

The feeding system consists of a vessel containing an ethanol/water solution, a scale and an HPLC pump (Bischoff Model 2250). A capillary tubing connects the pump outlet with the entrance of the SCWG reactor. The reactor (I: SCWG) is made from nickel-based alloy 625. It is 1000 mm long, with an inner diameter of 8 mm. Heat is provided to reactor I through three heating coils in spiral form, located in series at the outer wall of the reactor. The temperature across the reactor is monitored and regulated by six thermocouples. The pressure in this reactor is regulated by a back-pressure regulator (BPR) capable of operating at temperatures as high as 500 °C (Equilibar, ULHT Series Precision, Pressure Control Solutions) and is set at 250 bar. Temperature losses in the small lab-scale layout are very high, thus several heating devices are necessary to avoid cooling of tubes and back-pressure regulator below 380 °C. A heating coil is installed to the bottom of the back-pressure regulator. Another heating coil is used to heat the pipe between the SCWG reactor and the pressure regulator and keep its temperature around 500 °C so that the condensation of water does not occur.

The second reactor (II) is installed on top of the BPR and is connected to the outlet port of it so that the product gas from the first reactor is directly led into the second reactor. This reactor is also made from nickel-based alloy, its length is 800 mm, and its inner diameter is 8 mm. For its heating, three heating coils are used. A thermocouple is placed vertically in the centre of the reactor to measure the temperature of the catalytic bed.

The catalytic bed consists of the catalyst particles (250-500 μm), and it is supported by a metallic net and quartz wool. The catalyst used is the ReforMax 210 LDP, a commercially available one (purchased from C&CS catalysts and chemicals specialties GmbH) based on NiO (18 wt.%) and supported on a $CaK_2Al_{22}O_{34}$ support. The quantity of the catalyst is adjusted according to the desired Gas Hourly Space Velocity (GHSV in h^{-1}) of each experiment. The GHSV is calculated from the following equation:

$$GHSV = \frac{(Q_{reactants})^{ambient\ conditions}\left(\frac{m^3}{h}\right)}{V_{cat.bed}\ (m^3)} \quad (2.1)$$

The volumetric flow of the reactants, $Q_{reactants}$, is the volumetric flow of the SCWG product under ambient conditions. The contribution of the water flow is also considered, assuming that under these conditions water behaves as an ideal gas. The volume of the catalytic bed, $V_{cat.bed}$, is defined as the quotient of the mass of the catalyst, m_{cat}, to its apparent density $d_{cat.}$:

$$V_{cat.bed} = \frac{m_{cat.}}{d_{cat.}} \quad (2.2)$$

The apparent density of the catalyst was measured to be equal to 0.915 g mL^{-1}.

The product stream exiting the second reactor, is driven to a gas sampling bulb, a liquid-gas separator, and a gas meter (type TG0.5/7, provided by Ritter). The liquid condensate is separated from the product gas and is collected in the phase separator, where its weight is also measured by a scale. Figure 2.1 depicts the system described above. An intermediate gas sampling point consisting of three valves (V02, V03, V04) and a gas bulb are installed for measuring the product gas composition from the first reactor.

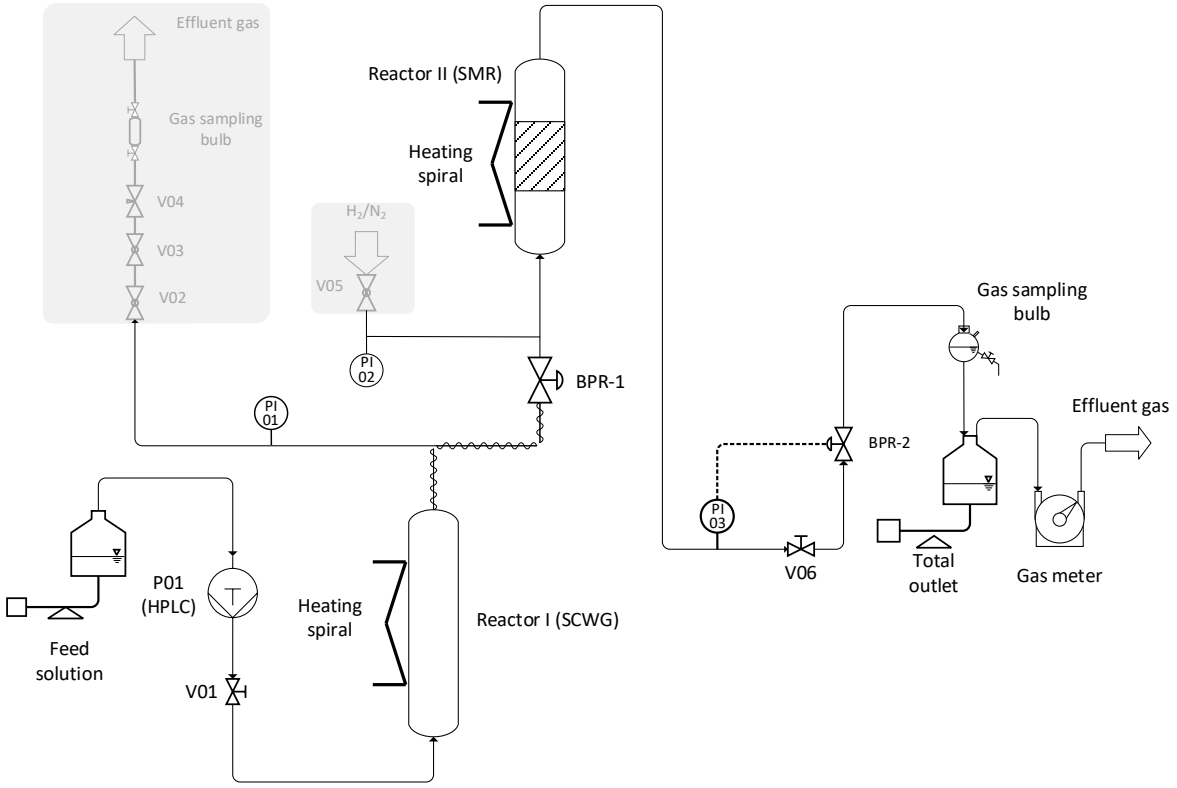

Figure 2.1 Experimental layout. The gray areas identify the parts of the layout which are not part of the main function of the installation but belong to ancillary equipment.

2.2.2 Experimental procedure

Initially, a mixture of H_2(20vol.%)/N_2 gas, which acts as a reducing agent for the active metal phase, is introduced to the catalyst bed for 2 hours with a flow of 50-60 mL/min, at 700 °C and ambient pressure. While the reduction of the catalyst is conducted, the first reactor is heated up at 600 °C (desired value for SCWG). Next, water is added to the system with a flow of 1 mL/min, until the pressure in the first part of the system reaches its desired value of 250 bar. After this step, feed is introduced to the system with a volumetric flow rate of 1.6 mL/min. The ethanol concentration in the feed was 8 wt.%. The operating temperature of the reactor I was set at 600 °C in all experiments. Different temperatures in the catalytic bed reactor II were studied, from 450 °C to 700 °C with an increment of 50. Different pressures in the second reactor were also studied, in the range 1 to 40 bar. This range corresponds to that applied in industry for hydrogen and syngas production [126–128]. The GHSV received the following values: 14852 h^{-1}, 22234 h^{-1}, 29665 h^{-1}, 44557 h^{-1}, 59331 h^{-1} and 74163 h^{-1}.

During each experiment, every half hour, a gas sample was taken for analysis in a Gas Chromatograph (Hewlett-Packard Series II 5890 Plus model) equipped with a thermal conductivity and flame ionisation detectors and a silica capillary column (Carboxen 1010 PLOT 30 m, SUPELCO). Samples from the feed and from the liquid effluent are analysed in a DIMATOC 2100 (DIMATEC), so that the total organic carbon (TOC) content of both can be determined.

Prior to the experiments combining the two reactors, several experiments with only the SCWG system were conducted, to define the input to the pre-reforming reactor. The conditions of those experiments were: p = 250 bar and T = 600 °C. Ethanol with an 8 wt.% concentration was used with a volumetric flow of 1.6 mL min^{-1}. It should be noted here that the first reactor was previously used for the same application but with 50 ppm K^+ by adding $KHCO_3$. Although the reactor has a total length of 1000 mm, the heated part accounts for 650 mm; thus, only this length was considered for the residence time calculation. The value of the latter parameter at experimental conditions (600 °C, 250 bar) was thus steady at 1.51 min. The TOC content of the liquid effluent is determined here as well.

The parameters used for the evaluation of the performance of the SCWG process are the Carbon Gasification Efficiency (CGE):

$$CGE(\%) = \frac{n_{C\ in\ product\ gas}}{n_{C,feed}} \tag{2.3}$$

and the yield of product gases:

$$Y_i\left(\frac{mol}{mol_{ethanol}}\right) = \frac{n_i(mol)}{n_{ethanol\ in\ feed}(mol)}, \qquad i = H_2, CH_4, CO_2, CO\ and\ C_{2+} \tag{2.4}$$

The steam to carbon ratio (S/C) of the SCWG product was calculated with the following equation:

$$\frac{S}{C} = \frac{\dot{n}_{H_2O,outlet}\left(\frac{mol}{h}\right)}{\dot{n}_{CH_4,outlet} + \dot{n}_{CO_2,outlet} + \dot{n}_{CO,outlet} + 2\cdot\dot{n}_{C_2H_6,outlet} + 3\cdot\dot{n}_{C_3H_8,outlet}\left(\frac{mol}{h}\right)} \tag{2.5}$$

The hydrocarbons higher than methane that are expected to be produced are C_2H_6 and C_3H_8. The parameters that are used for studying the performance of the pre-reforming catalyst are the conversion of methane and the yield of hydrogen. The CH_4 conversion is defined as:

$$CH_4\ conversion\ (\%) = \frac{CH_{4,inlet} - CH_{4,outlet}(mol)}{CH_{4,inlet}(mol)} \tag{2.6}$$

The yield of H_2 according to the Global reforming reaction of methane (GRM: $CH_4 + 2H_2O \leftrightarrow CO_2 + 4H_2$) is also used for the evaluation of the performance of the steam reforming reaction:

$$H_2\ yield\ (\%) = \frac{H_{2,outlet} - H_{2,inlet}(mol)}{4\ \cdot CH_{4,inlet}(mol)} \tag{2.7}$$

where, $H_{2,outlet}$ and $H_{2,inlet}$ denote the moles of hydrogen in the product and in the reactant of the second reactor, respectively.

Three equations are used to compare the yield of H_2 from SCWG to the additional respective yield from steam reforming. The first (2.9) is the yield from SCWG, the second (2.10) from steam reforming, and the total yield (2.11) is the third one, which accounts for the total hydrogen produced based on ethanol, according to reaction 2.8 [129]:

$$C_2H_5OH + 3H_2O \leftrightarrow 6H_2 + 2CO_2, \qquad \Delta H^{298K} = 173.5\frac{kJ}{mol} \tag{2.8}$$

$$Y_{H_2,SCWG}(\%) = \frac{\dot{n}_{H_2,SCWG}\left(\frac{mol}{h}\right)}{6 \cdot \dot{n}_{Ethanol}\left(\frac{mol}{h}\right)} \tag{2.9}$$

$$Y_{H_2,SR}(\%) = \frac{\Delta\dot{n}_{H_2}\left(\frac{mol}{h}\right)}{6 \cdot \dot{n}_{Ethanol}\left(\frac{mol}{h}\right)}, \qquad \Delta\dot{n}_{H_2} = \dot{n}_{H_2,total} - \dot{n}_{H_2,SCWG} \tag{2.10}$$

$$Y_{H_2,total}(\%) = \frac{\dot{n}_{H_2,total}\left(\frac{mol}{h}\right)}{6 \cdot \dot{n}_{Ethanol}\left(\frac{mol}{h}\right)} \tag{2.11}$$

where $\dot{n}_{Ethanol}$ is the amount of ethanol in the feed to the system, $\dot{n}_{H_2,SCWG}$ is the amount of H_2 produced from SCWG and $\dot{n}_{H_2,total}$ the total amount of H_2 produced from the whole process, which can be calculated by the flow of gas coming from the reformer.

Before studying the effect of a parameter in the reformer, at least one experiment was carried out, which involved the SCWG of 8 wt.% ethanol. This was done to observe any changes in the SCWG system that affect the CGE, the yield and the composition of the product gases. The mass and carbon balances were also taken into consideration for every experiment, not only for the SCWG experiments, but also for the experiments of SCWG and subsequent steam reforming. The mass balances ranged from 93% to 101%, while the range of the carbon balances was 95 – 107 %.

2.2.3 Characterization of fresh and used catalysts

The Brunauer-Emmett-Teller (BET) surface area and porosity of both fresh and reduced samples of the catalyst were determined by N_2 physisorption at 77 K with an Autosorb-1 (Quantachrome, Florida, UK) flow apparatus, installed in the Chemical Process & Energy Resources Institute (CPERI) of Center of Research and Technology Hellas.

A gas flow system equipped with a quadrupole mass analyzer (OMNIStarTM, PFEIFFER, Germany) was used for the H_2 temperature programmed reduction (TPR). 0.15 g of catalyst were placed in a U-shaped quartz reactor and treated with He gas at 250 °C for 0.5 h, followed by cooling to room temperature. The temperature was raised afterwards from room temperature to 800 °C at a rate of 10 °C/min in a gas mixture containing 10% H_2/He. During the experiment, the following mass-to-charge ratios were recorded: He = 4, H_2 = 2, and H_2O = 18. All measurements were carried out with an automated flow unit located in the Laboratory of Petrochemical Technology, at the Chemical Engineering Department, AUTh. The unit is equipped with Genie Advantech software that controls all functions and has two identical groups of gas inlet lines, each with four lines and an equal number of electronic flow controllers (Brooks Smart).

Powder diffractograms of the catalyst were obtained with a PANalytical X'Pert Pro diffractometer using Cu-K_α radiation and a Ni-filter. The data was recorded in a step size of 0.033 ° with 2θ ranging from 5-120 °. The full width at half maximum of the 111 reflection of nickel (44.5 °) was determined by peak fitting with Origin2019. The FWHM was used to estimate the domain size using the Scherrer equation and LaB_6 as reference.

For thermogravimetric analysis coupled with mass spectrometry (TGA-MS), about 40 mg of the sample were filled into a small crucible. The sample was flushed with 80 mL of Ar containing 10% O_2 for approximately 8 h. Afterwards the sample was heated with 5 °C/min to 1100 °C in the same flow. The gas concentration was monitored with a Netzsch QMS 403 D Aëolos. Background correction with an empty crucible was performed. The data were analyzed with Origin2019. For the measurements a Netzsch STA 449 F3 Jupiter was used.

X-ray absorption spectroscopy (XAS) of the fresh and spent catalyst, as well as Ni-foil reference were conducted at the P65 beamline at PETRA III (Deutsches Elektronen Synchrotron, Hamburg) at Ni K-edge (24.35 keV). They were performed in transmission mode using ionization chambers. The radiation came from an 11 period undulator. The

energy was selected using a Si(111) double-crystal monochromator. A pair of plane Si-mirrors rejected higher harmonics. The beam size was 1.5 x 0.3 mm for all samples. Powder samples were measured as pellets diluted with cellulose. The data analysis was carried out using Athena from the Demeter software package (version 0.9.26).

2.3 Results and Discussion

2.3.1 Determining the product from the SCWG reactor

As mentioned in section 2.2.2, the composition of product from the SCWG reactor was first determined. The average values of the dry product gas composition and the yields of product gases from the SCWG of an 8 wt.% ethanol-water solution are given in table 2.1. This table shows that the most abundant gas is H_2, and the second is CH_4. The content of carbon monoxide was found equal to around 6 vol.%. The hydrocarbons higher than methane account for approximately 1 vol.% of the dry product gas. These hydrocarbons consist mainly of ethane. On average, 16.6 L h^{-1} of dry gas is produced. The aqueous effluent is in the range of 4.5 – 5.0 mol h^{-1}. The carbon found in the aqueous effluent is 90 – 160 ppm. Practically, all the carbon content in the feed is gasified, i.e., the CGE was in the range of 99.6 – 99.9%. From eq. 2.9 the $Y_{H2,SCWG}$ is equal to 27.4%. The S/C ratio of the feed to the second reactor is 11.28 – 13.50. This composition, together with the average S/C ratio (= 12.39) and the average molar flows of the gases and steam are considered as feed to the second reactor.

Table 2.1 Dry gas composition and yields of the product gases from the SCWG of 8 wt.% ethanol at 600 °C and 250 bar.

	Concentration (vol.%)	Yield (mol mol_{EtOH}^{-1})
H_2	43	1.64
CH_4	28	1.06
CO	6	0.23
CO_2	22	0.82
C_{2+}	1	0.04

These data must be interpreted cautiously because, in the initial phase of the experiments, the gasification was conducted by adding 50 ppm K^+, by adding $KHCO_3$. K^+ acts as a homogeneous catalyst in SCWG of organic substances by promoting the WGS reaction [130]. Thus, with the addition of K^+, in the product gas from the SCWG of 8 wt.% ethanol, the CO concentration was around 1.4 vol.%. During these initial experiments the concentration of the C_{2+} hydorcarbons was around 5 vol.%. After around 70 h of operation with K^+, the concentration of C_{2+} hydrocarbons decreased to 0.5 - 1 vol.% and was steady afterwards. After performing experiments without adding $KHCO_3$, the concentration of C_{2+} hydrocarbons was constant at the aforementioned levels. These findings suggest that the surface of the SCWG reactor's inner walls was altered permanently. In a study that aimed to determine the effect of potassium salts in SC water on a Ni-based alloy 625, Habicht et al. [131] found that these salts can corrode the surface of this metal and result in the formation of areas on reactor's surface rich in NiO. During SCWG of ethanol, H_2 can reduce NiO and form metallic Ni, active in steam reforming of C_{2+} hydrocarbons.

2.3.2 Characterization of fresh catalyst

The BET surface area of the fresh and reduced catalyst is given in Table 3.2. The reduced one had higher surface area, pore volume, and diameter than the fresh one. However, the surface area of the reduced catalyst is still considered low due to the low surface area of the support used [132].

Table 2.2 Physicochemical properties of fresh and reduced catalyst.

	BET surface area ($m^2\,g^{-1}$)	Pore Volume ($cm^3\,g^{-1}$)	Pore diameter (nm)
Fresh catalyst	3.8	0.025	9
Reduced catalyst	14.6	0.039	12

The reduction pattern of the fresh catalyst was studied over a temperature range of 50 – 800 °C. The volumetric flow of hydrogen over the catalyst sample as a function of temperature is given in Figure 2.2. The drop in the flow of H_2 is due to its consumption in the reducing reaction of NiO to form Ni^0, as the XRD patterns of the fresh and reduced catalyst depicted (in Fig. 2.3). In the temperature range 400 – 590 °C, the H_2 flow begins to decrease and is minimized around 508 °C. A small consumption is still around 615 °C before the flow returns to pre-consumption levels. These temperatures agree with those from the literature [122,132–135], leading to the conclusion that this catalyst is easily reduced. This fact can be attributed to the weak interaction between the active metal and the support [132,135]. By calculating the theoretical and the experimental consumption of H_2, it is estimated that approximately 98.7% of Ni^{2+} is reduced.

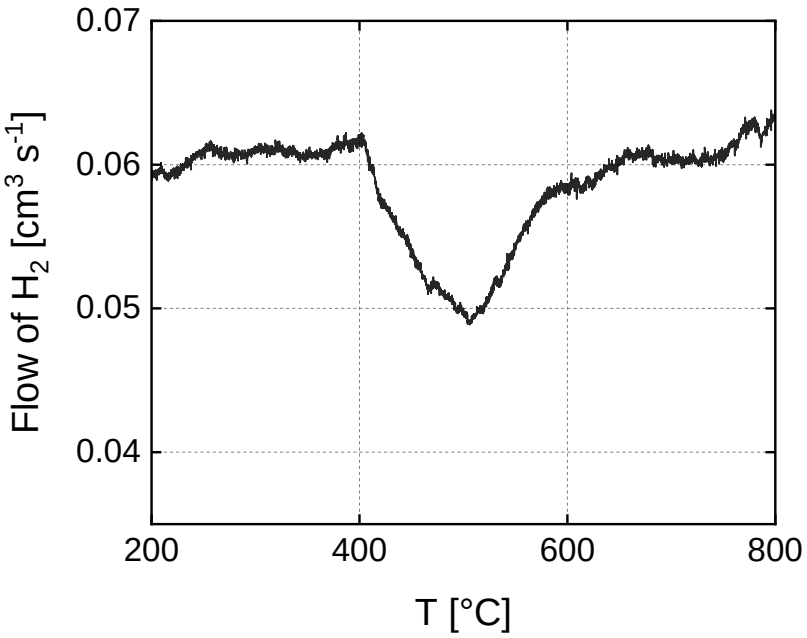

Figure 2.2 H_2 -TPR profile of the fresh catalyst.

The X-Ray diffractograms of the fresh and reduced catalyst are presented in Fig. 2.3. Both samples consisted of $CaAl_4O_7$ and $K_{2.6}Al_{21.82}O_{33.9}$ crystal phases, the former in significantly higher intensity implying that it is the main support component. The similarity in the intensity of the reflections of the support crystal phase between the fresh and the reduced samples ensures that they have not undergone any structural changes due to the reduction of the active metal. Regarding the Ni phases, the fresh sample shows diffraction

peaks of NiO, while the reduced one shows only those corresponding to metallic Ni. This indicates that the reduction conditions were sufficient for converting Ni^{2+} to Ni^{0}. The size of the Ni crystallites in the reduced catalyst was calculated by the Scherrer equation and was found to equal 35.8 nm. This value is later compared with the respective size of the Ni crystallites after the reaction to examine whether Ni sintering had taken place.

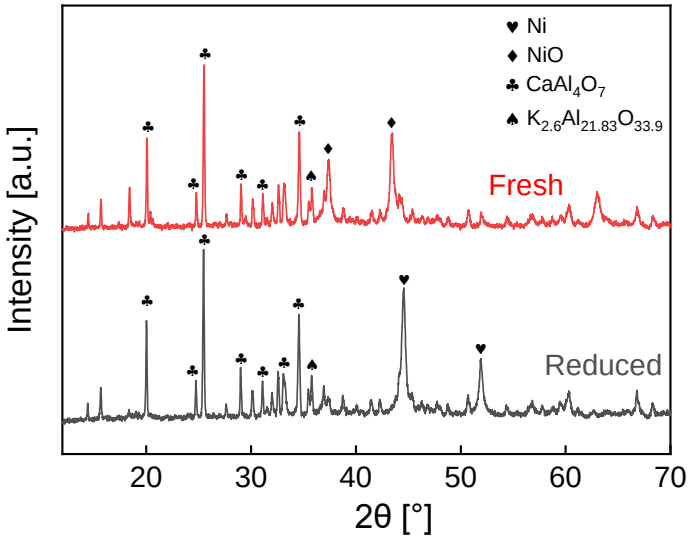

Figure 2.3 XRD graphs of the fresh and reduced catalyst.

2.3.3 Thermodynamic equilibrium

The catalytic performance of the pre-reforming catalyst is compared with the dry gas composition at thermodynamic equilibrium. The latter composition is calculated from the Aspen HYSYS V11, with an RGibbs reactor chosen to minimize the Gibb's free energy of the system [136]. The selected property package was the PRSV, which employs the Peng-Robinson equation. The product gas composition and CH_4 conversion were determined under varying temperatures of 450 – 700 °C and atmospheric pressure (Fig. 2.4.a), as well as under a pressure range of 1 – 41 bar and a constant temperature of 600 °C (Fig. 2.4.b). The product composition from the SCWG of an 8 wt.% ethanol solution, as shown in Table 2.1, was used as feed for the thermodynamic equilibrium calculations.

The effect of temperature on dry gas equilibrium composition is illustrated in Figure 2.4.a. The concentration of hydrogen increased while that of methane decreased due to the

promotion of the SMR reaction [121,124]. Conversely, WGS was promoted at lower temperatures, as shown by the lower carbon monoxide concentration because of its consumption towards CO_2 and H_2. At 700 °C, almost complete CH_4 conversion was calculated, and H_2 reached its highest concentration of 73.5 vol.%. The determined conversion of C_{2+} hydrocarbons was complete across all temperature and pressure ranges.

Pressure as expected has a strong inverse effect on CH_4 conversion due to the promotion of the methanation reaction, which inhibits the formation of CO and H_2 (Figure 2.4). At 20 bar the conversion is less than 60%. As WGS reaction is a reaction with no volume change, it is not affected by pressure. The variation seen mostly in H_2 concentration is due to the steadily increasing CH_4 concentration.

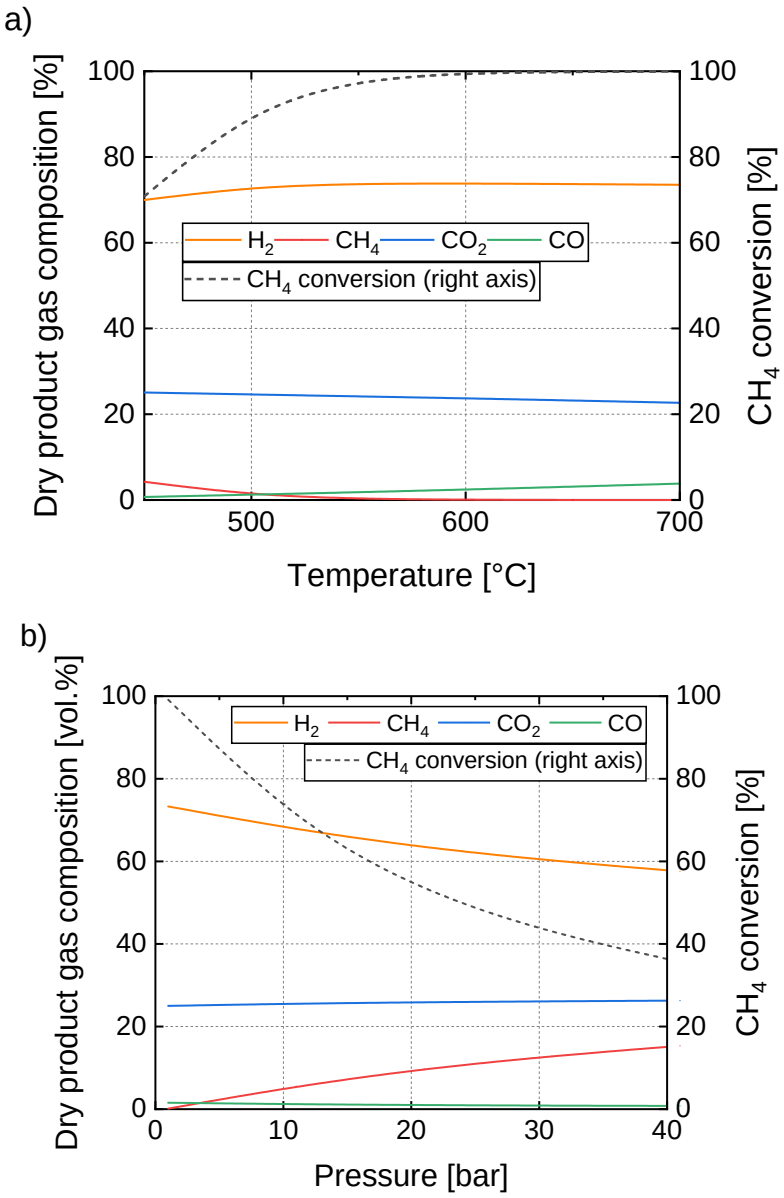

Figure 2.4 a) Effect of temperature and b) of pressure on the equilibrium composition of the dry product gas from steam reforming of the gas generated from the SCWG of 8 wt.% ethanol.

2.3.4 Effect of temperature on the steam reforming product

The experimental study first includes the effect of temperature on the dry product gas composition and the catalyst's performance in terms of CH_4 conversion and H_2 yield. Fig. 2.5 depicts the concentration of the product gases as a function of catalyst-bed temperature and the corresponding composition at thermodynamic equilibrium. It can be seen that H_2 concentration is increasing with temperature, from 57 vol.% at 450 °C to almost 70 vol.% at 700 °C. Respectively, the concentration of CH_4 decreased from 22

vol.% to 7 vol.%. The CO concentration was minimized at 450 °C, where it was 0.05 vol.% but increased up to 3.2 vol.% approximately, at 700 °C. This trend shows the strong effect of temperature on the reactions of SMR and WGS. The WGS reaction is promoted at low temperatures since it is exothermic, whereas higher temperatures forward its reverse reaction [137]. Therefore, with a temperature increase, the content of CO is increased. On the other hand, the endothermic SMR reaction is shifted towards the generation of H_2 and CO when the temperature rises, whereas it is shifted towards CH_4 and H_2O when the temperature decreases. At 450°C, the C_{2+} hydrocarbons made up 0.6% of the dry product gas, while at 700 °C they accounted for only 0.03%. Although they were present in small amounts, there was a noticeable pattern of increasing conversion as the temperature increased, as demonstrated in Figure 2.5.

As shown in Fig. 2.5 a), a significant deviation from the thermodynamic equilibrium exists, especially at lower temperatures. For high temperatures, the actual product gas composition reaches closer to the equilibrium. A significant deviation from the equilibrium is found for CH_4 concentration. Even at 450 °C, the CH_4 decreases drastically under thermodynamic equilibrium, reaching approximately 4.3 vol.%, due to the very high S/C ratio that drives the reactions of SMR and WGS to the side of H_2 formation. However, no significant increase in CH_4 conversion was found experimentally at 450 °C. The reaction rate of the SMR reaction is influenced strongly by the temperature, due to the high activation energy of this reaction. Xu et al. [138] for example, found an activation energy of 240.1 kJ mol^{-1} for a $Ni/MgAl_2O_4$ catalyst, while Obradovic et al. [139] found a slightly higher value (247,3 kJ mol^{-1}) for a structured plate-type $Pt/Ni/Al_2O_3$ catalyst. Abbas et al. [140] calculated the activation energy of a $NiO(18wt.\%)/Al_2O_3$ to be equal to 257 kJ mol^{-1}.

Consequently, the conversion of CH_4 and the yields of H_2 and CO were also expected to have a strong temperature dependence. Fig. 2.5 b) reveals that there has been a gradual increase in the conversion of CH_4 from around 18.5% at 450 °C to 63.3% at 700 °C. A similar trend was found for the H_2 yield, where it was around 18.2% at the lowest temperature, reaching approx. 59% at the highest temperature, respectively. The conversion of higher hydrocarbons increases with temperature as well, from around 32% at 450 °C to 95 % at 700 °C. Both graphs show that at low and moderate temperatures the activity of the catalyst increases slightly with temperature, whereas at temperatures

higher than 600 °C, the total increase in activity is remarkably steeper. Similar results were found by Yang et al. [141], who reported a 3-fold increase in CH_4 conversion from 550 °C to 650 °C, for SMR with an S/C ratio of 3 and CH_4 space velocity of 10^4 h^{-1} over a Ni-Ce/Al catalyst. Other researchers found a gradual noteworthy increase in H_2 yield from 500 °C to 700 °C, higher than the one of this study, probably due to the lower GHSV applied [142] and/or the higher activity of the catalyst used [122].

The yield of hydrogen from the SCWG ($Y_{H2,SCWG}$) was calculated to equal 27.4% and is considered steady during the variation of temperature in the second reactor, since no changes occurred in the first reactor. At the lowest applied reforming temperature, i.e. 450 °C, the $Y_{H2,SR}$ = 18.9%, while the $Y_{H2,total}$ was 46.3%. At the highest temperature, i.e. 700 °C, the total hydrogen yield increased to 76.6% due to the increase in the $Y_{H2,SR}$ to 49.2%. At low temperatures, the $Y_{H2,SR}$ is lower than the $Y_{H2,SCWG}$ but increases significantly with temperature. At temperatures of 600 °C and higher, the $Y_{H2,SR} > Y_{H2,SCWG}$.

a)

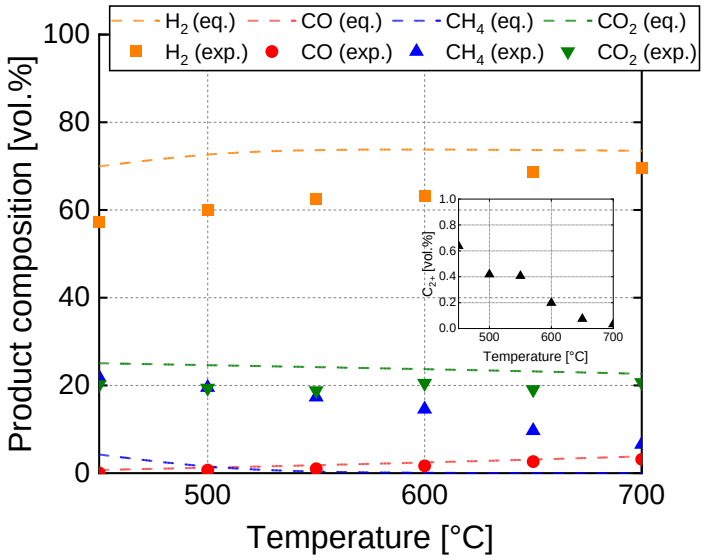

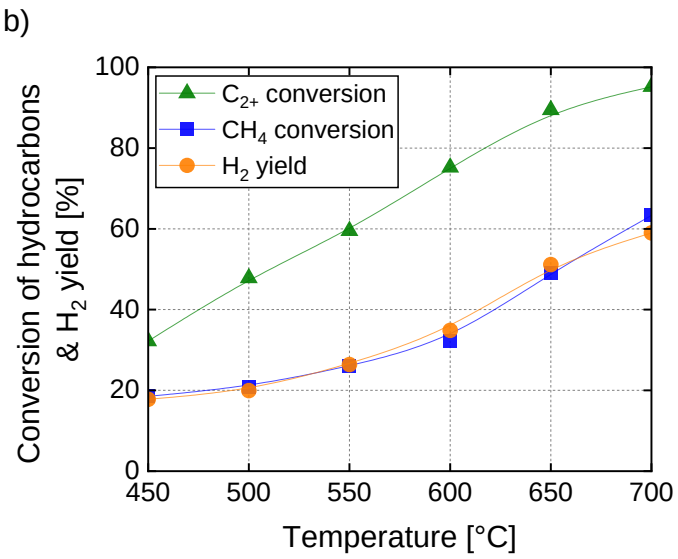

Figure 2.5 a) Dry product gas composition in the steam reforming reactor, compared with thermodynamic equilibrium and b) Conversion of hydrocarbons and hydrogen yield with temperature (p = 1 atm, the feed was the gas from SCWG of 8 wt.% ethanol (see table 2.1), and GHSV = 74163 h^{-1}).

2.3.5 Effect of GHSV

In a previous section, it was observed that a substantial deviation from thermodynamic equilibrium occurred at a GHSV of 74163 h^{-1}, even at high temperatures (T > 600 °C). The actual methane conversion was found to be only 32%, whereas the theoretical value was almost 100%. Consequently, the effect of GHSV needed to be investigated further, and a temperature of 600 °C was selected for this purpose. The feed was the product gas from the SCWG of 8 wt.% ethanol. The values from the Table 2.1 were used to describe the feed to the second reactor, regarding the SCWG product gas composition, the S/C ratio and the molar flows of all components.

The impact of GHSV on the product gas composition is shown in Figure 2.6. The concentration of H_2 reaches almost its equilibrium value at the lowest GHSV, i.e., 73.4 vol.%. Higher GHSVs as expected, cause a deviation from the equilibrium. Additionally, the concentration of CH_4 increases with GHSV, reaching its lowest value of 1.48 vol.% at a GHSV of 14852 h^{-1}. The concentration of CO_2 remains constant and slightly lower than the equilibrium value. However, the concentration of CO was 3.36 vol.% and 4.68 vol.% at GHSVs of 22234 h^{-1} and 14852 h^{-1}, respectively, while the equilibrium CO concentration is around 2.43 vol.%. It is possible that with increase in GHSV, the

reverse WGS reaction is promoted [135,143].The level of C_{2+} hydrocarbons remained steady at approximately 0.2 vol.% when the GHSV was between 44557 – 74163 h^{-1}, but then their concentration dropped below 0.02 vol.%, and at the lowest GHSV, they were not detectable. No signs of catalyst deactivation were observed throughout the studied range of GHSVs. Similarly, the CH_4 conversion shows a dramatic increase at lower GHSVs. Its highest value was approx. 90.4%, at GHSV of 14852 h^{-1}. The respective value of the H_2 yield (Equation 2.7) was 80.5%.

The GHSV is an essential parameter for the performance of this process [123]. At the studied temperature of 600 °C, the CH_4 conversion and H_2 yield were considerably dependent to the GHSV, consistent with the observations of previous researchers [144]. The GHSV is inversely related to the residence time. Higher GHSVs result in lower residence times, i.e., shorter contact times between the reactants and the catalyst, negatively affecting the conversion of CH_4 and the H_2 yield [140]. Apart from that, high GHSVs can result in more rapid activity losses, as Zhai et al. [145] demonstrated. Additionally, there are critical residence time values, above which thermodynamics controls the outcome of the process, whereas lower values lead to control by reaction kinetics [146].

Here, at the lowest GHSV, the hydrogen yield based on reforming of the intermediate stream (Equation 2.10) is $Y_{H2,SR}$ = 70.6% while total H_2 yield based on the ethanol fed to the reactor (Equation 2.11) approaches 98%. Through the entire range of applied space velocities, the $Y_{H2,SR}$ was higher than $Y_{H2,SCWG}$ which was also considered stable at 27.4%.

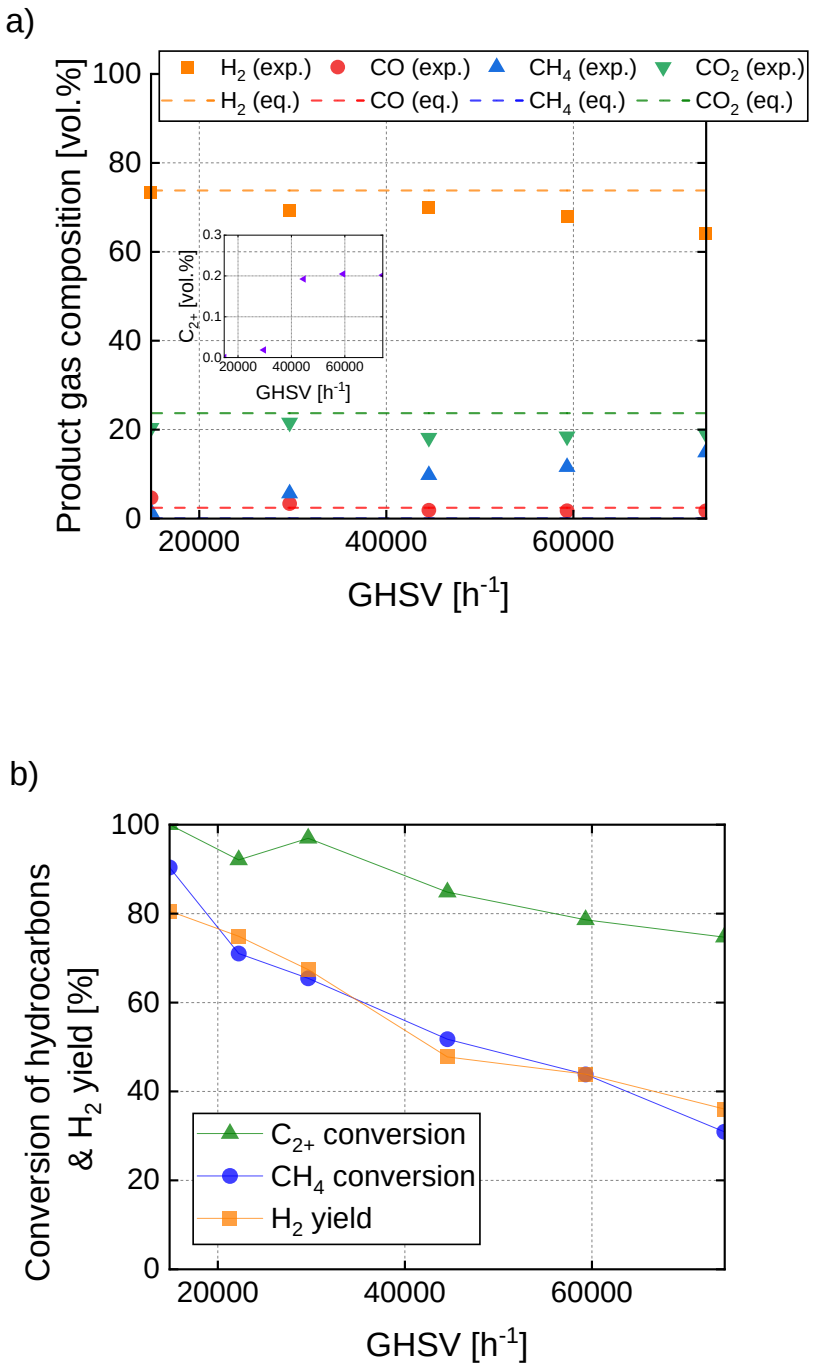

Figure 2.6 a) Product gas composition in the steam reforming reactor and b) Conversion of hydrocarbons and H_2 yield with GHSV (The feed was the product from the SCWG of 8 wt.% EtOH (see table 2.1), p = 1 atm T = 600 °C).

2.3.6 Effect of pressure

The effect of the pressure (1-40 bar) on the dry product gas composition (Fig. 2.7.a), CH_4 conversion and H_2 yield (Fig. 2.7.b) in the downstream steam reforming reactor was also

investigated. It strongly affects CH_4 concentration which rises gradually, from 4.13 vol.% at 1 atm, to 12.3 vol.% at 40 bars and H_2 which is reduced from 70.5 vol.% at atmospheric pressure, to 61 vol.% at 40 bar. Similarly, CO decreases from 4.26 vol.% to 1.7 vol.%. A slight increase in CO_2 concentration, from 21 vol.% at 1 atm, to 24.9 vol.% at 40 bar is also observed. The increase in pressure forwards the reverse SMR reaction, resulting in higher CH_4 concentration and lower CO and H_2 concentrations [144]. Although the CO_2 concentration rose slightly with pressure, the overall effect of pressure on the WGS reaction was small compared to the SMR reaction. The WGS has equal amount of moles on its both sides, and when it reaches equilibrium is not affected by pressure [140,144,147]. In this case, the SMR is inhibited with pressure and so this excess amount of steam reacts further with the CO, driving the slight rise in CO_2 concentration.

As expected, CH_4 conversion was decreased with pressure, showing a sharper drop at lower pressures than at higher ones, i.e., in the range 25 – 40 bar, the CH_4 conversion dropped from 27.2% to 25.6%, respectively. A similar trend is observed for the H_2 yield (Equation 2.7). This behavior might be ascribed to the kinetics of the SMR reaction under the high-pressure conditions [146,148]. There was a discrepancy between H_2 yield and CH_4 conversion, with the first being higher than the second, at every pressure. This discrepancy was constantly minimized with lower pressure. This behaviour indicates the inhibiting effect of pressure to the SMR and not to WGS which is unaffected. Concerning the concentration of C_{2+} hydrocarbons, there was no notable alteration in their level, with an average value of 0.02 vol.%, up to a pressure of 20 bar, and their corresponding conversion rate remained steady at about 92%. Nonetheless, at higher pressures, their conversion rate declined and reached a minimum of roughly 78% with a corresponding concentration of 0.06 vol.%. This behaviour could have derived from the favored reverse reaction of ethane hydrogenolysis [149]:

$$C_2H_6 + H_2 \leftrightarrow 2\,CH_4, \qquad \Delta H^0 = -187\frac{kJ}{mol} \tag{2.12}$$

The significance of pressure for the SMR process has already been studied in the literature. Many have used moderate temperature (600 °C) and a pressure up to 15 bar [140,144,150,151]. Others have applied higher temperatures (900 °C) and a maximum pressure of 20 bar [146].

Mosayebi and Nasabi [144] observed a decrease in CH_4 conversion from 57% at 1 bar to 45% at 15 bar using a $LaNiO_3$ perovskite-type oxide catalyst for SMR at 600 °C, S/C = 1, and GHSV of 900 h^{-1}. In this study, the CH_4 conversion dropped from 70.3% at 1 bar to 45.5% at 15 bar. The higher steam concentration, in this case, likely contributed to the increased CH_4 conversion compared to Mosayebi and Nasabi's equi-molar reaction. Katheria et al. [151] utilized a Ni(15 wt.%)/$MgAl_2O_4$ catalyst for SMR at 600 °C with an S/C ratio of 5, reporting CH_4 conversion of approximately 50% at 1 bar, decreasing to about 40% at 10 bar. Jaiswar et al. [150] studied SMR at 600 °C, S/C = 5, atmospheric pressure, and 10 bar, using a Ni(15 wt.%)/$MgAl_2O_4$ catalyst promoted with Pt. They achieved the highest CH_4 conversion of around 65% at 1 bar with 1 wt.% Pt doping, which decreased to approximately 50% at 10 bar. Both studies used a catalyst mass/inlet molar flow of methane ratio of 0.34 $g_{cat}\,h\,mol^{-1}$, while ours was 14.38 $g_{cat}\,h\,mol^{-1}$. The results of this work align more closely with Jaiswar et al.[150], likely due to the excess steam and Pt promotion. Zhang et al.[146] investigated pressure effects (5 – 20 bar) in a microchannel reactor at 900 °C. At high GHSV (160000 – 240000 h^{-1}), increasing pressure led to higher CH_4 conversion due to increased contact time between reactants and catalyst. For low GHSVs (40000 – 80000 h^{-1}) and low pressures (5 - 10 bar), the higher contact time approached thermodynamic equilibrium, causing a decrease in CH_4 conversion with pressure, following Le Chatelier's principle. However, at the highest GHSV, increasing pressure from 15 to 20 bar did not provide a sufficient contact time increase to reach equilibrium, resulting in decreased CH_4 conversion.

Direct comparison between our study and the literature references is challenging due to different catalyst properties, loading of active metal, and experimental conditions. Nevertheless, all aforementioned studies, and this one, indicate a significant effect of pressure on CH_4 conversion.

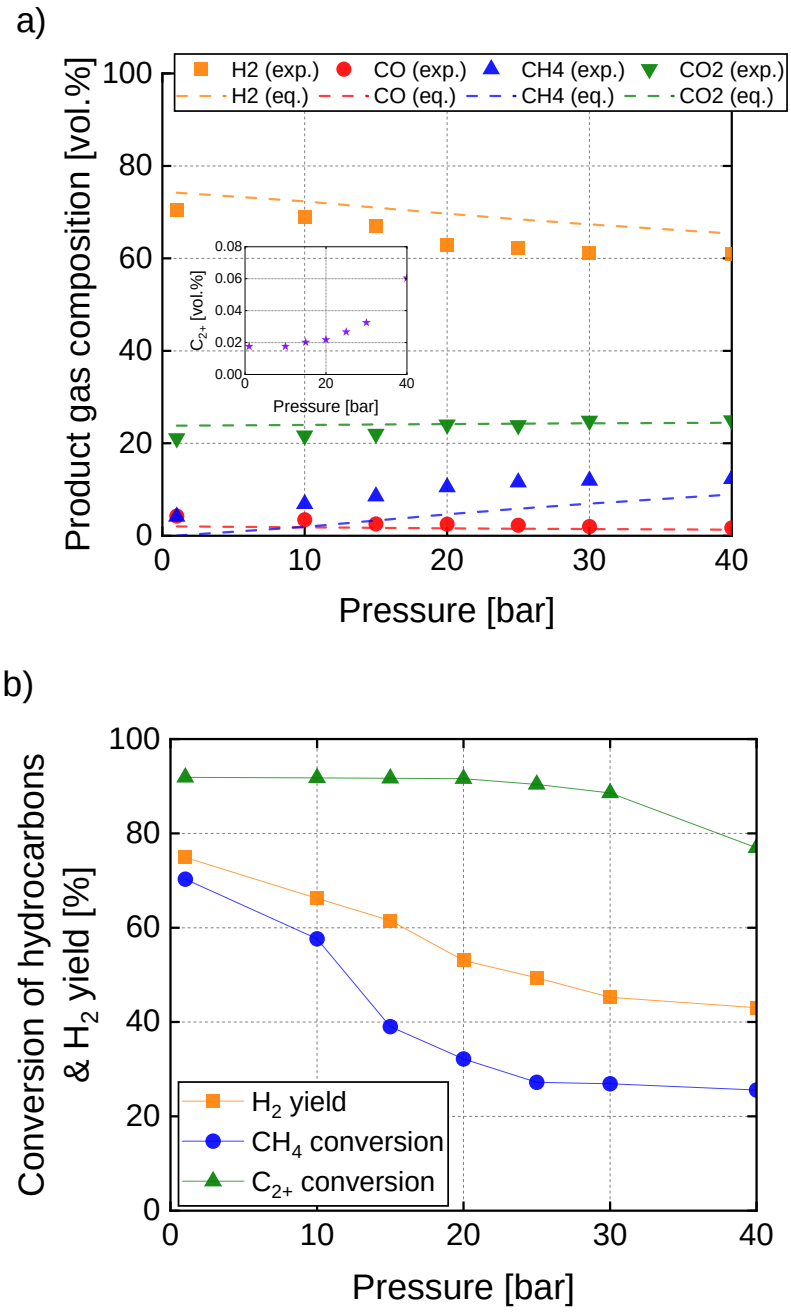

Figure 2.7 a) Product gas composition in the steam reforming reactor and b) Conversion of hydrocarbons and H_2 yield with pressure (GHSV = 22234 h^{-1}, the feed was the gas produced from SCWG of 8 wt.% ethanol (see table 2.1), and T = 600 °C).

2.3.7 Characterization of used catalysts

The TGA-MS measurements of the fresh and used catalyst were conducted to examine if any carbon was formed on the catalyst surface. The weight loss of the samples was measured as a function of temperature and is presented in Figure 2.8.a. Figure 2.8.b

shows the gas species detected during the thermal decomposition of the samples. In the temperature range of 100 – 300 °C, both samples exhibited a decrease in weight, which can be attributed to the release of water vapor [152]. The used catalyst demonstrated more significant weight loss than the fresh catalyst, with three distinct peaks corresponding to water. The first two peaks were observed between temperatures of 100 – 200 °C and 200 – 230 °C, respectively, and were related to physisorbed water. The third peak and the most intense peak, observed in the temperature range of 260 – 280 °C, corresponded to water that was either chemisorbed [153,154] or located in inner catalyst layers [155]. No weight gain was observed in the used catalyst due to re-oxidation of Ni atoms, which might be due to partial reoxidation of the catalyst or limited reduction of Ni during reaction [156]. In the temperature range 260 – 300 °C, two small peaks for CO_2 ad CO were found. As Angeli et al. [124] reported those peaks can be attributed to reactive carbon species. At temperatures between 640 – 700 °C, a slight mass loss of around 1.4% was observed in the used catalyst and was identified as CO_2 and CO. Generally, in this temperature range, the carbon oxides can be formed from the oxidation of filamentous carbon [157]. By analyzing the carbon deposits on the surface of the catalyst, it was calculated that 43.7 mg of carbon had been deposited as coke. This accounts for roughly 0.85% of the total carbon in the feed and corresponds to 17.27 mg of carbon per gram of catalyst (or 17.27 $mg_C\ g_{cat}^{-1}$).

The low carbon formation could be attributed, on the one hand, to the composition of the catalyst, which incorporated potassium (K). The addition of K has been proven not only to accelerate the rate of the gasification of carbonaceous species but also to prevent their formation [158–160]. However, the ample supply of steam during the reaction should be the main factor in avoiding carbon formation. At given temperature and pressure, in an SMR system, the decrease in S/C ratio drives the thermodynamic equilibrium towards carbon formation [100]. Generally, when the steam is in excess it can oxidize the deposited carbon, especially the polymeric species, while it can also inhibit the formation of filamentous carbon [161]. When the carbon content increases so should the S/C ratio otherwise the carbon deposition on the catalyst might increase [124,162]. Choi et al. [163] demonstrated that at medium reforming temperatures (450 – 500 °C), an S/C ratio > 3 can convert almost completely the C_{2+} hydrocarbons in an associated gas with a CH_4/C_{2+} ratio of approx. 4.2, on a Ni-Ru/CGO catalyst. Their long-term experiments showed that their catalyst could

operate for 900 h under 450 °C and 8.5 bar. Sperle et al. [162] determined the critical S/C ratio for net carbon formation for different mixtures of hydrocarbons with methane, at 500 °C. This value was increasing as the carbon atoms increased from 0.75 with only CH_4 to around 2.8 for $CH_4/C_3H_8/C_3H_6$. They also studied the effect of H_2 addition to a $CH_4/C_3H_8/C_3H_6$ feed. Increasing the H_2/C ratio from 2.7 to 13.4, lower critical S/C ratios were needed. At a H_2/C of 2.7, the critical S/C ratio at 510 °C and 20 bar was 3.5. In the SCWG-SMR system of this study, the S/C ratio of the feed to the SMR reactor is above 10 and the respective H_2/C is around 2.38, thus minimizing carbon formation. Nevertheless, the extensive increase in steam may lead to partial deactivation due to sintering of the active metal [164]. Therefore, it was crucial to investigate whether the high amount of steam used in the current process led to the aforementioned phenomena.

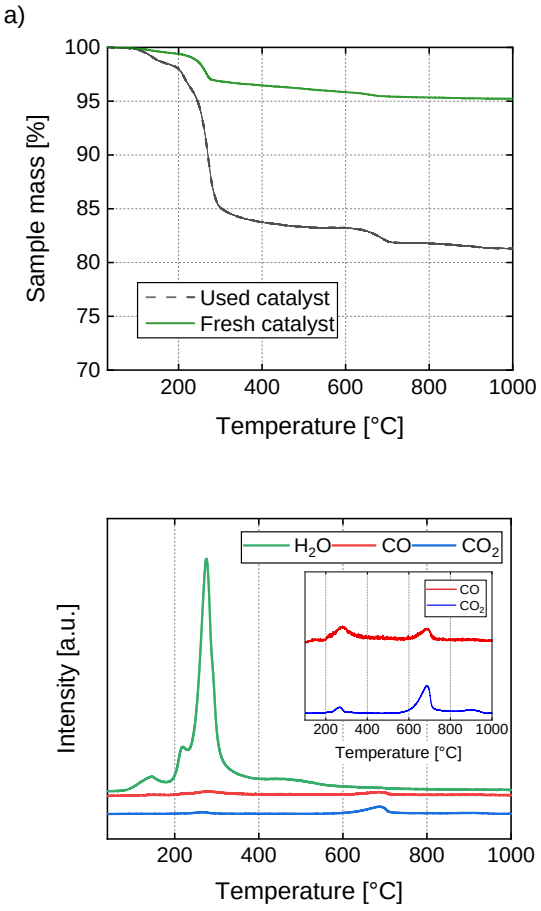

Figure 2.8 a) TGA of the fresh and used catalyst samples for steam reforming of the SCWG product gas and b) respective MS signals (SCWG of 8 wt.% ethanol, T = 600 °C, p = 1 atm, and GHSV = 44557 h^{-1}).

Figure 2.9 illustrates the XRD patterns of the reduced and used catalyst after steam reforming (at 600 °C, 1 atm, and 5 h on stream) of the product gas from SCWG of 8 wt.%

ethanol. The patterns of both the reduced and the used catalyst exhibited the same two peaks at 44.5° and 51.8°, which corresponded to the (111) and (200) planes of metallic Ni, respectively [165,166]. In the used catalyst, the reduced nickel structure was retained without the appearance of nickel oxides. This outcome can be attributed to the presence of H_2 in the feed of the SMR reactor, which reduces any NiO species formed during the reaction [167,168]. The peaks corresponding to the structure of the support that were identified for the fresh and reduced catalysts in Figure 2.3 were not present in the XRD pattern of the used catalyst. Nevertheless, under 5 h of TOS, the catalyst did not show any signs of deactivation.

Furthermore, the XRD peaks of the used catalyst were sharper, suggesting some degree of Ni sintering. Notably, the average size of the Ni crystallites in the used catalyst was estimated to be 53 nm using the Scherrer equation, whereas the size of the reduced catalyst was 35.8 nm. Several factors may lead to sintering, but here an attempt is made to determine only the factors that might have played a role in this case. Temperature is a critical factor in sintering, and increasing the temperature typically results in a higher sintering rate [169–171]. As Christensen et al. [172] reported, the interaction between the active metal and the support also strongly affects the sintering rate of Ni particles via the particle migration mechanism (coalescence). The TPR profile of the catalyst in this study suggests that the metal-support interaction is weak, which may have contributed to the sintering of the metal particles. Another factor that can enhance sintering is steam [164,169,172,173]. In this case, the large amount of steam fed to the SMR reactor may have accelerated the sintering rate of the metal particles. However, during the experiments, no deactivation was observed. According to Sehested [169], Ni sintering is a rapid process and quickly reaches a stable state, thereby suggesting that the sintering had taken place before the first measurement of the product gas sample and the recording of the results.

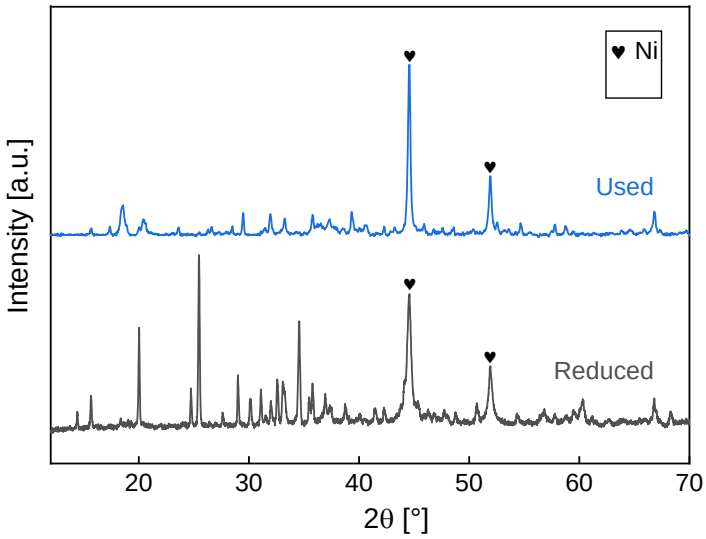

Figure 2.9 XRD graphs of reduced and used catalyst for steam reforming of the SCWG product gas (SCWG of 8 wt.% ethanol, T = 600 °C, p = 1 atm and GHSV = 44557 h^{-1}).

2.3.8 Long-time experiment

Characterization of the used catalyst revealed that the catalyst remained reduced during the reaction, did not suffer from severe carbon deposition but sintering of the active metal was not avoided. These did not have any noticeable effect on the catalyst activity during the short TOS of 5 h, however, a long-time experiment would provide solid evidence of any possible deactivation. Therefore, an experiment of 75 h was conducted at 600 °C and ambient pressure (Figure 2.10). During the first 48 h the composition of the product gas and the CH_4 conversion were stable, accounting for 84.05% of converted CH_4, 71.8 vol.% H_2, 2.1 vol.% CO, 2.4 vol.% CH_4 and 23.7 vol.% CO_2. However, a slight activity loss can be observed after 49 h of operation, which is depicted through a gradual decrease in CH_4 conversion from 49 h to 54 h. Afterwards the CH_4 conversion reached an average value of 77.5% for the rest TOS. Respectively, the concentration of CH_4 increased to 3.4 vol.%, CO decreased to 1.9 vol.% and H_2 decreased to 70.6 vol.%. Similarly, the concentration of heavier hydrocarbons was found to be 0.001 vol.% during the first 49 h, whereas afterwards their concentration increased to 0.009 vol.%.

Based on the observed changes in these values, it appears that the catalyst's activity in the steam methane reforming reaction has slightly deteriorated. Figure 2.11.a depicts the TGA measurement of the catalyst, with only a small increase in weight of 1.55% at 470 °C, possibly due to reoxidation of Ni. This weight increase is related to around 40% of the

reduced Ni before the feed introduction, becoming reoxidized after the reaction. Afterwards, the catalyst loses around 1.55% of its weight again, returning to its initial weight for the rest of the analysis. This rate of weight loss is similar to the rate found in the catalyst subjected to an experiment of 5 h (1.4% after 5 hours of TOS, Figure 2.8). However, the amount of fresh catalyst and the total amount of carbon in the feed were different from the 5-hour experiment. By MS measurements, this weight loss can be attributed mainly to release of CO_2 with a peak at 500 °C and 600 °C. It was found that this amount of carbon accounted for 0.019% of the total carbon inserted into the second reactor throughout the whole long-term experiment. The latter percentage of deposited carbon is very small compared to the one found in the short-term experiment (0.85% of total carbon). Besides, the temperature range of carbon occurrence in the latter case is lower than that in the short-term experiment. These differences are probably due to the different space velocity used in these two experiments, in particular the long duration experiment consisted of a lower space velocity, which may have led to the inhibition of carbon formation [174,175] and/or the variations in the rate of carbon deposition as a function of TOS with the higher rates attained during the first hours of operation.

The XRD profile of the used catalyst (Figure 2.12) indicates the reduced state of Ni after the reaction but also with sharper peaks, compared to the reduced catalyst from Figure 2.8, which accounted for an increase in Ni particle size to 75.5 nm. This increase means that during the reaction, the Ni sintering progressed, leading to a reduction in the surface area of the active metal. Since the formation of carbonaceous species on the catalyst was so small, it is proposed that most likely the increased Ni sintering was responsible for the moderate loss of catalyst activity.

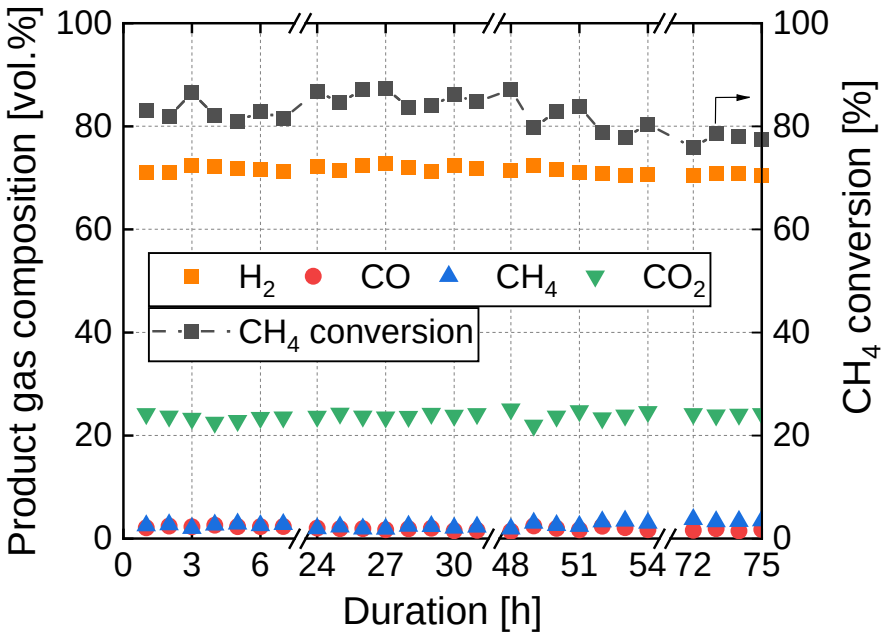

Figure 2.10 Steam reforming of the gas produced from SCWG of 8 wt.% ethanol (SR conditions: T = 600 °C, p = 1 atm, GHSV = 25000 h^{-1}).

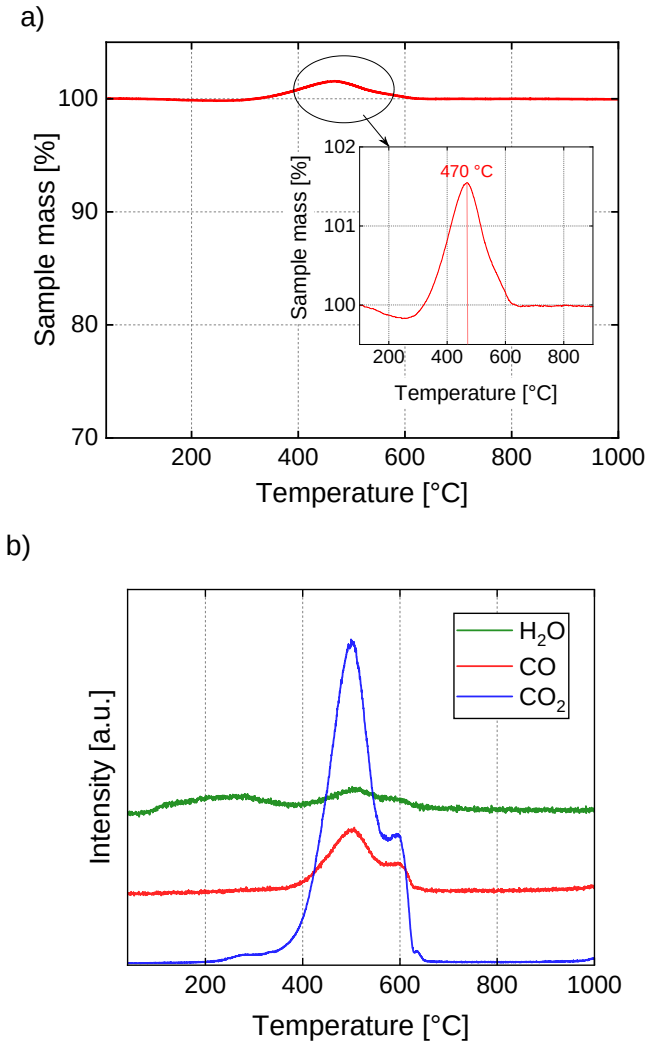

Figure 2.11 a) TGA of the catalyst used in the long-term experiment and b) respective MS signals.

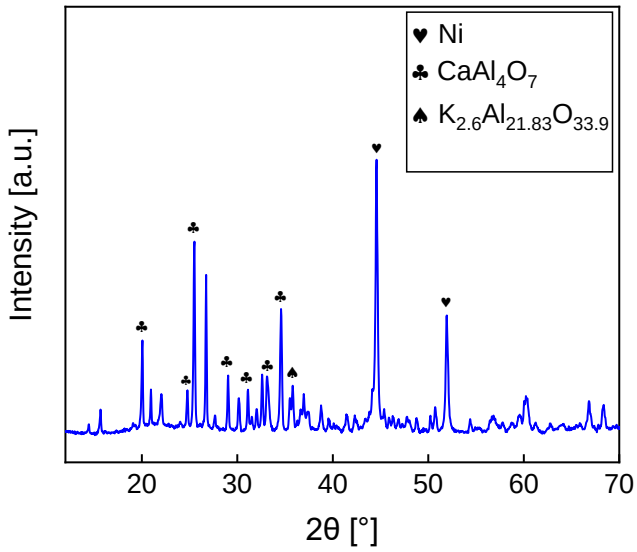

Figure 2.12 XRD profile of the catalyst used in the long-term experiment.

2.4 Conclusions

This study proposes the use of a fixed catalytic bed reactor downstream of the SCWG reactor to carry out steam reforming of the product gas. Ethanol was used in the SCWG reactor, and gasification occurred at 600 °C and 250 bar. A commercial Ni-based catalyst was employed in the SMR reactor. The primary objective was the parametric study of the steam reforming reactor to enhance the conversion of methane and carbon monoxide into hydrogen and carbon dioxide while minimizing heavier hydrocarbons traces.

It was found that an increase in temperature brought the product gas closer to thermodynamic equilibrium, with the H_2 concentration reaching approximately 70 vol.% and the CH_4 conversion reaching 63.3% at the highest applied temperature of 700 °C. The gas hourly space velocity played a crucial role in the process, with the H_2 concentration in the dry product gas reaching 73.4 vol.% and the CH_4 conversion 90.4% at the lowest GHSV of 14852 h^{-1}, when the temperature in the pre-reformer was 600 °C and the pressure atmospheric. At these conditions, the total hydrogen yield based on the ethanol admitted into the system ($Y_{H2,total}$) was approximately 98% with only 27.4% produced in the SCWG reactor and the rest in the steam reformer. The effect of pressure was more profound on CH_4 conversion and H_2 yield at low pressures (1.013 bar – 20 bar) than at high pressures, particularly at pressures ranging from 25 bar to 40 bar, due to the kinetics affecting the SMR reaction, under the studied conditions. The excessive steam

from the SCWG reactor helped to restrain the formation of carbon with only a low amount of coke found on the catalyst, but it resulted in the sintering of the active metal. The latter phenomenon was responsible for a slight activity loss during 75 h of TOS.

The operating conditions studied in the present work reveal the potential of applying this steam reforming reactor as a pre-reforming step. That would mean applying this reactor under mild conditions, e.g., 550 – 600 °C and 20 – 30 bar, in order to convert any unwanted side products from the SCWG, like C_{2+} hydrocarbons and CO, into H_2 and CO_2, prior to using a steam methane reformer that would work under higher temperatures.

Chapter 3. Supercritical water gasification and steam reforming of the product gas

The content of this chapter is sourced from the following publication:

Vadarlis A. A.; Neukum D.; Dutzi J.; Lemonidou A. A.; Boukis N.; Sauer J. Supercritical water gasification and subsequent steam reforming of the product gas under elevated temperature and pressure. *Int J Hydrogen Energy*. **2025**, *111*, 567-580. DOI: 10.1016/j.ijhydene.2025.02.197.

Declaration of contributions:

Athanasios A. Vadarlis conceptualized the work, performed the experiments, processed and analysed the data, evaluated the results, and wrote the manuscript.

Dominik Neukum supported the experimental procedure, the data analysis, evaluated the results, contributed to the discussion, and reviewed the manuscript.

Julian Dutzi supported the experimental procedure, evaluated the results, contributed to the discussion, and reviewed the manuscript.

Angeliki Lemonidou conceptualized the work, evaluated the results, contributed to the discussion, and reviewed the manuscript.

Nikolaos Boukis conceptualized the work, supervised the work, contributed to the discussion, and reviewed the manuscript.

Jörg Sauer supervised the work, contributed to the discussion, and reviewed the manuscript.

Summary of Chapter 3

The developed continuous process, combining supercritical water gasification (SCWG) of ethanol with steam reforming (SR) of the product gas, was further investigated. The study focused on higher temperatures and elevated pressures in the steam reforming reactor, the implementation of an additional catalyst to compare its performance with the previously used one, and the effect of ethanol concentration on the final product gas. An experimental study was conducted that involved the operating parameters in the SR reactor, the ethanol concentration, and a comparison of two commercial catalysts for SR. High SR pressures, i.e., 20 – 40 bar, required a temperature of 750 °C to achieve methane conversion higher than 90% at a constant gas hourly space velocity of 63500 h^{-1}. The increase in EtOH concentration significantly decreased the steam/carbon ratio of the SCWG product and increased the content of CH_4, C_{2+} hydrocarbons, and CO. This in turn resulted in a decrease in H_2 yield in the SR reactor from 98.6% to 58.3%, as the EtOH concentration increased from 5 wt.% to 20 wt.% at a temperature of 730 °C, pressure of 30 bar, and a space velocity of 47877 h^{-1}. Under atmospheric pressure, both catalysts showed similar CH_4 conversion. However, at higher pressures (30–40 bar), the catalyst with the higher Ni loading exhibited greater activity in SR.

3.1 Introduction

In the previous chapter a continuous laboratory-scale process for the combined SCWG of ethanol (EtOH) acting as a biomass model compound, with subsequent steam reforming of the resulting hydrocarbons in the presence of a Ni-based catalyst (18 wt.% NiO) supported on a $CaK_2Al_{22}O_{34}$ support [176] was demonstrated. The gasification of 8 wt.% EtOH (in water) was conducted at 600 °C and 250 bar. The SCWG product gas, after decompression to pressures ranging from 1 – 40 bar, together with the remaining steam from the gasification, entered the second reactor, where SR of the produced hydrocarbons was conducted on a commercial Ni-based catalyst. It was found that the integration of the reformer, operating under atmospheric pressure, 600 °C and with a gas hourly space velocity (GHSV) of 14850 h^{-1}, increased the hydrogen yield based on the EtOH in the feed from 27.4% (only with SCWG) to 98%. Additionally, under the studied temperature and pressure range, the higher C_{2+} hydrocarbons were easily reformed, demonstrating that the implementation of a pre-reformer is an effective pre-treatment process for removing C_{2+} hydrocarbons prior to the main steam methane reformer. The excess steam resulted in very high steam/carbon (S/C) ratios, inhibiting carbon formation on the catalyst but accelerating the sintering of the active metal. Other similar experimental studies could not be found in the literature.

The purpose of this work was to further investigate the effect of various parameters on the hydrogen yield and the conversion of hydrocarbons to elemental hydrogen. More specifically, the influence of temperature, pressure and space velocity were investigated by applying a new catalyst to the reformer, a Ni-based one with a support of $CaAl_{12}O_9$ and with a loading of 14 wt.% NiO. The new catalyst was then compared with the catalyst applied in the previous study. Furthermore, a new parameter investigated was the concentration of EtOH in the feed and how this affects the intermediate SCWG gas product and the final one following the tandem steam reforming step. Compared to the previous experimental study (chapter 2), the focus in the present work was on temperature and pressure in the second reactor that are relevant to those applied on an industrial scale for hydrocarbons steam reforming, i.e., temperatures between 700 °C and 800 °C, pressures in the range 20 – 30 bar [177–179]. In these experiments, the pre-reformer functioned solely as a pre-heater without a catalyst, as the steam reforming of

hydrocarbons generated from the SCWG of EtOH was achieved completely, with no catalyst deactivation occurring.

3.2 Materials and Methods

3.2.1 Experimental setup

The feeding system comprises a scale, a vessel with an EtOH/water solution, and an HPLC pump (Bischoff Model 2250). A capillary tubing connects the pump outlet to the SCWG reactor entrance. The SCWG reactor (I) is made of nickel-based alloy 625, measuring 1000 mm in length and 8 mm in inner diameter. Heat is supplied to reactor I through three spiral heating coils on the outer wall. Six thermocouples monitor and regulate the temperature across the reactor's outlet. The heated part of this reactor was 650 mm long. The pressure is controlled by a back-pressure regulator (Equilibar, ULHT Series Precision, Pressure Control Solutions) capable of operating at temperatures up to 500 °C, set at 265 bar. A heating coil maintains the temperature around 500 °C in the pipe between the SCWG reactor and the pressure regulator, preventing phase separation.

The pre-heater (II) is positioned downstream of the back-pressure regulator, connected to its outlet port. This nickel-based alloy 625 rod is 800 mm long with an 8 mm inner diameter. It is equipped with three heating coils.

After the pre-heater, the SCWG product gas is driven to the SMR reactor (Reactor II). The SMR has a length of 880 mm and an 8 mm inner diameter and is a Ni-based alloy 602. A heating coil welded on the outer surface of the reactor keeps the reactor heated at temperatures up to 800 °C. The fixed catalytic bed is located in the center of the reactor. A thermocouple coming from the entrance of the reactor via a t-piece connection measures the temperature of the catalytic bed. The catalytic bed consists of the catalyst particles (250-500 µm) supported by a metallic net and quartz wool. The catalysts used are the commercially available ReforMax 330 LDP and ReforMax 210 LDP (R330 and R210, respectively), purchased from C&CS catalysts and chemicals specialties GmbH. The nominal NiO content of R330 is 14 wt.% and the rest is a $CaAl_{12}O_9$ support, while the R210 has 18 wt.% NiO supported on $CaK_2Al_{22}O_{34}$.

The product stream from the SMR passes through a gas sampling bulb, a liquid-gas separator, and a gas meter (type TG0.5/7, provided by Ritter), after depressurization by a

Tescom back-pressure regulator. The liquid condensate is collected in the phase separator and its weight is measured by a scale. Figure 3.1 depicts the system described above. An intermediate gas sampling point consisting of three valves (V02, V03, V04) and a gas bulb are installed for measuring the product gas composition from the first reactor.

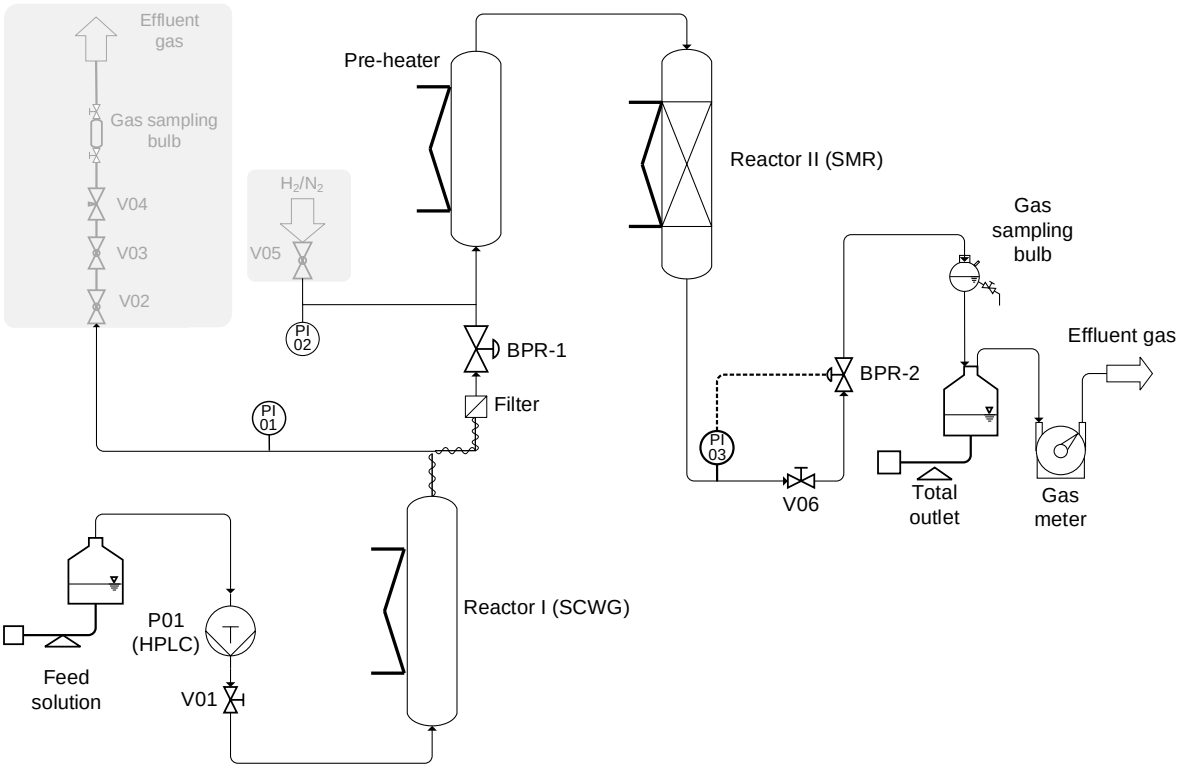

Figure 3.1 Experimental layout. The auxiliary parts of the equipment are highlighted in grey. BPR: Back-pressure regulator.

3.2.2 Experimental procedure

Before the experiments, an H_2(20 vol.%)/N_2 gas was introduced to the catalyst bed for 2 hours with a flow of 50 ml min^{-1} at 700 °C and ambient pressure. While the catalyst reduction was conducted, the first reactor was heated at 600 °C. Next, water was added to the system with a flow of 1 ml min^{-1} until the pressure in the first part of the system reached its desired value of 265 bar. After this step, the liquid feed was introduced to the system with a volumetric flow rate of 1.6 ml min^{-1}. The EtOH concentration in the feed varied between 5 wt.% and 20 wt.%. The temperature and pressure of reactor I were set

at 600 °C and 265 bar in all experiments. The mean residence time in this reactor was 1.5 min (calculated at experimental conditions), with the deviations from this value due to the change in EtOH concentration being very small (standard deviation was 0.025 min). The temperature of the reactor II ranged from 700 °C to 800 °C and its pressure from 1 bar to 40 bar.

Gas samples were taken for analysis every half hour in a Gas Chromatograph (Hewlett-Packard Series II 5890 Plus model) equipped with a thermal conductivity and flame ionisation detectors and a silica capillary column (Carboxen 1010 PLOT 30 m, SUPELCO). Samples from the feed and from the liquid effluent are analysed in a DIMATOC 2100 (DIMATEC), so that the total organic carbon (TOC) content of both can be determined.

For investigating the effect of operating conditions in the SMR reactor (temperature, pressure, and space velocity) and for the comparison between the two reforming catalysts the feed to the system was an EtOH/water solution with 8 wt.% EtOH.The effect of the EtOH concentration on the product gas was explored using, five different concentrations from 5 wt.% to 20 wt.%. For this final set of experiments, in order to be sure that the system would operate with high gasification efficiency even under high EtOH concentration, 100 ppm of potassium in the form of $KHCO_3$ salt was added to each feed solution. The differences in the gasification product, due to the $KHCO_3$ addition, are discussed in section 3.3.2. The mass and carbon balances were calculated in every experiment. The mass balances ranged from 99% to 102%, while the range of the carbon balances was 95 – 105%.

The experimental data are compared with the thermodynamic equilibrium. The equilibrium values were calculated with the Aspen HYSYS V14 software. There, an RGibbs reactor was selected for simulating the SR of the SCWG product gas at various temperatures and pressures. The property package that was chosen for the calculations was the PRSV, which uses the Peng-Robinson equation of state.

Technical problems, such as leaks and clogging, prevented the system from operating with increased pressure in the second reactor at the beginning of the experiment. Usually, the problems were solved during the experiment gradually and by first checking the

operation of the second reactor under atmospheric pressure. The same problems also prevented the continuous overnight operation of the process, with no effective solution so far. For this reason, the time on stream (TOS) for all experiments was 4 h. For the experiments comparing the activity of the two catalysts under different pressures, each catalyst was first subjected to atmospheric pressure for 4 h and then to an elevated value again for 4 h.

The effect of the gas hourly space velocity (GHSV) on hydrocarbon conversion and SR product gas composition was studied by varying the catalyst mass in the SR reactor. The GHSV is the ratio of the volumetric flow rate of the SCWG product at ambient conditions to the volume of the catalyst [176]. For the calculation of the catalyst bed volume, the apparent densities of the catalysts were used. The apparent density of the R210 was equal to 0.915 g ml^{-1} and that of the R330 was 1.01 g ml^{-1}. The parameters used for the evaluation of the performance of the SCWG process are the Carbon Gasification Efficiency (CGE, eq. 3.1) and the yield of product gases (eq. 3.2):

$$CGE(\%) = \frac{n_{C\ in\ product\ gas}(mol)}{n_{C,feed}(mol)} \tag{3.1}$$

and the yield of product gases:

$$Y_i\left(\frac{mol}{mol_{ethanol}}\right) = \frac{n_i(mol)}{n_{ethanol\ in\ feed}(mol)}, \qquad i = H_2, CH_4, CO_2, CO\ and\ C_{2+} \tag{3.2}$$

The S/C ratio of the SCWG product was calculated via equation 3.3:

$$\frac{S}{C} = \frac{\dot{n}_{H_2O_{SCWG}}\left(\frac{mol}{h}\right)}{\dot{n}_{CH_4,SCWG} + \dot{n}_{CO_2,SCWG} + \dot{n}_{CO_{SCWG}} + 2\cdot\dot{n}_{C_2H_6,SCWG} + 3\cdot\dot{n}_{C_3H_8,SCWG}\left(\frac{mol}{h}\right)} \tag{3.3}$$

where, $\dot{n}_{H_2O_{SCWG}}$, $\dot{n}_{CH_4,SCWG}$, $\dot{n}_{CO_2,SCWG}$, $\dot{n}_{CO_{SCWG}}$, $\dot{n}_{C_2H_6,SCWG}$, and $\dot{n}_{C_3H_8,SCWG}$ are the molar flow rates of the products from the SCWG reactor.

In order to study the performance of the SMR catalyst the conversion of CH_4 (eq. 3.4) and higher hydrocarbons (eq. 3.5) were used.

$$CH_4\ conversion\ (\%) = \frac{n_{CH_4,inlet} - n_{CH_4,outlet}}{n_{CH_4,inlet}} \tag{3.4}$$

$$C_{2+}\ conversion\ (\%) = \frac{\dot{n}_{C_{2+,inlet}} - \dot{n}_{C_{2+,outlet}}}{\dot{n}_{C_{2+,inlet}}} \quad (3.5)$$

In addition to those equations, one more was used to assess the H_2 yield (eq. 3.7), according to the stoichiometric reaction of EtOH steam reforming (eq. 3.6):

$$C_2H_5OH + 3H_2O \rightarrow 6H_2 + 2CO_2, \qquad \Delta H^0 = 173.5\frac{kJ}{mol} \quad (3.6)$$

$$Y_{H_2,SR}(\%) = \frac{\dot{n}_{H_2,total}\left(\frac{mol}{h}\right)}{6 \cdot \dot{n}_{Ethanol}\left(\frac{mol}{h}\right)} \quad (3.7)$$

3.2.3 Characterization of fresh and used catalysts

Inductively coupled plasma-optical emission spectrometry (ICP-OES) was used for determining the actual composition of the catalysts. Digestion of the catalysts for ICP-OES was carried out in a mixture of 6 ml conc. H_2O_2, 2 ml conc. HNO_3 and 4 ml conc. HCl. Microwave irradiation of 600 W was applied for 90 min. The solution was diluted to a volume of 25 ml before being measured in an Agilent 725 spectrometer with a plasma excitation of 49 MHz and 2 kW.

The Brunauer-Emmett-Teller (BET) surface area and porosity of both fresh and reduced catalyst samples were determined by N_2 physisorption at 77 K with an Autosorb-1 (Quantachrome) flow apparatus.

Powder diffractograms of the catalyst were acquired with a PANalytical X'Pert Pro diffractometer using Cu-K_a radiation and a Ni-filter. The data was recorded in a step of 0.033° with 2θ ranging from 5-120°. The full width at half maximum of the 111 reflection of nickel (44.5°) was determined by peak fitting with Origin2019. The FWHM was used to estimate the domain size using the Scherrer equation and LaB_6 as reference.

For thermogravimetric analysis coupled with mass spectrometry (TGA-MS), about 40 mg of the sample were loaded into a small crucible. The sample was flushed with 80 ml min^{-1} of Ar containing 10% O_2 for approximately 8 h. Afterwards the sample was heated with 5 °C min^{-1} to 1100 °C in the same flow. The gas concentration was monitored with a

Netzsch QMS 403 D Aëolos. Background correction with an empty crucible was performed. The data were analyzed with Origin2019. For the measurements a Netzsch STA 449 F3 Jupiter was used.

The H_2 temperature programmed reduction (TPR) was carried out in an Altamira AMI-300 device. A sample of 0.0808 g of catalyst was placed in a U-shaped quartz reactor and first dried with Ar at 200 °C (flow 30 ml min^{-1}, temperature ramp 10 K min^{-1} then 15 min at 200 °C) followed by cooling down to room temperature under Ar (20 K min^{-1}). The temperature was raised afterwards from room temperature to 950 °C at a rate of 5 °C min^{-1} (950 °C held for 10 min), in a gas mixture containing 10% H_2/Ar (flow 30 ml min^{-1}).

3.3 Results and Discussion

3.3.1 Characterization of fresh catalysts

Table 3.1 presents the determined composition of the two catalysts from the ICP-OES measurements. The Ni-content of the R210 is 13.2 wt.% while that of R330 is 9.6 wt.%. Another difference between the two samples is the content in K, which is higher in R210. The physicochemical properties of the two fresh catalysts are presented in Table 3.2. Both catalysts had very low surface area due to the low surface area of the support [180,181], with the R330 having almost double the surface area of the R210.

Table 3.1 Composition of the two catalysts employed for SR.

Catalyst	Ni content (wt.%)	K content (wt.%)	Ca content (wt.%)	Al content (wt.%)
R210	13.2	1.5	8.8	30.7
R330	9.6	0.2	9.5	30.8

Table 3.2 Physicochemical properties of the fresh catalysts.

Catalyst	BET surface area ($m^2\ g^{-1}$)	Pore volume ($cm^3\ g^{-1}$)	Pore diameter (nm)
R210	3.8	0.025	9.2
R330	7.4	0.028	6.7

Figure 3.2 presents the X-ray diffractograms of the fresh and reduced catalysts. The main support crystal phases of the R330 were $CaAl_4O_7$ and $CaAl_{12}O_9$, while the crystal phases of the R210 were the $CaAl_4O_7$ and the $K_{2.6}Al_{21.83}O_{33.9}$. Both fresh catalysts consisted of NiO, which was sufficiently reduced to Ni^0, as the profiles of the reduced samples show. Traces of $NiAl_2O_4$ could be present since the TPR profile (Figure 3.3) of both of them showed peaks at temperatures higher than 700 °C, but NiO and metallic Ni probably overlapped them. The sizes of the Ni crystallites in the reduced catalysts were calculated by the Scherrer equation to equal 40.3 nm for R330 and 35.8 nm for R210.

a) R330

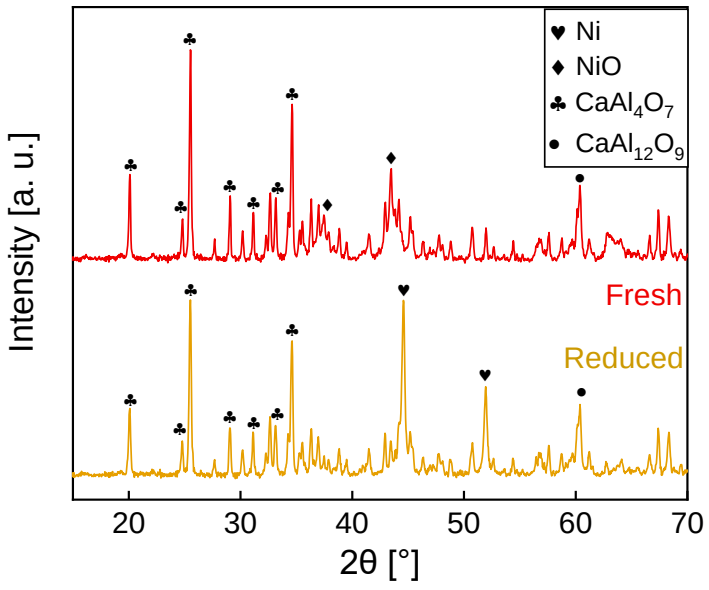

b) R210

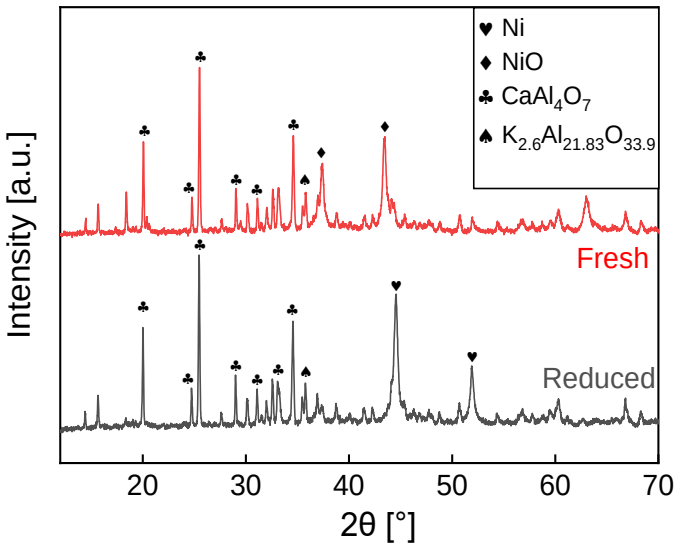

Figure 3.2 a) XRD graphs of the fresh and reduced a) R330 and b) R210 catalysts.

The TPR profile of the fresh NiO(14wt.%)/$CaAl_{12}O_9$ (R330) catalyst is given in Figure 3.3, where it is shown that the main reduction peak centers at around 475 °C, followed by three shoulder peaks at 545 °C, 699 °C and 823 °C. The profile of the R210 catalyst is characterized by a main peak at 466 °C, a second one at 692 °C, and a third one at 782 °C. The peaks of the R210 were close to the ones of the R330 but shifted to slightly lower temperatures indicating the slightly enhanced reducibility of the R210. Both catalysts presented the most intense peaks at relatively low temperatures, which are ascribed to free NiO species closely connected with the support [122,182]. The last two peaks correspond to structures characterized by strong interaction between the Ni and the support and thus, are difficult to reduce, such as $NiAl_2O_4$ [182–186].

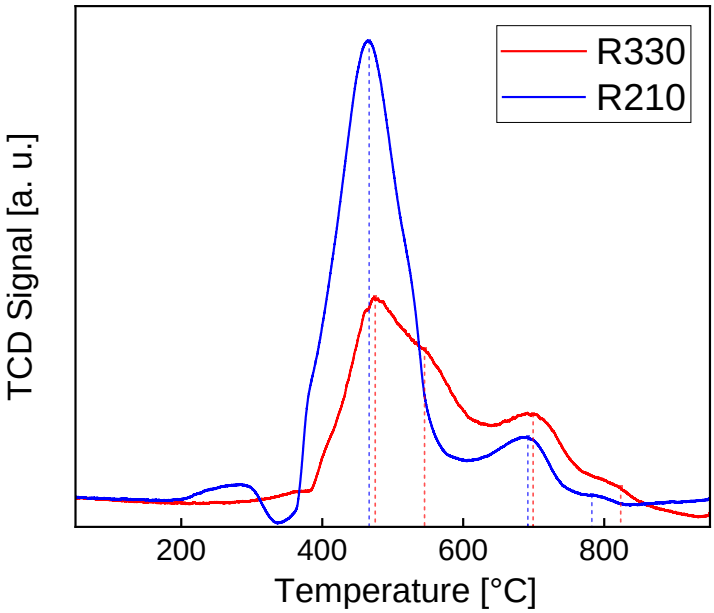

Figure 3.3 H_2-TPR profile of the fresh catalysts.

3.3.2 Assessing the product from the SCWG reactor

The investigation of the effect of temperature, pressure, and space velocity on the product gas from the second reactor (reformer) was carried out with an 8 wt.% EtOH solution fed in the first reactor. Preliminary experiments addressed only the gasification in the first reactor, to determine its product. The average concentration of the dry product gas and the average yields of the products based on EtOH are given in Table 3.3. Hydrogen was the dominant component in terms of volumetric percentage, followed by CH_4. The average flow rate of the product gas was 13.4 NL h^{-1}, while the S/C ratio of the total product was 15.2. The average values of the carbon gasification efficiency (CGE) CGE and $Y_{H_2,SCWG}$ were 99.2% and 28.8%, respectively.

Table 3.3 Concentrations and yield of the product gas species from 8 wt.% EtOH SCWG at 600 °C and 265 bar.

Product gas	Dry gas composition (vol.%)	Products' yield (mol mol_{EtOH}^{-1})
H_2	48.6	1.7
CO	10.6	0.4
CH_4	22.7	0.8
CO_2	14.6	0.5
C_{2+}	3.7	0.1

The effect of EtOH concentration (5 – 20 wt.%) on the SCWG product composition investigated first. In all tests the ethanol conversion was complete. Figure 3.4 illustrates the composition of the dry product gas and how it varied with EtOH concentration. A remarkable decrease in H_2 concentration from around 52.5 vol.% to 38.5 vol.%, was observed when the EtOH concentration increased from 5 wt.% to 20 wt.%. The concentrations of CH_4 and C_{2+} hydrocarbons followed the opposite trend with gradual increase from 16 vol.% to 24.6 vol.%, and from 4.2 vol.% to 8.7 vol.%, respectively, while that of CO_2 showed a slight decrease from 26.9 vol.% to 23.6 vol.%. The hydrocarbons higher than CH_4 contain mostly C_2H_6. A notable upward shift in CO concentration was also observed, being more profound at higher EtOH concentrations than at lower ones, i.e., from 0.4 vol.% at 5 wt.% EtOH, it rose to 2.2 and 4.6 vol.%, at 15 and 20 wt.%, respectively.

The increase in C_{2+} hydrocarbons with the increase in EtOH concentration may result from the reaction of EtOH dehydration, forming ethylene (eq. 3.8), which reacts subsequently with a H_2 molecule to form ethane (eq. 3.9) [187,188]:

$$C_2H_5OH \rightarrow C_2H_4 + H_2O, \qquad \Delta H^0 = 45.8\frac{kJ}{mol} \tag{3.8}$$

$$C_2H_4 + H_2 \leftrightarrow C_2H_6, \qquad \Delta H^0 = -136.3\frac{kJ}{mol} \tag{3.9}$$

By comparing the concentration of CO in Table 3.3 and Figure 3.4, for 8 wt.% EtOH a significant drop in its concentration can be observed owing to the addition of $KHCO_3$. It has been reported by several studies that potassium can act as a catalyst, increasing gasification efficiency, promoting the WGS reaction and minimizing coke formation [13,47,48,189,190].

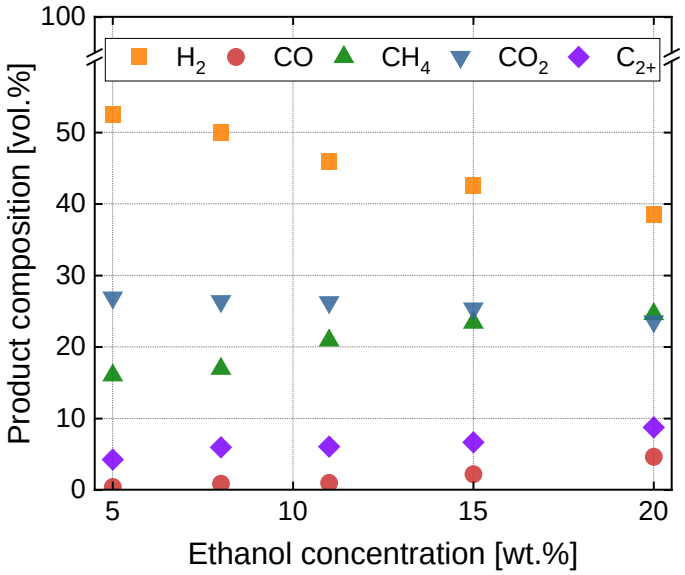

Figure 3.4 Composition of the dry SCWG-product gas with concentration of EtOH in the inlet to the SCWG reactor.

Table 3.4 presents the S/C ratio, the CGE, the amount of gas produced, and the $Y_{H_2,SCWG}$ of the SCWG product at different EtOH concentrations. The CGE was ≥ 97%, indicating almost complete gasification of EtOH, even at high organic feed concentrations. The factors that led to high CGEs, were the applied temperature of 600 °C [9], the long residence time of 1.5 min [129,191], and the addition of K^+. The S/C ratio as expected decreases drastically with increasing EtOH concentration. This parameter is very important for the operation of the SMR reactor, as it plays an important role in the conversion of hydrocarbons and the hydrogen yield. This is because of the effect on the equilibrium of the SMR and WGS reactions [100], but also on formation of coke [161]. It has been reported that in steam reforming of CH_4 and other hydrocarbons, or mixtures thereof, there are critical S/C ratios, at given temperature and pressure, above which the carbon formation is inhibited [162,163]. Generally, with an increase in the carbon content, the S/C ratio should also increase to avoid the formation and deposition of carbon on the catalyst [124]. As the EtOH concentration increases, the amount of steam decreases while the amount of

carbonate species increases. Therefore, after a certain concentration of EtOH, the remaining steam will not be enough to prevent carbon formation and deposition. Additionally, the $Y_{H_2,SCWG}$ decreases with EtOH concentration as does the percentage of hydrogen in the dry product gas.

Table 3.4 Main features of EtOH SCWG for different feed concentrations.

EtOH concentration (wt.%)	S/C ratio (mol_{H2O} mol_C^{-1})	Amount of product gas (L g_{EtOH}^{-1})	$Y_{H_2,SCWG}$ (mol mol_{EtOH}^{-1})	CGE (%)
5	22.0	2.02	0.37	99.6
8	12.9	1.90	0.32	99.6
11	7.8	1.94	0.31	99.4
15	6.3	1.62	0.24	97.9
20	4.5	1.48	0.20	97.0

3.3.3 Effect of temperature and pressure on the products of the steam reformer

To study the effect of temperature and pressure on the conversion of CH_4 and the composition of the product gas in the steam reformer, an 8 wt.% EtOH solution was used as feed to the SCWG reactor and the catalyst in the steam reformer was the R330. Figure S1 in the Supplementary Material (SM) depicts the conversion of CH_4 with temperature and pressure at thermodynamic equilibrium, and Figure S2 shows the respective dry product gas composition. From Figure S1, it is evident that increasing temperature has a positive effect on CH_4 conversion, whereas increasing pressure has a negative effect. More specifically, under thermodynamic equilibrium, CH_4 conversion drops from almost 100% to 86% at 700 °C when the pressure increases from 1 to 40 bar. At 750 °C, the corresponding CH_4 conversion at 40 bar is 94.6%. Similarly, the concentration of hydrogen produced at equilibrium falls from 75.5 vol.% at 700 °C and 1 bar to 74 vol.% at 700 °C and 40 bar. At 750 °C, the concentration of H_2 at equilibrium ranges from 75.4 vol.% at 1 bar to 74.9 vol.% at 40 bar. The CH_4 concentration was found to increase with pressure

and decrease with temperature. At atmospheric pressure, CH_4 levels remained close to zero across all temperatures tested. Under conditions of 700 °C and 40 bar, the CH_4 concentration reached 1.6 vol.%, whereas at 750 °C and the same pressure, it only reached 0.6 vol.%. Additionally, an increase in temperature resulted in a slight rise in CO concentration: at 700 °C and 30 bar, CO was at 2.6 vol.%, while at 750 °C and 30 bar, it increased to 3.3 vol.%. Conversely, increasing pressure had a minor negative impact on CO levels. In contrast, CO_2 concentration was higher at lower temperatures, due to the WGS reaction [121]. Specifically, at 700 °C and 40 bar, CO_2 concentration was 21.8 vol.%, which dropped to 21.3 vol.% at 750 °C under the same pressure. Overall, within the studied range of pressures and temperatures for the product gas from 8 wt.% EtOH in SCWG (at 600 °C and 265 bar), the effect of temperature and pressure on CH_4, H_2, CO, and CO_2 concentrations remains relatively minor.

Figure 3.5 depicts the experimental CH_4 conversion as a function of pressure in the second reactor, for different temperatures. By comparing the results from Figure 3.5 to those in Figure S1, a close agreement between the experimental results and the equilibrium values can be observed at pressures close to 1 bar, where CH_4 conversion is almost complete. As pressure increases, the deviation from thermodynamic equilibrium also increases. However, increasing temperature counteracts this deviation, reducing it. At 700 and 720 °C, the difference between the experimental results and equilibrium values is already significant at 20 bar. For example, the experimental CH_4 conversion at 720 °C and 20 bar was 93%, while the equilibrium value was 97%. This is not the case at 750 °C, where the largest difference between the experiments and equilibrium occurs at 40 bar, with the experimental CH_4 conversion at 90%, compared to the equilibrium value of 94.6%.

The variations in product composition with pressure and temperature are rather minimal in agreement with thermodynamic equilibrium. Regarding the experimental results for the concentration of CH_4 (Figure 3.5.c), it decreased with temperature and increased with pressure. At 700 °C, the CH_4 content in the dry product gas amounted for 0.2 vol.% at 1 bar, whereas at 750 °C it reduced to 0.02 vol.%. Likewise, at 40 bar and 700 °C its value was equal to 2.5 vol.%, but dropped eventually to 1.1 vol.% at 750 °C. At equilibrium, the

CH_4 concentration ranges from 0.001 vol.% at 1 bar, to 1.7 vol.% at 40 bar, under 700 °C, but at 750 °C, its concentration is $4 \cdot 10^{-4}$ vol.% at 1 bar, and 0.6 vol.% at 750 °C.

These experimental findings demonstrate the profound effect of temperature and pressure on the reactions of SMR and WGS. The temperature increase promotes the forward SMR reaction and the reverse WGS, thereby increasing the percentage of H_2 and CO, and the methane conversion [192,193]. Increasing pressure favors the reverse SMR reaction, decreasing CH_4 conversion and the concentrations of H_2 and CO [194], but it does not affect the WGS reaction, leaving the residual steam to react with CO, forwarding the slight increase in CO_2 [140,176].

Temperatures higher than 750 °C were tested but rapid deactivation of the R330 catalyst was observed. BET analysis indicated a surface area loss from 7.4 $m^2\ g^{-1}$ to 1.7 $m^2\ g^{-1}$, a pore volume loss from 0.028 to 0.014 $cm^3\ g^{-1}$ and a pore diameter shrinkage from 6.7 to 1.7 nm. Most likely the catalyst pores have been blocked during the reaction under T > 750 °C. The XRD diffraction profile of the catalysts subjected to 770 °C is given in SM (S1.2). All peaks that were found in the reduced catalyst, related to the support, were found here too. No NiO peaks were found, only metallic Ni, with a crystallite size of 45.7 nm, calculated by the Scherrer equation. However, as will be seen in the following sections (3.5 and 3.6), sintering was comparable to values of other samples that did not show dramatic deactivation. No carbon was found on the used catalyst via TGA-MS (see S2). A possible reason for deactivation might be the collapse of the porous structure of the support [172,195].

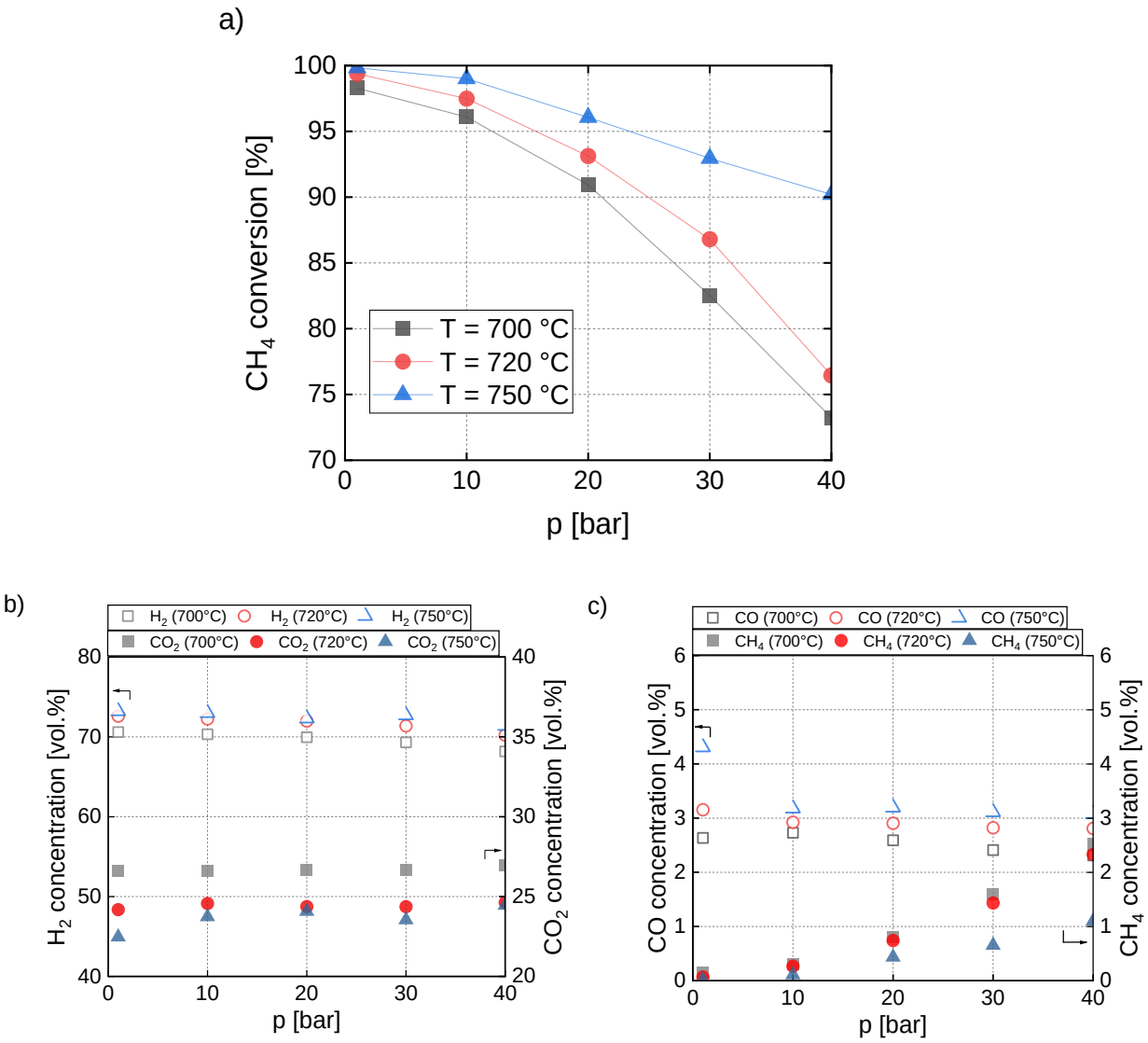

Figure 3.5 a) Conversion of CH_4 versus pressure for different temperatures in the SR reactor, b) Concentration of H_2 and CO_2 in the SR dry product gas, and c) Concentration of CH_4 and CO respectively (SCWG with 8 wt.% EtOH at 600 °C and 265 bar; GHSV in SR reactor = 63500 h^{-1}).

3.3.4 Effect of space velocity on the SR product

The effect of the GHSV and its effect on the product gas from the reformer was also studied. The temperature of the catalytic bed was 730 °C and measurements were performed for two different pressures (1 and 30 bar). The results regarding CH_4 conversion are summarized in Figure 3.6.a. The GHSV spans from 42400 h^{-1} to 127000 h^{-1}. Under a pressure of 1 bar, the deviation from the thermodynamic equilibrium (CH_4 conversion almost 100%) is negligible for GHSVs, up to 63500 h^{-1}. As the GHSV increases

to 127000 h^{-1}, the CH_4 conversion under atmospheric pressure deviates significantly from equilibrium as it falls to 84.1%. At a pressure of 30 bar, the deviation of the equilibrium is already apparent at a GHSV of 50900 h^{-1}, where it falls to 89.3%, while the equilibrium value is around 94%. The highest GHSV of 127000 h^{-1} resulted in a CH_4 conversion equal to 75%. However, a GHSV of 42400 h^{-1} was enough for the CH_4 conversion to reach close to equilibrium and be equal to 93.7%.

Figures 3.6.b and 3.6.c depict the dry product gas composition as a function of GHSV at 730 °C and for 1 and 30 bar. The percentage of H_2 at 1 bar falls from 72.6 vol.% to 70.8 vol.%, from 42400 h^{-1} to 127000 h^{-1}. Its percentage is also reduced at 30 bar, from 71.4 vol.% to 69.4 vol.%, under 42400 h^{-1} and 127000 h^{-1}, respectively. The percentage of CO_2 was slightly increased with increasing GHSV, from 22.9 vol.% to 24.3 vol.%, at 1 bar, and from 24.5 vol.% to 25.0 vol.% at 30 bar. In Figure 3.6.b an increase in CH_4 concentration is observed at both pressures, i.e., from 0.05 vol.% to 1.6 vol.% at 1 bar, and from 0.6 vol.% to 2.5 vol.% at 30 bar. Last, the concentration of CO follows a downward trend with rising GHSV, from 4.5 vol.% to 3.4 vol.%, and from 3.5 vol.% to 3.1 vol.%, at 1 bar and 30 bar, respectively. No hydrocarbons higher than CH_4 were observed in the SR product gas.

a)

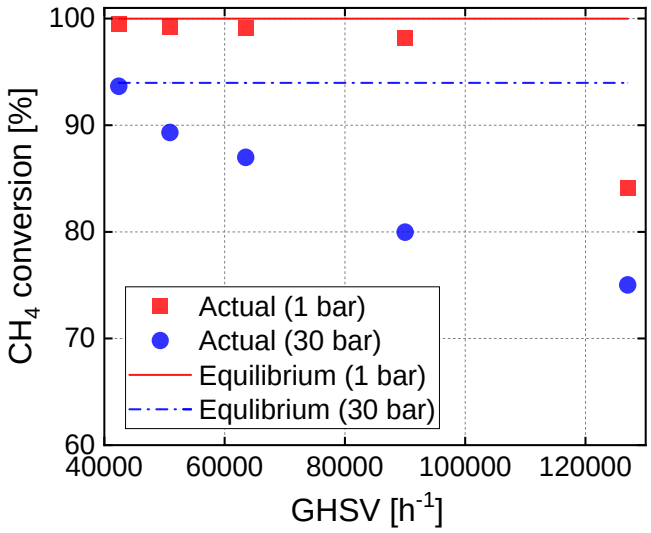

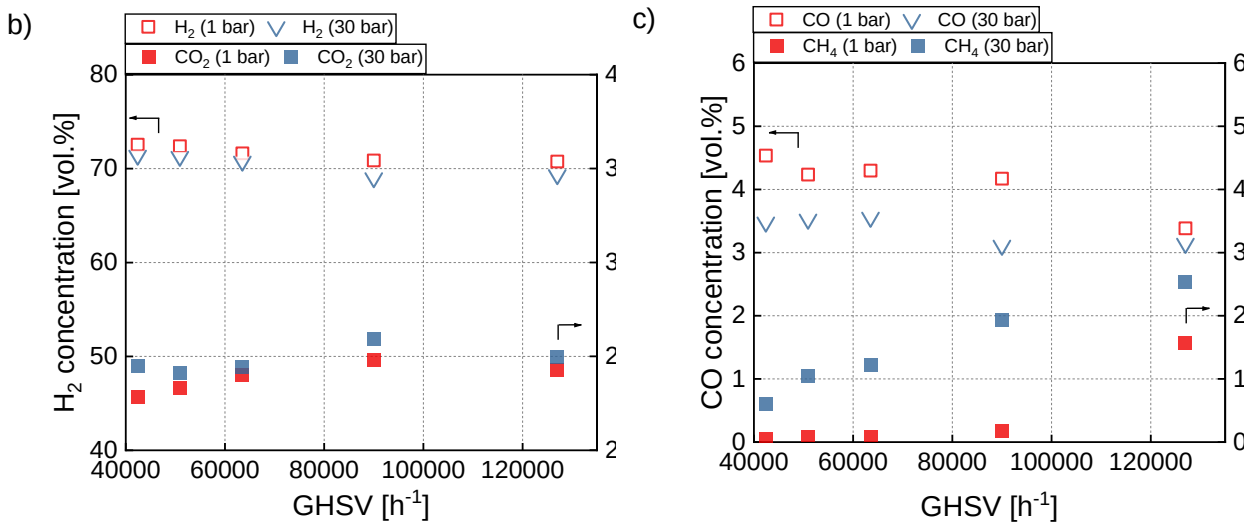

Figure 3.6 a) Conversion of CH_4 with GHSV for different pressures in the SR reactor, b) Concentration of H_2 and CO_2 in the SR dry product gas, and c) Concentration of CH_4 and CO respectively (SCWG with 8 wt.% EtOH at 600 °C and 265 bar; T in the SR reactor = 730 °C).

3.3.5 Effect of EtOH concentration on the SR product and on the catalyst

The concentration of EtOH in the SCWG reactor varied from 5 wt.% to 20 wt.%. The effect of ethanol concentration on the product distribution exiting the supercritical gasifier was already presented in 3.2. Figure 3.4 demonstrates the change in the outlet dry product gas composition from the SCWG reactor. Table 3.4 indicates how the S/C ratio, the hydrogen yield, and the amount of the SCWG product gas vary with the concentration of organic feedstock. This section investigated the effect of the EtOH concentration on the reformate product gas. The SR reactor operated at 730 °C, 30 bar, with a constant catalyst mass of 2.5 g. The catalyst used was the R330, i.e., the NiO(14wt.%)/$CaAl_{12}O_9$. Due to changes in the volumetric flow of the product gas with varying EtOH, the GHSV varied accordingly. However, the differences in GHSV were minimal, with the mean value and the standard deviation being equal to 47877 h^{-1} and 2134 h^{-1}, respectively. This GHSV value is near the one reported in the previous section (section 3.3.4, Figure 3.6), i.e., 42400 h^{-1}, which was sufficient to drive the reactions in the SR reactor close to thermodynamic equilibrium.

The CH_4 conversion and the total H_2 yield after SCWG and subsequent SR for different EtOH concentrations are given in Figure 3.7.a. Figure 3.7.b depicts the respective SR product gas composition. The CH_4 conversion falls from 97.5% with 5 wt.% EtOH to 22.5% with 20 wt.% EtOH. Likewise, the H_2 yield falls from 98.6% to 58.3%, as the EtOH concentration increases from 5 wt.% to 20 wt.%. The volumetric percentages of H_2 and CO_2 in the SR product gas follow a decreasing trend with EtOH concentration increase, with the first dropping from 72.0 vol.% to 62.3 vol.%, and the second from 25.8 vol.% to 21.8 vol.%, from 5 wt.% to 20 wt.% EtOH, respectively. On the other hand, in this EtOH concentration range, the concentration of CH_4 and CO increase, i.e., methane increases from 0.2 vol.% to 9.5 vol.%, and carbon monoxide from 2.1 vol.% to 6.5 vol.%. It is worth noting that there were no C_{2+} hydrocarbons in the SR product, even at high EtOH concentrations. Section S1.3 in the SM includes the corresponding results at thermodynamic equilibrium. The differences between the experimental values and those at thermodynamic equilibrium are relatively minor, with the experimental results following the same trend as the equilibrium values in terms of CH_4 conversion, H_2 yield, and product gas composition. The deviation from equilibrium in CH_4 conversion becomes more significant at high EtOH concentrations. For example, at 20 wt.% EtOH, the equilibrium CH_4 conversion was 36%, while the experimental value was 22.5%.

According to the results from Figure 3.4 and Table 3.4, the increase in EtOH concentration results in an SCWG product gas with a higher CH_4, C_{2+}, and CO content and a significantly lower S/C ratio. At high EtOH concentrations, the consumption of steam for the SR of the C_{2+} hydrocarbons further decrease the available steam for SR of CH_4. The increase in these components and the simultaneous decrease in the steam content in the gas fed to the SR reactor drive the equilibrium of the SMR reaction towards lower CH_4 conversion [196–198] and the equilibrium of the WGS reaction towards CO production [198].

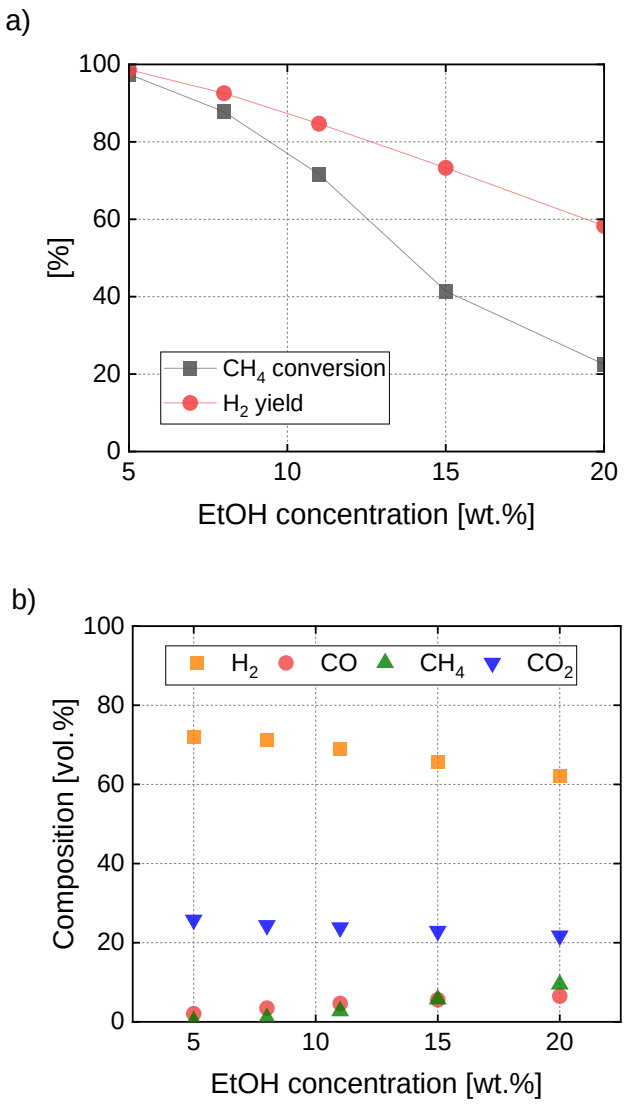

Figure 3.7 a) Conversion of CH_4 and H_2 yield after SR with different EtOH concentrations in the SCWG reactor and b) SR product gas composition (SCWG at 600 °C and 265 bar; T in the SR reactor = 730 °C; p in t in the SR reactor = 30 bar; mean GHSV value was 47877 h^{-1}).

The S/C ratio dropped from 22.0 to 4.5, when the EtOH concentration increased from 5 wt.% to 20 wt.%. An additional aim of this study was to investigate if this significant change in the S/C ratio would affect the catalyst structure. For this, two experiments were carried out, one with 5 wt.% EtOH and one with 20 wt.%. This time, however, the amount of catalyst was adjusted so that the parameter $m_{cat.}/\dot{F_{HCs}}$, with $\dot{F_{HCs}}$ being the molar flow of the hydrocarbons generated in the SCWG reactor, to be the same in both cases and equal to its value when the EtOH concentration was 8 wt.% and the catalyst mass was 2.5 g. The adjusted catalyst mass was thus 1.5 g at 5 wt.% EtOH and 7.0 g at 20 wt.% EtOH.

$$\left[\frac{m_{cat.}}{\dot{F}_{HCs}}\right]_{5\ wt.\%} = \left[\frac{m_{cat.}}{\dot{F}_{HCs}}\right]_{20\ wt.\%} = \left[\frac{m_{cat.}}{\dot{F}_{HCs}}\right]_{8\ wt.\%} = 16.7\ \frac{g_{cat.} \cdot h}{mol_{HCs}}$$

The overall GHSV under 5 wt.% EtOH was now 84405 h^{-1}, and 17017 h^{-1} under 20 wt.% EtOH. Figure 3.8 presents the resulting CH_4 conversion, H_2 yield, and the dry product gas composition for these two cases. The conversion of CH_4, in the case of 5 wt.% EtOH, was 93.8%, while its respective value under equilibrium is 98.6%. Similarly, for the case of 20 wt.% EtOH, the experimental value of the CH_4 conversion was 32.0% and its equilibrium value is 36.0%. The respective product gas compositions were close with their equilibrium values. Therefore, although there is a difference in the overall GHSV between these two cases, both deviate roughly the same from their individual equilibrium. Their main difference still lies in the composition of the feed, i.e., S/C ratio and dry gas composition.

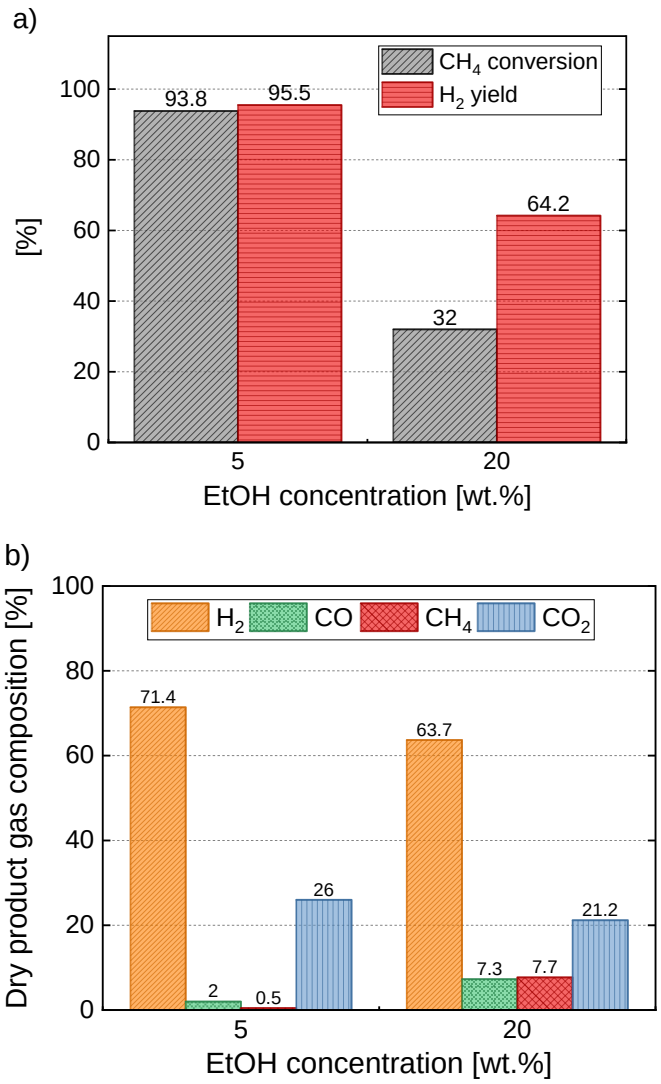

Figure 3.8. a) Conversion of CH_4 and H_2 yield and b) Dry product gas composition, after SCWG-SR with 5 wt.% and 20 wt.% EtOH (SCWG at 600 °C and 265 bar; T in the SR reactor = 730 °C; p in the SR reactor = 30 bar; $m_{cat.}/\dot{F}_{HCs}$= 16.7 $g_{cat.}$ h mol_{HCs}^{-1}).

Figure 3.9 presents the TGA profiles and the corresponding MS profiles of the catalysts exposed to the SR of product gas derived from 5 wt.% and 20 wt.% EtOH and also the reduced catalyst prior to reaction. The catalyst subjected to the lower EtOH concentration exhibited a slight mass loss, reaching 98.8% in the temperature range of 100–340 °C, likely due to water vaporization, as indicated by Figure 3.9.b. Subsequently, its weight increased to 101.1%, possibly due to the reoxidation of Ni. The small CO_2 peak observed around 635 °C corresponded to a negligible weight decrease from 101.10% to 101.08%. The catalyst subjected to the higher EtOH concentration showed a more significant weight loss at approximately 95.8% in the same temperature range of 100–340 °C. This was

followed by a 1.32% weight increase possibly due to the reoxidation of Ni. On the contrary, the catalyst subjected at lower EtOH concentration had a weight gain of 2.3%, due to Ni reoxidation, aligned with the reduced catalyst sample. The reason for the lower weight increase might be ascribed to catalyst reoxidation under reaction conditions. A subsequent weight decrease, down to 95.7%, was observed between 600 °C and 800 °C. As shown in Figure 3.9.c, a CO_2 peak at 660 °C indicated part of this weight loss was due to the oxidation of filamentous carbon deposited on the catalyst [199]. However, this did not cause deactivation during the 4-hour operation.

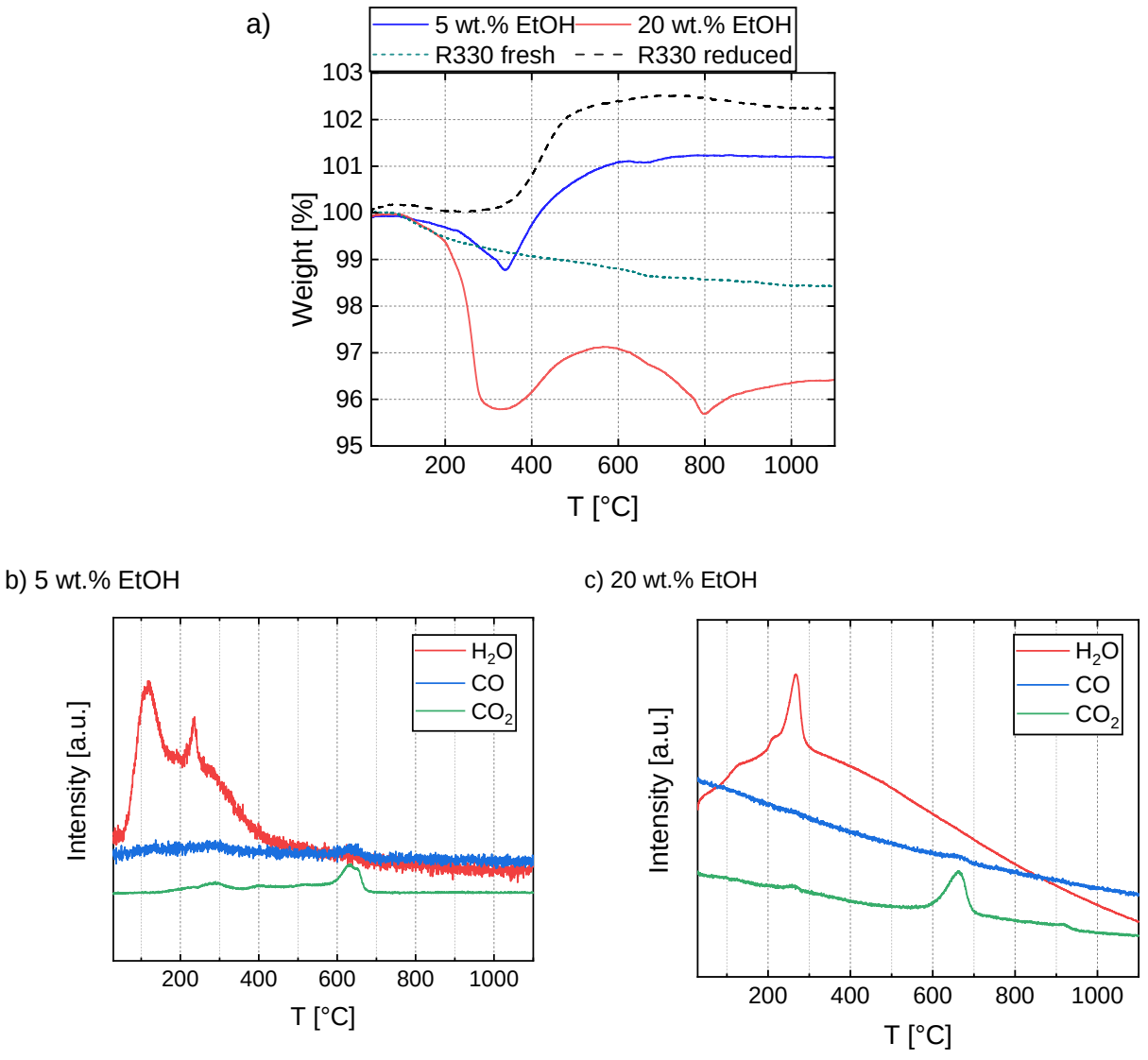

Figure 3.9 a) TGA of the fresh, reduced, and used catalyst samples that were subjected at SR of the product gas from 5 and 20 wt.% EtOH SCWG, b) MS signals of water vapor and carbon oxides of the used catalyst sample at SR of the product gas from 5 wt.% EtOH SCWG, and c)

corresponding MS signals of the used catalyst sample at SR of the product gas from 20 wt.% EtOH SCWG.

The relatively low formation of carbon in both the 5 wt.% and 20 wt.% EtOH cases can be attributed to the excess steam, which suppresses carbon formation and deposition [161–163]. Additionally, the presence of H_2 in the feedstock for the SR reactor has been shown to inhibit carbon formation [162,200]. Furthermore, the basicity of the Ca-Al support contributes to reduced carbon formation [201,202].

Figure 3.10 illustrates the XRD profiles of the used catalysts under SR following the SCWG of 5 wt.% and 20 wt.% EtOH. Both used catalysts demonstrated the same support structure with the reduced catalyst prior to the reaction (see Fig. 3.2). The dominant phase for the Ni species in the bulk catalyst was still the monometallic Ni, indicating that the H_2 produced in the SCWG reactor maintained the reduced state of Ni in both cases [167,176]. The catalyst subjected to the product gas from 20 wt.% EtOH SCWG had a Ni crystallite size of 41.7 nm, whereas the one from 5 wt.% EtOH SCWG had a Ni crystallite size of 40.9 nm. The difference in the Ni sizes between the two experiments is very small and both are close to the size of the reduced catalyst (40.3 nm). Therefore, sintering did not play a role in catalyst activity and overall process performance, for a TOS of 4 h. Long-term experiments are required in both cases in order to study the evolution of sintering.

The differences in the dry product gas composition and S/C ratio under the studied EtOH concentration range (5 – 20 wt.%) seemed to have not affected the catalyst structure. Christensen et al. [170] performed sintering experiments on a commercial $Ni/CaAl_2O_4$ with a BET surface area of 5.5 m^2 $g_{cat.}^{-1}$. They argued that a significant change in the particle size or the surface area of this catalyst was difficult, since it already had a very small initial surface area, hindering, thus, the diffusion of Ni on it.

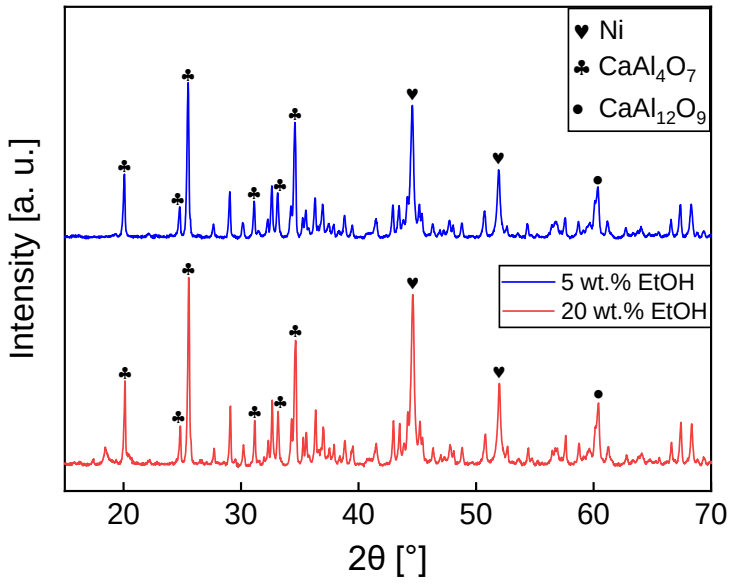

Figure 3.10 XRD profiles of the used catalysts under SCWG and SR with 5 wt.% and 20 wt.% EtOH.

3.3.6 Comparison of the two catalysts

The catalysts R330 and R210 were tested under different pressures, constant temperature of 740 °C, constant catalyst mass of 2 g, so that the parameter $m_{cat.}/\dot{F}_{HCs}$ was equal to 12.5 $g_{cat.}$ h mol_{HCs}^{-1} for both catalysts, and a TOS of 8 h. The SCWG conditions were 600 °C and 265 bar, with the EtOH concentration in the feed being 8 wt.%. Figures 3.11.a, 3.11.b, and 3.11.c depict the conversion of CH_4 and the SR product gas composition for the two catalysts, respectively. The CH_4 conversion of R330 was slightly higher than that of R210 for pressures in the range 1 – 10 bar. Specifically, the CH_4 conversion for the R330 was 98.3% and 96.5%, under 1 bar and 10 bar, respectively, whereas, the conversion for R210 was 96.8% and 94.5%. However, for pressures higher than 20 bar the CH_4 conversion of the R330 had a sharper decrease and fell to lower values than the R210, e.g., the conversion of the R330 at 40 bar was 74.3%, while that of the R210 was 84.1%. Similarly, it can be seen in Figure 3.11.b that, under a pressure in the range 1 – 10 bar, the concentration of CH_4 for the R330 was 0.2 – 0.3 vol.%, while for the R210 it was 0.3 – 0.6 vol.%. However, the pressure increase led to higher final CH_4 concentrations for R330 than R210, e.g., at 40 bar, the CH_4 concentration was 2.4 vol.% for R330 and 1.6 vol.% for R210.

It was examined whether this difference in the activity of the two catalysts between low and high pressures could be attributed to the external and/or internal mass transfer control. For external diffusion control, the Mears criterion was applied [203].

$$M = \frac{r_A \cdot d_{cat.} \cdot R \cdot n}{k_c \cdot C_{A(bulk)}} \ll 0.15 \qquad (3.10)$$

where r_A is the reaction rate of the limiting reactant in mol $kg_{cat.}^{-1}$ s^{-1}, $d_{cat.}$ is the apparent density of the catalyst in kg m^{-3}, R is the radius of the catalyst particles in m, n the reaction order, k_c the gas-particle mass transfer coefficient in m s^{-1}, and $C_{A(bulk)}$ the concentration of the limiting reactant in the bulk gas phase in mol m^{-3}. The Weisz-Prater criterion was applied for internal diffusion control [204].

$$WP = \frac{r_A \cdot \rho_c \cdot R^2}{D_{eff.} \cdot C_{A(surface)}} \ll 1 \qquad (3.11)$$

where ρ_c is the actual density of the catalyst in kg m^{-3}, $D_{eff.}$ the effective diffusivity in m^2 s^{-1}, and $C_{A(surface)}$ the concentration of the limiting reactant on the catalyst surface in mol m^{-3}.

The values of both criteria as well as the methods for calculating them for both catalysts are given in Supporting Information (S1.4). The Mears criterion is satisfied, and therefore, the effect of external mass transfer is not considered as likely. On the other hand, at atmospheric pressure, the Weisz-Prater ratio receives values higher than unity. At pressures higher than 20 bar, the Weisz-Prater ratio falls two orders of magnitude lower than unity. Thus, under low pressures (1 – 10 bar), there is a strong resistance to the chemical reaction within the catalyst pores due to the intraparticle diffusion. Thus, the rather unexpected performance of the catalysts under low pressures (1-10 bar) can be ascribed to the intraparticle diffusion.

The resistance to the reaction due to intraparticle diffusion becomes insignificant under high pressures (p > 20 bar), where the R210 dominated over the R330 in terms of CH_4 conversion. The higher activity in SR reaction of R210 compared to that of R330 could be attributed to its higher Ni content (13.2 wt.% and 9.6 wt.%, respectively) and the smaller initial Ni crystallite size (35.8 nm and 43.1 nm, respectively) [154,186,205]. However, as will be shown later with the XRD profiles of the used catalyst samples, the Ni crystallite sizes of

both catalysts after the reaction were found to be nearly identical (59.2 nm and 60.0 nm), indicating that the dispersion does not play the primary role in the difference in activity, but rather the Ni loading. Apart from those two aspects that can similarly promote the WGS reaction, according to Garbarino et al. [206], the promotion of a commercial Ni-based catalyst with calcium aluminate as support with K_2O may hinder the reverse WGS at high temperatures, allowing the R210 to reach lower CO concentrations.

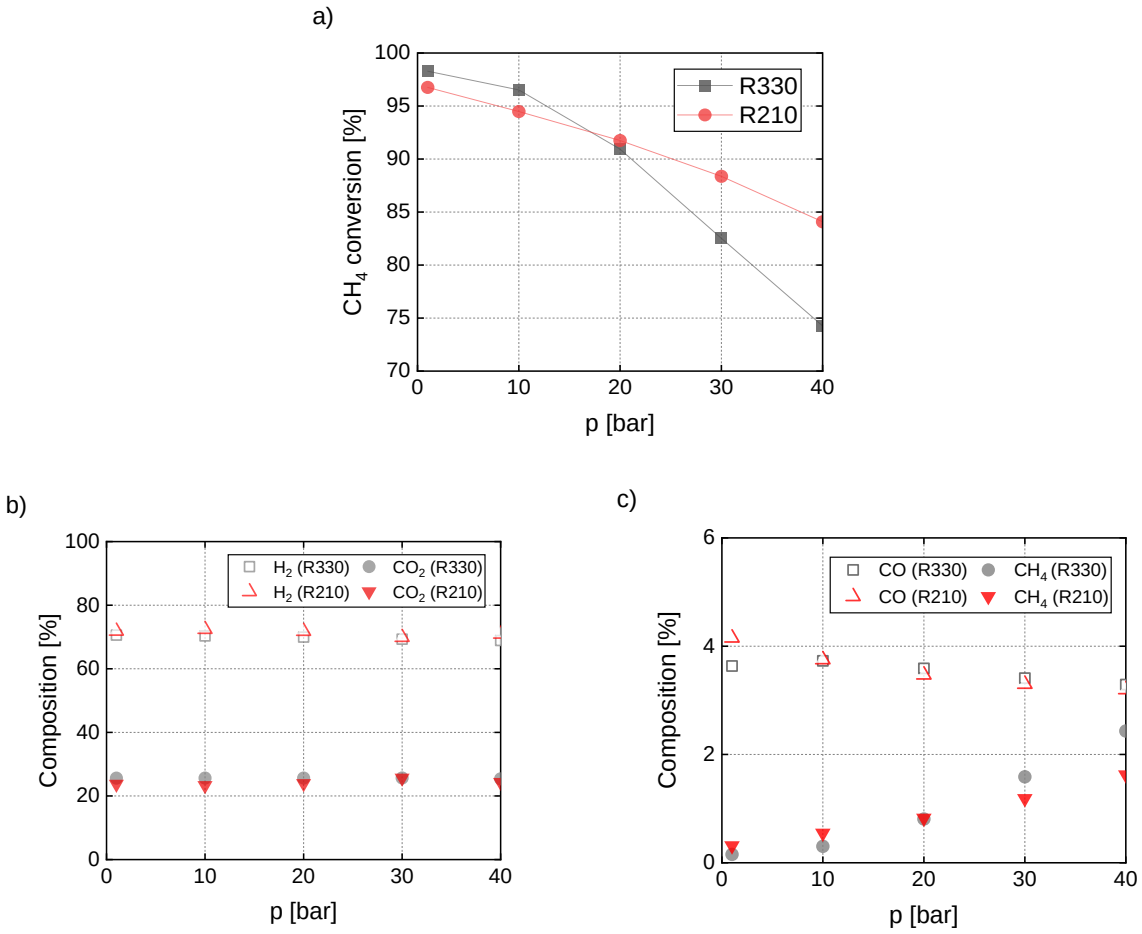

Figure 3.11 a) CH_4 conversion for R330 and R210 after SR at 740 °C with a constant catalyst mass of 2 g, under varied pressure, b) respective concentration of H_2 and CO_2 for both catalysts in the SR products, and c) respective concentration of CO and CH_4 (SCWG conditions: 600 °C, 265 bar, EtOH in the feed was 8 wt.%).

The catalysts exposed to 30 bar pressure were characterized using TGA-MS and XRD. Figure 3.12.a shows the TGA profiles, and Figures 3.12.b and 3.12.c display the corresponding MS profiles for the two catalysts. Both catalysts began to lose weight around 120 °C, attributed to water evaporation. This weight loss due to water release continued at approximately 200 °C and 278 °C, corresponding to the desorption of

chemisorbed water [154]. Between 260 °C and 300 °C, both catalysts exhibited small peaks of CO_2 and CO, related to reactive carbon species [207]. At 400 °C, the weight of R210 decreased to 84.5%, while R330 reached 81.5%. Since the intensity of the water-related peaks was much higher than that of the carbon oxides, it can be implied that the primary cause of the weight loss is due to water desorption. R210 also showed a slight CO_2 release at around 340 °C. However, the overall weight loss for R330 was higher, suggesting that the carbon oxide peaks observed between 200 °C and 400 °C were of minor significance. Beyond 400 °C, a further weight decrease, likely due to water adsorbed in the inner layers of the catalyst, was observed. R210 showed a small CO_2 peak at 664 °C, resulting in a negligible weight loss of 0.3%. Similarly, R330 experienced a loss of 0.3% due to CO_2 release at a higher temperature (720 °C). In both cases, the CO_2 formation could be attributed to the oxidation of carbon filaments [199]. Additionally, both catalysts exhibited minor weight loss with small CO_2 peaks in the 890 °C to 940 °C range, likely due to the oxidation of graphitic carbon [202,208]. R210 showed a decrease of 0.3%, and R330 a decrease of 0.5%.

a)

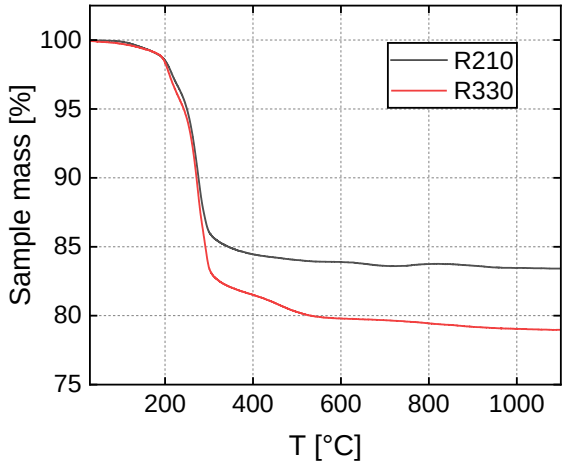

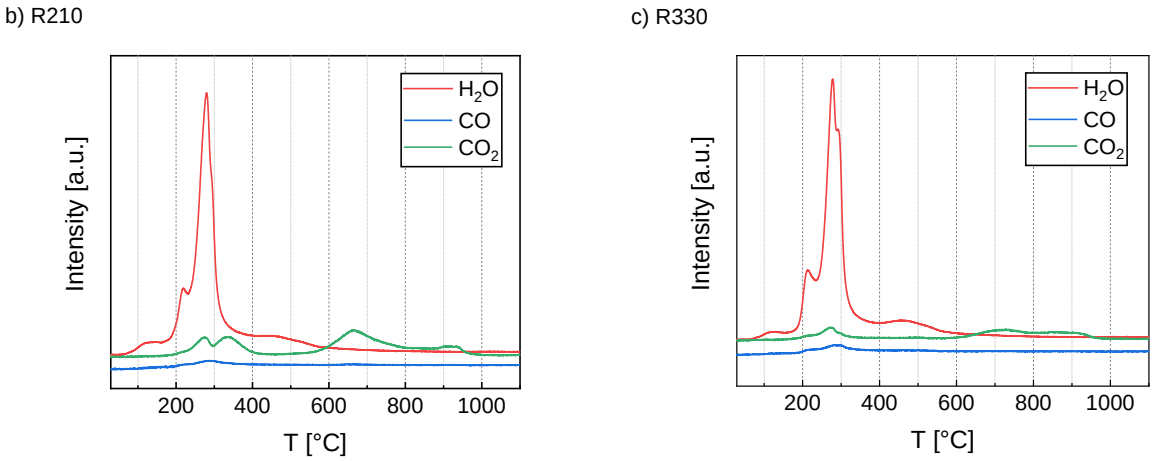

Figure 3.12 a) TGA profiles of the used catalyst samples of R210 and R330 after SR of the gas produced from 8 wt.% EtOH SCWG, b) MS signals of water vapor and carbon oxides of the R210 used catalyst sample and c) respective MS signals of the R330 used catalyst.

The XRD profiles of R210 and R330 are given in Figure 3.13. Both used catalysts depicted peaks at 44.5° and 51.8°, which resembled metallic Ni [134]. Unlike the R330, the R210 showed no peaks related to its support structure without however indicating signs of deactivation. The Ni particle sizes of the used catalysts were calculated by the Scherrer equation and were found to be almost similar. The Ni particle size of R210 was equal to 59.2 nm, accounting for a 65.4% increase compared to the initial size in the reduced state of the catalyst, while the respective one of R330 was 60 nm, and its relevant increase was 48.9%. It is thus apparent that the Ni crystallites on the R210 were more prone to sintering than the ones on the R330. Sehested et al. [195] showed that under 31 bar and a feed consisting of an H_2O:H_2 ratio of 10, the carrier's promotion with potassium accelerated the sintering of nickel crystallites compared to an unpromoted catalyst. The amorphization that the R210 underwent, without any loss in its activity, was also evident in the previous experimental study of the pre-reformer (Chapter 2), where the catalyst was also used for the SR (600 °C, 1 atm, GHSV = 44557 h^{-1}) of the SCWG product gas from 8 wt.% EtOH gasification [176].

The loss in activity due to sintering could not be identified, because both samples were subjected at first to 1 bar and then, after 4 hours, to 30 bar. Thus, any deactivation that would occur due to sintering was overlapped by the changes induced by the pressure increase. Longer TOS are required to depict the effect of sintering on the stability of both

catalysts. Future research will address this by also aiming to overcome any technical hurdles associated with the continuous operation of the process.

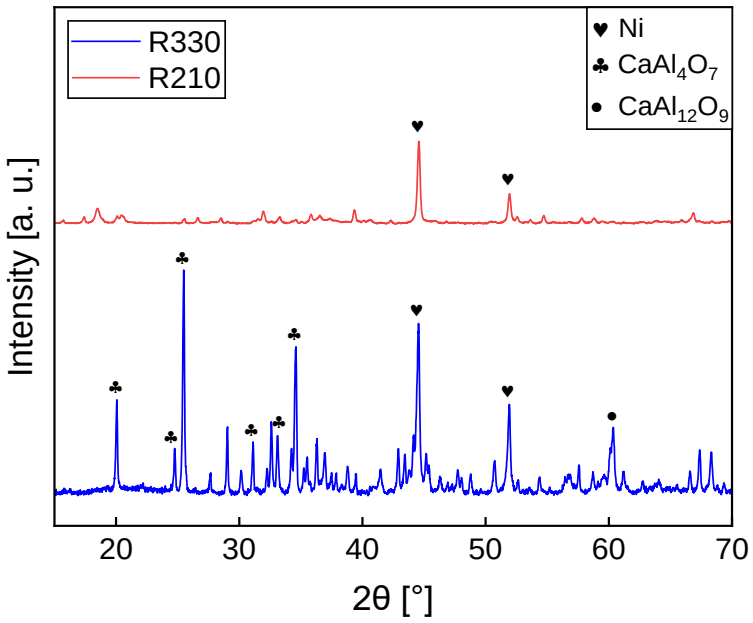

Figure 3.13 X-ray diffractograms of used catalysts at SR with 740 °C, catalyst mass of 2 g, and a pressure of 30 bar (SCWG conditions: 600 °C, 265 bar, EtOH in the feed was 8 wt.%).

3.4 Conclusions

In this chapter, the developed continuous process combining the SCWG of EtOH with the subsequent steam reforming of the product gas is demonstrated through an experimental study that involved the operating parameters in the SR reactor, the EtOH concentration, and a comparison of two commercial Ni-based catalysts for the SR of the SCWG product gas. The SCWG was carried out at 600 °C and 265 bar with ethanol as a model compound with concentrations ranging from 5 wt.% to 20 wt.%.

The effects of temperature, pressure, and space velocity of the SR reactor on the hydrocarbons' conversion and hydrogen yield were investigated. Increasing the temperature enhances methane conversion and boosts the concentrations of hydrogen and carbon monoxide, while higher pressures reduce methane conversion and the concentrations of these gases, slightly increasing carbon dioxide levels. High SR pressures, i.e., 20 – 40 bar, required a temperature of 750 °C to achieve methane conversion higher than 90%. The GHSV significantly affected the performance of the

reforming reactor, especially at high pressures, e.g., at 30 bar, where a GHSV in the range of 40000 – 50000 h^{-1} was needed to keep the methane conversion close to equilibrium.

The concentration of EtOH had a crucial role in the product gas of the combined SCWG-SR process. The increase in EtOH concentration affected the SCWG product by significantly decreasing its S/C ratio, but also increasing the content of CH_4, C_{2+} hydrocarbons, and CO. As a result, SMR and WGS were shifted towards their reactants' side, decreasing CH_4 conversion from 97.5% to 22.5% and H_2 yield from 98.6% to 58.3%, as the EtOH concentration increased from 5 wt.% to 20 wt.%. Despite the significant decrease in the S/C ratio and the change in the SCWG product gas composition, between 5 wt.% and 20 wt.% EtOH, there was a minor carbon formation on both catalysts and not any considerable difference in the Ni sintering rate, under short TOS.

Two different commercial catalysts were tested, a NiO(14wt.%)/$CaAl_{12}O_9$ (R330) and a NiO(18wt.%)/$CaK_2Al_{22}O_{34}$ (R210). Both catalysts were under diffusion control at atmospheric pressure, demonstrating almost the same CH_4 conversion. At high SR pressures (30 – 40 bar), where both catalysts were under kinetic control, the catalyst with the higher Ni loading (R210) showed higher activity. The NiO(18wt.%)/$CaK_2Al_{22}O_{34}$ catalyst resulted in higher sintering rate than the NiO(14wt.%)/$CaAl_{12}O_9$ but the final Ni crystallite size after testing was almost similar for both catalysts. Nevertheless, the former catalyst remained more active than the latter because of the higher Ni loading. The very low coke deposition over both catalysts even under high pressure revealed the resistance to coking mostly due to the excess steam and the high basicity of their supports.

This study verified the possibility of obtaining high hydrogen yields from the SCWG product gas by coupling it with a downstream steam reforming process. Out of the two tested catalysts, the NiO(18wt.%)/$CaK_2Al_{22}O_{34}$ showed to be a suitable catalyst for this specific SR process.

Chapter 4. Techno-economic analysis of the developed process

The content of this chapter is sourced from the following publication:

Vadarlis A. A.; Lacerda de Oliveira Campos B.; Lemonidou A. A.; Boukis N.; Sauer J. Supercritical Water Gasification of Ethanol as Biomass Model Compound in Tandem with Steam Reforming: Kinetic Modeling of the Reforming Step and Techno-Economic Analysis of the Integrated Concept. *Ind Eng Chem Res.* **2024**, *63 (39),* 16683-16700. DOI: 10.1021/acs.iecr.4c01486.

Declaration of contributions:

Athanasios A. Vadarlis conceptualized the work, performed the simulations, processed and analysed the data, evaluated the results, and wrote the manuscript.

Bruno Lacerda de Oliveira Campos contributed to the simulations, processed and analysed the data, evaluated the results, and wrote the manuscript.

Angeliki Lemonidou conceptualized the work, evaluated the results, contributed to the discussion, and reviewed the manuscript.

Nikolaos Boukis supervised the work, contributed to the discussion, and reviewed the manuscript.

Jörg Sauer supervised the work, contributed to the discussion, and reviewed the manuscript.

Summary of Chapter 4

A simulation of the conceptualised process chain SCWG-SR-WGS coupled with a final step for the purification of the produced H_2 in industrial scale is carried out, followed by a techno-economic and sensitivity analysis. After investigating the effect of ethanol concentration and feed flow rate on the price of the produced hydrogen, and considering the technical constraints imposed by the high organic matter content and the availability of actual waste biomass, the optimal values of the ethanol concentration and feed flow rate were 50 t h^{-1} and 15 wt.% ethanol, reaching a hydrogen break-even price of 6.8 $ kg_{H2}^{-1}. The sensitivity analysis identified the ethanol price as the primary cost driver. Exploring waste biomass feedstocks, such as sewage sludge, demonstrated potential break-even prices as low as 0 – 1.8 $ kg_{H2}^{-1}, which can compete with conventional technologies of hydrogen production, such as water electrolysis and steam methane reforming with carbon capture.

4.1 Introduction

The development of alternative processes to replace conventional technologies for processing fossil fuels, requires thorough economic analysis. A techno-economic analysis can assess the profitability of the chemical process proposed and developed in this thesis, identify strategies for cost minimization, and ultimately compare its competitiveness with other conventional processes. Within this context the experimentally developed process was scaled up in Aspen HYSYS V14, incorporating technologies like oxyfuel combustion to reduce its carbon footprint on an industrial scale. An economic analysis was carried out to determine the cost of such a chemical plant, considering as important parameters the organic matter concentration in the feed and the plant capacity in order to minimize the cost of hydrogen production. A follow-up sensitivity analysis helped to identify the most significant contributors to the cost of hydrogen produced. As a benchmark for comparing hydrogen production costs, recent studies suggest that by 2030, the cost of hydrogen produced through electrolysis in the EU will range between €3 and €5 per kilogram [209–212].

It should be noted that the process used EtOH as a biomass model compound because this substance was also used for the laboratory experiments in the previous experimental studies. Ethanol can be used as a biomass model compound to model the complete gasification with supercritical water of sewage sludge and microalgae. Ethanol is composed of 52.17 wt.% C, 13.04 wt.% H, and 34.78 wt.% O. Although the composition of microalgae and sewage sludge may vary, there have been several studies in the literature with compositions similar to EtOH with respect to the three components mentioned [213–218]. It should be mentioned, however, that the amount of ash in real biomasses should not be taken into account for the comparison. Furthermore, this work aims to formulate a base case that is not affected by obstacles like coke formation, salt deposition and eventually incomplete gasification and plugging as it might be the case when processing waste biomasses [42]. After successful process assessment with EtOH further investigation and development is required for processing waste biomasses.

4.2 Materials and Methods - Scale-up of the proposed process and techno-economic analysis

This part describes the scale-up process corresponding to the previously described lab-scale plant and the methodology followed for the techno-economic analysis. The chemical plant is assumed to be constructed in Germany. Figure 4.1 illustrates a simplified process flow diagram with the main process units and Figure 4.2 the detailed one. Figure S7 in SM presents the process flow diagram as depicted in the Aspen HYSYS software. Table S3 in SM contains the mass balances, the properties and molar compositions of all the streams from the simulated process in Aspen HYSYS.

The feed to the system is a water-EtOH solution that is pumped to 250 bar (P-1) and pre-heated to 320 °C (stream 6) prior to SCWG via four heat exchangers. EtOH has been used in both cases (experiments and process scale-up) as a biomass model compound establishing a preliminary base case. Gasification takes place at 250 bar and 600 °C. The required heat for the SCWG reactor is provided by electricity [219].

The product gas, together with the remaining steam (stream 7), is expanded in a turbine (EXP-1) to an outlet pressure of 30 bar (stream 8). Stream 8 is pre-heated (HE-1) before entering the steam-methane reforming (SMR) reactor. The outlet of the SMR reactor (stream 10) has a temperature of 804 °C and a pressure of 30 bar, providing heat to the inlet of SMR (stream 8) (HE-1).

The product from the SMR is further cooled by heating the feed to the SCWG in HE-2 and HE-3. Afterward, the cooled SMR product is inserted into the WGS adiabatic reactor at around 225 °C. The WGS outlet stream has a temperature increase to approximately 254 °C due to the exothermic WGS reaction.

The product from the WGS reactor is further cooled in HE-4 and HE-6 with the EtOH feed and in HE-5 and HE-7 with water. The heat exchange in HE-5 (heat transferred from stream 15 to W-5) generates low-pressure steam (4.5 bar) that can be sold to nearby industrial facilities [220]. The HE-7 utilizes water (W-2) to cool the WGS product down to 30 °C (stream 18). Afterward, the product gas is separated from condensed water in the gas-liquid separator FL-1. It consists primarily of H_2, CO_2, and traces of CH_4 and CO (stream 19). For the purification of H_2, a Pressure Swing Adsorption (PSA) unit is implemented.

This unit consists of adsorbers filled with zeolite 5A and generates an H_2-rich gas with 99.99% purity and 85% recovery [221]. The recovered water from the product contains a part of the produced CO_2, and it is degassed after pressure reduction close to atmospheric (FL-2), and the released CO_2 is driven to the final CO_2-rich side product (the stream leaving FL-3). Then, the water can be recycled and re-introduced to the feed.

The tail-gas from the PSA unit (stream 20) contains almost all of the CO_2, unreacted CH_4, CO, and part of the produced H_2. It is driven to the SMR oven for oxyfuel combustion to provide the heat required for the SMR reaction system. The oxyfuel combustion is carried out with O_2 separated from N_2 in a PSA unit. There, the air is slightly pressurized by a compressor (COMP) and driven to the PSA unit, where O_2 is recovered at a rate of 53% with a purity of 90%, utilizing a zeolite [222]. The oxyfuel combustion of the tail-gas results in a dry gas consisting primarily of CO_2 (>90 vol.%) that can also be sold. A series of heat exchangers reduce the temperature of the off-gas to 40 °C. From the off-gas cooling, high (25 bar) and low-pressure steam (4.5 bar) is generated and sold too. Water is separated from the CO_2 in FL-3 and mixed with the water from the stream W-9. The temperature of this stream is close to 42 °C, and an air-cooled heat exchanger is utilized (AC) to cool it down to 20 °C. Afterward, the cooled water is re-introduced to the system by a pump (P-2).

The scale-up process was simulated with Aspen HYSYS V14. The selected fluid property package was the PRSV, which employs the Peng-Robinson equation of state. A Gibbs reactor was used to simulate the SCWG reaction system by minimizing the Gibb's free energy of the system [223], which is an adequate approach for this application, as Dutzi et al. [47] demonstrated. They reported complete gasification of EtOH with a concentration ranging from 1.2 – 72 wt.%, under 650 °C and 280 bar. The product gas composition was in close agreement with the results from thermodynamic equilibrium when the same process was also simulated with a Gibbs reactor in Aspen HYSYS. The minimum Weight Hourly Space Velocity (WHSV) was 1715 $g_{feed}\ l_{reactor}^{-1}\ h^{-1}$. This value is applied here to design the SCWG reactor, ensuring that the selection of the Gibbs reactor generates satisfactory results in terms of complete carbon gasification efficiency and equilibrium approach.

A kinetic model was developed to simulate the SMR reactor based on the experimental data presented in Chapter 2 of this thesis. However, the detailed methodology and results of the kinetic modeling are not included in this thesis but can be found in the corresponding publication [224]. For accurate simulation of the SMR reactor, a Plug Flow reactor (PFR) is used in Aspen HYSYS. This unit requires all input related to the kinetic model that was developed. The reactor is considered to be of the multi-tubular type, with the tubes located inside a furnace. The detailed data for the design of the PFR is given in SM (see S2.3). The furnace (or fired heater) is simulated as a conversion reactor considering the combustion reactions of H_2, CH_4, and C_2H_6. More details regarding the design of this unit can be found in SM (see S2.3). An equilibrium reactor was used to model the WGS reactor, considering only the WGS reaction (see S2.3 in SM).

The heat exchangers (HE-1 up to HE-8) were modelled with the Rigorous Shell & Tube model provided by Aspen HYSYS. The gas-liquid separators and the PSA units were designed based on the book by Towler and Sinnott [225]. The specific methodology for both units can be found in SM (S2.3).

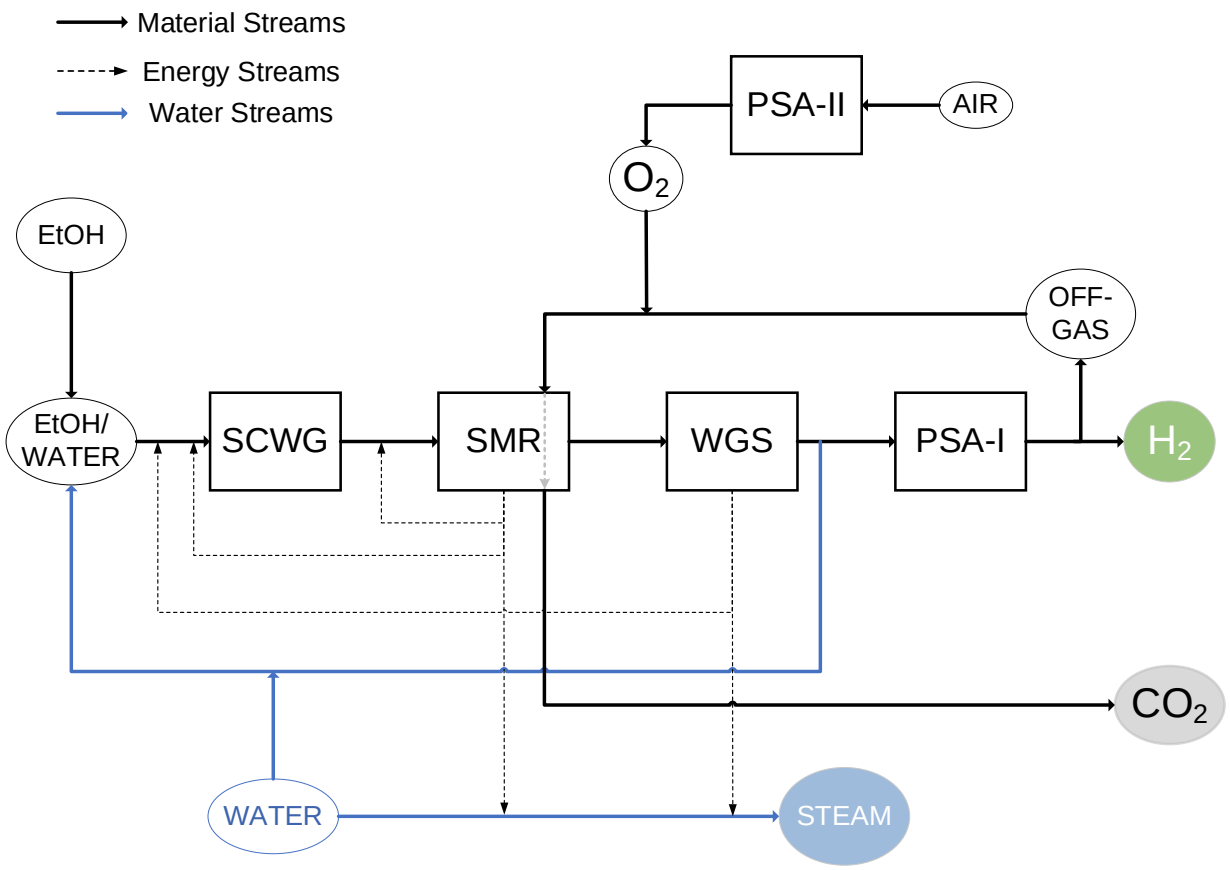

Figure 4.1 Simplified process flow diagram (PFD) of the scale-up process.

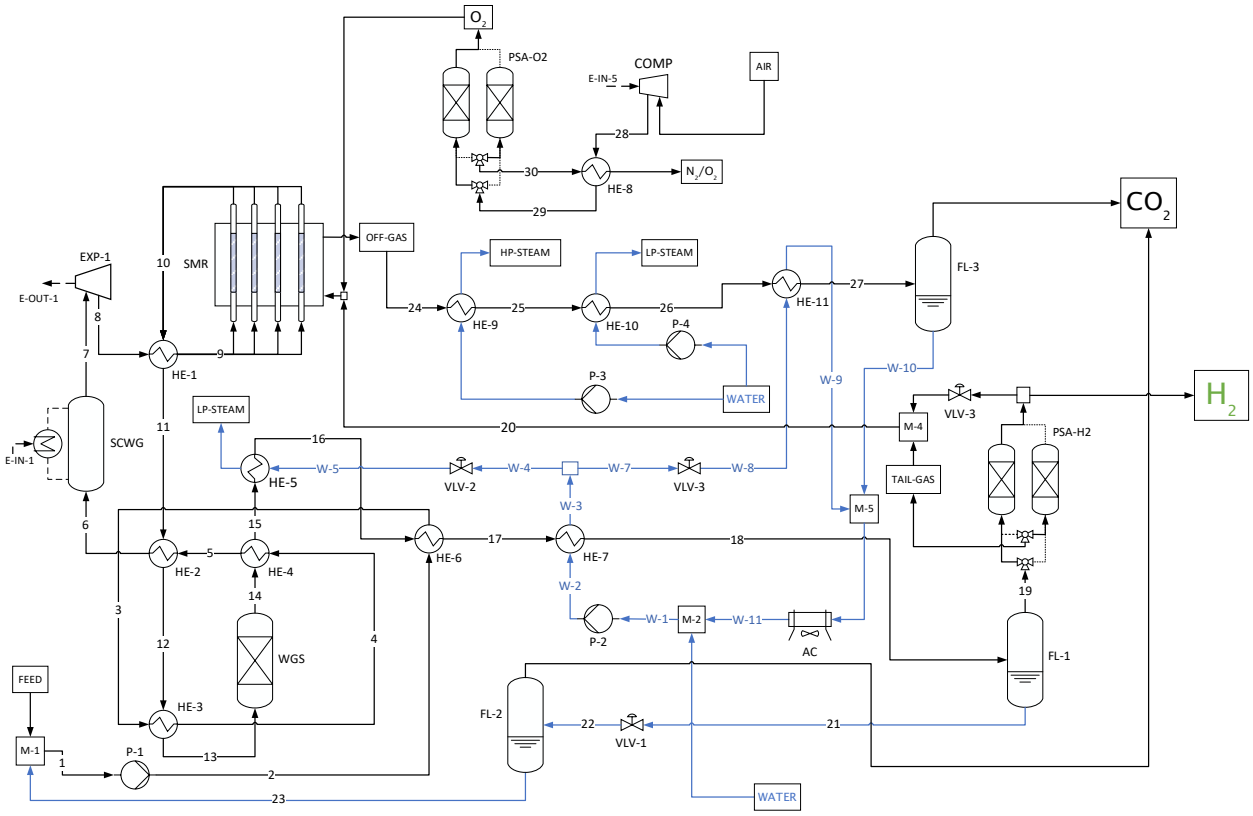

Figure 4.2 Process Flow Diagram of the scale-up process. The blue arrows indicate the water streams.

An exergy analysis was conducted by determining the exergy efficiency (n_{Ex}, Eq. 4.1) [226,227]:

$$n_{Ex} = \frac{\dot{m}_{H_2} \cdot e_{H_2} + \dot{m}_{CO_2} \cdot e_{CO_2} + \dot{m}_{steam} \cdot e_{steam}}{\dot{m}_{FEED} \cdot e_{FEED} + P_{electric} + E_Q} \tag{4.1}$$

where $\dot{m}_i$ is the mass flow rate of stream *i*, e_i is the specific exergy of the stream *i*, $P_{electric}$ is the total electric power required by the process operations, and E_Q is the total exergy input for heating purposes. The total exergy loss was calculated as the difference between the inlet exergy streams in the process and the outlet streams [226]. No distinction is made between exergy destruction and exergy loss [226,227]. The specific exergy of a stream (e_i) is calculated as the sum of its physical exergy and its chemical exergy, with the latter being equal to the higher heating value of a material stream (HHV_i, Eq. 4.2) [226]:

$$e_i = \left[e_{i,physical}\right] + e_{i,chemical} = [H_i - S_i \cdot T_0 - H_i^0 + S_i^0 \cdot T_0] + HHV_i \tag{4.2}$$

where H_i and S_i are the enthalpy and entropy, respectively, at the actual conditions, H_i^0 and S_i^0 are the enthalpy and entropy at reference conditions (298.15 K and 1 bar), and T_0 is the reference temperature. The physical exergy can be obtained from Aspen HYSYS. The reference conditions were 298.15 K and 1 bar. Table S4 in SM enlists the exergy flows of all process streams.

The costs of the equipment (C_j) were calculated from reference equipment costs [228], considering equipment scaling factors (M) and the effect of inflation on the prices of the equipment based on the Chemical Engineering Plant Cost Indexes ($CEPCI$), via the following equation (Eq. 4.3) [227]:

$$C_j = C_{j,ref} \cdot \left(\frac{Q_j}{Q_{j,ref}}\right)^M \cdot \left(\frac{CEPCI_{2023}}{CEPCI_{ref}}\right) \quad (4.3)$$

where, Q_j and $Q_{j,ref}$ are the characteristic capacities and M is the equipment scaling factor [228]. The prices of the equipment were corrected to 2023 with the corresponding value of $CEPCI$ for May 2023, which is 808.8 [229]. The values of $CEPCI_{ref}$ varied according to the available source of reference equipment.

The total cost of the main equipment (C_{total}), multiplied by the Lang Factor (F_L), corresponds to the fixed capital investment (CI_{fixed}, Eq. 4.4):

$$CI_{fixed} = F_L \cdot C_{total} \quad (4.4)$$

where C_{total} accounts for the sum of all main equipment costs:

$$C_{total} = \sum C_j \quad (4.5)$$

The Lang factor is frequently used to obtain order-of-magnitude cost estimates and takes into account the direct and indirect costs related to the construction of the plant, based on the equipment costs [228]. The Lang factor was estimated to be 4.86, according to Albrecht et al. [230]. Table S8 in SM contains all the different cost types that contributed to the CI_{fixed}. The total capital investment ($CAPEX$) was calculated by the following equation (Eq. 4.6) [227]:

$$CAPEX = CI_{fixed} + C_{working} \quad (4.6)$$

where $C_{working}$ stands for the working capital. According to Peters et al. [228] the $C_{working}$ lies between 10% - 20% of *CAPEX*. In this work, a value of 15% of the *CAPEX* was selected.

The annual capital costs (C_a) can be given as a function of the CI_{fixed} and $C_{working}$, based on the annuity method [227]:

$$C_a = \frac{CI_{fixed} \cdot r \cdot (1+r)^{t_P}}{(1+r)^{t_P} - 1} + r \cdot C_{working} \quad (4.7)$$

where r is the annual interest rate, assumed equal to 10%, and t_P is the operating lifetime of the plant which was considered to be 20 years [231]. No salvage value was considered.

The direct and indirect operating expenses ($OPEX_{dir}$ and $OPEX_{ind}$, respectively) were also estimated. The $OPEX_{dir}$ correspond to the costs of EtOH, cooling and clean water, electricity, catalysts for SMR and WGS, and adsorbents for the PSA units. Table 4.1 presents the unit costs of all the aforementioned utilities and the prices of the products to be sold, i.e., low pressure and high pressure steam and CO_2. The $OPEX_{ind}$ consist of costs associated with operating labor, operating supervision, maintenance labor, maintenance materials, operating supplies, laboratory expenses, insurance, taxes, plant overhead, administrative costs, distribution and selling, research and development. The methodology of calculating them was taken from Albrecht et al. [230].

Table 4.1 Unit costs of purchased utilities and of products for sale.

Utility	Unit cost	Ref.
Unit costs of utilities constituting the $OPEX_{dir}$		
EtOH	0.56 \$ L^{-1}	232
Cooling water	0.0013125 \$ m^{-3}	230
Clean water	2.1 \$ m^{-3}	230
Electricity	0.0945 \$ kWh^{-1}	230
SMR catalyst	29.7 \$ kg^{-1}	233
WGS catalyst	19 \$ kg^{-1}	227

Adsorbent (PSA-H_2)	2.0 \$ kg^{-1}	231
Adsorbent (PSA-O_2*[1])	2.0 \$ kg^{-1}	231
Unit costs of products to be sold		
Low-pressure steam (4 bar)	27.0 \$ t^{-1}	230
High-pressure steam (25 bar)	27.6 \$ t^{-1}	230
CO_2	46.5 \$ t^{-1}	227

*[1]No price for adsorbents in the PSA-O_2 was found in the literature, thus it was assumed that the price for a PSA-O_2 adsorbent is same with that of the adsorbent in the PSA-H_2 unit.

The operating labor costs (C_{OL}) were calculated according to the following equation:

$$C_{OL} = Wage_{OP} \cdot N_{OP} \tag{4.8}$$

where the $Wage_{OP}$ is the wage of every operator, equal to 72.000 € a^{-1} [227] (or 75.600 $\$_{2023}$ a^{-1}), and N_{OP} is the total number of operators calculated by equation 4.9[227,234]:

$$N_{OP} = F_{OP} \cdot \left[\left(6.29 + 0.23 \cdot N_{np}\right)^{0.5}\right] \tag{4.9}$$

Where N_{np} is the number of non-particulate processing units in the scaled-up plant, and F_{OP} the number of operators to cover every position in the plant at any time, which was estimated to be 4.5. A description on how C_{OL} is estimated at different plant capacities, is given in SM (S2.4). As the plant scales up, labor costs increase. Peters and Timmerhaus provide in their book [228] a diagram through which one can estimate the operating labor requirements when the capacity of the chemical plant increases.

The net production costs (NPC) can be estimated in $\$ \cdot a^{-1}$ (Eq. 4.10). The break-even price of H_2 is also calculated, taking into account the sale of CO_2 and steam of low and high pressure (LP and HP, respectively) as follows (Eq. 4.11):

$$NPC(\$ \cdot a^{-1}) = C_a + OPEX_{dir} + OPEX_{ind} \tag{4.10}$$

$$P_{BE}\left(\$ \cdot kg_{H_2}^{-1}\right) = \frac{NPC - \left(\dot{m}_{CO_2} \cdot C_{CO_2} - \dot{m}_{steam_{LP}} \cdot C_{steam_{LP}} - \dot{m}_{steam_{HP}} \cdot C_{steam_{HP}}\right)}{\dot{m}_{H_2}} \tag{4.11}$$

All assumptions applied for the economic analysis are given in Table 4.2.

Table 4.2 Assumptions used for the economic analysis.

Assumption number	Parameter	Value
1	Working capital ($C_{working}$)	15% of *CAPEX*
2	Annual interest rate (r)	10%
3	Operating lifetime of the plant (t_P)	20 years
4	Hours of operations in a year	8000 h a^{-1}
5	Average labor costs	75,600 \$ a^{-1}
6	Number of non-particulate processing units in the chemical plant (N_{OP})	3
7	Number of operators to cover every position in the plant at any time (F_{OP})	4.5

4.3 Results and Discussion

4.3.1 Exergy analysis

For the exergy analysis, the case with 15 wt.% ethanol in the feed and a feed flow rate of 10 t h^{-1} was considered. Figure 4.3 shows the overall exergy balance. The total exergy input was 16.28 MW, with the process feed and the electric power input contributing 76.18% and 23.65% of it, respectively. Hydrogen accounted for the largest portion of the exergy output, representing 59.09% of the exergy input. The exergy efficiency, calculated using equation 4.1, was estimated to be 67.8%.

The total exergy destruction was 5.23 MW. The SCWG reactor accounted for the largest share of the total exergy destruction, at 32.13%, primarily due to the significant amount of electricity required for heating. The heat exchangers followed, contributing 30.98% to the total exergy destruction. These heat exchangers were used to preheat the feeds to the SCWG and SR reactors by cooling their product streams, cool the final H_2-rich product, and cool the off-gas from the fired heater in the steam reformer. The latter two tasks involved generating low- and high-pressure steam across large temperature differences.

The steam reformer was the third largest contributor to exergy destruction, at 26.27%, due to the combustion of some of the produced hydrogen and unreacted hydrocarbons to provide heat for the SR reactions, resulting in the production of CO_2, H_2O, and thermal energy. The remaining exergy losses were attributed to other process units, such as the WGS reactor, the PSA units, the expander, and the air compressor.

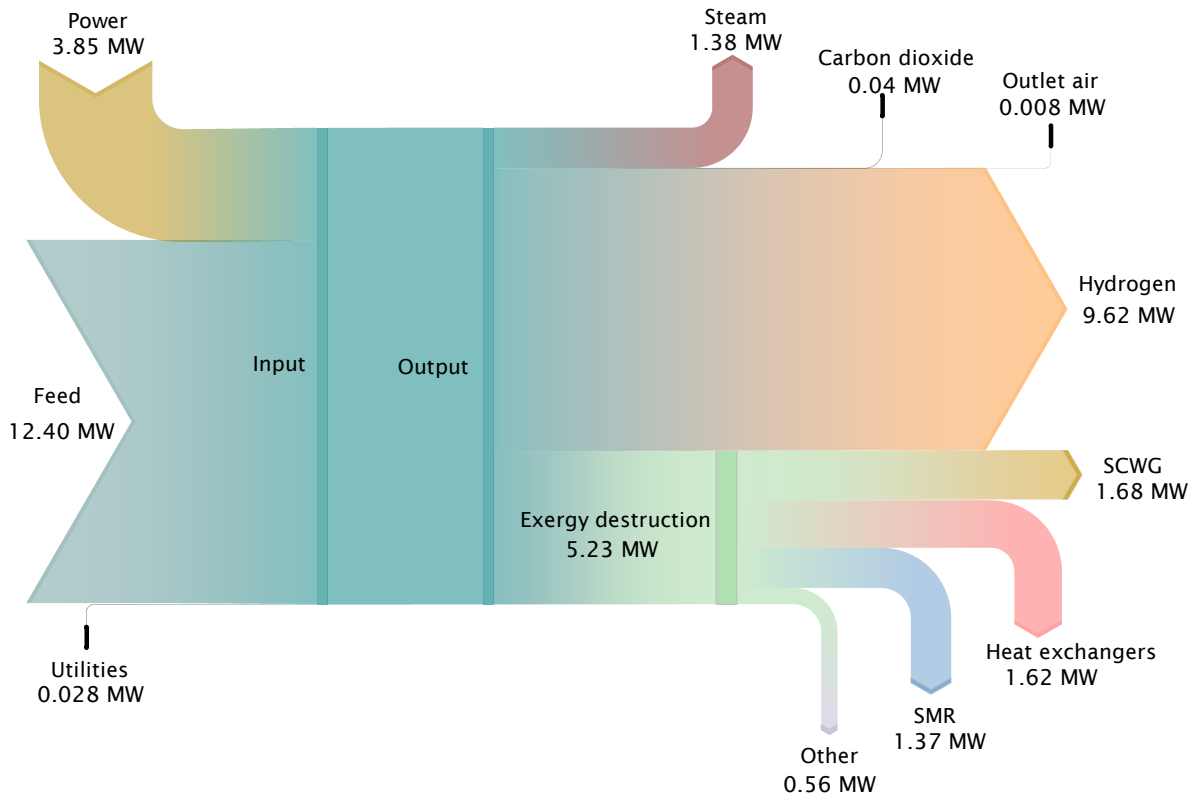

Figure 4.3 Exergy balances for the case of 15 wt.% EtOH with a feed flow rate of 10 t h^{-1}.

4.3.2 Effect of EtOH concentration on the break-even price of H_2

Chapter S2.1 in SM provides the mass balances and the molar composition of all the streams used in the simulation, for the case of 15 wt.% EtOH and 10 t h^{-1}. The equipment costs for this case are given in S2.4, together with the total equipment costs for different EtOH concentrations (Table S6) and different feed flow rates (S7). Section S8 also enlists the capital investments for every different simulated case.

Figure 4.4 shows the break-even price of produced hydrogen, the ratios of NPC and H_2 production to their value for 8 wt.% EtOH as a function of the feed concentration. A significant decrease in the P_{BE} is found from 8 wt.% to 18.5 wt.% of EtOH concentration. More specifically, the P_{BE} for 8 wt.% EtOH accounts for 40.1 \$ kg_{H2}^{-1}, whereas at 18.5 wt.% EtOH, the P_{BE} drops to 18.9 \$ kg_{H2}^{-1}. A further increase in the EtOH concentration leads to slighter drop in the P_{BE}, e.g., for 20 wt.% EtOH, the P_{BE} was calculated to be equal

to 17.9 \$ kg_{H2}^{-1}. Both H_2 production and NPC rates increase linearly with EtOH concentration, but that of H_2 is significantly greater than that of NPC. Considering therefore the equation 4.11 of P_{BE} and that the contributions of the LP-steam, HP-steam, and carbon dioxide terms are small, the drop in the hydrogen value with ethanol concentration is justified by the curve in Figure 4.4. The feed concentration of the organics thus, plays a crucial role in the profitability of this process. Al-Mosuli et al. [235] designed and simulated a SCWG plant for the gasification of 15 wt.% and 25 wt.% glucose, and 15 wt.% sewage sludge with a feed flow rate of 30 t h^{-1}. They estimated that their process became profitable, in terms of annual net income, when hydrogen had a minimum selling price of around 4 \$ kg_{H2}^{-1} for 25 wt.% glucose and 5 \$ kg_{H2}^{-1} for 15 wt.% glucose, respectively.

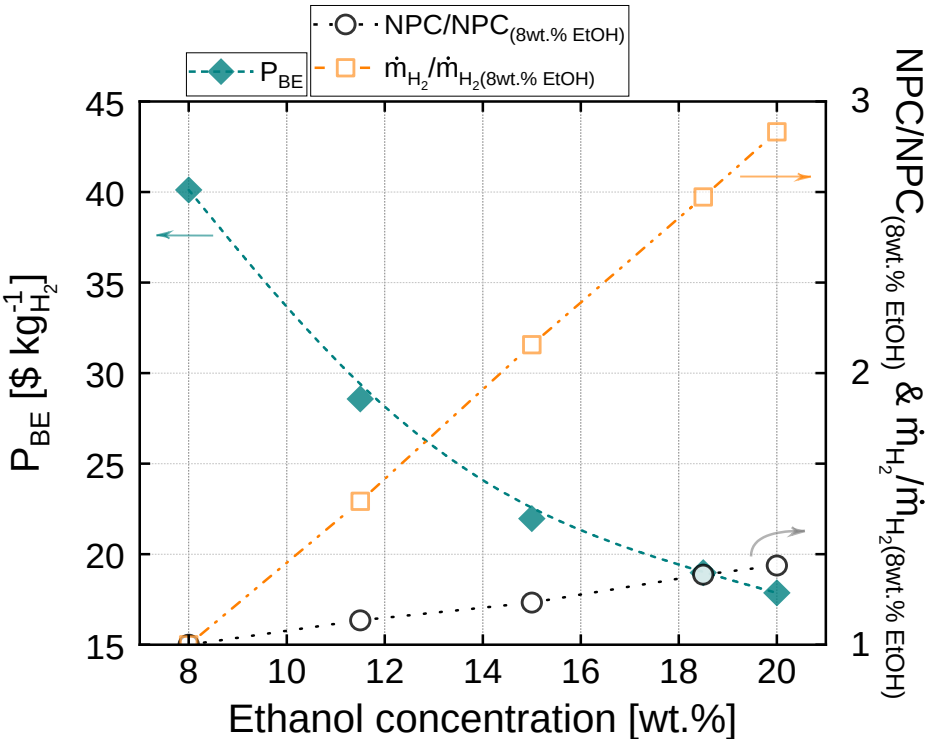

Figure 4.4 Break-even price of hydrogen with EtOH concentration in the feed. The feed flow rate is 1 t h^{-1}.

Higher biomass concentrations can lead to technical bottlenecks in the operation of continuous processes. The carbon gasification yield decreases with increasing biomass concentration, leaving more carbonaceous products as side products in the liquid effluent (tar and char) or as solid deposits [7,42,109]. A high concentration of such organic by-products in the liquid effluent or as precipitating solids can cause clogging [236] and also can poison

the downstream SMR catalyst [114]. Boukis and Stoll [109] argued that a positive energy balance (energy of the product being higher than the power and the utilities that are consumed) and relatively high yield of product gas can be generated when the feed concentration lies between 8 and 12 wt.% of dry matter. Previous experiments from the same group [109] with corn silage at 700 °C and 250 bar had shown that an increase in the biomass concentration from 5 to 19 wt.% leads to a reduction in the carbon gasification yield from almost 100% to 80%, respectively, and a rise in the total carbon content in the effluent from around 750 ppm, at 5 wt.%, to approx. 2600 ppm at 20 wt.%. Given this technical limitation faced by the SCWG of real biomass types, and considering the results of the Figure 4.4, the EtOH concentration chosen for further study was 15 wt.%.

4.3.3 Effect of feed flow rate on the break-even price of H_2

The effect of the feed flow rate on the H_2 break-even price is shown in Figure 4.5.a. A steep decline in the P_{BE} can be seen from 22.0 \$ kg_{H2}^{-1}, at 1 t h^{-1}, to 9.0 \$ kg_{H2}^{-1}, at 10 t h^{-1}. A further increase to 50 t h^{-1} results in a slighter drop in the P_{BE} price to 6.8 \$ kg_{H2}^{-1}. A further increase in the feed flow rate does not significantly improve P_{BE}, leading to a final price of 6 \$ kg_{H2}^{-1} at 160 t h^{-1}. Figure 4.5.b compares the NPC and their constituents for different feed flow rates. The NPC at 160 t h^{-1} are 51 times higher than the NPC at 1 t h^{-1}. What also stands out is the high increase rate of the $OPEX_{dir}$ with feed flow rate, compared to the C_a and $OPEX_{ind}$. Despite the large increase in production costs, the price of hydrogen tends to reach a stable price in the range studied, consistent with the economies of scale [237].

These results are similar to those of Kumar et al. [237], who found that a higher feed flow rate than 83.3 t h^{-1} in a SCWG process of microalgae would not yield further decrease in the price of H_2, which at that point was around 4.6 \$ kg_{H2}^{-1}. The latter price from Kumar et al. [237] at 83.3 t h^{-1} is lower than even the P_{BE} price of this study at 160 t h^{-1}. This difference is attributed to the high price of EtOH that was used here, i.e., 707 \$ t_{EtOH}^{-1}, compared to the price of the algal biomass from Kumar et al. [237], i.e., 392 \$ t^{-1} of dry biomass. Campanario and Gutierrez Ortiz [238] studied the effect of plant capacity from 20 t h^{-1} to 200 t h^{-1} in the process of bio-oil aqueous phase SCWG coupled with WGS, dry reforming and Fischer-Tropsch (FT) synthesis. The selling prices of the FT-biofuels had been halved

from 20 t h^{-1} to around 90 t h^{-1}, e.g., the price of gasoline decreased from 2.1 \$ kg^{-1} to around 1.1 \$ kg^{-1}. After this range, the decrease was less significant.

As can be seen from Figure 4.6, EtOH costs are the most significant contributor to $OPEX_{dir}$, followed by electricity. It is also apparent from the same Figure that the distribution of costs remains almost the same with increase in feed flow rate.

Based on Figure 4.5.a, a feed flow rate of 50 t h^{-1} can be sufficient to improve the profitability of this process, as described above. Above this scale, the availability of different feedstocks should be considered to determine a suitable plant size. For example, Campanario and Gutierrez Ortiz [238] proposed a theoretical optimum plant capacity for the processing of bio-oil aqueous phase in SCWG to be around 200 t h^{-1}, after which the reduction in production costs is negligible in their proposed process chain. However, they argued that a more realistic capacity should aim at 100 t h^{-1} due to feedstock availability. One relevant feedstock for the proposed process in this article is sewage sludge, as it is a wet feedstock that does not need to be dried in SCWG and thus can be energetically utilized very efficiently [66,109,213,239,240]. According to Mosuli et al. [235], a sewage sludge flow rate of 30 t h^{-1} with 15 wt.% dry biomass corresponds to the disposal capacity of a city with around 1.3 million citizens. Similarly, a flow rate of 50 t h^{-1} would correspond to a city of 2.16 million citizens. As an example, this roughly corresponds to the number of citizens of Hamburg, Germany [241]. As this is the second largest city in Germany, a capacity higher than 50 t h^{-1} of sewage sludge would not be meaningful in this country. Another suitable feedstock is glycerol, which can be easily gasified and is a cheap educt [242–245]. According to Attarbachi et al. [246], the supply of glycerol will exceed demand by about 2.33 million tons by 2025. Assuming that the proposed process uses 15 wt.% glycerol with a capacity in the range of 10 to 50 t h^{-1} of total feed flow rate, it will process about 0.5 to 2.6 percent of the world's total glycerol surplus by 2025. Therefore, for the proposed process, a maximal capacity of 50 t h^{-1} should be reached in order to increase sufficiently its profitability.

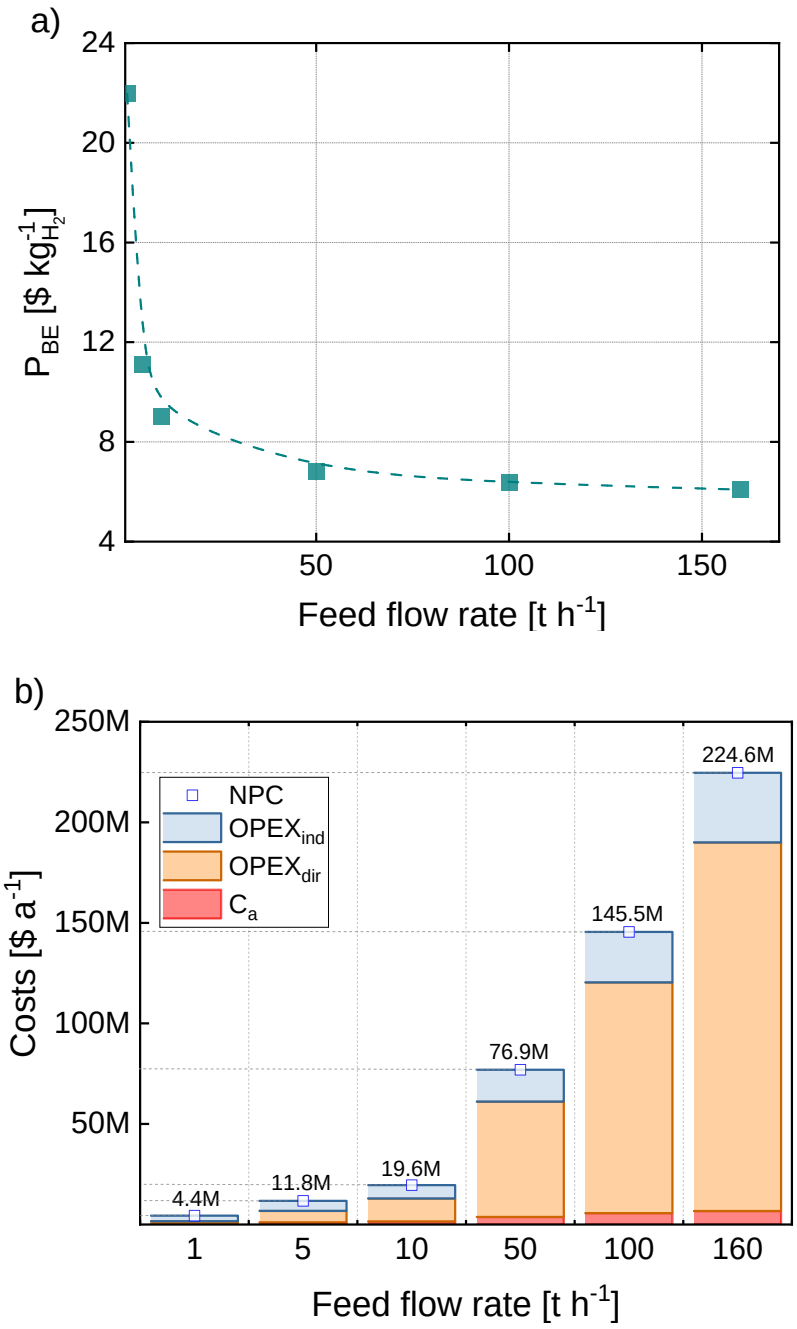

Figure 4.5 a) Break-even price of hydrogen with varying feed flow rate, b) NPC in $ a^{-1} and its components with feed flow rate. The concentration of EtOH in the feed is 15 wt.%.

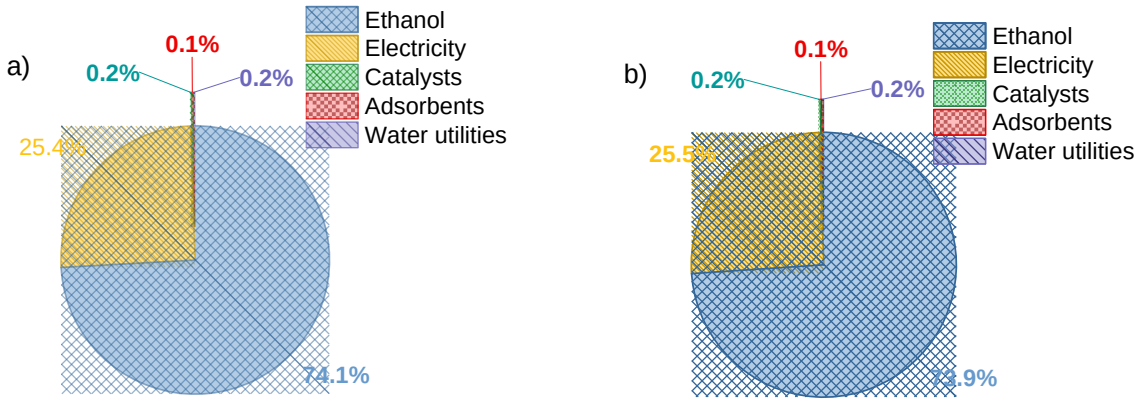

Figure 4.6 Component cost allocation of operating expenditures ($OPEX_{dir}$) for the case of 15 wt.% EtOH with a) 10 t h^{-1} and b) 50 t h^{-1}.

4.3.4 Sensitivity Analysis

A sensitivity analysis of specific parameters that affect the P_{BE} was carried out. The analysis was based on a feed flow rate of 10 t h^{-1}. The investigated parameters were the unit prices of EtOH, electricity, and clean water, the total purchase cost of equipment, and the operating labor costs. Each parameter varied from their reference value by ± 50%, while the others remained constant. The results are summarized in Figure 4.7. The price of EtOH seems to have the most significant effect on the P_{BE}, with a ± 50% change in its value resulting in a 27.6% variation in P_{BE} (i.e., 6.5 – 11.5 \$ kg_{H2}^{-1}). Kumar et al. [237] found that a 20% variation in the cost of algae leads to a change slightly higher than 20% in the hydrogen price. Galera et al. [242] varied the price of glycerol up to 50% in an SCWG process with a 1 t h^{-1} glycerol flow rate with around 26.5% concentration, coming up with a hydrogen selling price variation of around 17%. Gasafi et al. [240], who studied the SCWG of sewage sludge with 5 t h^{-1}, assuming a negative unit feedstock cost, estimated that an increase of 50% in sludge revenue would reduce hydrogen production costs by 72%.

Following the effect of EtOH price, the operating labor brings about a variation in P_{BE} of 11.9%. The equipment costs and the price of electricity cause a roughly similar change in the price of hydrogen, i.e., 8.3% and 9.5%, respectively. The price of clean water had a negligible impact on the break-even price of H_2. These results suggest a significant reduction in the break-even price of hydrogen can be achieved by reducing the price of

ethanol. Since ethanol was used as the biomass model in this study, it is reasonable to examine the effect of its price on P_{BE} in more detail, thus representing different biomass types.

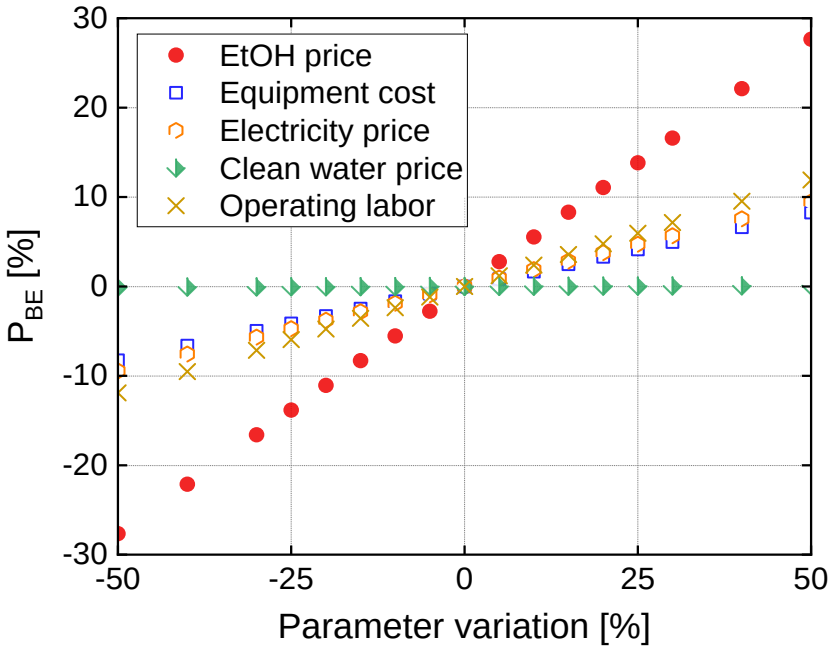

Figure 4.7 Effect of the percentage changes in the price of various parameters on P_{BE}, for the case of 15 wt.% EtOH with 10 t h^{-1} feed flow rate.

4.3.4 Effect of the EtOH price on the break-even price of H_2

The last chapter of the techno-economic analysis focuses on the effect of the EtOH price on the hydrogen break-even price. For this purpose, the two case studies, which represent the technically feasible operation range in feed flow rate, i.e., 10 - 50 t h^{-1}, were regarded. In both cases, the price of EtOH varied from -0.2 \$ l^{-1} up to 1 \$ l^{-1}, and the P_{BE} was calculated. The concentration of EtOH was 15 wt.%. The results were compared with the average prices of hydrogen produced by electrolysis (7.8 \$ kg_{H2}^{-1}), SMR (1.3 \$ kg_{H2}^{-1}), and SMR with carbon capture (SMR+CC, 1.9 \$ kg_{H2}^{-1}) in Germany between 2020 and 2022. The prices of H_2 from the different technologies are taken from George et al. [247], who investigated thoroughly the impact of state-induced price components on the levelized costs of green, blue, and grey hydrogen in Germany up to 2050. The average electricity price for large industrial consumers in the German market varied in the range

of 73.5 – 78.7 $ MWh^{-1} [247]. The H_2 selling prices that are used from their study are the ones where no excise tax and price for CO_2 emissions for SMR and SMR+CC are considered. The results are depicted in Figure 4.8.

The lowest price of EtOH, which is -0.2 $ l^{-1}, generates the lowest P_{BE} of 2.2 $ kg_{H2}^{-1} and 0 $ kg_{H2}^{-1} for 10 t h^{-1} and 50 t h^{-1}, respectively. The base case was 0.56 $ l^{-1}, accounting for 9.0 $ kg_{H2}^{-1} at 10 t h^{-1} and 6.8 $ kg_{H2}^{-1} at 50 t h^{-1}. To compete with electrolysis, prices lower than 0.4 $ l^{-1} are required for the SCWG of 10 t h^{-1}, whereas a price lower than 0.6 $ l^{-1} is needed for 50 t h^{-1}. Likewise, 50 t h^{-1} can generate hydrogen at the same price as SMR+CC when the feedstock price equals 0.01 $ l^{-1}. However, negative feedstock prices are needed to reach the value of SMR (i.e., lower than -0.06 $ l^{-1}). For 10 t h^{-1}, the lowest EtOH price is insufficient to compete with the price of hydrogen from SMR+CC. Therefore, for this technology to be competitive with the others, given that the capacity is in the range of 10 – 50 t h^{-1}, the price of the raw material must be reduced considerably. Fortunately, biomass offers this possibility.

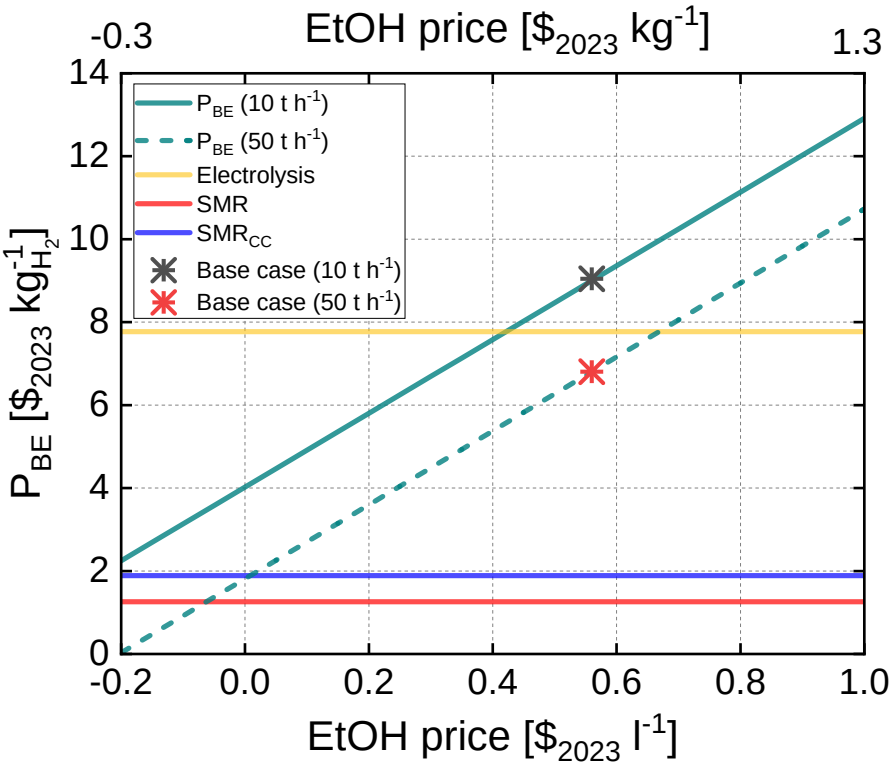

Figure 4.8 Break-even price of hydrogen as a function of the purchasing price of EtOH, for SCWG of 15 wt.% EtOH with 10 and 50 t h^{-1} feed flow rate. Prices of hydrogen from different production technologies are added from literature and are related to the average prices in Germany in the years 2020 - 2022 [247].

Alternative waste biomass resources that can be applied in SCWG include, but are not limited to, microalgae, glycerol, sewage sludge, phenol, sugarcane bagasse, and palm oil mill effluent [119,248,249]. If crude glycerol is used, for example, with a unit cost of 0.21 \$ kg^{-1} [246], this process will produce H_2 with a P_{BE} in the range 3.2 – 5.4 \$ kg_{H2}^{-1}, from 50 t h^{-1} to 10 t h^{-1}, respectively. Due to its excessive production compared to its demand, its price may fall further [242,246]. According to Thilakaratne et al. [250], algae costs can vary from 0.35 to 7.32 \$ kg^{-1}, depending on their geographic location, strain's properties, extraction and cultivation methods. If algae were used, a minimum price in the range of 4.0 – 6.2 \$ kg_{H2}^{-1} (for 50 and 10 t h^{-1}, respectively) would be possible. However, this technology can become extremely expensive if the highest unit price is considered. In the case of sewage sludge, there is a revenue associated with its collection and treatment. Gasafi et al. [240] used a revenue of around 0.26 \$ $kg_{dry\ matter}^{-1}$. By using this value as a negative feedstock price, the P_{BE} price falls in the aforementioned range of 0 – 2.2 \$ kg_{H2}^{-1} (for a feed flow rate in the specified range of 10 – 50 t h^{-1}). Even higher revenues for sewage sludge can be used, e.g., 0.481 \$ $kg_{dry\ matter}^{-1}$ [235]. Consequently, with appropriate incentives, sewage sludge gasification can be as competitive as steam reforming of natural gas.

The use of real biomass feedstocks is associated with certain technical challenges. Most of them contain inorganic salt building elements, which can lead to metals oxidation, clogging [42,109,246,251], and even deactivate the SMR catalyst [98]. The separation of salts can be achieved by specially designed arrangements of the SCWG reactor [42,43,251] or by a continuous treatment upstream of the SCWG reactor [237]. In particular, sewage sludge requires a feed conditioning process before gasification [237]. Gasafi et al. [240] estimated that the feeding equipment accounts for roughly 3.5% of the equipment purchasing costs. A decisive element in the design of this technology is the eventual presence of sulfur in the biomass, as the sulfur-containing species, especially the H_2S, can poison the SMR and WGS catalysts [223,252,253]. The adsorption of H_2S can be done in an adsorber filled with a ZnO-based adsorbent that can work under high temperatures (400 °C) [98,119]. These technical modifications lead to additional equipment purchasing costs that, in turn, increase production costs. In some cases, they even increase the $OPEX_{dir}$, e.g., for the case of H_2S adsorption. However, as the sensitivity analysis showed, a decrease in feedstock costs should most probably justify the additional investment costs, leading to

lower P_{BE}. Similarly, the increase in electricity and adsorbents demand is expected to be less significant than the decrease in feedstock costs.

4.3 Conclusions

The techno-economic analysis addressed a hydrogen production process by gasifying biomass model compounds with supercritical water and subsequent steam reforming of the gasification product. As already used in the experimental work, ethanol was used as a biomass model compound and its use accounts for a baseline case. The steam reformer uses the entire amount of water from the feedstock without intermediate separation. The energy needs of the steam reformer are met by the oxyfuel combustion of the residual gas and a small part of the produced hydrogen. Oxyfuel combustion is implemented using oxygen separated from air, so that carbon dioxide is produced at sufficiently high purity to be sold. In addition to hydrogen and carbon dioxide, high- and low-pressure steam is produced, which can serve as a sales product in adjacent chemical plants.

The economic analysis of the proposed process was based on the break-even price of the hydrogen produced. It was found that the price of hydrogen can be reduced significantly with increasing ethanol concentration, from 40.1 \$ kg_{H2}^{-1} for 8 wt.% EtOH to 17.9 \$ kg_{H2}^{-1} for 20 wt.% EtOH, at 1 t h^{-1} feed flow rate. In practice, however, technical constraints such as gasification efficiency do not allow very high concentrations of organics. Therefore, the concentration proposed for this chemical process is 15 wt.%. A further reduction in the hydrogen break-even price was achieved by increasing the feed flow rate. A sharp reduction was possible up to 50 t h^{-1}, with the hydrogen price falling to 6.8 \$ kg_{H2}^{-1}, but further capacity increases did not lead to significant differences. The latter results are consistent with the constraints imposed by biomass feedstock availability, making the upper feed rate limit 50 t h^{-1}.

A sensitivity analysis was performed and found that the most significant contributor to the break-even price of H_2 was the price of EtOH. The current price of ethanol does not accurately represent other waste biomass feedstocks with high water content; hence, other values were considered. The value of crude glycerol enabled the production of H_2 with a minimum break-even price of 3.2 \$ kg_{H2}^{-1}, at 50 t h^{-1} and 15 wt.% EtOH,

approximately 2.4 times lower than the current price of hydrogen produced by electrolysis in Germany. Using sewage sludge may result in the highest possible profitability due to the revenues associated with its treatment. A feedstock price in the range of -0.26 – 0 $ kg^{-1} leads to a break-even price between 0 $ kg_{H2}^{-1} and 1.8 $ kg_{H2}^{-1}, which falls to the same current price range with the conventional technologies, i.e., of natural gas steam reforming and steam reforming with carbon capture. These findings, however, rule out the specific technical modifications that must be integrated when dealing with actual waste biomass, e.g., feed conditioning and salt separation, which are expected to increase the final break-even price of H_2 somewhat.

Chapter 5. Concluding insights and future perspectives

5.1 Concluding Insights

The main objective of this thesis was to develop a process to upgrade the product gas from the supercritical water gasification (SCWG) of waste biomass, with the aim of maximizing pure hydrogen yield. For this purpose, a process was conceptualized, developed, and tested at a laboratory scale. This process combines the gasification of organics in supercritical water with the subsequent steam reforming of resulting hydrocarbons and involves four reactors connected in series:

1. **Gasification Reactor**: In this reactor, simple organics (e.g., ethanol) are gasified in supercritical water, with the potential addition of homogeneous potassium-based catalysts such as $KHCO_3$.
2. **Pre-Reformer**: Installed downstream of the gasification reactor, this reactor directly receives the gasification product gas and uses a heterogeneous Ni-based catalyst to reform hydrocarbons larger than methane into hydrogen and carbon oxides. This step ensures a cleaner feedstock for the main steam methane reformer by removing heavier hydrocarbons, thereby reducing the risk of coking on the catalyst in the steam methane reformer.
3. **Main Steam Methane Reformer**: Operating at higher temperatures but the same pressure as the pre-reformer, this reactor also contains Ni-based catalysts and is responsible for the complete reforming of methane.
4. **Water-Gas Shift Reactor**: This final reactor receives the fully reformed product gas and converts carbon monoxide to additional hydrogen and carbon dioxide, typically using a catalyst specific to the water-gas shift reaction.

The overall process yields a product gas composed of hydrogen and carbon dioxide, utilizing all hydrogen content from the organic feedstock and a portion of it from the added water. As this process had not been previously studied, it required detailed testing and feasibility analysis. Therefore, the experimental work was carried out in stages: first,

testing the initial two reactors, and then the three reactors in series. The fourth reactor has not yet been experimentally tested.

The first part of the experimental study examined the interaction between the first two reactors: the SCWG reactor and the pre-reformer. Ethanol was used as the feedstock in the SCWG reactor, and various temperatures, pressures, and space velocities were tested in the pre-reformer. Results showed that at the highest tested temperature in the pre-reformer, i.e., at 700 °C, H_2 concentration reached approximately 70 vol.%, with CH_4 conversion at 63.3%. The gas hourly space velocity in the pre-reformer significantly affected the final product gas composition; at the lowest GHSV of 14852 h^{-1} (and a temperature of 600 °C and a pressure of 1 atm) CH_4 conversion rose to 90.4%, H_2 concentration reached 73.4 vol.%, and the total hydrogen yield based on the ethanol fed into the system ($Y_{H_2,total}$) was approximately 98%.

This reaction system also impacted the catalyst structure, as the excess steam from the SCWG reactor effectively inhibited carbon formation, resulting in minimal coke deposition—a major advantage, given that excessive coke formation is often the primary cause of catalyst deactivation in conventional steam reforming. However, the high steam content did accelerate the sintering of Ni crystallites, leading to minor activity loss after 75 hours of operation. Overall, the study suggests that utilizing a pre-reformer at lower reforming temperatures (550–600 °C) and industrially relevant pressures (20–30 bar) offers an effective solution for producing an SCWG product gas free of heavier hydrocarbons. Using a pre-reformer upstream of the main steam reformer could also be extended to reform aromatics and tars, which are unreacted organic compounds formed when processing real waste biomass in the SCWG reactor, thereby efficiently protecting the catalyst in the steam methane reformer.

The incorporation of the main steam methane reformer involved a study of the effect of its operating parameters (T, p, and GHSV) and the EtOH concentration on the final product gas. Two commercial Ni-based catalysts were also tested for the SR of the SCWG product gas. High SR pressures, i.e., 20 – 40 bar, which are applied in industrial applications, required a temperature of at least 750 °C to achieve methane conversion higher than 90%. In this pressure range, a GHSV of 40000 – 50000 h^{-1} was required for the experimental value of methane conversion to reach close to its equilibrium one.

The concentration of EtOH had a profound effect on the SCWG-SR product gas. As it increased from 5 wt.% to 20 wt.%, the S/C ratio in the SCWG product gas dropped from 22.0 to 4.5. At the same time, the levels of CH_4, C_{2+} hydrocarbons, and CO in the SCWG product gas rose drastically as well. This change in the product gas shifted the equilibrium of the SMR and WGS reactions towards their reactants' side. As a result, the CH_4 conversion decreased from 97.5% to 22.5% and the H_2 yield from 98.6% to 58.3%. Despite the significant decrease in the S/C ratio and the increase in the carbonaceous species in the SCWG product gas, only a minor carbon formation was evident in both cases (5 wt.% and 20 wt.%). These findings are consistent with other studies indicating a critical S/C ratio, below which carbon formation becomes significant and may lead to catalyst deactivation. In these previous studies, the highest critical S/C ratio reported was 3.5. Processing ethanol at a 20 wt.% concentration, i.e., generating a SCWG product with an average S/C ratio of 4.5, appears to maintain an S/C ratio above this critical threshold, effectively mitigating carbon formation. Consequently, this process allows for the use of simple organics at a relatively high concentration (20 wt.%), which is often preferred as it enhances thermal efficiency and product yield. This, in turn, increases profitability (as will be discussed later) without significant risk of coking in the steam methane reformer.

Two different commercial catalysts were also tested in the steam methane reformer, a NiO(14wt.%)/$CaAl_{12}O_9$ and a NiO(18wt.%)/$CaK_2Al_{22}O_{34}$. At high SR pressures (30 – 40 bar), the NiO(18wt.%)/$CaK_2Al_{22}O_{34}$ catalyst showed higher activity, due to the higher Ni loading. The very low coke deposition over both catalysts revealed the resistance to coking mostly due to the excess steam. Owing to sintering, the Ni crystallite size of both catalysts increased remarkably. After 8 h of continuous operation, in the NiO(18wt.%)/$CaK_2Al_{22}O_{34}$ the increase was 65.4%, while in the NiO(14wt.%)/$CaAl_{12}O_9$ the increase in the Ni crystallites corresponded to 48.9%. This phenomenon can be attributed to the harsh reaction conditions, i.e., very high S/C ratios and high temperatures (700 – 800 °C), as well as to the structural properties of the catalysts, particularly the relatively weak interaction of Ni particles with the supports.

After the successful demonstration of the operation of the newly developed process in laboratory scale, the process was scaled up and a techno-economic analysis was carried

out to assess its potential profitability and its competitiveness against other technologies of hydrogen production.

It was found that the break-even price of the produced hydrogen, i.e., the price that compensates for the net production costs of building and operating the respective plant, was reduced from 40.1 \$ kg_{H2}^{-1} for 8 wt.% EtOH to 17.9 \$ kg_{H2}^{-1} for 20 wt.% EtOH, at 1 t h^{-1} feed flow rate. These results demonstrate the potential profitability of operating with high concentration of organics. The proposed concentration for this process is 15 wt.%, accounting for technical limitations that arise when processing highly concentrated organics in SCWG, such as reduced gasification efficiency, coking, and salt buildup that can lead to clogging.

Increasing the plant's capacity to 50 t h^{-1} remarkably reduced the price of the produced hydrogen to 6.8 \$ kg_{H2}^{-1}. Larger capacities did not lead to significant reductions in the price of hydrogen. Although EtOH was used as model compound, the final application regards real waste biomass. These resources impose availability limits, which in turn restrict plant capacity. For example, if sewage sludge is selected as the feedstock, a plant capacity of 50 t h^{-1} would roughly correspond to the disposal capacity of a city the size of Hamburg, Germany.

Applying negative feedstock prices in the calculations of the economic analysis, representing the revenue that comes with processing sewage sludge resulted in the highest possible profitability, with a hydrogen break-even price between 0 \$ kg_{H2}^{-1} and 1.8 \$ kg_{H2}^{-1}. This price range corresponds to the price range of hydrogen from natural gas steam reforming and steam reforming with carbon capture. However, processing actual waste biomass requires additional processing units, not only upstream of the SCWG reactor (feed pre-treatment and salts separation), but also downstream of it (removal of tars and aromatics, and desulfurization), that add to the production costs and thus, will somewhat increase the final hydrogen price. This fact should not be regarded as a significant limitation, since as it was evident from the sensitivity analysis, the main contributor to the hydrogen price is the feedstock price. Therefore, the anticipated decrease in feedstock price is expected to offset the increases in equipment purchase costs, as well as in direct and indirect operating expenses. Another important factor to consider is the potential future rise in the price of natural gas imported to Germany [254],

which would make conventional hydrogen production technologies more expensive, thereby increasing the competitiveness of the developed process.

5.2 Future perspectives

The experimental work on the developed process involves several steps yet to be carried out, aimed at demonstrating a fully feasible laboratory-scale process that efficiently converts real waste biomass feedstocks into hydrogen while ensuring long-term operational stability.

First, the fourth reactor, i.e., the WGS reactor, needs to be integrated. A catalyst has to be added in this reactor and tests with model compounds such as EtOH, have to be conducted. The focus here should be on optimizing operating conditions (pressure, temperature, and GHSV) to achieve complete conversion of CO into H_2 and CO_2. Subsequently, the EtOH concentration should also be varied with the WGS reactor in place.

A critical criterion is the stable operation of the process, including all reactors, over a period of several weeks, at least initially with biomass model compounds. To this end, the long-term stability of the most active catalyst in the steam methane reformer, i.e., the NiO(18wt.%)/$CaK_2Al_{22}O_{34}$, needs further investigation and comparison with the NiO(14wt.%)/$CaAl_{12}O_9$ and other suitable catalysts with strong resistance to active metal sintering. Implementing steam reforming catalysts that minimize sintering is essential to maintaining stable process operation. If no commercially available catalyst proves effective in preventing sintering in the reforming reactors, research can be extended to include the development and testing of new catalysts. Approaches may include using alternative supports with stronger interactions with the active metal or adding promoters, such as potassium, to enhance resistance to metal sintering [255].

Another objective for future experimental work is the use of real waste biomass, such as sewage sludge, algae, or crude glycerol. Addressing the challenges associated with SCWG of real waste biomass will be crucial. To avoid poor gasification efficiency, the

SCWG operating parameters, particularly residence time and organic concentration in the feed, must be carefully studied. Catalysts may also be used, either homogeneous ones like $KHCO_3$ or solid heterogeneous catalysts such as Ni-based catalysts. Additionally, inorganic compounds in the biomass will need to be effectively separated from the SCWG reaction mixture, possibly by installing a separator operating at the supercritical point of water upstream of the SCWG reactor [43]. The removal of sulfuric compounds after gasification must also be considered. For example, if sulfur is present as H_2S, an adsorption column packed with ZnO or other adsorbents would need to be installed and investigated downstream of the SCWG reactor and upstream of the pre-reformer.

For the scaled-up process and its techno-economic analysis, future studies should evaluate the process using real waste biomass and by implementing additional units for sulfur and salts removal, and the steam reforming of organics and tars, allowing thus, for a more accurate estimation of the hydrogen break-even price. Additionally, various configurations of energy-intensive units and heat exchangers should be explored to minimize the process's dependence on external energy sources.

References

(1) Masoudi Soltani, S.; Lahiri, A.; Bahzad, H.; Clough, P.; Gorbounov, M.; Yan, Y. Sorption-Enhanced Steam Methane Reforming for Combined CO2 Capture and Hydrogen Production: A State-of-the-Art Review. *Carbon Capture Science & Technology* **2021**, *1*. https://doi.org/10.1016/J.CCST.2021.100003.

(2) Erans, M.; Sanz-Pérez, E. S.; Hanak, D. P.; Clulow, Z.; Reiner, D. M.; Mutch, G. A. Direct Air Capture: Process Technology, Techno-Economic and Socio-Political Challenges. *Energy Environ Sci* **2022**, *15* (4), 1360–1405. https://doi.org/10.1039/D1EE03523A.

(3) Mohanty, U. S.; Ali, M.; Azhar, M. R.; Al-Yaseri, A.; Keshavarz, A.; Iglauer, S. Current Advances in Syngas (CO + H2) Production through Bi-Reforming of Methane Using Various Catalysts: A Review. *Int J Hydrogen Energy* **2021**, *46* (65), 32809–32845. https://doi.org/10.1016/j.ijhydene.2021.07.097.

(4) Pal, D. B.; Singh, A.; Bhatnagar, A. A Review on Biomass Based Hydrogen Production Technologies. *Int J Hydrogen Energy* **2022**, *47* (3), 1461–1480. https://doi.org/10.1016/J.IJHYDENE.2021.10.124.

(5) Arregi, A.; Amutio, M.; Lopez, G.; Bilbao, J.; Olazar, M. Evaluation of Thermochemical Routes for Hydrogen Production from Biomass: A Review. *Energy Convers Manag* **2018**, *165*, 696–719. https://doi.org/10.1016/j.enconman.2018.03.089.

(6) Holladay, J. D.; Hu, J.; King, D. L.; Wang, Y. An Overview of Hydrogen Production Technologies. *Catal Today* **2009**, *139* (4), 244–260. https://doi.org/10.1016/j.cattod.2008.08.039.

(7) Ferreira-Pinto, L.; Silva Parizi, M. P.; Carvalho de Araújo, P. C.; Zanette, A. F.; Cardozo-Filho, L. Experimental Basic Factors in the Production of H2 via Supercritical Water Gasification. *Int J Hydrogen Energy* **2019**, *44* (47), 25365–25383. https://doi.org/10.1016/j.ijhydene.2019.08.023.

(8) Ferreira-Pinto, L.; Silva Parizi, M. P.; Carvalho de Araújo, P. C.; Zanette, A. F.; Cardozo-Filho, L. Experimental Basic Factors in the Production of H2 via Supercritical Water Gasification. *Int J Hydrogen Energy* **2019**, *44* (47), 25365–25383. https://doi.org/10.1016/j.ijhydene.2019.08.023.

(9) Rodriguez Correa, C.; Kruse, A. Supercritical Water Gasification of Biomass for Hydrogen Production – Review. *Journal of Supercritical Fluids* **2018**, *133*, 573–590. https://doi.org/10.1016/j.supflu.2017.09.019.

(10) Lee, C. S.; Conradie, A. V.; Lester, E. Review of Supercritical Water Gasification with Lignocellulosic Real Biomass as the Feedstocks: Process Parameters, Biomass Composition, Catalyst Development, Reactor Design and Its Challenges. *Chemical Engineering Journal* **2021**, *415*, 128837. https://doi.org/10.1016/j.cej.2021.128837.

(11) Peterson, A. A.; Vogel, F.; Lachance, R. P.; Fröling, M.; Antal, M. J.; Tester, J. W. Thermochemical Biofuel Production in Hydrothermal Media: A Review of Sub- and Supercritical Water Technologies. *Energy Environ Sci* **2008**, *1* (1), 32–65. https://doi.org/10.1039/B810100K.

(12) Zhang, L.; Champagne, P.; Charles Xu, C. Supercritical Water Gasification of an Aqueous By-Product from Biomass Hydrothermal Liquefaction with Novel Ru Modified Ni Catalysts. *Bioresour Technol* **2011**, *102* (17), 8279–8287. https://doi.org/10.1016/j.biortech.2011.06.051.

(13) Sheikhdavoodi, M. J.; Almassi, M.; Ebrahimi-Nik, M.; Kruse, A.; Bahrami, H. Gasification of Sugarcane Bagasse in Supercritical Water; Evaluation of Alkali Catalysts for Maximum Hydrogen Production. *Journal of the Energy Institute* **2015**, *88* (4), 450–458. https://doi.org/10.1016/J.JOEI.2014.10.005.

(14) Shahbaz, M.; Al-Ansari, T.; Aslam, M.; Khan, Z.; Inayat, A.; Athar, M.; Naqvi, S. R.; Ahmed, M. A.; McKay, G. A State of the Art Review on Biomass Processing and Conversion Technologies to Produce Hydrogen and Its Recovery via Membrane Separation. *Int J Hydrogen Energy* **2020**, *45* (30), 15166–15195. https://doi.org/10.1016/J.IJHYDENE.2020.04.009.

(15) Matsumura, Y.; Minowa, T.; Potic, B.; Kersten, S. R. A.; Prins, W.; Van Swaaij, W. P. M.; Van De Beld, B.; Elliott, D. C.; Neuenschwander, G. G.; Kruse, A.; Antal, M. J. Biomass Gasification in Near- and Super-Critical Water: Status and Prospects. *Biomass Bioenergy* **2005**, *29* (4), 269–292. https://doi.org/10.1016/j.biombioe.2005.04.006.

(16) Elliott, D. C. Catalytic Hydrothermal Gasification of Biomass. *Biofuels, Bioproducts and Biorefining* **2008**, *2* (3), 254–265. https://doi.org/10.1002/bbb.74.

(17) Elliott, D. C.; Sealock, L. J.; Baker, E. Chemical Processing in High-Pressure Aqueous Environments. 3. Batch Reactor Process Development Experiments for Organics Destruction. *Ind Eng Chem Res* **1994**, *33* (3), 558–565. https://doi.org/10.1021/ie00027a012.

(18) Elliott, D. C.; Hart, T. R.; Neuenschwander, G. G.; Rotness, L. J.; Olarte, M. V.; Zacher, A. H. Chemical Processing in High-Pressure Aqueous Environments. 9. Process Development for Catalytic Gasification of Algae Feedstocks. *Ind Eng Chem Res* **2012**, *51* (33), 10768–10777. https://doi.org/10.1021/ie300933w.

(19) Waldner, M. H.; Krumeich, F.; Vogel, F. Synthetic Natural Gas by Hydrothermal Gasification of Biomass. Selection Procedure towards a Stable Catalyst and Its Sodium Sulfate Tolerance. *Journal of Supercritical Fluids* **2007**, *43* (1), 91–105. https://doi.org/10.1016/J.SUPFLU.2007.04.004.

(20) Sealock, L. J.; Elliott, D. C.; Butner, R. S.; Neuenschwander, G. G. Low-Temperature Conversion of High-Moisture Biomass: Topical Report January 1984-January 1988. *Pacific Northwest Laboratory: Richland, WA* **1988**.

(21) Elliott, D. C.; Hart, T. R.; Neuenschwander, G. G.; Rotness, L. J.; Olarte, M. V.; Zacher, A. H. Chemical Processing in High-Pressure Aqueous Environments. 9. Process Development for Catalytic Gasification of Algae Feedstocks. *Ind Eng Chem Res* **2012**, *51* (33), 10768–10777. https://doi.org/10.1021/ie300933w.

(22) Elliott, D. C.; Hart, T. R. *Low-Temperature Catalytic Gasification of Food Processing Wastes. 1995 Topical Report*; Richland, WA, 1996. https://doi.org/10.2172/379027.

(23) Elliott, D. C.; Neuenschwander, G. G.; Hart, T. R.; Scott Butner, R.; Zacher, A. H.; Engelhard, M. H.; Young, J. S.; Mccready, D. E. Chemical Processing in High-Pressure

Aqueous Environments. 7. Process Development for Catalytic Gasification of Wet Biomass Feedstocks. **2004**. https://doi.org/10.1021/ie034303o.

(24) Antal, M. J.; Allen, S. G.; Schulman, D.; Xu, X.; Divilio, R. J. Biomass Gasification in Supercritical Water. *Ind Eng Chem Res* **2000**, *39* (11), 4040–4053. https://doi.org/10.1021/ie0003436.

(25) Matsumura, Y.; Xu, X.; Antal, M. J. *GASIFICATION CHARACTERISTICS OF AN ACTIVATED CARBON IN SUPERCRITICAL WATER*; 1997; Vol. 35.

(26) Xu, X.; Matsumura, Y.; Stenberg, J.; Antal, M. J. *Carbon-Catalyzed Gasification of Organic Feedstocks in Supercritical Water †*. https://pubs.acs.org/sharingguidelines.

(27) Schubert, M.; Regler, J. W.; Vogel, F. Continuous Salt Precipitation and Separation from Supercritical Water. Part 1: Type 1 Salts. *J Supercrit Fluids* **2010**, *52* (1), 99–112. https://doi.org/10.1016/J.SUPFLU.2009.10.002.

(28) Schubert, M.; Regler, J. W.; Vogel, F. Continuous Salt Precipitation and Separation from Supercritical Water. Part 2. Type 2 Salts and Mixtures of Two Salts. *J Supercrit Fluids* **2010**, *52* (1), 113–124. https://doi.org/10.1016/J.SUPFLU.2009.10.003.

(29) Peng, G.; Vogel, F.; Refardt, D.; Ludwig, C. Catalytic Supercritical Water Gasification: Continuous Methanization of Chlorella Vulgaris. *Ind Eng Chem Res* **2017**, *56* (21), 6256–6265. https://doi.org/10.1021/ACS.IECR.7B00042.

(30) Müller, J. B.; Vogel, F. Tar and Coke Formation during Hydrothermal Processing of Glycerol and Glucose. Influence of Temperature, Residence Time and Feed Concentration. *J Supercrit Fluids* **2012**, *70*, 126–136. https://doi.org/10.1016/J.SUPFLU.2012.06.016.

(31) Haiduc, A. G.; Brandenberger, M.; Suquet, S.; Vogel, F.; Bernier-Latmani, R.; Ludwig, C. SunCHem: An Integrated Process for the Hydrothermal Production of Methane from Microalgae and CO2 Mitigation. *J Appl Phycol* **2009**, *21* (5), 529–541. https://doi.org/10.1007/S10811-009-9403-3/FIGURES/4.

(32) Stucki, S.; Vogel, F.; Ludwig, C.; Haiduc, A. G.; Brandenberger, M. Catalytic Gasification of Algae in Supercritical Water for Biofuel Production and Carbon Capture. *Energy Environ Sci* **2009**, *2* (5), 535–541. https://doi.org/10.1039/B819874H.

(33) Schmieder, H.; Abeln, J.; Boukis, N.; Dinjus, E.; Kruse, A.; Kluth, M.; Petrich, G.; Sadri, E.; Schacht, M. *Hydrothermal Gasification of Biomass and Organic Wastes*; 2000; Vol. 17. www.elsevier.com/locate/supflu.

(34) Kruse, A.; Meier, D.; Rimbrecht, P.; Schacht, M. Gasification of Pyrocatechol in Supercritical Water in the Presence of Potassium Hydroxide. In *Industrial and Engineering Chemistry Research*; ACS, 2000; Vol. 39, pp 4842–4848. https://doi.org/10.1021/ie0001570.

(35) Sinag, A.; Kruse, A.; Schwarzkopf, V. Key Compounds of the Hydropyrolysis of Glucose in Supercritical Water in the Presence of K2CO3. *Ind Eng Chem Res* **2003**, *42* (15), 3516–3521. https://doi.org/10.1021/ie030079r.

(36) Boukis, N.; Katharina Stoll, I. Gasification of Biomass in Supercritical Water, Challenges for the Process Design—Lessons Learned from the Operation Experience of the First Dedicated Pilot Plant. *Processes* **2021**, *9* (3), 1–17. https://doi.org/10.3390/pr9030455.

(37) Boukis, N.; Galla, U.; D´jesus, P.; Müller, H.; Dinjus, E. GASIFICATION OF WET BIOMASS IN SUPERCRITICAL WATER. RESULTS OF PILOT PLANT EXPERIMENTS. In *14th European Biomass Conference*; 2005.

(38) Boukis, N.; Galla, U.; Müller, H.; Dinjus, E. BIOMASS GASIFICATION IN SUPERCRITICAL WATER. EXPERIMENTAL PROGRESS ACHIEVED WITH THE VERENA PILOT PLANT. In *15th European Biomass Conference & Exhibition*; 2007.

(39) Boukis, N.; Galla, U.; Müller, H.; Dinjus, E. Hydrothermal Gasification of Glycerol On the Pilot Plant Scale. In *16th European Biomass Conference & Exhibition*; 2008.

(40) Boukis, N.; Hauer, E.; Herbig, S.; Sauer, J.; Vogel, F. Catalytic Gasification of Digestate Sludge in Supercritical Water on the Pilot Plant Scale. https://doi.org/10.1007/s13399-017-0238-x.

(41) Boukis, N.; Hauer, E.; Herbig, S.; Sauer, J.; Vogel, F. Catalytic Gasification of Digestate Sludge in Supercritical Water on the Pilot Plant Scale. *Biomass Convers Biorefin* **2017**, *7* (4), 415–424. https://doi.org/10.1007/s13399-017-0238-x.

(42) Dutzi, J.; Boukis, N.; Sauer, J. Process Effluent Recycling in the Supercritical Water Gasification of Dry Biomass. *Processes 2023, Vol. 11, Page 797* **2023**, *11* (3), 797. https://doi.org/10.3390/PR11030797.

(43) Dutzi, J.; Boukis, N.; Sauer, J. Supercritical Water Gasification of Heavy Metal Contaminated Plants with Focus on Separation of Heavy Metal Contaminants. *Biomass Bioenergy* **2024**, *182*, 107059. https://doi.org/10.1016/j.biombioe.2024.107059.

(44) Dutzi, J.; Stoll, I. K.; Boukis, N.; Sauer, J. Screening of Ten Different Plants in the Process of Supercritical Water Gasification. *Sustainable Chemistry for the Environment* **2024**, *5*. https://doi.org/10.1016/j.scenv.2024.100062.

(45) D'Jesús, P.; Boukis, N.; Kraushaar-Czarnetzki, B.; Dinjus, E. Gasification of Corn and Clover Grass in Supercritical Water. *Fuel* **2006**, *85* (7–8), 1032–1038. https://doi.org/10.1016/j.fuel.2005.10.022.

(46) D'Jesús, P.; Boukis, N.; Kraushaar-Czarnetzki, B.; Dinjus, E. Influence of Process Variables on Gasification of Corn Silage in Supercritical Water. *Ind Eng Chem Res* **2006**, *45* (5), 1622–1630. https://doi.org/10.1021/ie050367i.

(47) Dutzi, J.; Vadarlis, A. A.; Boukis, N.; Sauer, J. Comparison of Experimental Results with Thermodynamic Equilibrium Simulations of Supercritical Water Gasification of Concentrated Ethanol Solutions with Focus on Water Splitting. *Ind Eng Chem Res* **2023**, *62* (32), 12501–12512. https://doi.org/10.1021/acs.iecr.3c01595.

(48) Kruse, A.; Meier, D.; Rimbrecht, P.; Schacht, M. Gasification of Pyrocatechol in Supercritical Water in the Presence of Potassium Hydroxide. *Ind Eng Chem Res* **2000**, *39* (12), 4842–4848. https://doi.org/10.1021/ie0001570.

(49) Yoshida, T.; Matsumura, Y. Gasification of Cellulose, Xylan, and Lignin Mixtures in Supercritical Water. *Ind Eng Chem Res* **2001**, *40* (23), 5469–5474. https://doi.org/10.1021/ie0101590.

(50) Ali, M. A. M.; Noguchi, T.; Zhang, M.; Inoue, S.; Matsumura, Y. Reaction Characteristics of Homogeneous and Heterogenous Reactions for Glucose Gasification in Supercritical Water Using Ruthenium Catalyst Supported on Carbon Nanotube. *Journal of Supercritical Fluids* **2024**, *206*. https://doi.org/10.1016/j.supflu.2023.106156.

(51) Ali, M. A. M.; Inoue, S.; Matsumura, Y. Gasification Characteristics of Carbon Nanotube in Supercritical Water. *Journal of Supercritical Fluids* **2022**, *182*. https://doi.org/10.1016/j.supflu.2022.105532.

(52) Ali, M. A. M.; Inoue, S.; Matsumura, Y. Carbon Nanotube as Catalyst Support in Supercritical Water. *Journal of Supercritical Fluids* **2022**, *190*. https://doi.org/10.1016/j.supflu.2022.105755.

(53) Rodriguez Correa, C.; Kruse, A. Supercritical Water Gasification of Biomass for Hydrogen Production – Review. *Journal of Supercritical Fluids* **2018**, *133* (May), 573–590. https://doi.org/10.1016/j.supflu.2017.09.019.

(54) Yanik, J.; Ebale, S.; Kruse, A.; Saglam, M.; Yüksel, M. Biomass Gasification in Supercritical Water: II. Effect of Catalyst. *Int J Hydrogen Energy* **2008**, *33* (17), 4520–4526. https://doi.org/10.1016/J.IJHYDENE.2008.06.024.

(55) Chakinala, A. G.; Brilman, D. W. F.; Van Swaaij, W. P. M.; Kersten, S. R. A. Catalytic and Non-Catalytic Supercritical Water Gasification of Microalgae and Glycerol. *Ind Eng Chem Res* **2010**, *49* (3), 1113–1122. https://doi.org/10.1021/ie9008293.

(56) Azadi, P.; Khan, S.; Strobel, F.; Azadi, F.; Farnood, R. Hydrogen Production from Cellulose, Lignin, Bark and Model Carbohydrates in Supercritical Water Using Nickel and Ruthenium Catalysts. *Appl Catal B* **2012**, *117–118*, 330–338. https://doi.org/10.1016/j.apcatb.2012.01.035.

(57) Louw, J.; Schwarz, C. E.; Burger, A. J. Catalytic Supercritical Water Gasification of Primary Paper Sludge Using a Homogeneous and Heterogeneous Catalyst: Experimental vs Thermodynamic Equilibrium Results. *Bioresour Technol* **2016**, *201*, 111–120. https://doi.org/10.1016/j.biortech.2015.11.043.

(58) Boukis, N. Verfahren Zur Vorbehandlung von Reaktoren Zur Wasserstofferzeugung Und Reaktor, 2001.

(59) Azadi, P.; Afif, E.; Azadi, F.; Farnood, R. Screening of Nickel Catalysts for Selective Hydrogen Production Using Supercritical Water Gasification of Glucose. *Green Chemistry* **2012**, *14* (6), 1766–1777. https://doi.org/10.1039/c2gc16378k.

(60) Okolie, J. A.; Mukherjee, A.; Nanda, S.; Dalai, A. K.; Kozinski, J. A. Catalytic Supercritical Water Gasification of Soybean Straw: Effects of Catalyst Supports and Promoters. *Ind Eng Chem Res* **2021**, *60* (16), 5770–5782. https://doi.org/10.1021/acs.iecr.0c06177.

(61) Li, S.; Lu, Y.; Guo, L.; Zhang, X. Hydrogen Production by Biomass Gasification in Supercritical Water with Bimetallic Ni-M/ΓAl2O3 Catalysts (M = Cu, Co and Sn). *Int J*

Hydrogen Energy **2011**, *36* (22), 14391–14400. https://doi.org/10.1016/j.ijhydene.2011.07.144.

(62) Sun, J.; Xu, L.; Dong, G. hua; Nanda, S.; Li, H.; Fang, Z.; Kozinski, J. A.; Dalai, A. K. Subcritical Water Gasification of Lignocellulosic Wastes for Hydrogen Production with Co Modified Ni/Al2O3 Catalysts. *Journal of Supercritical Fluids* **2020**, *162*, 2–11. https://doi.org/10.1016/j.supflu.2020.104863.

(63) Onwudili, J. A.; Williams, P. T. Hydrogen and Methane Selectivity during Alkaline Supercritical Water Gasification of Biomass with Ruthenium-Alumina Catalyst. *Appl Catal B* **2013**, *132–133*, 70–79. https://doi.org/10.1016/j.apcatb.2012.11.033.

(64) Barati, M.; Babatabar, M.; Tavasoli, A.; Dalai, A. K.; Das, U. Hydrogen Production via Supercritical Water Gasification of Bagasse Using Unpromoted and Zinc Promoted Ru/γ-Al2O3 Nanocatalysts. *Fuel Processing Technology* **2014**, *123*, 140–148. https://doi.org/10.1016/j.fuproc.2014.02.005.

(65) Tiong, L.; Komiyama, M.; Uemura, Y.; Nguyen, T. T. Catalytic Supercritical Water Gasification of Microalgae: Comparison of Chlorella Vulgaris and Scenedesmus Quadricauda. *Journal of Supercritical Fluids* **2016**, *107*, 408–413. https://doi.org/10.1016/j.supflu.2015.10.009.

(66) Chen, Y.; Yi, L.; Li, S.; Yin, J.; Jin, H. Catalytic Gasification of Sewage Sludge in near and Supercritical Water with Different Catalysts. *Chemical Engineering Journal* **2020**, *388*, 124292. https://doi.org/10.1016/j.cej.2020.124292.

(67) Kang, K.; Azargohar, R.; Dalai, A. K.; Wang, H. Systematic Screening and Modification of Ni Based Catalysts for Hydrogen Generation from Supercritical Water Gasification of Lignin. *Chemical Engineering Journal* **2016**, *283*, 1019–1032. https://doi.org/10.1016/J.CEJ.2015.08.032.

(68) Lu, Y.; Zhu, Y.; Li, S.; Zhang, X.; Guo, L. Behavior of Nickel Catalysts in Supercritical Water Gasification of Glucose: Influence of Support. *Biomass Bioenergy* **2014**, *67*, 125–136. https://doi.org/10.1016/J.BIOMBIOE.2014.04.038.

(69) Lu, Y.; Li, S.; Guo, L.; Zhang, X. Hydrogen Production by Biomass Gasification in Supercritical Water over Ni/ΓAl2O3 and Ni/CeO2-ΓAl 2O3 Catalysts. *Int J Hydrogen Energy* **2010**, *35* (13), 7161–7168. https://doi.org/10.1016/j.ijhydene.2009.12.047.

(70) Ding, N.; Azargohar, R.; Dalai, A. K.; Kozinski, J. A. Catalytic Gasification of Glucose to H2 in Supercritical Water. *Fuel Processing Technology* **2014**, *127*, 33–40. https://doi.org/10.1016/J.FUPROC.2014.05.014.

(71) Lu, Y.; Li, S.; Guo, L. Hydrogen Production by Supercritical Water Gasification of Glucose with Ni/CeO2/Al2O3: Effect of Ce Loading. *Fuel* **2013**, *103*, 193–199. https://doi.org/10.1016/J.FUEL.2012.04.038.

(72) Shan, Y. Q.; Yin, L. X.; Djandja, O. S.; Wang, Z. C.; Duan, P. G. Supercritical Water Gasification of Waste Water Produced from Hydrothermal Liquefaction of Microalgae over Ru Catalyst for Production of H2 Rich Gas Fuel. *Fuel* **2021**, *292* (November 2020). https://doi.org/10.1016/j.fuel.2021.120288.

(73) Mastuli, M. S.; Kasim, M. F.; Mahat, A. M.; Asikin-Mijan, N.; Sivasangar, S.; Taufiq-Yap, Y. H. Structural and Catalytic Studies of Mg1-XNixO Nanomaterials for Gasification of Biomass in Supercritical Water for H2-Rich Syngas Production. *Int J Hydrogen Energy* **2020**, *45* (58), 33218–33234. https://doi.org/10.1016/j.ijhydene.2020.09.020.

(74) Kang, K.; Azargohar, R.; Dalai, A. K.; Wang, H. Hydrogen Generation via Supercritical Water Gasification of Lignin Using Ni-Co/Mg-Al Catalysts. *Int J Energy Res* **2017**, *41* (13), 1835–1846. https://doi.org/10.1002/ER.3739.

(75) Li, S.; Guo, L. Stability and Activity of a Co-Precipitated Mg Promoted Ni/Al2O3 Catalyst for Supercritical Water Gasification of Biomass. *Int J Hydrogen Energy* **2019**, 15842–15852. https://doi.org/10.1016/j.ijhydene.2018.08.205.

(76) Li, S.; Guo, L.; Zhu, C.; Lu, Y. Co-Precipitated Ni–Mg–Al Catalysts for Hydrogen Production by Supercritical Water Gasification of Glucose. *Int J Hydrogen Energy* **2013**, *38* (23), 9688–9700. https://doi.org/10.1016/J.IJHYDENE.2013.05.002.

(77) Li, S.; Zhu, B.; Wang, W.; Zhang, H.; Li, Q. Efficient and Stable Supercritical-Water-Synthesized Ni-Based Catalysts for Supercritical Water Gasification. *Journal of Supercritical Fluids* **2020**, *160*, 104790. https://doi.org/10.1016/j.supflu.2020.104790.

(78) Yan, B.; Wu, J.; Xie, C.; He, F.; Wei, C. Supercritical Water Gasification with Ni/ZrO2 Catalyst for Hydrogen Production from Model Wastewater of Polyethylene Glycol. *Journal of Supercritical Fluids* **2009**, *50* (2), 155–161. https://doi.org/10.1016/j.supflu.2009.04.015.

(79) Zhu, B.; Li, S.; Wang, W.; Zhang, H. Supercritical Water Synthesized Ni/ZrO2 Catalyst for Hydrogen Production from Supercritical Water Gasification of Glycerol. *Int J Hydrogen Energy* **2019**, *44* (59), 30917–30926. https://doi.org/10.1016/j.ijhydene.2019.10.044.

(80) Liu, Q.; Liao, L.; Liu, Z.; Dong, X. Hydrogen Production by Glycerol Reforming in Supercritical Water over Ni/MgO-ZrO2 Catalyst. *Journal of Energy Chemistry* **2013**, *22* (4), 665–670. https://doi.org/10.1016/S2095-4956(13)60088-1.

(81) Li, S.; Savage, P. E.; Guo, L. Stability and Activity Maintenance of Sol-Gel Ni-MxOy (M=Ti, Zr, Ta) Catalysts during Continuous Gasification of Glycerol in Supercritical Water. *Journal of Supercritical Fluids* **2019**, *148* (February), 137–147. https://doi.org/10.1016/j.supflu.2019.02.028.

(82) Huang, J.; Lian, X.; Wang, L.; Zhu, C.; Jin, H.; Wang, R. Hydrogen Production from Glucose by Supercritical Water Gasification with Ni/Zr(Ce,Y)O2-δ Catalysts. *Int J Hydrogen Energy* **2017**, *42* (7), 4613–4625. https://doi.org/10.1016/J.IJHYDENE.2016.10.012.

(83) Sivasangar, S.; Mastuli, M. S.; Islam, A.; Taufiq-Yap, Y. H. Screening of Modified CaO-Based Catalysts with a Series of Dopants for the Supercritical Water Gasification of Empty Palm Fruit Bunches to Produce Hydrogen. *RSC Adv* **2015**, *5* (46), 36798–36808. https://doi.org/10.1039/C5RA03430B.

(84) Yin, J.; Cheng, Z.; Guo, L.; Li, S.; Jin, H. Products Distribution and Influence of Nickel Catalyst on Glucose Hydrothermal Decomposition. *Int J Hydrogen Energy* **2017**, *42* (7), 4642–4650. https://doi.org/10.1016/J.IJHYDENE.2016.07.065.

(85) Jin, H.; Zhao, X.; Wu, Z.; Cao, C.; Guo, L. Supercritical Water Synthesis of Nano-Particle Catalyst on TiO2 and Its Application in Supercritical Water Gasification of Biomass. *J Exp Nanosci* **2017**, *12* (1), 72–82. https://doi.org/10.1080/17458080.2016.1262066.

(86) Guan, Q.; Chen, S.; Chen, Y.; Gu, J.; Li, B.; Miao, R.; Chen, Q.; Ning, P. High Performance Noble-Metal-Free NiCo/AC Bimetal for Gasification in Supercritical Water. *Int J Hydrogen Energy* **2017**, *42* (10), 6511–6518. https://doi.org/10.1016/j.ijhydene.2016.11.191.

(87) Kang, K.; Azargohar, R.; Dalai, A. K.; Wang, H. Hydrogen Production from Lignin, Cellulose and Waste Biomass via Supercritical Water Gasification: Catalyst Activity and Process Optimization Study. *Energy Convers Manag* **2016**, *117*, 528–537. https://doi.org/10.1016/j.enconman.2016.03.008.

(88) Yang, M.; Zhang, J.; Guo, Y. Supercritical Water Gasification of Phenol over Ni-Ru Bimetallic Catalyst: Intermediates and Kinetics. *Journal of Supercritical Fluids* **2020**, *160*, 104810. https://doi.org/10.1016/j.supflu.2020.104810.

(89) Pei, A.; Zhang, L.; Jiang, B.; Guo, L.; Zhang, X.; Lv, Y.; Jin, H. Hydrogen Production by Biomass Gasification in Supercritical or Subcritical Water with Raney-Ni and Other Catalysts. *undefined* **2009**, *3* (4), 456–464. https://doi.org/10.1007/S11708-009-0069-Y.

(90) Jin, H.; Lu, Y.; Guo, L.; Zhang, X.; Pei, A. Hydrogen Production by Supercritical Water Gasification of Biomass with Homogeneous and Heterogeneous Catalyst. *Advances in Condensed Matter Physics* **2014**, *2014*. https://doi.org/10.1155/2014/160565.

(91) Yin, J.; Cheng, Z.; Guo, L.; Li, S.; Jin, H. Products Distribution and Influence of Nickel Catalyst on Glucose Hydrothermal Decomposition. *Int J Hydrogen Energy* **2017**, *42* (7), 4642–4650. https://doi.org/10.1016/J.IJHYDENE.2016.07.065.

(92) Mastuli, M. S.; Kamarulzaman, N.; Kasim, M. F.; Zainal, Z.; Matsumura, Y.; Taufiq-Yap, Y. H. Comparative Study between Supported and Doped MgO Catalysts in Supercritical Water Gasification for Hydrogen Production. *Int J Hydrogen Energy* **2019**, *44* (7), 3690–3701. https://doi.org/10.1016/j.ijhydene.2018.12.102.

(93) Sato, T.; Furusawa, T.; Ishiyama, Y.; Sugito, H.; Miura, Y.; Sato, M.; Suzuki, N.; Itoh, N. Effect of Water Density on the Gasification of Lignin with Magnesium Oxide Supported Nickel Catalysts in Supercritical Water. *Ind Eng Chem Res* **2006**, *45* (2), 615–622. https://doi.org/10.1021/ie0510270.

(94) Furusawa, T.; Sato, T.; Saito, M.; Ishiyama, Y. The Evaluation of the Stability of Ni / MgO Catalysts for the Gasification of Lignin in Supercritical Water. **2007**, *327*, 300–310. https://doi.org/10.1016/j.apcata.2007.05.036.

(95) Kou, J.; Yi, L.; Li, G.; Cheng, K.; Wang, R.; Zhang, D.; Jin, H.; Guo, L. Structural Effect of ZrO2 on Supported Ni-Based Catalysts for Supercritical Water Gasification of Oil-Containing Wastewater. *Int J Hydrogen Energy* **2021**, *46* (24), 12874–12885. https://doi.org/10.1016/j.ijhydene.2021.01.082.

(96) Lee, I. G.; Nowacka, A.; Yuan, C. H.; Park, S. J.; Yang, J. B. Hydrogen Production by Supercritical Water Gasification of Valine over Ni/Activated Charcoal Catalyst Modified with Y, Pt, and Pd. *Int J Hydrogen Energy* **2015**, *40* (36), 12078–12087. https://doi.org/10.1016/J.IJHYDENE.2015.07.112.

(97) Sina, A.; Yumak, T.; Balci, V.; Kruse, A. Catalytic Hydrothermal Conversion of Cellulose over SnO2 and ZnO Nanoparticle Catalysts. *J Supercrit Fluids* **2011**, *56* (2), 179–185. https://doi.org/10.1016/J.SUPFLU.2011.01.002.

(98) Peng, G.; Ludwig, C.; Vogel, F. Catalytic Supercritical Water Gasification: Interaction of Sulfur with ZnO and the Ruthenium Catalyst. *Appl Catal B* **2017**, *202*, 262–268. https://doi.org/10.1016/J.APCATB.2016.09.011.

(99) Azadi, P.; Farnood, R. Review of Heterogeneous Catalysts for Sub- and Supercritical Water Gasification of Biomass and Wastes. *Int J Hydrogen Energy* **2011**, *36* (16), 9529–9541. https://doi.org/10.1016/J.IJHYDENE.2011.05.081.

(100) Angeli, S. D.; Monteleone, G.; Giaconia, A.; Lemonidou, A. A. State-of-the-Art Catalysts for CH4 Steam Reforming at Low Temperature. *Int J Hydrogen Energy* **2014**, *39* (5), 1979–1997. https://doi.org/10.1016/j.ijhydene.2013.12.001.

(101) Chen, L.; Qi, Z.; Zhang, S.; Su, J.; Somorjai, G. A. Catalytic Hydrogen Production from Methane: A Review on Recent Progress and Prospect. *Catalysts* **2020**, *10* (8). https://doi.org/10.3390/catal10080858.

(102) Mohanty, U. S.; Ali, M.; Azhar, M. R.; Al-Yaseri, A.; Keshavarz, A.; Iglauer, S. Current Advances in Syngas (CO + H2) Production through Bi-Reforming of Methane Using Various Catalysts: A Review. *Int J Hydrogen Energy* **2021**, *46* (65), 32809–32845. https://doi.org/10.1016/J.IJHYDENE.2021.07.097.

(103) Zhang, H.; Sun, Z.; Hu, Y. H. Steam Reforming of Methane: Current States of Catalyst Design and Process Upgrading. *Renewable and Sustainable Energy Reviews* **2021**, *149*, 111330. https://doi.org/10.1016/j.rser.2021.111330.

(104) Song, X.; Chen, X.; Sun, L.; Li, K.; Sun, X.; Wang, C.; Ning, P. Synergistic Effect of Fe2O3 and CuO on Simultaneous Catalytic Hydrolysis of COS and CS2: Experimental and Theoretical Studies. *Chemical Engineering Journal* **2020**, *399*, 125764. https://doi.org/10.1016/J.CEJ.2020.125764.

(105) Aasberg-Petersen, K.; Dybkjær, I.; Ovesen, C. V.; Schjødt, N. C.; Sehested, J.; Thomsen, S. G. Natural Gas to Synthesis Gas - Catalysts and Catalytic Processes. *J Nat Gas Sci Eng* **2011**, *3* (2), 423–459. https://doi.org/10.1016/j.jngse.2011.03.004.

(106) Marcantonio, V.; De Falco, M.; Capocelli, M.; Bocci, E.; Colantoni, A.; Villarini, M. Process Analysis of Hydrogen Production from Biomass Gasification in Fluidized Bed Reactor with Different Separation Systems. *Int J Hydrogen Energy* **2019**, *44* (21), 10350–10360. https://doi.org/10.1016/j.ijhydene.2019.02.121.

(107) Ratnasamy, C.; Wagner, J. Water Gas Shift Catalysis. *Catal Rev Sci Eng* **2009**, *51* (3), 325–440. https://doi.org/10.1080/01614940903048661.

(108) Boukis, N.; Vadarlis, A. A.; Sauer, J. Process for Producing Hydrogen and Carbon Dioxide from Organic Substances. EP4166499A2, DE102021126595A1, April 20, 2023. https://depatisnet.dpma.de/DepatisNet/depatisnet?action=bibdat&docid=DE102021126595A1 (accessed 2024-08-09).

(109) Boukis, N.; Stoll, I. K. Gasification of Biomass in Supercritical Water, Challenges for the Process Design-Lessons Learned from the Operation Experience of the First Dedicated Pilot Plant. **2021**. https://doi.org/10.3390/pr9030455.

(110) Gao, N.; Li, A.; Quan, C.; Gao, F. Hydrogen-Rich Gas Production from Biomass Steam Gasification in an Updraft Fixed-Bed Gasifier Combined with a Porous Ceramic Reformer. *Int J Hydrogen Energy* **2008**, *33* (20), 5430–5438. https://doi.org/10.1016/j.ijhydene.2008.07.033.

(111) Gao, N.; Li, A.; Quan, C. A Novel Reforming Method for Hydrogen Production from Biomass Steam Gasification. *Bioresour Technol* **2009**, *100* (18), 4271–4277. https://doi.org/10.1016/j.biortech.2009.03.045.

(112) Zhang, J.; Wang, M.; Xu, S.; Feng, Y. Hydrogen and Methane Mixture from Biomass Gasification Coupled with Catalytic Tar Reforming, Methanation and Adsorption Enhanced Reforming. *Fuel Processing Technology* **2019**, *192*, 147–153. https://doi.org/10.1016/J.FUPROC.2019.04.023.

(113) Shien, R.; Amran, T.; Abdullah, T.; Ripin, A.; Ahmad, A.; Isa, K. Hydrogen-Rich Gas Production by Steam Reforming of Gasified Biomass Tar over Ni/Dolomite/La2O3 Catalyst. *J Environ Chem Eng* **2019**, No. September, 103490. https://doi.org/10.1016/j.jece.2019.103490.

(114) Gao, N.; Wang, X.; Li, A.; Wu, C.; Yin, Z. Hydrogen Production from Catalytic Steam Reforming of Benzene as Tar Model Compound of Biomass Gasification. *Fuel Processing Technology* **2016**, *148*, 380–387. https://doi.org/10.1016/j.fuproc.2016.03.019.

(115) Xu, M.; Liu, Z.; Zhang, X.; Di, J.; Meng, X.; Zhao, L.; Lu, Q. Steam Reforming of Biomass Gasification Tar over Ni-Based Catalyst Supported by TiO2-SiO2 Composite. *Fuel* **2023**, *343*, 127934. https://doi.org/10.1016/J.FUEL.2023.127934.

(116) Grams, J.; Ryczkowski, R.; Sadek, R.; Chałupka-Śpiewak, K.; Casale, S.; Dzwigaj, S. Enhanced Activity of NiZrBEA Catalyst for Upgrading of Biomass Pyrolysis Vapors to H2-Rich Gas. *Int J Hydrogen Energy* **2022**, *47* (82), 34909–34923. https://doi.org/10.1016/j.ijhydene.2022.08.082.

(117) Sun, Y.; Tu, R.; Wang, J. min; Wu, Y. jian; Fan, X. dong; Jiang, E. C.; Xu, X. wei; Shen, X. wen. Biomass Derived Low Concentration CO2 Mixed Gas Combined Steam to Reform Methane through Ni Based Volcanic Rock Catalyst. *Int J Hydrogen Energy* **2022**, *47* (55), 23139–23150. https://doi.org/10.1016/j.ijhydene.2022.05.065.

(118) Rahbari, A.; Shirazi, A.; Venkataraman, M. B.; Pye, J. Solar Fuels from Supercritical Water Gasification of Algae: Impacts of Low-Cost Hydrogen on Reformer Configurations. *Appl Energy* **2021**, *288*, 116620. https://doi.org/10.1016/j.apenergy.2021.116620.

(119) Ruya, P. M.; Lim, S. S.; Purwadi, R.; Zunita, M. Sustainable Hydrogen Production from Oil Palm Derived Wastes through Autothermal Operation of Supercritical Water Gasification System. *Energy* **2020**, *208*, 118280. https://doi.org/10.1016/j.energy.2020.118280.

(120) Zhang, C.; Li, Y.; Chu, Z.; Fang, Y. Thermodynamic Analysis of Integrated Sorption-Enhanced Staged-Gasification of Biomass and in-Situ CO2 Utilization by Methane Reforming Process Based on Calcium Looping. *Energy Convers Manag* **2023**, *278*, 116710. https://doi.org/10.1016/j.enconman.2023.116710.

(121) Hantoko, D.; Su, H.; Yan, M.; Kanchanatip, E.; Susanto, H.; Wang, G.; Zhang, S.; Xu, Z. Thermodynamic Study on the Integrated Supercritical Water Gasification with Reforming Process for Hydrogen Production: Effects of Operating Parameters. *Int J Hydrogen Energy* **2018**, *43* (37), 17620–17632. https://doi.org/10.1016/j.ijhydene.2018.07.198.

(122) Angeli, S. D.; Turchetti, L.; Monteleone, G.; Lemonidou, A. A. Catalyst Development for Steam Reforming of Methane and Model Biogas at Low Temperature. *Appl Catal B* **2016**, *181*, 34–46. https://doi.org/10.1016/j.apcatb.2015.07.039.

(123) Kechagiopoulos, P. N.; Angeli, S. D.; Lemonidou, A. A. Low Temperature Steam Reforming of Methane: A Combined Isotopic and Microkinetic Study. *Appl Catal B* **2017**, *205*, 238–253. https://doi.org/10.1016/J.APCATB.2016.12.033.

(124) Angeli, S. D.; Pilitsis, F. G.; Lemonidou, A. A. Methane Steam Reforming at Low Temperature: Effect of Light Alkanes' Presence on Coke Formation. *Catal Today* **2015**, *242* (Part A), 119–128. https://doi.org/10.1016/j.cattod.2014.05.043.

(125) Schädel, B. T.; Duisberg, M.; Deutschmann, O. Steam Reforming of Methane, Ethane, Propane, Butane, and Natural Gas over a Rhodium-Based Catalyst. *Catal Today* **2009**, *142* (1–2), 42–51. https://doi.org/10.1016/J.CATTOD.2009.01.008.

(126) Aasberg-Petersen, K.; Dybkjær, I.; Ovesen, C. V.; Schjødt, N. C.; Sehested, J.; Thomsen, S. G. Natural Gas to Synthesis Gas - Catalysts and Catalytic Processes. *J Nat Gas Sci Eng* **2011**, *3* (2), 423–459. https://doi.org/10.1016/j.jngse.2011.03.004.

(127) Chaubey, R.; Sahu, S.; James, O. O.; Maity, S. A Review on Development of Industrial Processes and Emerging Techniques for Production of Hydrogen from Renewable and Sustainable Sources. *Renewable and Sustainable Energy Reviews* **2013**, *23*, 443–462. https://doi.org/10.1016/j.rser.2013.02.019.

(128) Rostrup-Nielsen, J. R.; Sehested, J.; Nørskov, J. K. Hydrogen and Synthesis Gas by Steam- and C02 Reforming. In *Advances in Catalysis*; Academic Press, 2002; Vol. 47, pp 65–139. https://doi.org/10.1016/S0360-0564(02)47006-X.

(129) Byrd, A. J.; Pant, K. K.; Gupta, R. B. Hydrogen Production from Ethanol by Reforming in Supercritical Water Using Ru/Al $_2$ O $_3$ Catalyst. *Energy & Fuels* **2007**, *21* (6), 3541–3547. https://doi.org/10.1021/ef700269z.

(130) Sinağ, A.; Kruse, A.; Rathert, J. Influence of the Heating Rate and the Type of Catalyst on the Formation of Key Intermediates and on the Generation of Gases during Hydropyrolysis of Glucose in Supercritical Water in a Batch Reactor. *Ind Eng Chem Res* **2004**, *43* (2), 502–508. https://doi.org/10.1021/ie030475+.

(131) Habicht, W.; Boukis, N.; Hauer, E.; Dinjus, E. Analysis of Hydrothermally Formed Corrosion Layers in Ni-Base Alloy 625 by Combined FE-SEM and EDXS. *X-RAY Spectrometry* **2011**.

(132) Lemonidou, A. A.; Goula, M. A.; Vasalos, I. A. Carbon Dioxide Reforming of Methane over 5 Wt.% Nickel Calcium Aluminate Catalysts – Effect of Preparation Method. *Catal Today* **1998**, *46* (2–3), 175–183. https://doi.org/10.1016/S0920-5861(98)00339-3.

(133) Li, C.; Chen, Y. W. Temperature-Programmed-Reduction Studies of Nickel Oxide/Alumina Catalysts: Effects of the Preparation Method. *Thermochim Acta* **1995**, *256* (2), 457–465. https://doi.org/10.1016/0040-6031(94)02177-P.

(134) Chatterjee, R.; Banerjee, S.; Banerjee, S.; Ghosh, D. Reduction of Nickel Oxide Powder and Pellet by Hydrogen. *Transactions of the Indian Institute of Metals* **2012**, *65* (3), 265–273. https://doi.org/10.1007/s12666-012-0130-0.

(135) Ranjbar, A.; Rezaei, M. Dry Reforming Reaction over Nickel Catalysts Supported on Nanocrystalline Calcium Aluminates with Different CaO/Al2O3 Ratios. *Journal of Natural Gas Chemistry* **2012**, *21* (2), 178–183. https://doi.org/10.1016/S1003-9953(11)60351-4.

(136) Chattanathan, S. A.; Adhikari, S.; McVey, M.; Fasina, O. Hydrogen Production from Biogas Reforming and the Effect of H2S on CH4 Conversion. *Int J Hydrogen Energy* **2014**, *39* (35), 19905–19911. https://doi.org/10.1016/j.ijhydene.2014.09.162.

(137) Ratnasamy, C.; Wagner, J. Water Gas Shift Catalysis. *Catal Rev Sci Eng* **2009**, *51* (3), 325–440. https://doi.org/10.1080/01614940903048661.

(138) Xu, J.; Froment, G. F. Methane Steam Reforming, Methanation and Water-Gas Shift: I. Intrinsic Kinetics. *AIChE Journal* **1989**, *35* (1), 88–96. https://doi.org/10.1002/aic.690350109.

(139) Obradović, A.; Likozar, B.; Levec, J. Steam Methane Reforming over Ni-Based Pellet-Type and Pt/Ni/Al2O3 Structured Plate-Type Catalyst: Intrinsic Kinetics Study. *Ind Eng Chem Res* **2013**, *52* (38), 13597–13606. https://doi.org/10.1021/ie401551m.

(140) Abbas, S. Z.; Dupont, V.; Mahmud, T. Kinetics Study and Modelling of Steam Methane Reforming Process over a NiO/Al2O3 Catalyst in an Adiabatic Packed Bed Reactor. *Int J Hydrogen Energy* **2017**, *42* (5), 2889–2903. https://doi.org/10.1016/J.IJHYDENE.2016.11.093.

(141) Yang, X.; Da, J.; Yu, H.; Wang, H. Characterization and Performance Evaluation of Ni-Based Catalysts with Ce Promoter for Methane and Hydrocarbons Steam Reforming Process. *Fuel* **2016**, *179*, 353–361. https://doi.org/10.1016/j.fuel.2016.03.104.

(142) Mosayebi, A.; Nasabi, M. Steam Methane Reforming on LaNiO 3 Perovskite-Type Oxide for Syngas Production, Activity Tests, and Kinetic Modeling. **2020**. https://doi.org/10.1002/er.5300.

(143) Ahmed, S.; Lee, S. H. D.; Ferrandon, M. S. Catalytic Steam Reforming of Biogas - Effects of Feed Composition and Operating Conditions. *Int J Hydrogen Energy* **2015**, *40* (2), 1005–1015. https://doi.org/10.1016/j.ijhydene.2014.11.009.

(144) Mosayebi, A.; Nasabi, M. Steam Methane Reforming on LaNiO3 Perovskite-Type Oxide for Syngas Production, Activity Tests, and Kinetic Modeling. *Int J Energy Res* **2020**, *44* (7), 5500–5515. https://doi.org/10.1002/ER.5300.

(145) Zhai, X.; Cheng, Y.; Zhang, Z.; Jin, Y.; Cheng, Y. Steam Reforming of Methane over Ni Catalyst in Micro-Channel Reactor. *Int J Hydrogen Energy* **2011**, *36* (12), 7105–7113. https://doi.org/10.1016/j.ijhydene.2011.03.065.

(146) Zhang, N.; Chen, X.; Chu, B.; Cao, C.; Jin, Y.; Cheng, Y. Catalytic Performance of Ni Catalyst for Steam Methane Reforming in a Micro-Channel Reactor at High Pressure.

Chemical Engineering and Processing - Process Intensification **2017**, *118*, 19–25. https://doi.org/10.1016/j.cep.2017.04.015.

(147) Farshchi Tabrizi, F.; Mousavi, S. A. H. S.; Atashi, H. Thermodynamic Analysis of Steam Reforming of Methane with Statistical Approaches. *Energy Convers Manag* **2015**, *103*, 1065–1077. https://doi.org/10.1016/J.ENCONMAN.2015.07.005.

(148) Rostrup-Nielsen, J. R. Activity of Nickel Catalysts for Steam Reforming of Hydrocarbons. *J Catal* **1973**, *31*, 173–199.

(149) Taylor, W. F.; Sinfelt, J. H.; Yates, D. J. C. Catalysis over Supported Metals. IV. Ethane Hydrogenolysis over Dilute Nickel Catalysts. *Journal of Physical Chemistry* **1965**, *69* (11), 3857–3863. https://doi.org/10.1021/J100895A036/ASSET/J100895A036.FP.PNG_V03.

(150) Jaiswar, V. K.; Katheria, S.; Deo, G.; Kunzru, D. Effect of Pt Doping on Activity and Stability of Ni/MgAl2O4 Catalyst for Steam Reforming of Methane at Ambient and High Pressure Condition. *Int J Hydrogen Energy* **2017**, *42* (30), 18968–18976. https://doi.org/10.1016/j.ijhydene.2017.06.096.

(151) Katheria, S.; Gupta, A.; Deo, G.; Kunzru, D. Effect of Calcination Temperature on Stability and Activity of Ni/MgAl2O4 Catalyst for Steam Reforming of Methane at High Pressure Condition. *Int J Hydrogen Energy* **2016**, *41* (32), 14123–14132. https://doi.org/10.1016/j.ijhydene.2016.05.109.

(152) Świrk, K.; Rønning, M.; Motak, M.; Beaunier, P.; Da Costa, P.; Grzybek, T. Ce-and Y-Modified Double-Layered Hydroxides as Catalysts for Dry Reforming of Methane: On the Effect of Yttrium Promotion. *Catalysts* **2019**, *9* (1). https://doi.org/10.3390/catal9010056.

(153) Dou, B.; Dupont, V.; Pan, W.; Chen, B. Removal of Aqueous Toxic Hg(II) by Synthesized TiO2 Nanoparticles and TiO2/Montmorillonite. *Chemical Engineering Journal* **2011**, *166* (2), 631–638. https://doi.org/10.1016/J.CEJ.2010.11.035.

(154) Jiang, B.; Zhang, C.; Wang, K.; Dou, B.; Song, Y.; Chen, H.; Xu, Y. Highly Dispersed Ni/Montmorillonite Catalyst for Glycerol Steam Reforming: Effect of Ni Loading and Calcination Temperature. *Appl Therm Eng* **2016**, *109*, 99–108. https://doi.org/10.1016/J.APPLTHERMALENG.2016.08.041.

(155) Parker, L. M.; Milestone, N. B.; Newman, R. H. The Use of Hydrotalcite as an Anion Absorbent. *Ind. Eng. Chem. Res* **1995**, *34*, 1196–1202.

(156) Vogt, C.; Kranenborg, J.; Monai, M.; Weckhuysen, B. M. Structure Sensitivity in Steam and Dry Methane Reforming over Nickel: Activity and Carbon Formation. *ACS Catal* **2020**, *10* (2), 1428–1438. https://doi.org/10.1021/acscatal.9b04193.

(157) Świrk, K.; Zhang, H.; Li, S.; Chen, Y.; Rønning, M.; Motak, M.; Grzybek, T.; Da Costa, P. Carbon-Resistant NiO-Y2O3-Nanostructured Catalysts Derived from Double-Layered Hydroxides for Dry Reforming of Methane. *Catal Today* **2021**, *366*. https://doi.org/10.1016/j.cattod.2020.03.032.

(158) Lin, B.; Guo, Y.; Lin, J.; Ni, J.; Lin, J.; Jiang, L.; Wang, Y. Deactivation Study of Carbon-Supported Ruthenium Catalyst with Potassium Promoter. *Appl Catal A Gen* **2017**, *541*, 1–7. https://doi.org/10.1016/J.APCATA.2017.04.020.

(159) Carlsson, M. Carbon Formation in Steam Reforming and Effect of Potassium Promotion. *Johnson Matthey Technology Review* **2015**, *59* (4), 313–318. https://doi.org/10.1595/205651315X688992.

(160) Fowles, M.; Carlsson, M. Steam Reforming of Hydrocarbons for Synthesis Gas Production. *Top Catal* **2021**, *64* (17–20), 856–875. https://doi.org/10.1007/S11244-021-01496-Z/FIGURES/19.

(161) Zhao, Q.; Wang, Y.; Wang, Y.; Li, L.; Zeng, W.; Li, G.; Hu, C. Steam Reforming of CH4 at Low Temperature on Ni/ZrO2 Catalyst: Effect of H2O/CH4 Ratio on Carbon Deposition. *Int J Hydrogen Energy* **2020**, *45* (28), 14281–14292. https://doi.org/10.1016/j.ijhydene.2020.03.112.

(162) Sperle, T.; Chen, D.; Lødeng, R.; Holmen, A. Pre-Reforming of Natural Gas on a Ni Catalyst. Criteria for Carbon Free Operation. *Appl Catal A Gen* **2005**, *282* (1–2), 195–204. https://doi.org/10.1016/j.apcata.2004.12.011.

(163) Choi, S.; Bae, J.; Lee, S.; Oh, J.; Katikaneni, S. P. Pre-Reforming of Higher Hydrocarbons Contained Associated Gas Using a Pressurized Reactor with a Ni19.5-Ru0.05/CGO Catalyst. *Chem Eng Sci* **2017**, *168*, 15–22. https://doi.org/10.1016/j.ces.2017.04.033.

(164) Prasad, D. H.; Park, S. Y.; Ji, H.; Kim, H. R.; Son, J. W.; Kim, B. K.; Lee, H. W.; Lee, J. H. Effect of Steam Content on Nickel Nano-Particle Sintering and Methane Reforming Activity of Ni–CZO Anode Cermets for Internal Reforming SOFCs. *Appl Catal A Gen* **2012**, *411–412*, 160–169. https://doi.org/10.1016/J.APCATA.2011.10.035.

(165) Rouquette, J.; Haines, J.; Fraysse, G.; Al-Zein, A.; Bornand, V.; Pintard, M.; Papet, P.; Hull, S.; Gorelli, F. A. High-Pressure Structural and Vibrational Study of PbZr 0.40Ti0.60O3. *Inorg Chem* **2008**, *47* (21), 9898–9904. https://doi.org/10.1021/IC8008688/ASSET/IMAGES/LARGE/IC-2008-008688_0008.JPEG.

(166) Suh, I. K.; Ohta, H.; Waseda, Y. High-Temperature Thermal Expansion of Six Metallic Elements Measured by Dilatation Method and X-Ray Diffraction. *J Mater Sci* **1988**, *23* (2), 757–760. https://doi.org/10.1007/BF01174717/METRICS.

(167) Hashemnejad, S. M.; Parvari, M. Deactivation and Regeneration of Nickel-Based Catalysts for Steam-Methane Reforming. *Chinese Journal of Catalysis* **2011**, *32* (1–2), 273–279. https://doi.org/10.1016/S1872-2067(10)60175-1.

(168) Ioannidou, G.; Loukia Yfanti, V.; Lemonidou, A. A. Optimization of Reaction Conditions for Hydrodeoxygenation of Bio-Glycerol towards Green Propylene over Molybdenum-Based Catalyst. *Catal Today* **2022**, No. September. https://doi.org/10.1016/j.cattod.2022.09.008.

(169) Sehested, J. Sintering of Nickel Steam-Reforming Catalysts. *J Catal* **2003**, *217* (2), 417–426. https://doi.org/10.1016/S0021-9517(03)00075-7.

(170) Christensen, K. O.; Chen, D.; Lødeng, R.; Holmen, A. Effect of Supports and Ni Crystal Size on Carbon Formation and Sintering during Steam Methane Reforming. *Appl Catal A Gen* **2006**, *314* (1), 9–22. https://doi.org/10.1016/J.APCATA.2006.07.028.

(171) Tsyganov, S.; Kästner, J.; Rellinghaus, B.; Kauffeldt, T.; Westerhoff, F.; Wolf, D. Analysis of Ni Nanoparticle Gas Phase Sintering. https://doi.org/10.1103/PhysRevB.75.045421.

(172) Christensen, K. O.; Chen, D.; Lødeng, R.; Holmen, A. Effect of Supports and Ni Crystal Size on Carbon Formation and Sintering during Steam Methane Reforming. *Appl Catal A Gen* **2006**, *314* (1), 9–22. https://doi.org/10.1016/j.apcata.2006.07.028.

(173) Iglesias, I.; Baronetti, G.; Mariño, F. Ni/Ce0.95M0.05O2−d (M = Zr, Pr, La) for Methane Steam Reforming at Mild Conditions. *Int J Hydrogen Energy* **2017**, *42* (50), 29735–29744. https://doi.org/10.1016/j.ijhydene.2017.09.176.

(174) Robertson, S. D. CARBON FORMATION FROM METHANE PYROLYSIS OVER SOME TRANSITION METAL SURFACES-I. NATURE AND PROPERTIES OF THE CARBONS FORMED. *Carbon N Y* **1970**, *8*, 365–374.

(175) ROSTRUPNIELSEN, J. Mechanisms of Carbon Formation on Nickel-Containing Catalysts. *J Catal* **1977**, *48* (1–3), 155–165. https://doi.org/10.1016/0021-9517(77)90087-2.

(176) Vadarlis, A. A.; Neukum, D.; Lemonidou, A. A.; Boukis, N.; Sauer, J. Direct Steam Reforming of the Product Gas from Ethanol Gasification with Supercritical Water. *Int J Hydrogen Energy* **2024**, *49*, 992–1008. https://doi.org/10.1016/j.ijhydene.2023.08.108.

(177) Rostrup-Nielsen, J. R. Catalytic Steam Reforming. In *Catalysis*; Anderson, J. R., Boudart, M., Eds.; Springer: Berlin, Heidelberg, 1984; Vol. 5, pp 1–117. https://doi.org/10.1007/978-3-642-93247-2_1.

(178) Pinaeva, L. G.; Noskov, A. S. Modern Level of Catalysts and Technologies for the Conversion of Natural Gas into Syngas. *Catal Ind* **2022**, *14* (1), 66–85. https://doi.org/10.1134/S2070050422010081.

(179) Antzaras, A. N.; Lemonidou, A. A. Recent Advances on Materials and Processes for Intensified Production of Blue Hydrogen. *Renewable and Sustainable Energy Reviews* **2022**, *155*, 111917. https://doi.org/10.1016/j.rser.2021.111917.

(180) Lemonidou, A. A.; Goula, M. A.; Vasalos, I. A. Carbon Dioxide Reforming of Methane over 5 Wt.% Nickel Calcium Aluminate Catalysts – Effect of Preparation Method. *Catal Today* **1998**, *46* (2–3), 175–183. https://doi.org/10.1016/S0920-5861(98)00339-3.

(181) Goula, M. A.; Lemonidou, A. A.; Grünert, W.; Baerns, M. Methane Partial Oxidation to Synthesis Gas Using Nickel on Calcium Aluminate Catalysts. *Catal Today* **1996**, *32* (1–4), 149–156. https://doi.org/10.1016/S0920-5861(96)00168-X.

(182) Pirzadi, Z.; Meshkani, F.; Vo, D. V. N. Enhanced Syngas Production from CO2 Reforming of Biomass-Derived Glycerol: Influence of CaO.Al2O3 Support Composition on the Catalytic Performance of Ni-Based Catalysts. *Energy Convers Manag* **2024**, *311*, 118227. https://doi.org/10.1016/J.ENCONMAN.2024.118227.

(183) Fernandez, E.; Santamaria, L.; Artetxe, M.; Amutio, M.; Arregi, A.; Lopez, G.; Bilbao, J.; Olazar, M. Conditioning the Volatile Stream from Biomass Fast Pyrolysis for the Attenuation of Steam Reforming Catalyst Deactivation. *Fuel* **2022**, *312*, 122910. https://doi.org/10.1016/j.fuel.2021.122910.

(184) Lopez, G.; Erkiaga, A.; Artetxe, M.; Amutio, M.; Bilbao, J.; Olazar, M. Hydrogen Production by High Density Polyethylene Steam Gasification and In-Line Volatile

Reforming. *Ind Eng Chem Res* **2015**, *54* (39), 9536–9544. https://doi.org/10.1021/ACS.IECR.5B02413.

(185) Erkiaga, A.; Lopez, G.; Barbarias, I.; Artetxe, M.; Amutio, M.; Bilbao, J.; Olazar, M. HDPE Pyrolysis-Steam Reforming in a Tandem Spouted Bed-Fixed Bed Reactor for H 2 Production. *J Anal Appl Pyrolysis* **2015**, *116*, 34–41. https://doi.org/10.1016/j.jaap.2015.10.010.

(186) Sabokmalek, S.; Alavi, S. M.; Rezaei, M.; Akbari, E. Fabrication and Catalytic Evaluation of Ni/CaO–Al2O3 in Glycerol Steam Reforming: Effect of Ni Loading. *Journal of the Energy Institute* **2023**, *109*, 101270. https://doi.org/10.1016/J.JOEI.2023.101270.

(187) Arita, T.; Nakahara, K.; Nagami, K.; Kajimoto, O. Hydrogen Generation from Ethanol in Supercritical Water without Catalyst. *Tetrahedron Lett* **2003**, *44* (5), 1083–1086. https://doi.org/10.1016/S0040-4039(02)02704-1.

(188) B Kistiakowsky, B. G.; Romeyn, H.; Ruhoff, J. R.; Smith, H. A.; Vaughan, W. E. *Heats of Organic Reactions. I. The Apparatus and the Heat of Hydrogenation of Ethylene*; UTC, 2023; Vol. 16. https://pubs.acs.org/sharingguidelines.

(189) Onwudili, J. A.; Lea-Langton, A. R.; Ross, A. B.; Williams, P. T. Catalytic Hydrothermal Gasification of Algae for Hydrogen Production: Composition of Reaction Products and Potential for Nutrient Recycling. *Bioresour Technol* **2013**, *127*, 72–80. https://doi.org/10.1016/J.BIORTECH.2012.10.020.

(190) Xu, Z. R.; Zhu, W.; Gong, M.; Zhang, H. W. Direct Gasification of Dewatered Sewage Sludge in Supercritical Water. Part 1: Effects of Alkali Salts. *Int J Hydrogen Energy* **2013**, *38* (10), 3963–3972. https://doi.org/10.1016/J.IJHYDENE.2013.01.164.

(191) Voll, F. A. P.; Rossi, C. C. R. S.; Silva, C.; Guirardello, R.; Souza, R. O. M. A.; Cabral, V. F.; Cardozo-Filho, L. Thermodynamic Analysis of Supercritical Water Gasification of Methanol, Ethanol, Glycerol, Glucose and Cellulose. *Int J Hydrogen Energy* **2009**, *34* (24), 9737–9744. https://doi.org/10.1016/J.IJHYDENE.2009.10.017.

(192) Palma, V.; Ricca, A.; Meloni, E.; Martino, M.; Miccio, M.; Ciambelli, P. Experimental and Numerical Investigations on Structured Catalysts for Methane Steam Reforming Intensification. *J Clean Prod* **2016**, *111*, 217–230. https://doi.org/10.1016/j.jclepro.2015.09.004.

(193) Wang, S.; Shen, Z.; Osatiashtiani, A.; Nabavi, S. A.; Clough, P. T. Ni-Based Bimetallic Catalysts for Hydrogen Production via (Sorption-Enhanced) Steam Methane Reforming. *Chemical Engineering Journal* **2024**, *486* (November 2023), 150170. https://doi.org/10.1016/j.cej.2024.150170.

(194) Wang, Y.; Yoshiba, F.; Kawase, M.; Watanabe, T. Performance and Effective Kinetic Models of Methane Steam Reforming over Ni/YSZ Anode of Planar SOFC. *Int J Hydrogen Energy* **2009**, *34* (9), 3885–3893. https://doi.org/10.1016/J.IJHYDENE.2009.02.073.

(195) Sehested, J.; Gelten, J. A. P.; Helveg, S. Sintering of Nickel Catalysts: Effects of Time, Atmosphere, Temperature, Nickel-Carrier Interactions, and Dopants. *Appl Catal A Gen* **2006**, *309* (2), 237–246. https://doi.org/10.1016/J.APCATA.2006.05.017.

(196) Xu, J.; Yeung, C. M. Y.; Ni, J.; Meunier, F.; Acerbi, N.; Fowles, M.; Tsang, S. C. Methane Steam Reforming for Hydrogen Production Using Low Water-Ratios without Carbon Formation over Ceria Coated Ni Catalysts. *Appl Catal A Gen* **2008**, *345* (2), 119–127. https://doi.org/10.1016/J.APCATA.2008.02.044.

(197) Roy, P. S.; Raju, A. S. K.; Kim, K. Influence of S/C Ratio and Temperature on Steam Reforming of Model Biogas over a Metal-Foam-Coated Pd–Rh/(CeZrO2–Al2O3) Catalyst. *Fuel* **2015**, *139*, 314–320. https://doi.org/10.1016/J.FUEL.2014.08.062.

(198) Brito, J.; Pinto, F.; Ferreira, A.; Soria, M. A.; Madeira, L. M. Steam Reforming of Biomass Gasification Gas for Hydrogen Production: From Thermodynamic Analysis to Experimental Validation. *Fuel Processing Technology* **2023**, *250*, 107859. https://doi.org/10.1016/j.fuproc.2023.107859.

(199) Khavarian, M.; Chai, S. P.; Mohamed, A. R. Direct Use of As-Synthesized Multi-Walled Carbon Nanotubes for Carbon Dioxide Reforming of Methane for Producing Synthesis Gas. *Chemical Engineering Journal* **2014**, *257*, 200–208. https://doi.org/10.1016/j.cej.2014.05.079.

(200) Sidjabat, O.; Trimm, D. L. Nickel-Magnesia Catalysts for the Steam Reforming of Light Hydrocarbons. *Top Catal* **2000**, *11–12* (1–4), 279–282. https://doi.org/10.1023/A:1027212301077.

(201) Meshkani, F.; Golesorkh, S. F.; Rezaei, M.; Andache, M. Nickel Catalyst Supported on Mesoporous MgAl2O4 Nanopowders Synthesized via a Homogenous Precipitation Method for Dry Reforming Reaction. *Research on Chemical Intermediates* **2017**, *43* (1), 545–559. https://doi.org/10.1007/s11164-016-2639-z.

(202) Keshavarz, A. R.; Soleimani, M. Steam Pre-Reforming of Natural Gas over Nanostructured Ni/12CaO–7Al2O3 Catalyst for Hydrogen Production: Effect of Support Preparation Method. *Research on Chemical Intermediates* **2018**, *44* (3), 1485–1503. https://doi.org/10.1007/S11164-017-3180-4/FIGURES/12.

(203) Mears, D. E. Tests for Transport Limitations in Experimental Catalytic Reactors. *Ind. Eng. Chem. Process Des. Develop* **1970**, *10* (8), 397.

(204) Vannice, M. A. *Kinetics of Catalytic Reactions*; Springer Science+Business Media, Inc, 2005. https://doi.org/10.1055/sos-sd-202-00181.

(205) Bangala, D. N.; Abatzoglou, N.; Chornet, E. Steam Reforming of Naphthalene on Ni-Cr/Al2O3 Catalysts Doped with MgO, TiO2, and La2O3. *AIChE Journal* **1998**, *44* (4), 927–936. https://doi.org/10.1002/aic.690440418.

(206) Garbarino, G.; Pugliese, F.; Cavattoni, T.; Busca, G.; Costamagna, P. A Study on CO2 Methanation and Steam Methane Reforming over Commercial Ni/Calcium Aluminate Catalysts. *Energies (Basel)* **2020**, *13* (11). https://doi.org/10.3390/en13112792.

(207) Parizotto, N. V.; Rocha, K. O.; Damyanova, S.; Passos, F. B.; Zanchet, D.; Marques, C. M. P.; Bueno, J. M. C. Alumina-Supported Ni Catalysts Modified with Silver for the Steam Reforming of Methane: Effect of Ag on the Control of Coke Formation. *Appl Catal A Gen* **2007**, *330*, 12–22. https://doi.org/10.1016/j.apcata.2007.06.022.

(208) Bao, Z.; Lu, Y.; Han, J.; Li, Y.; Yu, F. Highly Active and Stable Ni-Based Bimodal Pore Catalyst for Dry Reforming of Methane. *Appl Catal A Gen* **2015**, *491*, 116–126. https://doi.org/10.1016/j.apcata.2014.12.005.

(209) Lagioia, G.; Spinelli, M. P.; Amicarelli, V. Blue and Green Hydrogen Energy to Meet European Union Decarbonisation Objectives. An Overview of Perspectives and the Current State of Affairs. *International Journal of Hydrogen Energy*. Elsevier Ltd January 12, 2023, pp 1304–1322. https://doi.org/10.1016/j.ijhydene.2022.10.044.

(210) Cardinale, R. From Natural Gas to Green Hydrogen: Developing and Repurposing Transnational Energy Infrastructure Connecting North Africa to Europe. *Energy Policy* **2023**, *181*. https://doi.org/10.1016/j.enpol.2023.113623.

(211) Zhou, Y.; Searle, S. *COST OF RENEWABLE HYDROGEN PRODUCED ONSITE AT HYDROGEN REFUELING STATIONS IN EUROPE*; 2022. www.theicct.orgcommunications@theicct.org.

(212) Clerici, A.; Furfari, S. *The present and future green hydrogen production cost*. https://www.science-climat-energie.be/2021/07/16/the-present-and-future-green-hydrogen-production-cost/ (accessed 2024-08-09).

(213) Gong, M.; Zhu, W.; Xu, Z. R.; Zhang, H. W.; Yang, H. P. Influence of Sludge Properties on the Direct Gasification of Dewatered Sewage Sludge in Supercritical Water. *Renew Energy* **2014**, *66*, 605–611. https://doi.org/10.1016/j.renene.2014.01.006.

(214) Xue, X.; Chen, D.; Song, X.; Dai, X. Hydrothermal and Pyrolysis Treatment for Sewage Sludge: Choice from Product and from Energy Benefit. In *Physics Procedia*; Elsevier B.V., 2015; Vol. 66, pp 301–304. https://doi.org/10.1016/j.egypro.2015.02.064.

(215) Migliaccio, R.; Brachi, P.; Montagnaro, F.; Papa, S.; Tavano, A.; Montesarchio, P.; Ruoppolo, G.; Urciuolo, M. Sewage Sludge Gasification in a Fluidized Bed: Experimental Investigation and Modeling. *Ind Eng Chem Res* **2021**, *60* (13), 5034–5047. https://doi.org/10.1021/acs.iecr.1c00084.

(216) Gao, N.; Kamran, K.; Quan, C.; Williams, P. T. Thermochemical Conversion of Sewage Sludge: A Critical Review. *Prog Energy Combust Sci* **2020**, *79*, 100843. https://doi.org/10.1016/j.pecs.2020.100843.

(217) Hantoko, D.; Antoni; Kanchanatip, E.; Yan, M.; Weng, Z.; Gao, Z.; Zhong, Y. Assessment of Sewage Sludge Gasification in Supercritical Water for H2-Rich Syngas Production. *Process Safety and Environmental Protection* **2019**, *131*, 63–72. https://doi.org/10.1016/j.psep.2019.08.035.

(218) Elsayed, S.; Boukis, N.; Patzelt, D.; Hindersin, S.; Kerner, M.; Sauer, J. Gasification of Microalgae Using Supercritical Water and the Potential of Effluent Recycling. *Chem Eng Technol* **2016**, *39* (2), 335–342. https://doi.org/10.1002/CEAT.201500146.

(219) Peloquin, J.-F.; Francoeur, D.; Leclerc, W.; Mehanovic, D.; Dufault, J.-F.; Camus, P.; Castellanos-Beltran, I. J.; Braidy, N.; Fréchette, L. G.; Picard, M. Electrified Steam Methane Reforming Microreactor. *Int J Hydrogen Energy* **2024**, *49*, 907–915. https://doi.org/10.1016/j.ijhydene.2023.07.343.

(220) Meerman, J. C.; Hamborg, E. S.; van Keulen, T.; Ramírez, A.; Turkenburg, W. C.; Faaij, A. P. C. Techno-Economic Assessment of CO2 Capture at Steam Methane Reforming Facilities Using Commercially Available Technology. *International Journal of Greenhouse Gas Control* **2012**, *9*, 160–171. https://doi.org/10.1016/j.ijggc.2012.02.018.

(221) Yang, J.; Han, S.; Cho, C.; Lee, C. H.; Lee, H. Bulk Separation of Hydrogen Mixtures by a One-Column PSA Process. *Separations Technology* **1995**, *5* (4), 239–249. https://doi.org/10.1016/0956-9618(95)00128-X.

(222) Sircar, S.; Rao, M. B.; Golden, T. C. Fractionation of Air by Zeolites. In *Studies in Surface Science and Catalysis*; Dabrowski, A., Ed.; Elsevier Science B. V.: Lublin, Poland, 1999; Vol. 120, pp 3–1067.

(223) Chattanathan, S. A.; Adhikari, S.; McVey, M.; Fasina, O. Hydrogen Production from Biogas Reforming and the Effect of H2S on CH4 Conversion. *Int J Hydrogen Energy* **2014**, *39* (35), 19905–19911. https://doi.org/10.1016/J.IJHYDENE.2014.09.162.

(224) Vadarlis, A. A.; Lacerda de Oliveira Campos, B.; Lemonidou, A. A.; Boukis, N.; Sauer, J. Supercritical Water Gasification of Ethanol as Biomass Model Compound in Tandem with Steam Reforming: Kinetic Modeling of the Reforming Step and Techno-Economic Analysis of the Integrated Concept. *Ind Eng Chem Res* **2024**, *63* (39), 16683–16700. https://doi.org/10.1021/acs.iecr.4c01486.

(225) Towler, G. P.; Sinnott, R. K. *Chemical Engineering Design : Principles, Practice, and Economics of Plant and Process Design*; Butterworth-Heinemann, 2013.

(226) Bongartz, D.; Burre, J.; Mitsos, A. Production of Oxymethylene Dimethyl Ethers from Hydrogen and Carbon Dioxide - Part I: Modeling and Analysis for OME1. *Ind Eng Chem Res* **2019**, *58* (12), 4881–4889. https://doi.org/10.1021/acs.iecr.8b05576.

(227) Lacerda de Oliveira Campos, B.; John, K.; Beeskow, P.; Herrera Delgado, K.; Pitter, S.; Dahmen, N.; Sauer, J. A Detailed Process and Techno-Economic Analysis of Methanol Synthesis from H2 and CO2 with Intermediate Condensation Steps. *Processes* **2022**, *10* (8), 1535. https://doi.org/10.3390/pr10081535.

(228) Peters, M. S.; Timmerhaus, K. D.; West, R. E. *PLANT DESIGN AND ECONOMICS FOR CHEMICAL ENGINEERS*, Fifth.; Glandt, E. D., Klein, M. T., Edgar, T. F., Eds.; McGraw-Hill, 1959; Vol. 5. https://doi.org/10.1080/00137915908965075.

(229) Chemical Engineering Essentials for the CPI Professional - November 2021 - 48. *www.chemengonline.com*. New York September 2023. www.chemengonline.com (accessed 2023-12-12).

(230) Albrecht, F. G.; König, D. H.; Baucks, N.; Dietrich, R. U. A Standardized Methodology for the Techno-Economic Evaluation of Alternative Fuels – A Case Study. *Fuel* **2017**, *194*, 511–526. https://doi.org/10.1016/J.FUEL.2016.12.003.

(231) Lee, S.; Kim, H. S.; Park, J.; Kang, B. M.; Cho, C.-H.; Lim, H.; Won, W. Scenario-Based Techno-Economic Analysis of Steam Methane Reforming Process for Hydrogen Production. *Applied Sciences* **2021**, *11* (13), 6021. https://doi.org/10.3390/app11136021.

(232) *Ethanol Price*. https://www.finanzen.net/rohstoffe/ethanolpreis (accessed 2023-10-10).

(233) Yan, Y.; Manovic, V.; Anthony, E. J.; Clough, P. T. Techno-Economic Analysis of Low-Carbon Hydrogen Production by Sorption Enhanced Steam Methane Reforming (SE-SMR) Processes. *Energy Convers Manag* **2020**, *226*, 113530. https://doi.org/10.1016/j.enconman.2020.113530.

(234) Granjo, J. F. O.; Oliveira, N. M. C. Process Simulation and Techno-Economic Analysis of the Production of Sodium Methoxide. *Ind Eng Chem Res* **2016**, *55* (1), 156–167. https://doi.org/10.1021/acs.iecr.5b02022.

(235) *Near-Critical and Supercritical Water and Their Applications for Biorefineries*; Fang, Z., Xu, C., Eds.; Biofuels and Biorefineries; Springer Dordrecht, 2014; Vol. 2. https://doi.org/10.1007/978-94-017-8923-3.

(236) Vivanpatarakij, S.; Assabumrungrat, S. Thermodynamic Analysis of Combined Unit of Biomass Gasifier and Tar Steam Reformer for Hydrogen Production and Tar Removal. *Int J Hydrogen Energy* **2013**, *38* (10), 3930–3936. https://doi.org/10.1016/j.ijhydene.2012.12.039.

(237) Kumar, M.; Oyedun, A. O.; Kumar, A. A Comparative Analysis of Hydrogen Production from the Thermochemical Conversion of Algal Biomass. *Int J Hydrogen Energy* **2019**, *44* (21), 10384–10397. https://doi.org/10.1016/j.ijhydene.2019.02.220.

(238) Campanario, F. J.; Gutiérrez Ortiz, F. J. Techno-Economic Assessment of Bio-Oil Aqueous Phase-to-Liquids via Fischer-Tropsch Synthesis and Based on Supercritical Water Reforming. *Energy Convers Manag* **2017**, *154*, 591–602. https://doi.org/10.1016/j.enconman.2017.10.096.

(239) Acelas, N. Y.; López, D. P.; Wim Brilman, D. W. F.; Kersten, S. R. A.; Kootstra, A. M. J. Supercritical Water Gasification of Sewage Sludge: Gas Production and Phosphorus Recovery. *Bioresour Technol* **2014**, *174*, 167–175. https://doi.org/10.1016/j.biortech.2014.10.003.

(240) Gasafi, E.; Reinecke, M. Y.; Kruse, A.; Schebek, L. Economic Analysis of Sewage Sludge Gasification in Supercritical Water for Hydrogen Production. *Biomass Bioenergy* **2008**, *32* (12), 1085–1096. https://doi.org/10.1016/J.BIOMBIOE.2008.02.021.

(241) *Einwohnerzahl der größten Städte in Deutschland am 31. Dezember 2022*. Statistisches Bundesamt. https://de.statista.com/statistik/daten/studie/1353/umfrage/einwohnerzahlen-der-grossstaedte-deutschlands/ (accessed 2024-01-22).

(242) Galera, S.; Gutiérrez Ortiz, F. J. Techno-Economic Assessment of Hydrogen and Power Production from Supercritical Water Reforming of Glycerol. *Fuel* **2015**, *144*, 307–316. https://doi.org/10.1016/j.fuel.2014.12.033.

(243) Chakinala, A. G.; Brilman, D. W. F.; Van Swaaij, W. P. M.; Kersten, S. R. A. Catalytic and Non-Catalytic Supercritical Water Gasification of Microalgae and Glycerol. *Ind Eng Chem Res* **2010**, *49* (3), 1113–1122. https://doi.org/10.1021/IE9008293.

(244) Gutiérrez Ortiz, F. J.; Ollero, P.; Serrera, A.; Galera, S. Process Integration and Exergy Analysis of the Autothermal Reforming of Glycerol Using Supercritical Water. *Energy* **2012**, *42* (1), 192–203. https://doi.org/10.1016/J.ENERGY.2012.03.069.

(245) Gutiérrez Ortiz, F. J.; Ollero, P.; Serrera, A.; Galera, S. An Energy and Exergy Analysis of the Supercritical Water Reforming of Glycerol for Power Production. *Int J Hydrogen Energy* **2012**, *37* (1), 209–226. https://doi.org/10.1016/J.IJHYDENE.2011.09.058.

(246) Attarbachi, T.; Kingsley, M. D.; Spallina, V. New Trends on Crude Glycerol Purification: A Review. *Fuel* **2023**, *340*, 127485. https://doi.org/10.1016/j.fuel.2023.127485.

(247) George, J. F.; Müller, V. P.; Winkler, J.; Ragwitz, M. Is Blue Hydrogen a Bridging Technology? - The Limits of a CO2 Price and the Role of State-Induced Price Components for Green Hydrogen Production in Germany. *Energy Policy* **2022**, *167*, 113072. https://doi.org/10.1016/j.enpol.2022.113072.

(248) Fiori, L.; Valbusa, M.; Castello, D. Supercritical Water Gasification of Biomass for H2 Production: Process Design. *Bioresour Technol* **2012**, *121*, 139–147. https://doi.org/10.1016/j.biortech.2012.06.116.

(249) Safari, F.; Tavasoli, A.; Ataei, A. Gasification of Sugarcane Bagasse in Supercritical Water Media for Combined Hydrogen and Power Production: A Novel Approach. *International Journal of Environmental Science and Technology* **2016**, *13* (10), 2393–2400. https://doi.org/10.1007/s13762-016-1055-7.

(250) Thilakaratne, R.; Wright, M. M.; Brown, R. C. A Techno-Economic Analysis of Microalgae Remnant Catalytic Pyrolysis and Upgrading to Fuels. *Fuel* **2014**, *128*, 104–112. https://doi.org/10.1016/J.FUEL.2014.02.077.

(251) Boukis, N.; Galla, U.; Müller, H.; Dinjus, E. Hydrothermal Gasification of Glycerol on the Pilot Scale. *16th European Biomass Conference & Exhibition*. 2008.

(252) Koningen, J.; Sjöström, K. Sulfur-Deactivated Steam Reforming of Gasified Biomass. *Ind Eng Chem Res* **1998**, *37* (2), 341–346. https://doi.org/10.1021/IE970452T.

(253) Gillan, C.; Fowles, M.; French, S.; Jackson, S. D. Ethane Steam Reforming over a Platinum/Alumina Catalyst: Effect of Sulfur Poisoning. *Ind Eng Chem Res* **2013**, *52* (37), 13350–13356. https://doi.org/10.1021/ie401999t.

(254) Ruhnau, O.; Stiewe, C.; Muessel, J.; Hirth, L. *Gas Demand in Times of Crisis: Energy Savings by Consumer Group in Germany*; 2022. https://hdl.handle.net/10419/265522 (accessed 2024-11-02).

(255) Chen, I.; Chen, F.-L. Effect of Alkali and Alkaline-Earth Metals on the Resistivity to Coke Formation and Sintering of Nickel-Alumina Catalysts. *Ind Eng Chem Res* **1990**, *29* (4), 534–539.

(256) Weisz, P. B.; Prater, C. D. Interpretation of Measurements in Experimental Catalysis. *Advances in Catalysis* **1954**, *6* (C), 143–196. https://doi.org/10.1016/S0360-0564(08)60390-9.

(257) Green, D. W.; Perry, R. H. *Perry's Chemical Engineers' Handbook, Eighth Edition*; McGraw-Hill Education, 2008.

(258) Green, D. W.; Perry, R. H. *Perry's Chemical Engineers' Handbook, Eighth Edition*; McGraw-Hill Education, 2008.

(259) Düren, T.; Q. Snurr, R. Using Molecular Simulation to Characterise Metal-Organic Frameworks and Judge Their Performance as Adsorbents. In *Studies in Surface Science and Catalysis*; Elsevier, 2007; Vol. 160, pp 161–168. https://doi.org/10.1016/S0167-2991(07)80022-X.

(260) Yang, J.; Lee, C. H.; Chang, J. W. Separation of Hydrogen Mixtures by a Two-Bed Pressure Swing Adsorption Process Using Zeolite 5A. *Ind Eng Chem Res* **1997**, *36* (7), 2789–2798. https://doi.org/10.1021/IE960728H/ASSET/IMAGES/LARGE/IE960728HF00015.JPEG.

(261) Tian, C.; Fu, Q.; Ding, Z.; Han, Z.; Zhang, D. Experiment and Simulation Study of a Dual-Reflux Pressure Swing Adsorption Process for Separating N2/O2. *Sep Purif Technol* **2017**, *189*, 54–65. https://doi.org/10.1016/J.SEPPUR.2017.06.041.

Supplementary Material (SM)

S1. Supplementary Material of Chapter 3

S1.1 Thermodynamic equilibrium: steam reforming of the gas produced by SCWG of 8 wt.% EtOH

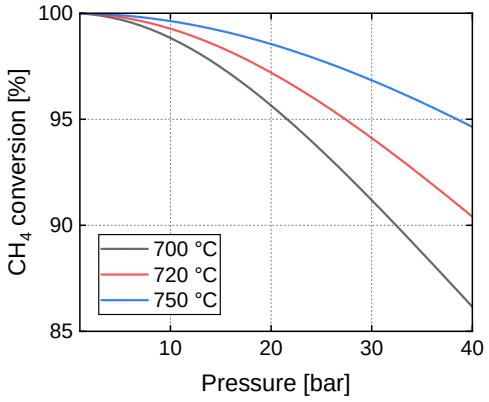

Figure S1. Conversion of CH_4 versus pressure for different temperatures in the SR reactor at thermodynamic equilibrium (SCWG with 8 wt.% EtOH at 600 °C and 265 bar).

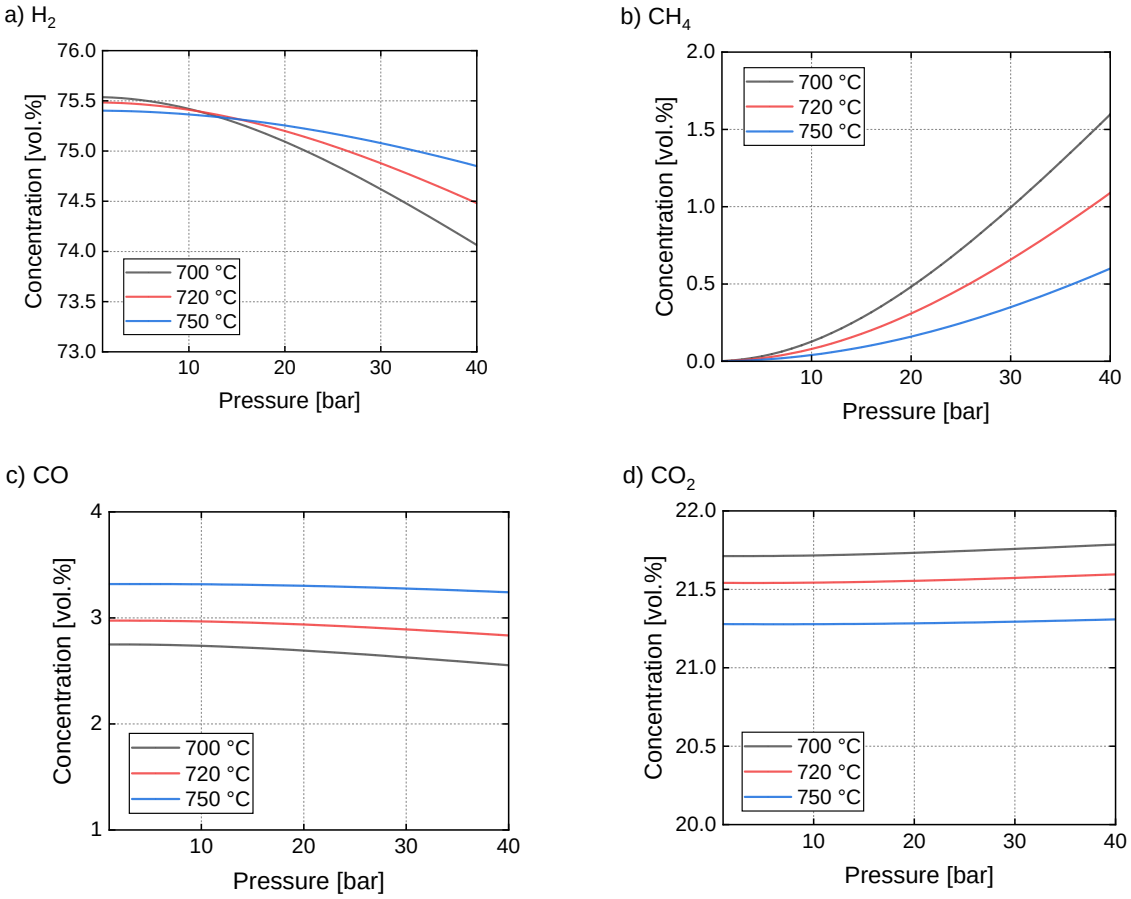

Figure S2. Dry product gas composition of SR product at thermodynamic equilibrium with pressure for different temperatures in the SR reactor. a) Concentration of H_2, b) Concentration of CH_4, c) Concentration of CO, and d) Concentration of CO_2 (SCWG with 8 wt.% EtOH at 600 °C and 265 bar).

S1.2 Characterization techniques of the deactivated catalyst at 770 °C

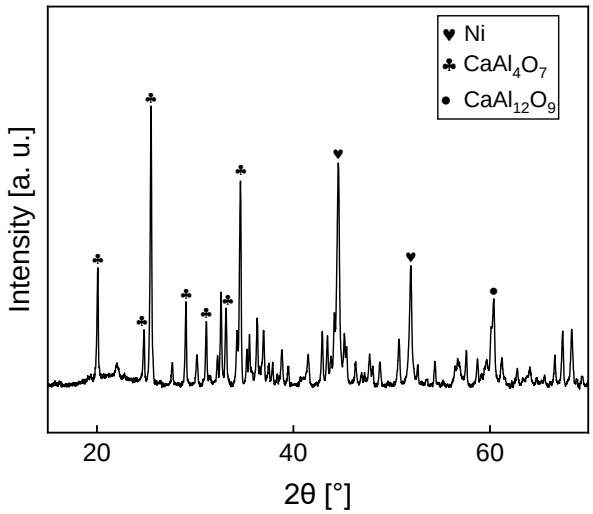

Figure S3. XRD profile of the catalyst subjected to 770 °C, atmospheric pressure, and GHSV = 65000 h^{-1}. SCWG conditions: p = 265 bar, T = 600 °C.

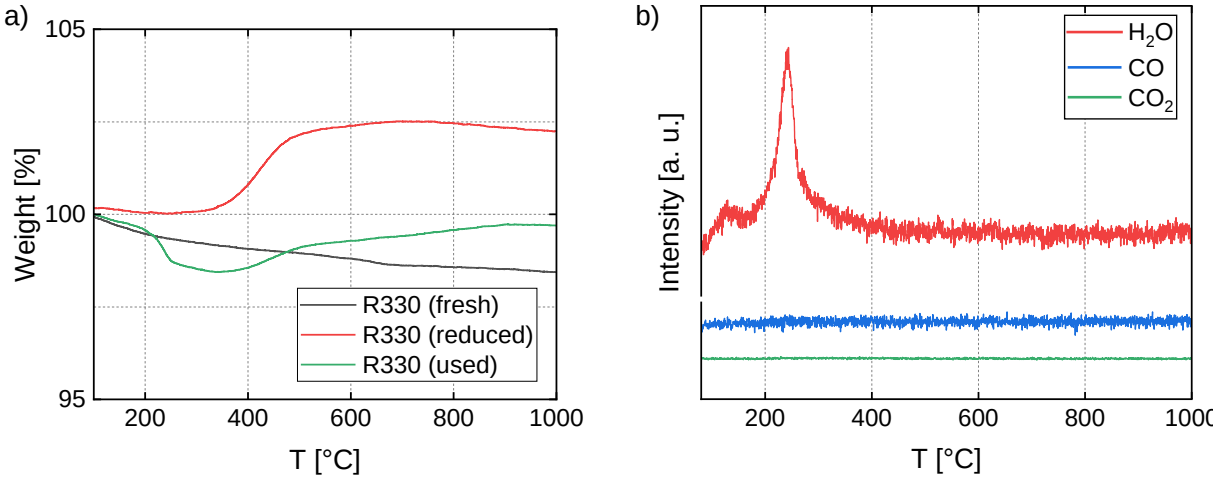

Figure S4. a) TGA of the catalyst used at 770 °C and b) respective MS signals of water vapor and carbon oxides.

S1.3 Thermodynamic equilibrium: steam reforming of the gas produced by SCWG of EtOH with different concentrations

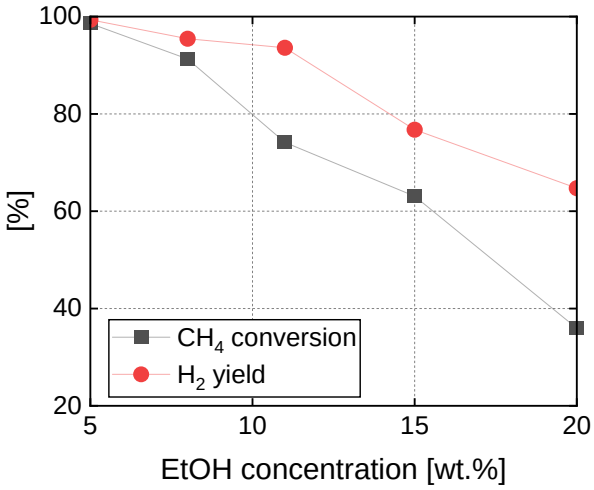

Figure S5. Equilibrium CH_4 conversion and H_2 yield from SR of the product gas from SCWG of EtOH versus the concentration of EtOH in the feed to the system (SCWG at 600 °C and 265 bar; T in the SR reactor = 730 °C; p in the SR reactor = 30 bar).

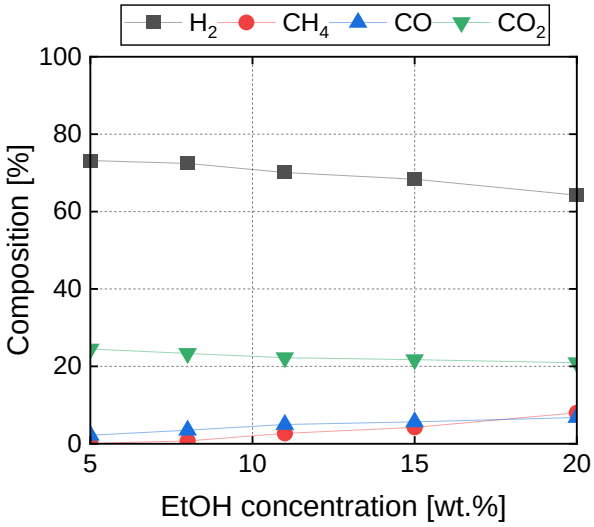

Figure S6. SR product gas equilibrium composition with different EtOH concentrations in the SCWG reactor (SCWG at 600 °C and 265 bar; T in the SR reactor = 730 °C; p in the SR reactor = 30 bar).

S1.4 Mass transfer control criteria

In order to determine if there are mass transfer restrictions in the steam reforming catalytic bed, two diffusion control criteria have been applied. First the Mears criterion [203,204] for external diffusion:

$$M_{criterion} = \frac{r_A \cdot \rho_b \cdot R \cdot n}{k_c \cdot C_{CH_4(bulk)}} \ll 0.15 \qquad (S1)$$

where r_A denotes the reaction rate (mol kg_{cat}^{-1} s^{-1}), ρ_b the apparent density of the catalytic bed (kg m^{-3}), R the radius of the catalyst particles (m), n the reaction order, k_c the mass transport coefficient (m s^{-1}) and $C_{CH4(bulk)}$ the concentration of methane in the bulk (mol m^{-3}). The Weisz-Prater criterion was applied for determining possible internal diffusion limitations [204,256]:

$$WP_{criterion} = \frac{r_A \cdot \rho_c \cdot R^2}{D_{eff.} \cdot C_{CH_4(surface)}} \ll 1 \qquad (S2)$$

where, ρ_c refers to the actual density of the catalyst (kg m^{-3}), $D_{eff.}$ the effective diffusion (m^2 s^{-1}) and $C_{CH4(surface)}$ the concentration of methane on the catalyst surface (mol m^{-3}).

The criteria of external and internal diffusion control were applied under steam reforming of an 8 wt.% ethanol SCWG (600 °C, 265 bar) product gas, at SR conditions of 740 °C, with 2 g of catalyst, and varying pressures. An example with calculations is given for the case of 1 bar pressure in the SR reactor, with the catalyst R210, and with a GHSV = 63500 h^{-1}.

First, the external diffusion control criterion is calculated from Eq. S1:

$$M_{criterion} = \frac{r_A \cdot d_{cat.} \cdot R \cdot n}{k_c \cdot C_{CH_4(bulk)}} \ll 0.15$$

where:

- r_A is the rate of methane consumption. In this experiment, the inlet molar flow of methane was $CH_{4,in}$ = 0.135 mol h^{-1} and the respective outlet molar flow was $CH_{4,out}$ = 0.0044 mol h^{-1}. Given that the catalyst mass was 2 g, these data generate an r_A of 0.0182 mol_{CH4} kg_{cat}^{-1} s^{-1}.
- $d_{cat.}$ was the bulk density of the catalyst, calculated to be equal to 915 kg m^{-3}.
- *R* is the radius of the catalyst particles. Since there were particles of a diameter ranging from 250 to 500 μm, R is to be the radius of the largest particles, i.e., half the largest diameter, *R* = 250 μm [204],

- n is the reaction order for methane overall consumption, considered to be equal to 1.
- k_C is the mass transfer coefficient (m s^{-1}):

$$k_C = \frac{Sh \cdot D_{AB}}{d_p} \quad (S3)$$

where d_p is the particles diameter, equal to 500 μm and Sh is the Sherwood number [204]:

$$Sh = 2 + 1.1 \cdot Re^{0.6} \cdot Sc^{0.33} \quad (S4)$$

The Sherwood number represents the ratio of convective mass transfer to the rate of diffusive mass transfer. The higher the Sh number is, the lower the diffusion rate is, compared to the convective mass transfer rate. Thus, the lowest possible value of this number is selected, in order to simulate the worst-case scenario. D_{AB} is the molecular diffusivity of CH_4 on water in m^2 s^{-1} (water in the form of steam is the highly abundant gas in the reactor) [257]:

$$D_{AB} = D_{CH_4-water} = \frac{0.1013 \cdot T^{1.75} \cdot \left(\frac{1}{M_{CH_4}} + \frac{1}{M_{H_2O}}\right)^{\frac{1}{2}}}{p\left\{\left(\sum \theta_{CH_4}\right)^{\frac{1}{3}} + \left(\sum \theta_{H_2O}\right)^{\frac{1}{3}}\right\}} \quad (S5)$$

p = 101,325 Pa, T = 873.15 K, θ_{CH4}, and θ_{H2O} are the atomic diffusion volumes of methane and water, given by tables from chemical engineering handbooks, like Perry's Chemical Engineering Handbook [258]. Its value is calculated to be $D_{CH4\text{-}water}$ = 2.31 · 10^{-3} m^2 s^{-1}. Therefore, the value of mass transfer coefficient k_c is found to be 9.25 m s^{-1}.

- $C_{CH4(bulk)}$ is the bulk concentration of CH_4 in mol m^{-3}:

$$C_{CH_4\,(bulk)} = \frac{n_{CH_4}}{V} = \frac{p_{CH_4}}{RT}$$

p_{CH4} = 0.0331 atm, n_{CH4} = 0.0335 mol mol^{-1}, and R is the ideal gas constant (8.2 · 10^{-5} m^3 atm K^{-1} mol^{-1}). Therefore, the bulk methane concentration equals 0.461 mol m^{-3}.

Based on the above parameter values, the Eq. 1 results in $M_{criterion}$ = 0.001576 << 0.15. The values of the $M_{criterion}$ for the rest experimental data are given in Table S1.

Table S1. External diffusion criteria for the two tested catalysts at different pressures.

P (bar) (T = 740 °C, GHSV = 63500 h^{-1})	Mears criterion (R210)	Mears criterion (R330)
1	0.001576	0.001767
10	0.001539	0.001735
20	0.001494	0.001634
30	0.001439	0.001483
40	0.001369	0.001335

The Weisz-Prater criterion (WP) is applied for investigating the possible importance of internal diffusion in the catalyst particles [204]:

$$WP_{criterion} = \frac{r_{CH_4} \cdot \rho_c \cdot R^2}{D_{eff.} \cdot C_{CH_4(surface)}} \ll 1 \qquad (S6)$$

- The methane consumption rate r_{CH4} is already calculated (= 0.0182 mol_{CH4} kg_{cat}^{-1} s^{-1}).
- The ρ_c is the actual density of the catalyst:

$$\rho_c = \frac{\rho_b}{1-\varepsilon} \qquad (S7)$$

$$\varepsilon = \frac{V_p}{V_b} \qquad (S8)$$

where ε is the porosity, V_p is the total pore volume, found equal to 0.025 cm^3 g^{-1} from the BET measurements and V_b is the bulk catalyst volume (= $1 \cdot \rho_b^{-1}$ = 1.093 cm^3 g^{-1}). Thus, the porosity is ε = 2.29% and the ρ_c = 936.4 kg m^{-3}.

- The $D_{eff.}$ is the effective diffusivity (cm^2 s^{-1}) [204]:

$$D_{eff.} = \frac{1}{\frac{1}{D_b} + \frac{1}{D_{Kn}}} \qquad (S9)$$

where, D_b is the gas bulk diffusivity: $D_b = \frac{\bar{v}\lambda}{3}$, with λ being the mean free path of methane in m (distance between collisions), and $\bar{v}_{CH_4}$ the mean velocity (m s^{-1}):

$$\lambda = \frac{1}{\sqrt{2}\pi\sigma_{CH_4}^2\left(\frac{n_{CH_4}}{V}\right)} = \frac{RT}{\sqrt{2}\pi\sigma_{CH_4}^2 P_A} = \frac{1}{\sqrt{2}\pi\sigma_{CH_4}^2 C_{CH_4,bulk}} \quad (S10)$$

σ_{CH4} is the molecular diameter (or collision diameter) of methane, which equals 3.73 Å = 3.73 · 10^{-8} cm [259],

$$\bar{v}_{CH_4} = \sqrt{\frac{8k_B T}{\pi m_{CH_4}}} \quad (S11)$$

m_{CH4} is the mass of one methane molecule (= 2.66 ·10^{-26} kg per molecule), k_B is the Boltzmann's constant (= 1.38 ·10^{-23} J K^{-1}). D_{Kn} is the Knudsen diffusion constant (m^2 s^{-1}):

$$D_{Kn} = \frac{\bar{v}d_p}{3} \quad (S12)$$

If the $\lambda >> d_p$ then the Knudsen diffusion dominates (frequent collision with the walls of the pores) [204]. In this example, λ = 9412 nm, while d_p = 9.2 nm. Thus, Knudsen diffusion dominates, thus $D_{eff.} \cong D_{Kn} = 0.0354$ cm^2 s^{-1}.

- The $C_{CH4(surface)}$ is considered equal to $C_{CH4(bulk)}$ (= 0.286 mol m^{-3}) because according to the Mears criterion, the external diffusion phenomena are weak and do not affect significantly the concentration of methane on the surface of the catalyst.

The Weisz-Prater criterion at GHSV = 63500 h^{-1}, 740 °C, and 1 bar is thus equal to 1.05193. Table S2 gives the WP values of the two catalysts at the different pressures tested.

Table S2. External diffusion criteria for the two tested catalysts at different pressures.

P (bar) (T = 740 °C, GHSV = 63500 h^{-1})	WP criterion (R210)	WP criterion (R330)
1	1.05193	1.63338
10	0.10271	0.16040
20	0.04987	0.07555
30	0.03202	0.04571

40	0.02285	0.03085

The diffusion in the catalyst pores is measured by the effective pore diffusivity, D_{eff}. It was determined that under atmospheric pressure, Knudsen pore diffusion dominates in both catalysts, thus, the effective diffusivities were calculated by equation S12. The $D_{eff.}$ of the R330 was equal to $2.6 \cdot 10^{-6}$ m^2 s^{-1}, while the $D_{eff.}$ of the R210 had a higher value of $3.5 \cdot 10^{-6}$ m^2 s^{-1}. Since $\bar{v}_{CH_4}$ is the same for both catalysts, according to equation S12, the lower diffusivity value stems from the smaller pore size of the R330 compared to that of R210 ($d_{p,R330}$ = 6.7 nm < $d_{p,R210}$ = 9.2 nm). The higher the value of $D_{eff.}$, the more intensive the diffusion of the reactant molecules in the pores becomes; thus, the resistance to the reaction on the surface of the catalyst pores gets stronger.

S2. Supplementary Material of Chapter 4

S2.1 Mass balances

The design of the equipment was based primarily on the results of the simulation in Aspen HYSYS V14. In Figure S7, the process flow diagram of the process presented in main text is presented as developed in the software. Table S3 Part 1 represents the properties of the streams found in the PFD of Aspen HYSYS, while S3 Part 2 presents their respective molar compositions.

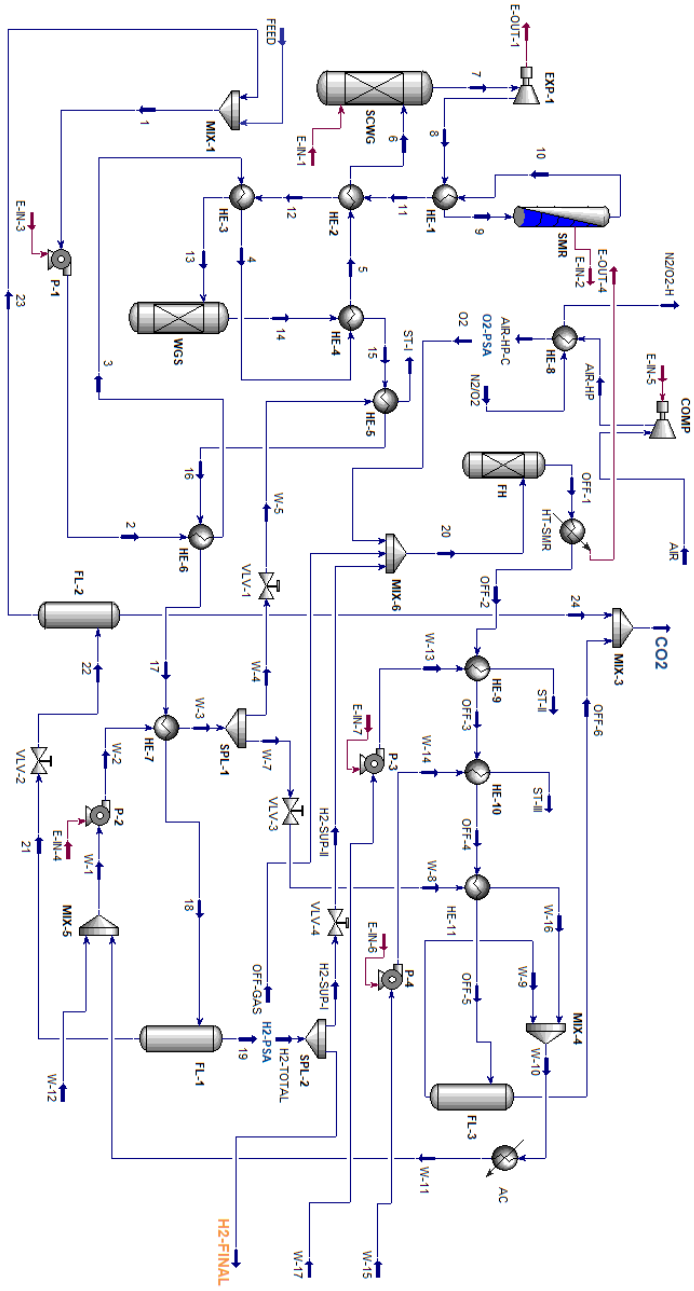

Figure S7. Process flow diagram as presented in Aspen HYSYS.

Table S3. Mass balances for the process with 10 t h^{-1} and 15 wt.% EtOH.

Stream ID	Mole flow [kmol h^{-1}]	Mass flow [t h^{-1}]	Temperature [°C]	Pressure [bar]	Molar enthalpy [MJ $kmol^{-1}$]	Molar entropy [kJ $kmol^{-1}$ $°C^{-1}$]
FEED	109.9	2.9	16.4	1.0	-283.8	38.75
1	504.4	10.0	17.7	1.0	-285.5	51.2
2	504.4	10.0	20.0	250	-284.8	51.4
3	504.4	10.0	91.0	249.7	-279.3	68.4
4	504.4	10.0	136.0	249.4	-275.6	77.8
5	504.4	10.0	200.0	249.1	-270.2	90.2
6	504.4	10.0	317.0	248.7	-257.7	113.5
7	554.5	10.0	600.0	248.7	-202.7	167.7
8	554.5	10.0	331.1	30.0	-211.1	172.6
9	554.5	10.0	578.0	29.7	-201.0	186.7
10	614.2	10.0	803.4	29.7	-162.6	187.3
11	614.2	10.0	574.9	29.4	-171.7	177.9
12	614.2	10.0	305.3	29.4	-181.9	163.4
13	614.2	10.0	224.3	29.3	-184.9	157.9
14	614.2	10.0	246.9	29.3	-184.9	158.6
15	614.2	10.0	204.5	29.3	-189.4	149.4
16	614.2	10.0	150.0	29.3	-209.6	105.2
17	614.2	10.0	109.3	29.2	-214.2	93.9
18	614.2	10.0	30.2	29.2	-219.6	78.3
19	219.6	2.9	30.2	29.2	-101.7	117.0
20	145.9	4.0	29.7	1.4	-153.1	161.9
21	394.6	7.1	30.2	29.2	-285.2	56.7
22	394.6	7.1	30.8	1.0	-285.2	56.9

23	394.5	7.1	20.0	1.0	-286.0	54.2
24	0.1	$5.0 \cdot 10^{-3}$	20.0	1.0	-390.0	172.7
H2-TOTAL	131.1	0.3	30.2	29.2	0.2	95.9
H2-SUP-I	14.5	$2.9 \cdot 10^{-2}$	30.2	29.2	0.2	95.9
H2-FINAL	116.6	0.2	30.2	29.2	0.2	95.9
AIR	352.9	10.2	17.0	1.0	-0.2	150.9
AIR-HP	352.9	10.2	54.3	1.4	0.8	151.7
AIR-HP-C	351.9	10.2	50.0	1.4	0.5	150.8
N2/O2	313.6	8.9	45.0	1.0	$-4.0 \cdot 10^{-2}$	147.8
N2/O2-H	313.6	8.9	49.8	1.0	0.3	149.0
O2	43.6	1.4	24.0	1.4	$-4.2 \cdot 10^{-2}$	145.2
OFF-2	127.4	4.0	1027.0	1.4	-266.1	238.9
OFF-3	127.4	4.0	400.0	1.4	-295.5	208.2
OFF-4	127.4	4.0	200.0	1.4	-303.7	193.8
OFF-5	127.4	4.0	40.0	1.4	-328.0	125.6
OFF-6	73.6	3.1	40.0	1.4	-359.7	174.2
OFF-GAS	88.5	2.6	31.7	1.4	-252.4	166.6
W-1	4241	76.4	20.0	1.0	-286.0	54.2
W-2	4241	76.4	20.3	32.0	-285.9	54.2
W-3	4241	76.4	31.0	32.0	-285.1	56.8
W-4	263.2	4.7	31.0	32.0	-285.1	56.8
W-5	263.2	4.7	31.6	4.5	-285.1	57.0
ST-I	263.2	4.7	148.0	4.5	-237.9	172.6
W-7	3978	71.7	31.0	32.0	-285.1	56.8
W-8	3978	71.7	31.7	1.0	-285.1	57.1

W-9	53.8	1.0	40.0	1.4	-284.5	59.0
W-10	4031	72.6	42.4	1.0	-284.3	59.6
W-11	4031	72.6	20.0	1.0	-286.0	54.2
W-12	209.4	3.8	19.7	1.0	-286.0	54.1
W-13	75.5	1.4	20.0	25.0	-285.9	54.2
W-14	21.6	0.4	20.0	4.5	-286.0	54.2
W-15	21.6	0.4	20.0	1.0	-286	54.2
W-16	3978.0	71.7	42.4	1.0	-284.3	59.6
W-17	75.5	1.4	19.8	1.0	-286.0	54.2
ST-II	75.5	1.4	224.9	25.0	-236.2	162.9
ST-III	21.7	0.4	152.6	4.5	-237.7	173.0

Table S4. Molar composition of the process streams (15 wt.% EtOH with 10 t h^{-1}).

Stream ID	C_2H_6O	H_2O	H_2	CH_4	CO_2	CO	N_2	O_2
FEED	0.3	0.7	0	0	0	0	0	0
1	0.07	0.93	0	0	0	0	0	0
2	0.07	0.93	0	0	0	0	0	0
3	0.07	0.93	0	0	0	0	0	0
4	0.07	0.93	0	0	0	0	0	0
5	0.07	0.93	0	0	0	0	0	0
6	0.07	0.93	0	0	0	0	0	0
7	0	0.82	0.06	0.07	0.04	0.0013	0	0
8	0	0.82	0.06	0.07	0.04	0.0013	0	0
9	0	0.82	0.06	0.07	0.04	0.0013	0	0

10	0	0.7	0.23	0.02	0.07	0.02	0	0
11	0	0.7	0.23	0.02	0.07	0.02	0	0
12	0	0.7	0.23	0.02	0.07	0.02	0	0
13	0	0.7	0.23	0.02	0.07	0.02	0	0
14	0	0.64	0.25	0.02	0.09	0.0004	0	0
15	0	0.64	0.25	0.02	0.09	0.0004	0	0
16	0	0.64	0.25	0.02	0.09	0.0004	0	0
17	0	0.64	0.25	0.02	0.09	0.0004	0	0
18	0	0.64	0.25	0.02	0.09	0.0004	0	0
19	0	0.0017	0.70	0.05	0.25	0.001	0	0
20	0	0.003	0.254	0.07	0.37	0.0016	0.03	0.27
21	0	0.9997	0	0	0.0003	0	0	0
22	0	0.9997	0	0	0.0003	0	0	0
23	0	1.0	0	0	0	0	0	0
24	0	0.024	0	0	0.9751	0	0	0
H2-TOTAL	0	0	0.9999	0	0.0001	0	0	0
H2-SUP-I	0	0	0.9999	0	0.0001	0	0	0
H2-FINAL	0	0	0.9999	0	0.0001	0	0	0
AIR	0	0	0	0	0	0	0.79	0.21
AIR-HP	0	0	0	0	0	0	0.79	0.21
AIR-HP-C	0	0	0	0	0	0	0.79	0.21
N2/O2	0	0	0	0	0	0	0.8887	0.1113
N2/O2-H	0	0	0	0	0	0	0.8887	0.1113
O2	0	0	0	0	0	0	0.0992	0.9008
OFF-2	0	0.4544	0	0	0.5083	0.002	0.034	0.002

OFF-3	0	0.4544	0	0	0.5083	0.002	0.034	0.002
OFF-4	0	0.4544	0	0	0.5083	0.002	0.034	0.002
OFF-5	0	0.4544	0	0	0.5083	0.002	0.034	0.002
OFF-6	0	0.056	0	0	0.88	0.0032	0.0586	0.0028
OFF-GAS	0	0.0042	0.2614	0.12	0.62	0.003	0	0
W-1	0	1	0	0	0	0	0	0
W-2	0	1	0	0	0	0	0	0
W-3	0	1	0	0	0	0	0	0
W-4	0	1	0	0	0	0	0	0
W-5	0	1	0	0	0	0	0	0
ST-I	0	1	0	0	0	0	0	0
W-7	0	1	0	0	0	0	0	0
W-8	0	1	0	0	0	0	0	0
W-9	0	1	0	0	0	0	0	0
W-10	0	1	0	0	0	0	0	0
W-11	0	1	0	0	0	0	0	0
W-12	0	1	0	0	0	0	0	0
W-13	0	1	0	0	0	0	0	0
W-14	0	1	0	0	0	0	0	0
W-15	0	1	0	0	0	0	0	0
W-16	0	1	0	0	0	0	0	0
W-17	0	1	0	0	0	0	0	0
ST-II	0	1	0	0	0	0	0	0
ST-III	0	1	0	0	0	0	0	0

S2.2 Exergy flows

Table S4 presents the exergy flows of all the process streams for the base case of 15 wt.% and 10 t h^{-1}. These values were used for the calculation of the exergy efficiency and exergy losses distribution.

Table S5. Exergy of the material streams for the case of 10 t h^{-1} with 15 wt.% EtOH.

Stream	Physical exergy [MW]	Chemical exergy [kJ kg^{-1}]	Exergy flow [MW]
FEED	0,000373	12,37	12,38
1	0,001000	12,37	12,38
2	0,083537	12,37	12,46
3	0,153241	12,37	12,53
4	0,269011	12,37	12,64
5	0,516280	12,37	12,89
6	1,285654	12,37	13,66
7	4,166444	12,70	16,86
8	2,645874	12,70	15,34
9	3,559323	12,70	16,26
10	4,638097	14,78	19,42
11	3,557296	14,78	18,34
12	2,549461	14,78	17,33
13	2,323315	14,78	17,10
14	2,349623	14,79	17,14
15	2,054181	14,79	16,85
16	0,847809	14,79	15,64
17	0,642815	14,79	15,43
18	0,520551	14,79	15,31

19	0,509512	14,79	15,30
20	0,032633	5,54	5,57
21	0,007005	0,00	0,01
22	0,000439	0,00	0,00
23	0,000339	0,00	0,00
24	0,000000	0,00	0,00
OFF-GAS	0,019711	4,39	4,41
H2-TOTAL	0,301222	10,41	10,71
H2-SUP-I	0,033323	1,15	1,18
H2-SUP-II	0,003239	1,15	1,15
H2-FINAL	0,267900	9,25	9,52
O2	0,009697	0,00	0,01
AIR	0,000312	0,00	0,00
AIR-HP	0,082389	0,00	0,08
AIR-HP-C	0,081357	0,00	0,08
N2/O2	0,001637	0,00	0,00
N2/O2-H	0,002502	0,00	0,00
OFF-1	3,779002	0,02	3,80
OFF-2	1,015457	0,02	1,03
OFF-3	0,293973	0,02	0,31
OFF-4	0,155614	0,02	0,17
OFF-5	0,016203	0,02	0,04
OFF-6	0,015790	0,02	0,03
CO2	0,000630	0,02	0,02
W-1	0,003724	0,00	0,00

W-2	0,080727	0,00	0,08
W-3	0,082573	0,00	0,08
W-4	0,005124	0,00	0,01
W-5	0,000929	0,00	0,00
W-7	0,077449	0,00	0,08
W-8	0,006008	0,00	0,01
W-9	0,000413	0,00	0,00
W-10	0,040085	0,00	0,04
W-11	0,003460	0,00	0,00
AC Inlet air	0,021156	0,00	0,02
AC Outlet air	0,005561	0,00	0,01
W-12	0,000201	0,00	0,00
W-13	0,001132	0,00	0,00
W-14	0,000063	0,00	0,00
W-15	0,000019	0,00	0,00
W-16	0,039694	0,00	0,04
W-17	0,000072	0,00	0,00
ST-I	0,932931	0,00	0,93
ST-II	0,365101	0,00	0,37
ST-III	0,077293	0,00	0,08

S2.3 Equipment design

GAS – LIQUID SEPARATORS

To separate the gases from the steam in the scale-up process, gas – liquid separators are used. The equations that are used for this purpose were taken from Towler and Sinnot [225]. First, the settling velocity of the liquid droplet, u_t is calculated:

$$u_t = k \cdot \left(\frac{\rho_L - \rho_v}{\rho_v}\right)^{\frac{1}{2}} \quad (S13)$$

where ρ_L = liquid density in kg m^{-3} and ρ_v = vapor density in kg m^{-3}, and k = 0.07 [225]. Peters, Timmerhaus and West [228], in their book, mention that k = 0.1 with a mesh deentrainer and k = 0.03 without a mesh deentrainer. Thus, the value that is selected here is 0.03.

The minimum diameter of the separator allowed is given from the following equation:

$$D_v = \left(\frac{4\dot{V}_v}{\pi u_s}\right)^{\frac{1}{2}} \quad (S14)$$

where D_v = minimum separator diameter in m, $\dot{V}_v$ = gas or vapor volumetric flow rate in m^3 s^{-1}, $u_s = 0.15 \cdot u_t$ (no demister pad is required). The respective height of the separator can be calculated by the following equation:

$$H = 1.5 \cdot D + 0.4 + \frac{\dot{V}_L}{A_c} \cdot t_h \quad (S15)$$

where $\dot{V}_L$ = liquid volumetric flow rate in m^3 s^{-1}, A_c = cross – sectional area of the vessel in m^2, and t_h = the liquid hold-up time in s, which is typically 10 minutes.

PRESSURE SWING ADSORPTION (PSA) UNITS

For the design of the PSA unit, the methodology from Towler and Sinnott [225] is applied. The amount of adsorbent required is estimated from the following equation that describes the mass balance on a single adsorption bed:

$$(F_1 y_1 - F_2 y_2) M_w t_a = 1000 (m_1 - m_2) M_a f_L \quad (S16)$$

where F_1 the feed molar flow rate (mol s^{-1}), F_2 the product molar flow rate (mol s^{-1}), y_1 the feed mole fraction of adsorbed component, y_2 the product mole fraction of adsorbed component, M_w the molecular weight of adsorbed component (g mol^{-1}), t_a the duration of the adsorption step of the cycle (s), m_1 the maximum adsorbent loading (g $g_{adsorbent}^{-1}$), m_2 the minimum adsorbent loading (g $g_{adsorbent}^{-1}$), M_a the mass of adsorbent per bed (kg), and f_L the fraction of the bed that is fully loaded, i.e., reaches loading m_1, at the end of the adsorption step.

In the case of hydrogen purification, the adsorbed component is CO_2, therefore the M_w = 44 g mol^{-1}. The duration of the adsorption phase of the cycle is set at 30 minutes, thus t_a = 1800 s [225]. The f_L is equal to 0.7 [225]. The adsorbent is zeolite 5A and data regarding its performance can be found from Yang et al. [221,260]. More specifically, the H_2 purity and recovery are 99.99% and 85%, respectively, while the adsorbent bulk density was given as equal to 795 kg m^{-3}, and the maximum and minimum adsorbent loadings based on their isotherm plot were found to be equal to 3.37 mmol g^{-1} and 0.37 mmol g^{-1}, respectively. Finally, a void volume fraction equal to 20% of the total volume occupied by the calculated adsorbent mass has also been considered, for inert packing and good flow distribution [225].

The same methodology was followed for the air separation unit. The recovery of O_2 was equal to 53% and its purity 90% [222]. Data on the isotherm of N_2, on the adsorbent's bulk density (641 kg m^{-3}) and on the interparticle void fraction (0.53) were taken from Tian et al. [261]. The maximum and minimum adsorbent loadings were equal to 0.99 mmol g^{-1} and 0.72 mmol g^{-1}, respectively.

HEAT EXCHANGERS

The heat exchangers were designed with the model Rigorous Shell & Tube of Aspen HYSYS V14. The construction material was carbon steel for every heat exchanger, except from the HE-1 and HE-2, which had SS304 and SS410, respectively. As an example, in Figure S8 the complete TEMA (Tubular Exchanger Manufacturers Association) document for the HE-2 for a feed flow rate of 1 t h^{-1} and 8 wt.% EtOH is given.

Heat Exchanger Specification Sheet

1	Company:									
2	Location:									
3	Service of Unit:		Our Reference:							
4	Item No.:		Your Reference:							
5	Date:	Rev No.:	Job No.:							
6	Size: 178 - 2550 mm	Type: DEU	Horizontal			Connected in: 1 parallel		1 series		
7	Surf/unit(eff.) 2,1 m²	Shells/unit 1				Surf/shell(eff.)		2,1 m²		
8	**PERFORMANCE OF ONE UNIT**									
9	Fluid allocation			Shell Side				Tube Side		
10	Fluid name			11-B->12				5-B->6		
11	Fluid quantity, Total		kg/h	1000				1000		
12	Vapor (In/Out)		kg/h	1000	1000			0	0	
13	Liquid		kg/h	0	0			1000	1000	
14	Noncondensable		kg/h	0	0			0	0	
15										
16	Temperature (In/Out)		°C	558	325,99			215	313,9	
17	Bubble / Dew point		°C	195,98 / 218,93	195,43 / 218,47			357,92 / 372,21	357,98 / 372,26	
18	Density Vapor/Liquid		kg/m³	7,39 /	10,47 /			/ 847,35	/ 723,26	
19	Viscosity		cp	0,0254 /	0,0179 /			/ 0,0948	/ 0,0904	
20	Molecular wt, Vap			16,75	16,75					
21	Molecular wt, NC									
22	Specific heat		kJ/(kg-K)	2,341 /	2,245 /			/ 4,619	/ 6,68	
23	Thermal conductivity		W/(m-K)	0,0966 /	0,0692 /			/ 0,6185	/ 0,4517	
24	Latent heat		kJ/kg							
25	Pressure (abs)		kPa	3009	2981,59			25130	25126,45	
26	Velocity (Mean/Max)		m/s	6,03 / 9,83				0,57 / 0,61		
27	Pressure drop, allow./calc.		kPa	70	27,41			70	3,549	
28	Fouling resistance (min)		m²-K/W	0,0001				0,0001	0,00018 Ao based	
29	Heat exchanged 147,5		kW				MTD (corrected)	140,57		°C
30	Transfer rate, Service 501,6			Dirty 501,7			Clean	583,2		W/(m²-K)
31	**CONSTRUCTION OF ONE SHELL**								**Sketch**	
32				Shell Side		Tube Side				
33	Design/Vacuum/test pressure:g		kPa	3400 / /		27700 / /				
34	Design temperature / MDMT		°C	595 /		355 /				
35	Number passes per shell			1		2				
36	Corrosion allowance		mm	0		0				
37	Connections	In	mm	1 73,66 / -		1 15,8 / -				
38	Size/Rating	Out		1 38,1 / -		1 15,8 / -				
39	ID	Intermediate		/ -		/ -				
40	Tube #: 7 U's	OD: 19,05	Tks. Average 4,19	mm	Length: 2550	mm	Pitch: 25,4	mm	Tube pattern:45	
41	Tube type: Plain		Insert:None		Fin#:	#/m	Material:SS 410			
42	Shell SS 410	ID 177,83	OD 219,08	mm	Shell cover	SS 410				
43	Channel or bonnet	SS 410			Channel cover	SS 410				
44	Tubesheet-stationary	SS 410	-		Tubesheet-floating	-				
45	Floating head cover	-			Impingement protection	None				
46	Baffle-cross SS 410	Type	Single segmental	Cut(%d) 29,8	Horiz	Spacing: c/c 50,8	mm			
47	Baffle-long -	Seal Type			Inlet 0	mm				
48	Supports-tube	U-bend	0	Type						
49	Bypass seal	Tube-tubesheet joint	Expanded only (2 grooves)(App.A 'f')							
50	Expansion joint	-	Type None							
51	RhoV2-Inlet nozzle 575	Bundle entrance 235	Bundle exit 34	kg/(m-s²)						
52	Gaskets - Shell side	Flat Metal Jacket Fibe	Tube side	Flat Metal Jacket Fibe						
53	Floating head	-								
54	Code requirements	ASME Code Sec VIII Div 1	TEMA class	R - refinery service						
55	Weight/Shell	672,6 Filled with water 728,4	Bundle 103	kg						
56	Remarks									
57										
58										

Figure S8. TEMA Sheet of HE-2 in the simulation where the feed flow rate was 1 t h^{-1} and the concentration of EtOH 8 wt.%.

SCWG REACTOR

The pre-liminary design of this reactor is based on estimating its volume. To do that, the following space velocity is used (SV) in $g_{feed}\ l_{reactor}^{-1}\ h^{-1}$:

$$SV = \frac{\dot{m_{feed}}}{V_{reactor}} \qquad (S17)$$

where $\dot{m_{feed}}$ is the mass flow rate of the feed to the reactor in g_{feed} h^{-1} and $V_{reactor}$ the volume of the reactor in l or m^3. This value is taken from Dutzi et al. [47], and is equal to 1715 g_{feed} $l_{reactor}^{-1}$ h^{-1}.

SMR REACTOR

For simulating the SMR reactor, the Plug Flow Reactor (PFR) model was used. The reaction set that was integrated to the PFR model consisted of three reactions, the SMR, the WGS, and the SER. Every reaction was chosen as *Heterogeneous Catalytic*. The Basis was set to be the partial pressure (*Partial Pres*), the reaction phase was chosen to be vapour (*VapourPhase*), the Basis and Rate units were bar and gmole l^{-1} s^{-1}, respectively. The Base Component for the SMR was CH_4, and for the WGS and SER it was water.

The objectives followed for the design of the SMR reactor was i) to produce a dry product gas, at stream 19 (see PFD), with a H_2 concentration of around 70%, because the PSA unit requires a H_2 concentration of at least 70% to produce a H_2-rich product with 99.99% purity and 85% recovery [221], and ii) that the SMR's outlet temperature was constant at 804 °C. The volume was calculated as a function of the number of tubes. The length of each tube (6 m), their inner diameter (70 mm), and their wall thickness (10 mm) were taken from Rostrup-Nielsen [177]. Apart from that, the heat provision was via a *Direct Value* of *Q* in the *Heat Transfer* field.

FIRED HEATER (FH)

The heat required to heat the SMR reactor and promote the corresponding reactions was provided by a fired heater. In industrial applications, the SMR reactor consists of tubes containing the catalyst located inside a furnace, in which the combustion of a gas provides the heat necessary to promote the reforming reactions [177]. This unit was designed with the implementation of a Conversion Reactor. This model requires a reaction set, which consisted of two reactions, i.e., the combustion of H_2 ($2H_2 + O_2 \rightarrow 2H_2O$) and CH_4 ($CH_4 + 2O_2 \rightarrow CO_2 + 2H_2O$) with oxygen. These two reactions in particular were simulated as

conversion reactions, with hydrogen and methane as their *Base Component*, respectively, with a *Rxn Phase* chosen as *Overall*, and only considering the parameter *CO* equal to 100.

The amount of flue gas and produced hydrogen needed for the combustion was based on the required energy of the SMR reactor and on the assumption that the hot flue gas (basically, CO_2 and H_2O) exited the furnace with a fixed temperature. According to Rostrup-Nielsen [177], the hot flue gas leaves the furnace with a temperature around 1300 K (i.e., around 1027 °C). This is the temperature that it was selected for the temperature of the product gas from the FH unit (OFF-2). The cooler HT-SMR simulates the heat transport from the flue gas to the reformer.

WGS REACTOR

For the WGS reactor, an Equilibrium Reactor model was applied. The only reaction taken into account in the reaction set was the WGS. The Basis for the calculations was the partial pressure of the reactants (*Partial Press*), the selected phase was vapour (*VapourPhase*), and the corresponding units were atm. The equilibrium constant (*Keq*) and its variation with temperature is already enlisted in the library of the software, thus, its value was taken from the software by selecting the option *Keq vs T Table*.

The estimation of the WGS reactor's volume was done based on the GHSV from Lee et al. [231]. They used a WGS catalyst with a GHSV of 6000 $Nm^3\ h^{-1}\ m_{cat}^{-3}$. This value is applied here too. The inlet flow rate in the WGS reactor in $Nm^3\ h^{-1}$ is given by Aspen HYSYS. The bulk density of the catalyst ShiftMax 210 was measured to be equal to 1140.5 kg m^{-3}.

AIR COOLER

The air-cooled heat exchanger is used to cool down the recycled water (after mixing stream W-9 and W-10). The methodology from the book of Towler and Sinnott [225] is applied to estimate the needed surface area in m^2. The surface area is calculated from the following equation:

$$Q = U \cdot A \cdot \Delta T_m \quad (S18)$$

where Q is the cooling duty provided by Aspen HYSYS in W, U is the overall heat transfer coefficient, which is taken equal to 300 W m^{-2} °C^{-1} [225], A the heat transfer area in m^2, and ΔT_m the mean temperature difference, given by equation S19:

$$\Delta T_m = F_t \cdot \Delta T_{ln} \quad (S19)$$

where F_t the correction factor, which is assumed to be equal to 0.9, according to Towler and Sinnott [225], and ΔT_{ln} is the log-mean temperature difference:

$$\Delta T_{ln} = \frac{\left(T_{h,in} - T_{c,out}\right) - \left(T_{h,out} - T_{c,in}\right)}{ln\frac{T_{h,in} - T_{c,out}}{T_{h,out} - T_{c,in}}} \quad (S20)$$

By assuming an average air temperature of 15 °C and adding 2 °C to compensate for recirculation, the inlet cold stream temperature ($T_{c,in}$) is 17 °C. The temperature of air remains almost constant at the outlet, thus $T_{c,out}$ = 17 °C [225]. The inlet hot water has a temperature of 42 °C and the outlet cooled water has 20 °C.

The fan power consumption is also estimated by the following equation:

$$W_f = \frac{u_f A_b \Delta P_b}{n_f} \quad (S21)$$

where u_f is the air face velocity and its typical value is 2.5 m s^{-1}, ΔP_b is the pressure drop across the bundle and is usually very low, i.e., an estimation of 150 N m^{-2} can be used for preliminary calculations, n_f is the fan efficiency, taken equal to 0.7, and A_b is the bundle area:

$$A_b = L' p_t N_{bk} \quad (S22)$$

where L' is the effective tube length, p_t is the tube pitch, and N_{bk} is the number of tubes per bank. After estimating the fan power consumption, one can assume a motor efficiency (m_f) of 95% and then calculate the total power consumption:

$$W_{total} = \frac{W_f}{m_f} \quad (S23)$$

The methodology from the book of Towler and Sinnott [225] is also applied here to estimate the bundle area and the total power consumption.

S2.4 Economic analysis

EQUIPMENT COSTS

The costs of the main equipment were calculated by equation 4.3 (see main text). Costs of reference equipment were found in the book of Peters et al. [228], except from the cost of the SCWG reactor and the high-pressure pump (P-1), which were found in the study of Gasafi et al. [240]. The scaling factors are also given by Peters et al. [228]. The reference equipment given by Peters et al. is for 2002, while the equipment by Gasafi et al. [240] for 2008. The CEPCI values for these years are 395.6 and 575.4, respectively, and are published by the Chemical Engineering Magazine [229]. Table S5 enlists the estimated purchasing costs of the main equipment for the case of 15 wt.% EtOH with a feed flow rate of 10 t h^{-1}. Table S6 presents the total equipment purchasing costs for different EtOH concentrations and S7 for different feed flow rates.

Table S6. Characteristic capacities and equipment costs of the main equipment for the case of 15 wt.% EtOH with 10 t h^{-1} feed flow rate.

Equipment ID	Type / Application	Characteristic capacity	Scaling factor	Construction material	Costs ($)
P-1	High-pressure pump	10.1 $m^3 h^{-1}$	0.33	Carbon steel	152,130
P-2	Reciprocating pump	79.1 $m^3 h^{-1}$		Cast iron	13,479
P-3		1.3 $m^3 h^{-1}$			3,513
P-4		0.4 $m^3 h^{-1}$			2,326
SCWG	Gasification reactor	10 t h^{-1}	0.56	Alloy 617	108,795
SMR	Steam methane reformer	0.5 m^3	0.6	Stainless steel	494,584
WGS	Water-gas shift reactor	2.4 m^3	0.6	Carbon steel	345,529
FL-1	Flash drum	5.0 m^3	0.6	Carbon steel	11,340
FL-2		0.6 m^3			3,151
FL-3		16.2 m^3			22,844

EXP-1	Steam turbine	1294.2 kW	0.6	Carbon steel	312,220
PSA-H_2	Pressure swig adsorption unit	23.3 m^3/adsorber	0.56	Carbon steel	85,985 (total unit)
PSA-O_2		67.4 m^3/adsorber	0.56		200,910 (total unit)
HE-1	Heat exchanger	9.99 m^2	0.6	SS304	44,165
HE-2		22.1 m^2		SS410	110,560
HE-3		18.3 m^2		Carbon steel	88,947
HE-4		31.8 m^2			79,974
HE-5		107.4 m^2			54,897
HE-6		34.7 m^2			86,517
HE-7		51.4 m^2			62,782
HE-8		2.4 m^2			4,186
HE-9		13.8 m^2			16,037
HE-10		6.6 m^2			10,331
HE-11		45.3 m^2			58,199
AC	Air-cooled heat exchanger	687.5 m^2	0.6	Carbon steel	112,447
Total Purchasing Equipment Cost (C_{total})					2,625,960

Table S7. Total Equipment Purchasing Costs for different EtOH concentrations with 1 t h^{-1}.

	EtOH feed concentration (wt.%)				
	8	11.5	15	18.5	20
Total Purchasing Equipment Cost (C_{total}) in $	663,809	786,364	834,620	1,008,565	1,057,084

Table S8. Total Equipment Purchasing Costs for different feed flow rates with 15 wt.% EtOH.

	Feed flow rate (t h^{-1})					
	1	5	10	50	100	160
Total Purchasing Equipment	834,620	1,850,388	2,625,960	6,599,083	9,937,748	11,761,840

Cost (C_{total}) in $						

OPERATING LABOR

The operating labor costs (C_{OL}) were calculated according to the following equation:

$$C_{OL} = Wage_{OP} \cdot N_{OP} \quad (S24)$$

where the $Wage_{OP}$ is the wage of every operator, equal to 72.000 € a^{-1} [227] (or 75.600 $\$_{2023}$ a^{-1}), and N_{OP} is the total number of operators [227,234]:

$$N_{OP} = F_{OP} \cdot \left(\left(6.29 + 0.23 \cdot N_{np}\right)^{0.5}\right) \quad (S25)$$

where N_{np} is the number of non-particulate processing units in the scaled-up plant, and F_{OP} the number of operators to cover every position in the plant at any time, which is estimated to be equal to 4.5.

From the book of Peters et al. [228], a relation between the employee-hours $(day)^{-1}$ $(processing\ step)^{-1}$ is given:

$$\log(Y) = a \cdot \log(X) \quad (S26)$$

where Y the employee-hours $(day)^{-1}$ $(processing\ step)^{-1}$ and X the plant capacity in kg day^{-1}. For a highly automated process with large equipment and only fluid processing, a can take the value of 0.26 [228]. Thus, for every plant capacity studied, considering that the relation between Y and C_{OL} is linear, the value of Y can be found and subsequently the value of C_{OL} at different plant capacities from the equation S27:

$$C_{OL,x} = \frac{Y_x}{Y_{ref}} \cdot C_{OL,ref.} \quad (S27)$$

where Y_x and $C_{OL,ref.}$ the values of employee-hours $(day)^{-1}$ $(processing\ step)^{-1}$ and operating labor costs, respectively, for a plant capacity X kg day^{-1}.

CAPITAL INVESTMENT

According to the methodology described in the main text, the direct and indirect costs that are given as a percentage of the total purchase cost of equipment (C_{total}), are used for the estimation of the fixed capital investment (CI_{fixed}) and the total capital investment (CI_{total}). These are taken from Albrecht et al. [230] and are presented in Table S8. Table S9 presents the CI_{fixed}, $C_{working}$ and CI_{total} at 1 t h^{-1} for different EtOH concentrations and S10 for different feed flow rates.

Table S9. Total capital investment, fixed capital investment, and working capital, calculated based on the total equipment costs (C_{total}).

Cost type	Percentage of C_{total}
Installation	$47\% \cdot C_{total}$
Instrumentation & control	$36\% \cdot C_{total}$
Piping	$68\% \cdot C_{total}$
Electrical systems	$11\% \cdot C_{total}$
Buildings	$18\% \cdot C_{total}$
Yard improvements	$10\% \cdot C_{total}$
Service facilities	$55\% \cdot C_{total}$
Indirect costs (I)	
Engineering & supervision	$33\% \cdot C_{total}$
Construction expenses	$41\% \cdot C_{total}$
Legal expenses	$4\% \cdot C_{total}$
Costs as function of D and I	
Contractor's fee	$5\% \cdot (D + I)$
Contingency	$10\% \cdot (D + I)$
Fixed capital investment (CI_{fixed})	$486\% \cdot C_{total}$
Working capital ($C_{working}$)	$86\% \cdot C_{total}$
Total capital investment (CI_{total})	$572\% \cdot C_{total}$

Table S10. Working capital, Fixed capital investment, and Total capital investment for different EtOH concentrations with 1 t h^{-1}.

	EtOH feed concentration (wt.%)				
	8	11.5	15	18.5	20
Working Capital ($C_{working}$) in $	569,841	675,048	716,472	865,794	907,445
Fixed capital investment (CI_{fixed}) in $	3,229,098	3,825,270	4,060,007	4,906,166	5,142,187
Total capital investment (CI_{total}) in $	3,798,939	4,500,318	4,776,479	5,771,960	6,049,632

Table S11. Working capital, Fixed capital investment, and Total capital investment for different feed flow rates of 15 wt.% EtOH.

	Feed flow rate (t h^{-1})					
	1	5	10	50	100	160
Working Capital ($C_{working}$) in $	716,472	1,588,449	2,254,232	5,664,924	8,530,972	10,096,848
Fixed capital investment (CI_{fixed}) in $	4,060,007	9,001,214	12,773,982	32,101,237	48,342,177	57,215,472
Total capital investment (CI_{total}) in $	4,776,479	10,589,663	15,028,214	37,766,161	56,873,150	67,312,320

Nomenclature

List of Symbols – Latin Letters

A Air cooler's heat transfer area (m^2)

A_b Tube bundle area in an air-cooler (m^2)

A_c Cross – sectional area of the gas – liquid separator (m^2)

$C_{A(bulk)}$ Concentration of the limiting reactant in the bulk gas phase (mol m^{-3})

$C_{A(surface)}$ Concentration of the limiting reactant on the catalyst surface (mol m^{-3})

C_a Annual capital costs ($)

C_j Purchasing costs of equipment j ($)

$C_{j,ref}$ Reference costs of equipment j ($)

C_{total} Total equipment purchasing cost ($)

$C_{working}$ Working capital ($)

$CAPEX$ Total capital investment ($)

$CEPCI_{2023}$ Chemical engineering plant cost index of the year 2023 (no units)

$CEPCI_{ref}$ Chemical engineering plant cost index of the reference equipment year

CGE Carbon gasification efficiency (%)

CI_{fixed} Fixed capital investment ($)

C_{OL} Operating labor costs ($ a^{-1})

D_{AB} Molecular diffusivity (m^2 s^{-1})

D_b Gas bulk diffusivity (cm^2 s^{-1})

$d_{cat.}$ Apparent density of catalyst (g mL^{-1} or kg m^{-3})

$D_{eff.}$ Effective diffusivity (m^2 s^{-1})

D_{Kn} Knudsen diffusion constant (m^2 s^{-1})

d_p Catalyst pore diameter (nm)

D_v Minimum gas – liquid separator diameter (m)

e_i Specific exergy of stream i in the scaled-up process (kJ kg^{-1})

$e_{i,chemical}$ Chemical exergy of stream i in the scaled-up process (kJ kg^{-1})

$e_{i,physical}$ Physical exergy of stream i in the scaled-up process (kJ kg^{-1})

E_Q Total exergy input for heating purposes (MW)

$\dot{F_{HCs}}$	Hydrocarbons molar flow produced from ethanol gasification (mol h^{-1})
f_L	Fraction of the fully loaded bed in a pressure swing adsorber (-)
F_L	Lang factor (-)
F_{OP}	Number of operators to cover every position in the plant at any time (-)
F_t	Correction factor (-)
F_1	Feed molar flow rate in the pressure swing adsorption units (mol s^{-1})
F_2	Product molar flow rate in the pressure swing adsorption units (mol s^{-1})
$GHSV$	Gas hourly space velocity in the steam reforming reactor (h^{-1})
H	Height of gas – liquid separator (m)
H_i	Enthalpy of stream i in the scaled-up process (kJ kg^{-1})
HHV_i	Higher heating value of stream i in the scaled-up process (kJ kg^{-1})
k_B	Boltzmann's constant (J K^{-1})
k_C	Gas-particle mass transfer coefficient (m s^{-1})
L'	Effective tube length in an air-cooler (m)
M_a	Mass of the adsorbent in a single bed in a pressure swing adsorber (kg)
$m_{cat.}$	Mass of catalyst (g)
M_{CH_4}	Molecular weight of methane (g mol^{-1})
m_{CH_4}	Mass of methane molecule (kg per molecule)
m_f	Fan motor efficiency in an air-cooler (%)
M_{H_2O}	Molecular weight of methane (g mol^{-1})
$\dot{m}_i$	Mass flow rate of steam i in the scaled-up process (kg h^{-1})
M_w	Molar mass of adsorbed component in a pressure swing adsorber (g mol^{-1})
m_1	Maximum adsorbent loading in a pressure swing adsorber (g $g_{adsorbent}^{-1}$)
m_2	Minimum adsorbent loading in a pressure swing adsorber (g $g_{adsorbent}^{-1}$)
n	Reaction order (-)
$\dot{n}$	Molar flow of a reactant or product (mol h^{-1})
N_{bk}	Number of tubes per bank in an air-cooler (non-dimensional)
$n_{C,prod.gas}$	Moles of carbon in the gasification product gas (mol)
$n_{C,feed}$	Moles of carbon in the feed to the gasification reactor (mol)
n_{Ex}	Exergy efficiency (%)

n_f Fan efficiency in an air-cooler (-)

$n_{Hyd.in\ HCs}$ Hydrogen bound in hydrocarbons (mol)

N_{np} Number of non-particulate processing units in the scaled-up plant (-)

N_{OP} Total number of operators (-)

NPC Net production costs ($ a^{-1})

$OPEX_{dir}$ Direct operating expenditures ($ a^{-1})

$OPEX_{ind}$ Indirect operating expenditures ($ a^{-1})

p Pressure (Pa)

$P_{electric}$ Total electric power required by the process operations (MW)

p_t Tube pitch in an air-cooler (m)

Q Air cooler's cooling duty (W)

Q_j Characteristic capacity of process equipment j (for pumps: $m^3\ h^{-1}$, for gasification reactor: $t\ h^{-1}$, for steam reformer and water-gas shift reactor: m^3, for steam turbine: kW, for heat exchanger: m^2)

$Q_{j,ref}$ Capacity of reference process equipment j (same units with Q_j)

$Q_{reactants}$ Volumetric flow of reactants in the steam reforming reactor ($m^3\ h^{-1}$)

R Radius of the catalyst particles (m)

r Annual interest rate (%)

r_A Reaction rate of the limiting reactant (mol $kg_{cat.}^{-1}\ s^{-1}$)

R_{Hb} Ratio of H_2 bound in hydrocarbons to total H_2 (%)

Re Reynolds number

$\frac{S}{C}$ Steam to carbon ratio (mol mol^{-1})

Sc Schmidt number (-)

Sh Sherwood number (-)

S_i Entropy of stream i in the scaled-up process ($kJ\ kg^{-1}$)

SV Space velocity in the gasification reactor ($g_{feed}\ l_{reactor}^{-1}\ h^{-1}$)

t_a Adsorption step duration of the cycle in a pressure swing adsorber (s)

t_h Liquid hold-up time in gas – liquid separator (s)

t_P Operating lifetime (years, or a)

T_0 Reference temperature (298.15 K)

U Overall heat transfer coefficient in a heat exchanger (W m^{-2} °C^{-1})

u_t Liquid droplet settling velocity (m s^{-1})

u_f Air face velocity in an air-cooler (m s^{-1})

V_b Bulk catalyst volume (cm^3 g^{-1})

$V_{cat.bed}$ Volume of the catalytic bed in the steam reforming reactor (m^3)

$\bar{v}_{CH_4}$ Methane molecular mean velocity (m s^{-1})

$\dot{V}_L$ Liquid volumetric flow rate in the gas – liquid separator (m^3 s^{-1})

V_p Total catalyst pore volume (cm^3 g^{-1})

$V_{reactor}$ Volume of the gasification reactor (m^3)

$\dot{V}_v$ Gas or vapor volumetric flow rate (m^3 s^{-1})

$Wage_{OP}$ Wage of an operator (\$ a^{-1})

W_f Fan power consumption in an air-cooler (W)

W_{total} Total power consumption of a fan in an air-cooler (W)

X Plant capacity (kg day^{-1})

Y Employee working hours per day per processing step

$Y_{H_2,SCWG}$ Hydrogen yield from supercritical water gasification (%)

$Y_{H_2,SR}$ Hydrogen yield the steam reforming (%)

$Y_{H_2,total}$ Total yield of hydrogen from gasification and steam reforming (%)

Y_i Yield of a product gas *i* during gasification (mol kg^{-1})

Y_{total} Yield of all produced gases during gasification (mol kg^{-1})

y_1 Adsorbed component feed molar fraction in a pressure swing adsorber (non-dimensional)

y_2 Adsorbed component product molar fraction in a pressure swing adsorber (non-dimensional)

List of Symbols – Greek Letters

ΔH enthalpy of chemical reaction (kJ mol^{-1})

ΔP_b pressure drop across the bundle in an air-cooler (N m^{-2})

ΔT_m mean temperature difference (°C)

ΔT_{ln} log-mean temperature difference (°C)

ε porosity (%)

θ_{CH_4} atomic diffusion volume of methane

θ_{H_2O} atomic diffusion volume of water

λ mean free path of methane (m)

ρ_C actual catalyst density (kg m^{-3})

ρ_L liquid density in the gas liquid separators (kg m^{-3})

ρ_v vapor density in the gas liquid separators (kg m^{-3})

σ_{CH_4} methane molecular diameter (Å or cm)

Subscription

BE Break-even

dir Direct

i Component in reactants or products (H_2, CH_4, C_{2+}, CO, and CO_2) or specific stream of the upscaled process (in Chapter 4)

ind Indirect

j Process equipment in the upscaled process

$C, prod.gas$ Carbon in gasification product gas

$C, feed$ Carbon in feed to the gasification reactor

$inlet$ Refers to a reactant either in the gasification or the reforming reactor

$outlet$ Refers to a product either in the gasification or the reforming reactor

LP Low-pressure steam

HP High-pressure steam

Superscription

0 refers to the reference state (298.15 K and 1 bar)

M equipment scaling factor

Abbreviations

AC Activated carbon

BET Brunauer-Emmett-Teller

BPR Back-pressure regulator

BRM Bireforming

CA	Citric acid
CGE	Carbon gasification efficiency
CGO	Ceria doped with gadolinium
CNT	Carbon nanotube
CP	Coprecipitation
CYSZ	Ceria/yttria-stabilized zirconia
CZ	Ceria-stabilized zirconia
DLH	Double-layered hydroxide
DRM	Dry reforming of methane
EtOH	Ethanol
GHSV	Gas hourly space velocity
HTL	Hydrothermal liquefaction
MCM-41	Mobil oil corporation-41
MS	Mass spectrometry
NPC	Net production costs
$OPEX_{dir}$	Direct operating expenditures
$OPEX_{ind}$	Indirect operating expenditures
P_{BE}	Break-even price of hydrogen
PFR	Plug-flow reactor
PR	Pre-reforming
PSA	Pressure swing adsorption
PWS	Paper waste sludge
SBA-15	Santa Barbara-15
SCW	Supercritical water
SCWG	Supercritical water gasification
SER	Steam ethane reforming
SF	Silica fibers
SG	Sol-gel technique
SMR	Steam methane reforming
TGA	Thermogravimetric analysis
TOC	Total organic carbon
TOS	Time-on-stream

TPR	Temperature programmed reduction
WGS	Water-gas shift
WHSV	Weight hourly space velocity
WI	Wet impregnation
XRD	X-ray diffraction spectroscopy

List of Figures

List of Tables

List of Publications

The publications were enlisted in November 2024. An updated list is given in the following links:

- ResearchGate: https://www.researchgate.net/profile/Thanos-Vadarlis
- ORCID: https://orcid.org/my-orcid?orcid=0009-0000-3209-7896
- Google Scholar: Thanos Vadarlis - Google Scholar

Peer-reviewed publications

- Vadarlis A. A.; Angeli S. D.; Lemonidou A. A.; Boukis N.; Sauer J. Catalytic Biomass Gasification in Supercritical Water and Product Gas Upgrading. *ChemBioEng Reviews*. **2023**, *10* (4), 370–398. DOI: 10.1002/cben.202300007.
- Vadarlis A. A.; Neukum D.; Lemonidou A. A.; Boukis N.; Sauer J. Direct steam reforming of the product gas from ethanol gasification with supercritical water. *Int J Hydrogen Energy*. **2024**, *49*, 992–1008. DOI: 10.1016/j.ijhydene.2023.08.108.
- Vadarlis A. A.; Lacerda de Oliveira Campos B.; Lemonidou A. A.; Boukis N.; Sauer J. Supercritical Water Gasification of Ethanol as Biomass Model Compound in Tandem with Steam Reforming: Kinetic Modeling of the Reforming Step and Techno-Economic Analysis of the Integrated Concept. *Ind Eng Chem Res.* **2024**, *63 (39),* 16683-16700. DOI: 10.1021/acs.iecr.4c01486.
- Dutzi, J.; Vadarlis, A. A.; Boukis, N.; Sauer, J. Comparison of Experimental Results with Thermodynamic Equilibrium Simulations of Supercritical Water Gasification of Concentrated Ethanol Solutions with Focus on Water Splitting. *Ind Eng Chem Res* **2023**, *62* (32), 12501–12512. DOI: 10.1021/acs.iecr.3c01595.
- Neukum, D.; Nilayam, A. R. L.; Ludwig, M. E.; Vadarlis, A. A.; Grunwaldt, J.D.; Saraçi, E. Continuous flow oxidation of HMF using a supported AuPd-alloy. *Cata. Sci. Technol.* **2024**, *14* (8), 2130–2138. DOI: 10.1039/D3CY01722B.
- Vadarlis A. A.; Neukum D.; Dutzi J.; Lemonidou A. A.; Boukis N.; Sauer J. Supercritical water gasification and subsequent steam reforming of the product gas under elevated

temperature and pressure. *Int J Hydrogen Energy*. **2025**, *111*, 567-580. DOI: 10.1016/j.ijhydene.2025.02.197.

Patent submission

Boukis, N.; Vadarlis, A. A.; Sauer, J. Process for Producing Hydrogen and Carbon Dioxide from Organic Substances. EP4166499A2, DE102021126595A1, April 20, 2023.https://depatisnet.dpma.de/DepatisNet/depatisnet?action=bibdat&docid=DE102021126595A1 (accessed 2024-08-09).

Conference oral presentations

Vadarlis A. A.; Boukis N.; Sauer J. Generation of hydrogen by supercritical water gasification and sequential steam reforming. *31st European Biomass Conference & Exhibition*, Bologna, Italy, June 5-8, 2023.

Conference poster presentations

- Vadarlis A. A.; Lacerda de Oliveira Campos B.; Lemonidou A. A.; Boukis N.; Sauer J. SCWG of biomass model compounds with subsequent steam reforming of hydrocarbons for increased H_2 production. *Annual Meeting on Reaction Engineering and Electrochemical Processes 2024, DECHEMA*, Würzburg, Germany, May 6-8, 2024.
- Vadarlis A. A.; Boukis N.; Sauer J. Generation of pure hydrogen from wet waste biomass via gasification in supercritical water and sequential reforming of the hydrocarbons. *5th Doctoral Colloquium Bioenergy*, Leipzig, Germany, September 13-14, 2022.
- Vadarlis A. A.; Boukis N.; Sauer J. Generation of pure hydrogen from wet waste biomass via gasification in supercritical water and subsequent steam reforming. 4*th Doctoral Colloquium Bioenergy*, Karlsruhe, Germany, September 13-14, 2021.